Geo-Referenced Digital Data Acquisition and Processing System Using LiDAR Technology

Charles Toth[1], Ph.D. and Dorota A. Grejner-Brzezinska[2] Ph.D.
Center for Mapping[1]
Department of Civil and Environmental Engineering and Geodetic Science[2]
The Ohio State University

for the
Ohio Department of Transportation
Office of Research and Development

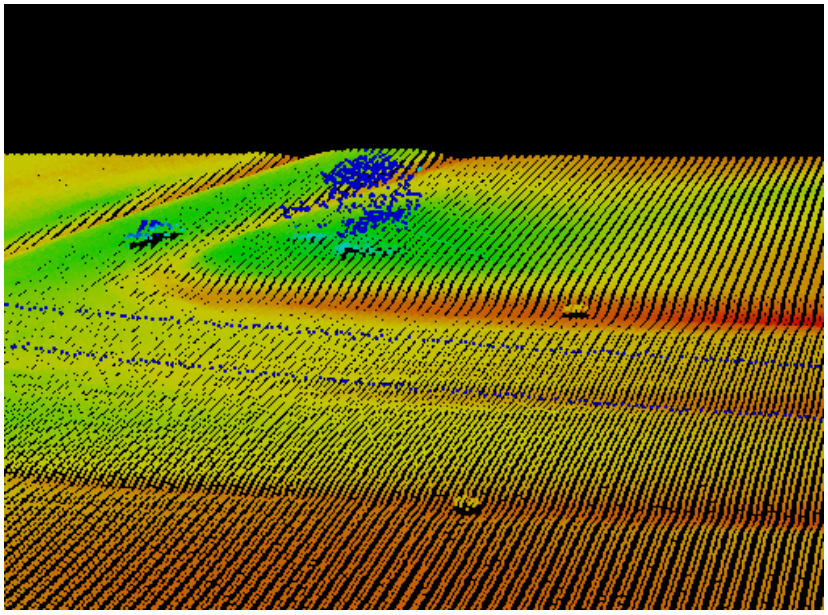

State Job Number 14799

February 2006

RESEARCH & DEVELOPMENT

1. Report No.	2. Government Accession No.	3. Recipient's Catalog No.
FHWA/OH-2006/5		

4. Title and subtitle	5. Report Date
Geo-Referenced Digital Data Acquisition and Processing System Using LiDAR Technology	**February 2006**
	6. Performing Organization Code

7. Author(s)	8. Performing Organization Report No.
Charles Toth, Ph.D. **Dorota A. Grejner-Brzezinska, Ph.D.**	
	10. Work Unit No. (TRAIS)
9. Performing Organization Name and Address	
The Ohio State University **Center for Mapping** **1216 Kinnear Road** **Columbus, Ohio 43212**	11. Contract or Grant No. **147990**
	13. Type of Report and Period Covered
12. Sponsoring Agency Name and Address	
Ohio Department of Transportation **1980 West Broad Street** **Columbus, Ohio 43223**	14. Sponsoring Agency Code

15. Supplementary Notes

16. Abstract

LiDAR technology, introduced in the late 90s, has received wide acceptance in airborne surveying as a leading tool for obtaining high-quality surface data at decimeter-level vertical accuracy in an unprecedentedly short turnaround time. State-of-the-art LiDAR systems can easily achieve 2-3 cm ranging accuracy, which is certainly the accuracy range required by engineering-scale mapping. However, this is also the accuracy range that cannot be realized by routine navigation-based direct sensor platform orientation. The main objective of the project was to achieve this accuracy as closely as possible and then introduce it into the daily operation of ODOT Office of Aerial Engineering. Several tests confirmed that by using LiDAR specific ground targets, engineering-scale mapping accuracy can be achieved in normal production. The final report presents surface modeling studies, sensor calibration developments, the concept and design of LiDAR specific ground targets; followed by performance validation results, based on test flights performed by the OAE staff and preliminary investigation of image fusion with LiDAR data.

17. Key Words	18. Distribution Statement
LiDAR, QA/QC	No restrictions. This document is available to the public through the National Technical Information Service, Springfield, Virginia 22161

19. Security Classif. (of this report)	20. Security Classif. (of this page)	21. No. of Pages	22. Price
Unclassified	Unclassified	**189**	

Project title:

Geo-Referenced Digital Data Acquisition and Processing System Using LiDAR Technology

SJN: 14799

Authors:

Charles Toth and Dorota A. Grejner-Brzezinska

Research Agency:
The Ohio State University

Report date: June 2005

Sponsoring Agency
Ohio Department of Transportation, Office of Aerial Engineering

Prepared in cooperation with the Ohio Department of Transportation and the U.S. Department of Transportation, Federal Highway Administration

Disclaimer

The contents of this report reflect the views of the authors who are responsible for the facts and the accuracy of the data presented herein. The contents do not necessarily reflect the official views or policies of the Ohio Department of Transportation or the Federal Highway Administration. This report does not constitute a standard, specification or regulation.

Acknowledgments

The authors thank the staff of the ODOT Office of Aerial Engineering for their contributions to this project. In particular, we want to express our gratitude to John Ray, Administrator, Office of Aerial Engineering, for his continuing support and coordination of the system acquisition and the field testing.

Table of Content

List of Figures and Tables

1. INTRODUCTION

State-of-the-art airborne mapping is in major transition, which affects both the data acquisition and data processing technologies. The Information Technology (IT) age has brought powerful sensors and revolutionary new techniques to acquire spatial data in large volumes, rapidly, and at an accuracy level that was unprecedented in past production.

New positioning sensors, such as integrated Global Positioning Systems and Inertial Navigation Systems (GPS/INS), provide for the first time the capability to acquire sensor orientation through direct physical measurements and, thus, they provide the indispensable platform orientation for emerging active sensors such as LiDAR and Radar. Improved Light Detection and Ranging (LiDAR) systems, which have been in use for global scientific research for decades, have finally reached a performance level (increased data rate, higher flying heights, and better accuracy - all at an affordable price) that enables them to be put into production. In fact, LiDAR technology became the main source of Digital Elevation Model (DEM) and Digital Surface Model (DSM) in the early years of the third millennium and now it offers substantial benefits over traditional surface extraction techniques.

The major focus of this research effort was the seamless introduction of a highly automated multi-sensor image data acquisition and processing technology into the daily operations of the ODOT Office of Aerial Engineering (OAE). The direct geo-referencing component that had been implemented in the office of OAE just before this project started provided the necessary basis for the establishment of the new LIDAR-based technology.

The introduction of LIDAR into OAE daily operations posed real challenges since, besides the very different hardware (as compared to the traditional imaging sensors), the characteristics of the data, as well as the type of required processing, were significantly different from the methods used in the past. Therefore, the main objectives were: 1) to provide support for the procurement phase so that the system would have optimal configuration with respect to ODOT specific needs; 2) to assist in developing and implementing the workflow for the data processing and to assure a complete and seamless solution strategy; 3) to establish Quality Assurance/ Quality Control (QA/QC) procedures, which are essential to LIDAR systems due to the lack of redundancy in range data; 4) to develop techniques for LIDAR advanced post-processing to eliminate artifacts over flat areas; 5) to initiate research on fusion of LIDAR data with simultaneously acquired digital imagery, which will ultimately help both the ortho-production and the surface extraction process; and, 6) to provide training and technical support for ODOT personnel.

2. RESEARCH OBJECTIVES

The primary objectives of this research project were as follows:

- To introduce a new airplane sensor suite configuration integrated from commercially available sensor components,
- To increase the standard accuracy of LiDAR systems so that true design quality is achieved,
- To carry out test flights to benchmark the performance of the procured LiDAR system,
- To perform the extended quality assurance analysis based on the above mentioned airborne tests with ample ground control,
- To consult ODOT personnel in GPS/INS technology/data acquisition and processing,
- To consult ODOT personnel on future developments such as the introduction of high-resolution digital photogrammetric cameras.

3. GENERAL DESCRIPTION OF RESEARCH

3.1 LiDAR Overview

LiDAR technology, introduced in the late 1990s, has received wide acceptance in airborne surveying as a leading tool for obtaining high-quality surface data in an unprecedented short turnaround time. The adoption of the new technology was fairly smooth and quick, primarily due to the high-level of automation of the data processing. With increasing numbers of the systems sold, vendors have been able to refine the technology rather quickly, delivering a continuously improving performance, measured in terms of number of points. Not only has the number of points per surface area increased, but the number of returns has increased and the intensity signal has become available.

Without any doubt, LiDAR (also called airborne laser scanning) systems have established themselves as a dominant player in high-precision spatial data acquisition (Flood, 1999) in the last four to five years. Installed in aircraft and helicopters, these active sensor systems can routinely deliver surface data at decimeter-level vertical accuracy in an almost totally automated way. There has not been any revolutionary advancement in the laser sensing technique; gradual technological developments characterized the LiDAR systems developments. Figure 1 shows the progress in the number of pulses per second rate (PRF). The post spacing seems to drive the market, and about a 10 times increase in pulse rate produced about a 3-4 times increase in post spacing. The increasing point density not only results in better DEM or DSM data but, also opens up new applications, such as feature extraction, including mainly building and road extraction (Vosselman and Dijkman, 2001).

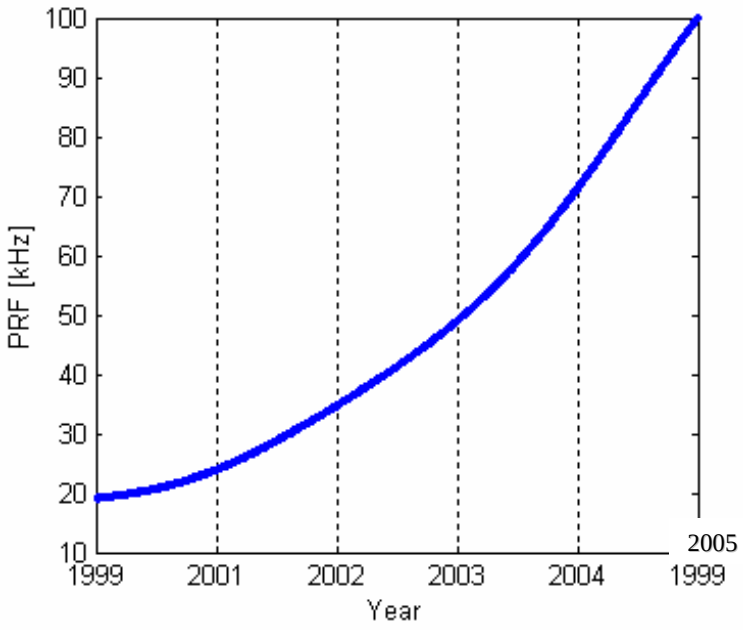

Figure 1. LiDAR pulse rate trend.

The number of returns and the intensity data developments for the same time period are shown in Table 1.

Year	1999	2000	2001	2002	2003	2004
Returns+Intensity	2-5	2-5	2-5 + 2	2-5 + 2	4 + 4	4 + 4

Table 1. Number of returns and intensity data availability.

There is an accelerating trend in both statistics, so the prediction of the future is clearly a challenging task. Even though it is not directly a technological trend, it is important to see the number of systems installed in the industry, too, as only a healthy market can sustain strong future system developments, see Table 2 and Figure 2.

Year	1999	2000	2001	2002	2003	2004
Systems Sold	17	15	13	12	24	25
Total Systems	37	52	65	77	101	126

Table 2. Number of system sold yearly and total number of systems installed.

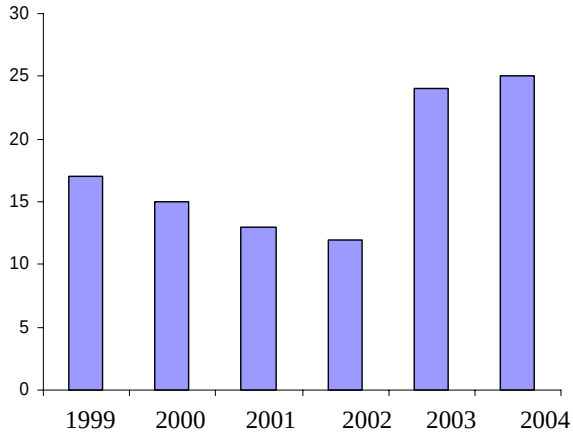

Figure 2. Number of LiDAR systems sold.

The key issue of the LiDAR technology is: what accuracy can be achieved, under what conditions, and how this accuracy impacts the end products. In general, the error budget of LiDAR mapping systems depends on individual error budgets of the core subsystems, such as navigation sensors and the laser range finder. The contributions come from a wide range of various sensory errors. For example, the range finder accuracy is driven by the time measuring performance of the receiver electronics, optical mismatch between transmitter and receiver, scanner angle encoder errors, sensor mounting bias, etc. The navigation component accuracy depends on the quality of the actual GPS and the Inertial Measurement Unit (IMU) sensors, and the methods of their integration (loose vs. tight model), as well as the Kalman filter design and the adopted error models. Other factors are the spatial relationships between the sensors such as lever arm, defined as the offset between the GPS antenna and the IMU frame, and the boresight misalignment, i.e., the angular biases between the navigation and imaging sensor frames. Then there are errors, which are independent from the instrumentation, such as GPS constellation during the survey (satellite geometry or Position Dilution of Precision (PDOP)), the baseline length, the atmospheric conditions, the flying height, terrain undulation and the material signature. To realize the maximum potential of a LiDAR system, all these error sources should be adequately modeled and estimated.

The overarching objective of the project was to ensure that the optimal accuracy of OAE's new LiDAR mapping system would be achieved and maintained in production, including both the primary data acquisition system and the data processing in the office. Although the LiDAR system manufacturing industry is rather small, there are still various parameters/options in the main systems which represent more than two thirds of the total market. In addition, besides turnkey solutions, there are custom-built systems, which can be tailored to various clients' needs.

3.2 Procuring the LiDAR System for OAE

The procurement of the LiDAR system was based on a careful analysis of the transportation specific needs of OAE. Since the OAE handles a large volume of mapping data every year, the efficiency of data processing is of utmost interest (besides the timeliness and accuracy of the final products). Hence, the main thrust of

the proposed research was to address the requirements of the office data processing. After the initial analysis and then discussion with OAE personnel, the decision was made to consider the two market-leader LiDAR vendors, Optech and Leica.

In the summer of 2002, both major LiDAR manufacturers had a chance to present their products and services at the Arial Engineering office. Both presentations were excellent and thus both vendors were invited to the next step of the experimental comparison of the two systems. During the discussions with the two vendors, a set of objectives were worked out with respect to test flights. Both companies agreed to do demo flights either here in Columbus or at their headquarters. The target LiDAR surveys were to include data collected over various roads at different altitudes and in multiple sessions. More specifically, low flying height missions were to be flown with different scan rates to collect data. Using the highest scan rate, data were to be collected to achieve a near even distribution of the LiDAR points on the ground. In repeat missions, high LiDAR point density profiles were expected to be collected, in other words the point density along the profiles would be high compared to the distance between the profiles. These low altitude missions could provide experimental data to assess the achievable quality for design engineering scale LiDAR mapping. Missions to be flown at a higher altitude were less critical in terms of performance as their purpose was planning level mapping. In addition, research would address the optimal definition of ground targets used for LiDAR calibration and performance validation.

By fall 2002, both selected vendors submitted their demo datasets, which were acquired during dedicated missions specified by OAE of ODOT. After intensive processing of these datasets, a comparative analysis of the performance was prepared. In addition to the visual interpretation, the LiDAR processing tools that were developed in the project were extensively used. The performance evaluation provided the technical data for issuing a request for bid and later to support the decision making process on which of the two systems would be acquired. The request for bid is in Appendix A.

In early April, 2003, both vendors submitted their quote in response to the RFQ sent to them in March, 2003. The process of selecting the right system for ODOT OAE was based on the documentation submitted with the quotes, additional phone conversations conducted with the vendors, phone conversations with users suggested by the vendors as references, and evaluation of test LiDAR data acquired earlier by both vendors. The evaluation process was a rather complex task as the specifics of the corridor mapping operations of ODOT OAE are different from mainstream LiDAR mapping and therefore limited prior information was available for comparing the two systems. The decision, in fact, was a rather difficult task as both systems are powerful and careful attention had to be paid to properly assess which one could better support the specific needs of high-precision road mapping. The key aspects that determined the selection of the Optech system were:

1) Optech offered a free upgrade to a higher frequency to 70 kHz. This information had been known to us but was not spelled out in the quote as the introduction of the new system and the press release were scheduled for the ASPRS 2003 Convention, May 5-9, 2003. The higher frequency is a decisive

factor for ODOT OAE as it serves the very dense sampling requirements needed to observe the pavement surface at high accuracy. In simple terms, the performance ratio measured in points per price between the systems changed more than the price difference between the two systems. In addition, the variable frequency rate offered by Leica was less attractive from an operational point of view. The comparison by ODOT OAE on this subject is included in Appendix A.

2) The Optech system was compared to the Leica system, which is a more open system and certain parts were still being developed at the bidding time. ODOT personnel are new to LiDAR and preferred simple operations with hopefully fewer complications.

3) The test datasets revealed some quality differences between the two systems. Specifically, the intensity signal was notably better in the Optech system. The range data were comparable, albeit the Optech system showed a slightly better spatial distribution.

In summary, the performance of the Optech system appeared considerably better than the performance of the Leica system, and with the sponsor, the agreement was reached that the value of the Optech system was justified. However, before the order was issued there was one more item, an accompanying digital camera procurement, that had to be decided. In the proposal, there was a 4K by 4K Megaplus camera budgeted; basically, representing a $100,000 hardware cost, assuming the no-cost availability of software that had been developed earlier at The OSU Center for Mapping for a similar system. However, two years had passed since the time of preparing the proposal and the medium size digital camera market changed a lot. By 2003, both vendors could offer 4K by 4K integrated camera systems. Therefore, discussions between ODOT OAE and OSU resulted in significant changes to the original scope and tasks of the project. In short, a $250,000 digital camera was added to the LiDAR purchase order. To offset the price difference, ODOT increased the funding by $150,000. In addition, the price of the Optech LiDAR system was also higher than budgeted. Therefore, some of the research tasks to be performed by OSU were also removed from the project to offset about a $100,000 shortage. The details of the agreed changes are in Appendix B.

The long-awaited acceptance test flight of the purchased Optech system took place in Toronto, Canada, on February 19, 2004. During the one hour flight, both the Optech 30/70 ALTM LiDAR and the DDS 4K by 4K digital camera worked well, and the initial data reduction right after the flight showed quality results. The system was shipped late spring to ODOT, but due to unexpected delays in airplane procurement, the system was installed only in the fall. The Delivery Performance Reports were based on the data flown on October 22-25, 2004. The first dedicated test flight using LiDAR specific ground controls developed in the project took place on December 2, 2004.

3.3 Research Developments to Support OAE LiDAR Operations

The accomplished research tasks were primarily concerned with the development of a LiDAR-based map production system where the accuracy requirements were driven

by the specifics of OAE operations. The algorithmic developments, techniques researched, and programs developed are discussed in the Results section.

4. RESULTS

The scientific progress has been continuously documented in journal papers and conference proceeding papers. All the relevant and related papers are included in Appendixes C-F.

4.1 Surface Modeling

Due to the irregular distribution of the LiDAR point cloud, interpolation is an essential component for any LiDAR data processing. On one side, most of the applications dealing with surfaces require evenly-spaced data (grid). On the other side, quality control and calibration processes involve surface comparisons, which, again, cannot be directly performed on unevenly-spaced data. Therefore, interpolation methods have been studied to accomplish this task. After searching the literature and reviewing available implementations, it was found that none of the widely used methods is tailored to the characteristic of the LiDAR point distribution and error characteristics. Testing several methods on real data, the decision was made to develop two techniques: (1) a Fourier-series based, and (2) a wavelet-based. The first method is a combination of polynomial and Fourier harmonics representations. The coefficients for both groups of parameters are determined in a least squares adjustment. The technique has been extensively tested and results are reported in Appendix C. The wavelet-based model produced an excellent tool for compressing the data. However, the irregularly spaced input data cannot be directly handled by wavelets at this point and no solution has been found to circumvent this problem. Obviously, if the data are converted to a grid then the wavelet method works fine. As the grid conversion is a key step, once it is done all the processing such as surface comparisons can be done without wavelets.

4.2 LiDAR Sensor Calibration and Processing

Sensor calibration is essential in achieving the highest quality data from any measurement system. LiDAR data are an excellent source of high volume and reasonably accurate spatial data; however, the points are featureless; in other words, there is no direct correspondence between the surface and the reflected points (such as whether a point was generated from a road surface, from a car, or from a building). The introduction of LiDAR intensity data or waveform certainly addresses this problem to some extent (the difficulty is the relative nature of the LiDAR intensity signal). The assessment of the LiDAR data is a non-trivial problem in this context. In addition, the moving component of the sensor system (rotating mirror) represents another difficulty of direct calibration. For these reasons, methods that deal with a larger amount of points, and possibly with a good spatial distribution over surface area from where they were collected, are favored for LiDAR calibration. In our investigation, we focused on the geometrical calibration of the system. Obviously, the waveform and travel time calibration tasks are equally important, but they are usually well controlled by the manufacturer's calibration. For example, cm-level ranging

accuracy can be routinely achieved for a single laser pulse over a km range. The increasing pulse rate, however, could present a problem as it comes with smaller laser pulse energy, and thus the lower Signal-to-Noise-Ratio (SNR) could impact the ranging accuracy. For that reason, an intensity table-based correction has been standardized. So the big question remains how well this accuracy can be approached under normal operations. Eventually, there are two major components in modeling of the geometrical behavior of a LiDAR system that are crucial in achieving high spatial accuracy: scan angle calibration and boresight misalignment. The first component compensates for the non-ideal encoding of the rotation sensor by establishing a correction profile. This task is usually accomplished by collecting data over a large flat area and then by analyzing the LiDAR measured surface. Without correction, just by directly using the encoder data, a surface bending up at the edges is obtained. The phenomenon is usually called "smiley" error. Applying the correction, the surface will flatten out. Since this task is rather simple, manufacturers as well as users can perform it so there was no effort in our project to address this calibration task (although, it can be built into our boresight misalignment technique). The spatial connection between the navigation system and the laser scanner is described by the boresight transformation. The mechanical adjustment of the two systems never can be so good that it would satisfy the required accuracy requirements. Therefore, calibrating for this discrepancy is important and is usually called boresight misalignment. Substantial efforts were devoted to address this problem, and the method developed, including results, is reported in Appendix D. It is important to note that to achieve the ultimate accuracy a further non-physical model based model can be used, which obviously requires the direct use of object space information such as dedicated LiDAR ground control targets that is discussed as a separate research item. To support the automated LiDAR boresight misalignment process, a segmentation of the LiDAR points is needed and therefore this task was addressed in our project. Results of the selected and refined segmentation are reported in Appendix D.

4.3 Using LiDAR-Specific Targets for Ground Control

The use of LiDAR-specific ground control targets represented a novel idea, not explored in practice yet. Therefore, extensive simulations were performed to determine a favorable LiDAR-target design, including optimal target size and shape, signal response, coating pattern, and methods to accurately determine the 3-dimensional target position in the LiDAR dataset. The horizontal target position is found by an algorithm similar to the generalized version of the Hough-transform (Hough, 1959). Duda and Hart (1972) first introduced the generalized version of the Hough transform to detect curves. The search is based on the known radius of the target circle; the process finds all the possible locations of the target circle center in a grid. To automate the processing of the target-based correction of LiDAR data, a software toolbox was developed. Simulation results indicated that at 5-10 points/m^2 LiDAR point density, circular 2-3 m diameter sized flat targets could provide sub-decimeter accuracy at virtually any flying height. In two manufacturing phases, OAE produced targets in a few varieties for testing. The detailed description of the developed method, including initial simulations, the optimal target design, and then test results based on two test flights are presented in Appendix E, providing a detailed performance analysis on the achievable improvements in LiDAR data accuracy using the LiDAR-specific ground control targets.

4.4 LiDAR and Image Fusion

With the addition of a 4K by 4K digital camera to the LiDAR system, a new objective presented itself to the project: to study and possibly create a technique to fuse LiDAR and image data to obtain better surface reconstruction and support the feature extraction of objects/targets. The difficulty of the fusion of LiDAR and image data lies in the correspondence problem. In other words, the LiDAR provides good but featureless points in space, while image data is weaker in geometry but provides a good amount of information on objects. As the formation of images represents a projection from 3D to 2D, the recovery of any 3D information requires the use of at least two (or more) overlapping images in order to recover the third lost dimension. Obviously, this photogrammetric process cannot easily compete with the excellent positioning accuracy of a LiDAR range measurement, which directly delivers a highly accurate 3D location. Comparing the error characteristics of the two datasets, the following can be said. The LiDAR points have excellent vertical accuracy and a somewhat modest horizontal accuracy, which is due to the unknown location of the return signal within the LiDAR footprint. In contrast, the multiple-image derived surface points (typically obtained from stereo) exhibit a slightly different characteristic such as better horizontal accuracy and somewhat modest vertical accuracy. Another important aspect is the dependency on the distance between the sensors and the objects. With higher flying height, the vertical accuracy remains more or less constant for the LiDAR; for the image-derived data there is a linear dependency on the flying height. After various models and testing, a method was investigated that addressed the problem of merging surface points from different sources in a very general way (although we used it only for LiDAR and image data). The heart of the concept is the individual description of the spatial error terms of the individual points. The points can come from multiple sources such as repeated LiDAR flights over the same area, and/or stereo-based points from single or multiple flights. Once the input points are defined, the objective is to find a surface that fits in an optimal way to all the input points in least squares terms. The problem as described is ill-posed and no direct answer is available. Our investigated solution is based on converting the horizontal accuracy terms into vertical ones and thus fixing the horizontal location of the points. This way, the problem becomes manageable, as a least squares adjustment can be formulated to optimize the RMS for all of the points. A question is what description of the surface is used. Obviously, the developed technique can be applied to any surface modeling method as long as there is an analytical description available. In our tests, the Fourier series and polynomial based surface modeling described above was used. The fusion method and initial results are also described in Appendix F. As the DDS digital camera offers a moderate spatial resolution (measured in GSD), the quality of DEMs extracted from this imagery is not always adequate to support fusion.

4.5 Software Developments

During the course of the project extensive code developments were carried out. Matlab environment represented the basic platform for algorithmic implementation and testing. All the simulations were carried out in Matlab. Then, once the techniques had settled, the performance critical components were transferred to Microsoft Visual

Studio, C++ environment. A large number of Matlab routines are available in different categories such as space-image forward/backward transformations, area-based correlation, least square matching, calibration, various 3D transformations, etc. Most of the macros can be easily reused for other purposes. The main outcome of the implementation of the LiDAR-specific ground control correction technique is the LIFT program (LiDAR and Image Fusion Technology). The program manual is in Appendix G.

5. CONCLUSIONS

LiDAR can routinely provide adequate accuracy to mainstream (basic) mapping projects – typical quoted vertical accuracy is about 50 cm at 90% Circular Error (CE), but 15-20 cm is also achievable under well-controlled circumstances. The main difficulties of improving accuracy are: the quality of the navigation solution can vary a lot, and the laser scanning device is a complex electro-optical-mechanical system that lacks the long-term stability; and thus, it's static calibration is not satisfactory. General practices to improve accuracy are: calibrating laser sensor by comparing overlapping strips and eliminating differences, and use flat vertical with known elevation to determine and then apply vertical offset to improve absolute accuracy of the acquired data.

To achieve or approach the theoretical limits of the LiDAR sensor ranging accuracy, which is about 2-3 cm at 67% CE, our research efforts focused on the only technique which offers a solution for both problems (navigation and sensor calibration): using ground control. We pursued intensive research to develop a LiDAR-specific target methodology. Extensive simulations were carried out to find out the optimal shape, size and coating pattern of the targets. The major findings were: 1) circular-shaped flat targets, horizontally leveled and elevated, could represent an optimal design, 2) obviously, the larger the size the better positioning accuracy; however, the results showed that at about 5 points per m^2 point density 2-3 m diameter size could already provide sufficient accuracy and further increasing the size wouldn't lead to measurable improvements, and 3) using two concentric circles (inner circle is about half the size of the outer one) with different coating (dissimilar reflection parameters) could produce a substantial difference in horizontal positioning accuracy. The typical expected accuracies, based on our simulations for a 5 points per m^2 density were about 5 cm (67% CE) vertically and about 10 cm (67% CE) horizontally. In this case, the laser footprint was 15 cm and the laser ranging accuracy was assumed to be 3-4 cm (67% CE), representing typical values for the Optech 30/70 system.

Based on the simulation results, actual targets were fabricated by OAE personnel and flight tests were carried out to validate the performance of the newly developed methods with real LiDAR data. A scaleable adjustment algorithm was developed and implemented to adjust the LiDAR data and to automate the overall data processing. The developed software can handle the following typical configurations: 1) single vertical shift compensation (z only), 2) three-dimensional transformation to account for horizontal discrepancies (in addition to the vertical one), 3) strip adjustment – each flight line has its own correction parameters, 4) segmented strip adjustment – strip is

divided into smaller segments for individual corrections, and 5) block adjustment – all the flight lines are adjusted in one step.

To assess the achievable accuracy improvement using the designed LiDAR-specific targets for LiDAR data refinement, data from two test flights were analyzed. The first test flight in Ashtabula, OH, was aimed at infrastructure mapping of a transportation corridor. To support our investigations 15 pairs of targets were placed symmetrically along the two sides of the road. The second test flight at the Madison Calibration range was a dedicated test flight for investigating the target identification accuracy and the effect of targets in the improvement of LiDAR data accuracy for various LiDAR settings and target densities. Results proved that the algorithms developed to determine ground target center coordinates in LiDAR data could provide 5-10 cm horizontal positioning accuracy (at 25 cm footprint size) and 2-3 cm vertical accuracy of the target coordinates at 5 points/m^2 LiDAR point density. Consequently, larger than 10 cm horizontal errors in the LiDAR data and vertical errors larger than 2-3 cm can be detected and corrected using the LiDAR targets.

6. IMPLEMENTATION PLAN

The OSU staff worked in close collaboration with ODOT OAE personnel to assure that all functional aspects of the system's operation were followed during the field procedure. This included test flights, calibration and training seminars for the OAE staff.

The system is fully implemented and installed in the OAE airplane, and has been operational since fall 2004. To support daily operations and effective data processing and analysis, the "LIFT" program is included in Appendix G.

BIBLIOGRAPHY

1. Duda R. O., Hart P. E., 1972. Use of the Hough Transformation to detect lines and curves in pictures, *Graphics and Image processing, 15: 11-15*.
2. Flood, M. (1999). Commercial Development of Airborne Laser Altimetry, *International Archives of Photogrammetry and Remote Sensing*, Vol. XXXII, part 3-W14, pp. 13-20.
3. Hough P.V.C., 1959. Machine analysis of bubble chamber pictures, International Conference on High Energy Accelerators and Instrumentation, CERN.
4. Maas, H.G. (2002). Methods for Measuring Height and Planimetry Discrepancies in Airborne Laserscanner Data. *Photogrammetric Engineering & Remote Sensing*, 68(9):933-940.
5. Vosselman, G.,and Dijkman, S., 3D Building Model Reconstruction From Point Clouds And Ground Plans. International Archives of Photogrammetry and Remote Sensing, XXXIV-3/W4:37-43, 2001.

APPENDIX A

Request for Quote
and
Evaluation by OAE (Tables)

Request for Quote

Ohio Department of Transportation, Office of Aerial Engineering, is in the process of procuring a state-of-the-art airborne LiDAR system. They will use it to support operations which primarily includes high-precision corridor mapping of the road network of the State of the Ohio. Therefore, ODOT OAE is seeking quotes on supplying a turn-key LiDAR system with the highest performance available for highway corridor work, including specification, options, financial terms, references, delivery and training schedule, maintenance and technical support. The proposal submitted for this RFQ should at least address the following items.

Anticipated typical operational conditions and objectives:

- Flying height (AGL) is in the 1,000-3,000 ft range.
- Aircraft velocity is in the 100-120 knots range.
- The highest point density with even spatial distribution as much as possible.
- The highest feasible point accuracy in both directions using ground control.

Specification (hardware):

1. Flying height, (FH): lowest and highest (AGL).

Optech	LH Systems
200-2000 m	500-4000 m (can be lowered if needed at no cost – they have done some recent tests at low flying height)

2. Pulse repetition rate (PRR).

Optech	LH Systems
50 kHz – fixed	47.5 kHz @ 1,000m and 36 kHz @ 2,000 at low flying height (< 1,000m) , it can be considered fixed, say 1+1 w/ 52 kHz or 2+2 w/47.5 kHz

3. Maximum scan angle (MSA).

Optech	LH Systems
40° FOV, 20° scan angle	75° FOV, 37.5° scan angle

4. Configuration flexibility/limitations of the FH, PRR and MSA parameters, including aircraft speed.

Optech	LH Systems
FOV, scan rate, adjustable in flight	PRP, FOV, scan rate adjustable in flight between flight lines (PRP is probably not needed as max frequency should be used)

5. Beam divergence control: fixed, switch-able or dynamically controlled, minimum and maximum values.

Optech	LH Systems
0.21 or 0.7 mrad, can be changed in flight (0.7 mrad works with the lowest flying height, 0.21 mrad can be only used for higher flying heights)	0.33 mrad – fixed (0.2 is an option but lowest flying height is affected due to eye-safety)

6. Mandatory roll compensation.

Optech	LH Systems
Yes	Yes (option, $10K)

7. Number of returns and intensity/waveform configuration options.

Optech	LH Systems
2+2 F and L return, waveform option	1+1, 2+2, 3+3, F and 2nd return, waveform option is offered within a year (< $100K)

8. Intensity/waveform signal resolution and noise characteristics.

Optech	LH Systems
13 bit resolution, intensity-based range compensation is available in the software (linear)	8 bit resolution with AGC (AGC can be recorded), intensity-based range compensation is available in the software (binary)

9. Absolute ranging accuracy of the laser sensor system.

Optech	LH Systems
3 cm	2 cm

10. Point measuring accuracy as advertised and typically achieved horizontally and vertically, with and without using ground control.

Optech	LH Systems
Advertised: V:15 cm, H: 1/2000 * altitude Typical: V: <10 cm, H: 1/3000 * altitude	Advertised: V:15 cm, H: 11-46 cm (15 cm) Typical: V: 6-10 cm

11. Main data storage device choices.

Optech	LH Systems
Removable harddrive	Removable harddrive

12. Navigation component choices.

Optech	LH Systems

RT display with moving map	LH Apcot system (optional)

13. Electronic viewfinder capability.

Optech	LH Systems
Video camera, 30 Hz analog	Web-cam, 2-0.2 Hz, (option, $10,000)

14. Standard mechanical system description, including weight, size, operating temperature, etc.

Optech	LH Systems
Yes	Yes

Specification (software):

1. Mission planning support.

Optech	LH Systems
ALTM – NAV	AeroPlane spreadsheet

2. Data acquisition user interface, including in-flight parameter control, monitoring and diagnostics.

Optech	LH Systems
ALTM – NAV diagnostic tools (data gaps)	Yes, but not clear

3. Data processing software, including navigation solution computation, raw point cloud computation, filtering components such as vegetation removal, feature extraction, etc.

Optech	LH Systems
Yes, vegetation removal included but no feature extraction (OEM)	Yes, but no feature extraction (OEM)

4. System calibration and diagnostics tools such as boresighting and using ground control to improve accuracy.

Optech	LH Systems
Yes, Autocalibrator – not clear	Attune and TerraScan/MicroStation

5. Data interface/translator support (LAS format)..

Optech	LH Systems
Yes	Yes

6. Licensing conditions, including number of seats.

Optech	LH Systems
Realm (2), Nav (2) and PosPak (2)	Attune, AeroPlan, ALS Post Processor, PosPak (1), TerraScan/TerraModeler (1) needs MS

Options:

1. Digital camera upgrade options (4K by 4K camera category).

Optech	LH Systems
Yes, Emerge OEM	No (any systems from the market)

2. Future upgrade to higher pulse rate (75-100 kHz).

Optech	LH Systems
Likely	Likely

3. Maintenance and/or extended warranty.

Optech	LH Systems
3-level system	3-year maximum (can be extended w/ similar terms)

4. Bathymetry capability.

Optech	LH Systems
SHOALS	No

5. Any other options appropriate to achieve better performance for highway corridor work.

Optech	LH Systems
No	No

Installation and Training:

1. Onsite and factory installation alternatives.

Optech	LH Systems
Yes, onsite and factory	Yes, onsite and factory (clarified)

2. Onsite training, including mission planning, data collection and data processing.

Optech	LH Systems
5 days before and 5 days after installation	1 wk before and 1 wk after installation (they have a new 3 wk schedule: 1 wk for data processing, then 1 wk for installation

	and testing, then after about a month another 1 wk to address problems/local specifics and so on).

3. Acceptance test.

Optech	LH Systems
Yes	Yes (clarified)

Additional Information:

1. Three references of clients using similar/predecessor LiDAR systems.

Optech	LH Systems
7 references	1 reference (they added EnerQuest and Merrick – can add more if needed)

2. Any supporting information about the company's dedication to assist with operational and data processing problems.

Optech	LH Systems
No	No

Financial Terms:

1. Price of the complete system with itemized quotes for options.

Optech	LH Systems

2. List of deliverables.

Optech	LH Systems

3. Schedule including delivery, installation, training and acceptance test.

Optech	LH Systems

4. Payment terms.

Optech	LH Systems

5. Warranty schedule.

Optech	LH Systems

6. Validity of quote.

Optech	LH Systems

APPENDIX B

Project Changes, April 2003

Changes to Project

Geo-Referenced Digital Data Acquisition and Processing System Using LIDAR Technology

ODOT reference number: 14799(0)
ODOT agreement number: 11322

A. Changes to the **Duration** of the project:

The old project completion date was August 1, 2004
The new project completion date is June 30, 2005

B. Changes to the **Task/Effort**

Original plan:

4.	Purchase of COTS software	1	3807.69													
7.	Road surface mark R&D	15	57115.35													
8.	Material signature correction R&D	15	57115.35													

Modified plan:

4.	Purchase of COTS software	0	0.00													
7.	Road surface mark R&D	6	22971.09													
8.	Material signature correction R&D	0	0													

C. Changes in the **Budget**:

- The cost for equipment purchased for ODOT is increased by **$244,000.00** to provide funding for a 4K by 4K color digital camera system.
- The cost of the research component by OSU is reduced by **$95,067.30** to partially cover the cost of the digital camera system..
- ODOT will provide additional funds of **$150,000.00** to partially cover the cost of the digital camera system.

APPENDIX C

Surface Modeling

1. Wavelet Transformation of LiDAR Data to Support Road Surface Modeling, Internal Report to ODOT, 2003.
2. Csanyi N., Paska E. and Toth C., 2003: Comparison of Various Surface Modeling Methods, Terrain Data: Applications and Visualization – Making the Connection, ASPRS/MAPPS, Charleston, SC, October 27-30, 2003, CD-ROM.

Preliminary Report

on

Wavelet Transformation of LiDAR Data to Support Road Surface Modeling

October 2003

Geo-Referenced Digital Data Acquisition and Processing System Using LIDAR Technology

1. Introduction

1.1. Objectives

The objective of this study is to show how wavelets can be used for efficient representation of LiDAR data and to demonstrate its performance by using a demo software developed for the feasibility test.

1.2. What is Wavelets?

Fourier series is useful mathematical tool for the representation of periodic signals and has trigonometric functions as basis functions. Consequently, we can model any signal by using a finite sum of infinite trigonometric (sine and cosine) series. However, it is not an efficient way to represent signals with Fourier series if we have, for example, piecewise constant signal, in which case, many more terms of trigonometric are needed to obtain the reasonable description. On the other hand, we can represent the original signal with better efficiency if we choose piecewise constant wave function (Haar wavelet function) as a basis function. Obviously, a key question is how to choose the appropriate basis function to model the signal efficiently. Figure 1-1 shows one of simple basis functions which can be used to model the signal.

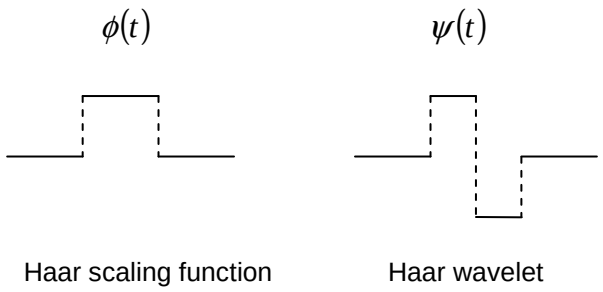

Figure 1-1. Haar scaling and wavelet functions.

Also, all other basis functions can be generated by linear combinations of scales by 2^{-j} and translations by $k/2^{j}$ of scaling and wavelet functions as followings:

$$\phi\left(2^{j}t-k\right) \text{ and } \psi\left(2^{j}t-k\right), \quad j,k \in Z = \{\cdots,-1,0,1,\cdots\}$$

Now, we can construct function spaces with basis functions as followings:

$$V_j = \left\{ \sum_k c_{j,k} \phi\left(2^j t - k\right) : \sum_k \left| c_{j,k} \right|^2 < \infty \right\},$$
$$W_j = \left\{ \sum_k d_{j,k} \psi\left(2^j t - k\right) : \sum_k \left| d_{j,k} \right|^2 < \infty \right\}$$

The subspaces, V and W have the following properties. First, the subspaces V_j, $j \in Z$ are nested such that

$$\cdots \subset V_{-1} \subset V_0 \subset V_1 \subset \cdots,$$

and for each $j \in Z$,

$$V_{j+1} = V_j + W_j \text{ and } V_j \perp W_j$$

where, $\perp$ means that two function spaces are orthogonal to each other.

Also, the unique decomposition is governed by the coefficients a_k, b_k and p_k, q_k in the form

$$\phi(2t - l) = \sum_k \left\{ a_{l-2k} \phi(t - k) + b_{l-2k} \psi(t - k) \right\}, \quad l \in Z.$$
$$\phi(t) = \sum_k p_k \phi(2t - k)$$
$$\psi(t) = \sum_k q_k \phi(2t - k)$$

Now, we can model the original signal as follows:

$$f_n(t) = \sum_k c_{n,k} \phi\left(2^n t - k\right).$$

$$f_n(t) = f_{n-1}(t) + g_{n-1}(t)$$

with $f_{n-1}(t) \in V_{n-1}$ and $g_{n-1}(t) \in W_{n-1}$.

$$f_{n-1}(t) = \sum_k c_{n-1,k} \phi\left(2^{n-1} t - k\right),$$
$$g_{n-1}(t) = \sum_k d_{n-1,k} \psi\left(2^{n-1} t - k\right)$$

1-3. Decomposition and reconstruction algorithm

To find the $f_{n-1}(t)$ and $g_{n-1}(t)$ from f_n, we can use following equations:

$$c_{n-1,k} = \sum_l a_{l-2k} c_{n,l}$$
$$d_{n-1,k} = \sum_l b_{l-2k} c_{n,l}$$

Also, the following equation can be used for the reconstruction of $f_n(t)$ from $f_{n-1}(t)$ and $g_{n-1}(t)$.

$$c_{n,k} = \sum_l \{p_{k-2l} c_{n-1,l} + q_{k-2l} d_{n-1,l}\}$$

1-4. Construction of 2-D wavelet functions

2-D scaling and wavelet functions for Haar wavelet can be obtained by tensor products of 1-D scaling and wavelet functions as followings:

- Two-dimensional scaling function

  $\phi(t_1, t_2) = \phi(t_1)\phi(t_2)$

- Two-dimensional horizontal wavelet

  $\psi^h(t_1, t_2) = \phi(t_1)\psi(t_2)$

- Two-dimensional vertical wavelet

  $\psi^v(t_1, t_2) = \psi(t_1)\phi(t_2)$

- Two-dimensional diagonal wavelet

  $\psi^d(t_1, t_2) = \psi(t_1)\psi(t_2)$

1-5. Descriptions on the wavelet decomposition and reconstruction

To illustrate the decomposition and reconstruction procedures in more detail, arbitrary sample data (similar to a LiDAR profile) are chosen and plotted in Figure 1-2. As shown in the Figure 1-3, each pair of data are added and subtracted after multiplied by ½ to get the decomposed data. Now, we have smoothed the signal in the left hand side and detail signal is in the right hand side. Also, these procedures can be applied to the smoothed

signals to obtain the smoothed and detail signals at the next level. Figure 1-4 shows the full decomposition steps from the original signals. One can also see that most of the data in detail signals are relatively small in amplitude. Moreover, if we have highly correlated signal, we can get many near-zero values in detail signals. Hence, we can use this characteristic of the signal decomposition to data compression by padding zeros in the position of which values are less than a predefined threshold value.

Figure 1-5 shows the reconstruction procedures with predefined threshold value. As can be seen in the Figure 1-5, half of the data points are zeros so that we can save the data storage by using the decomposition and reconstruction procedures.

$$ratio = \frac{\text{Total number of zeros in detail signals}}{\text{Total number of data points}}$$

Also, the RMS value between the original and reconstructed data can be used to determine the quality of reconstructed data and can be computed as follows:

$$RMS = \sqrt{\frac{1}{N}\sum_{i=1}^{N}\left(X_i^{reconstructed} - X_i^{original}\right)^2}$$

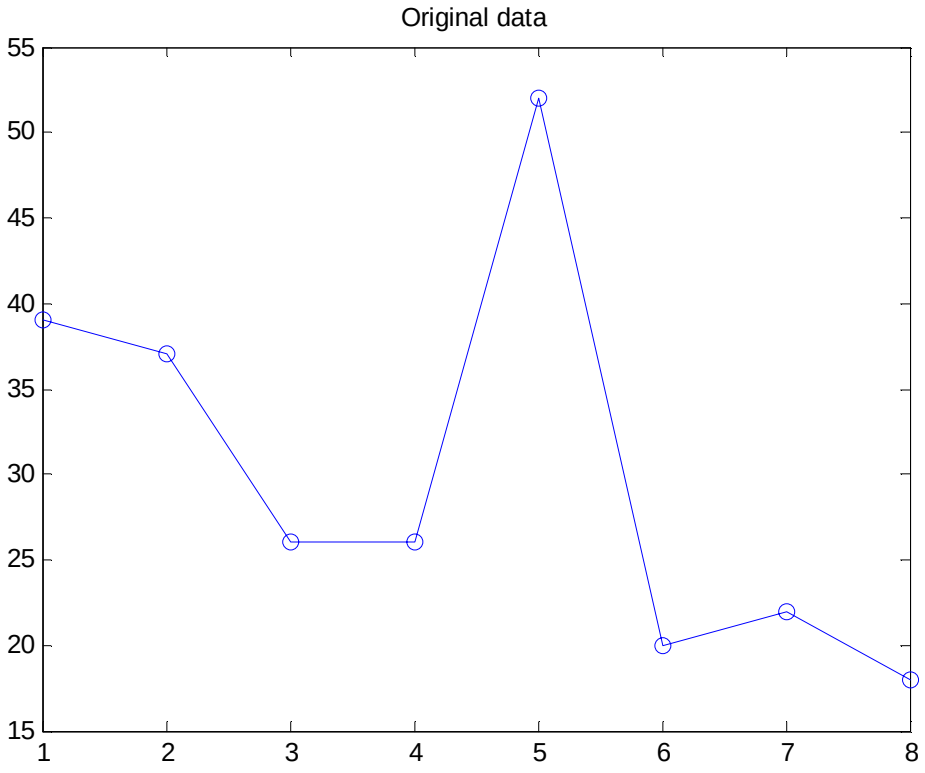

Figure 1-2. Plot of sample data.

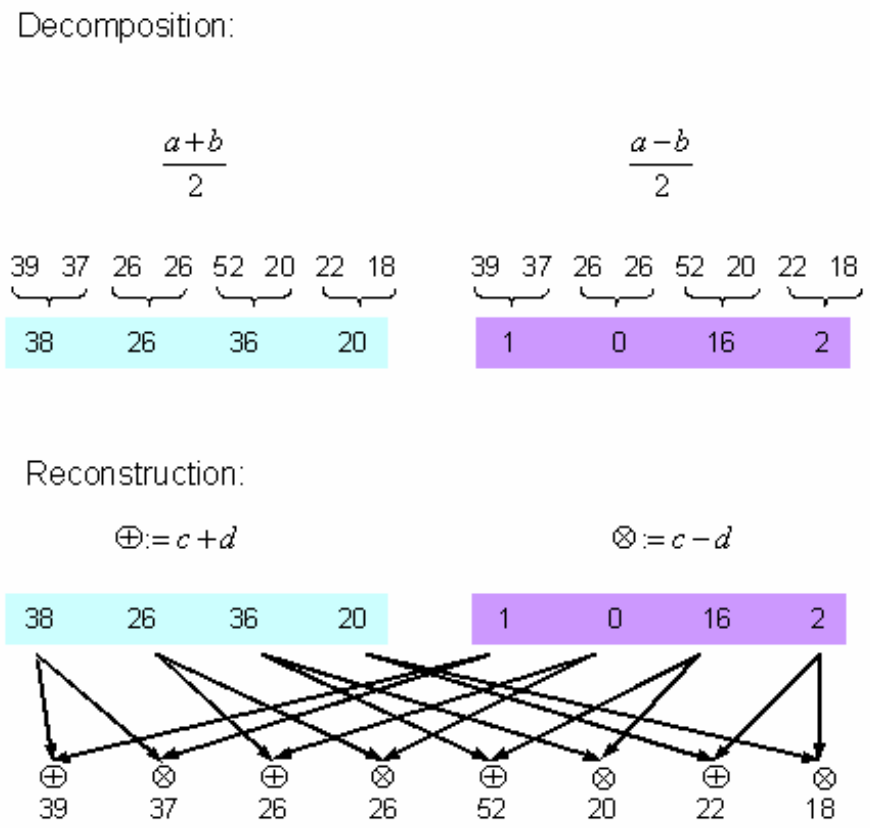

Figure 1-3. Schematic diagram of decomposition and reconstruction steps.

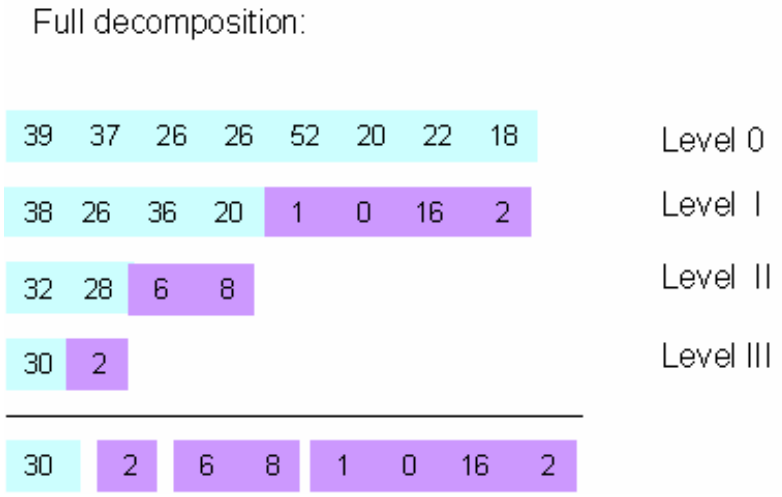

Figure 1-4. Schematic diagram which shows the full decomposition steps.

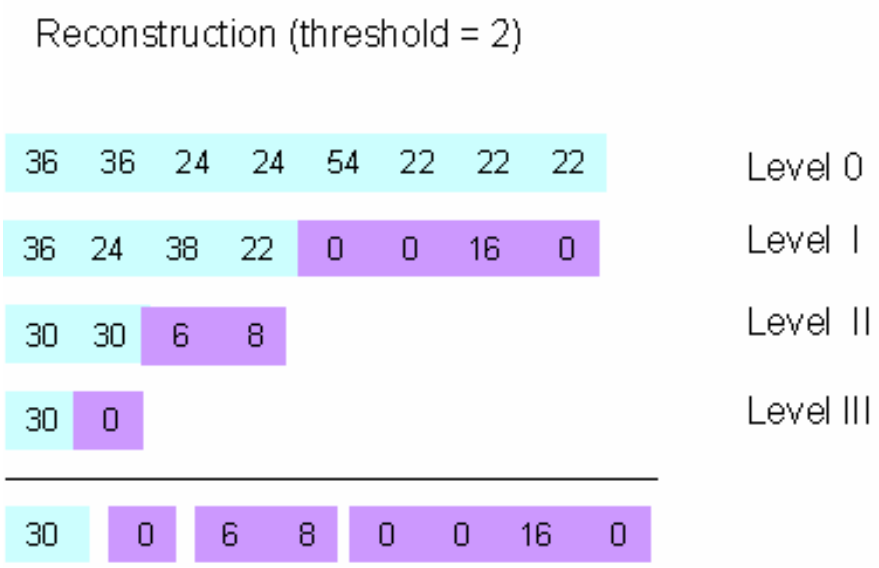

Figure 1-5. Reconstruction procedures with threshold value.

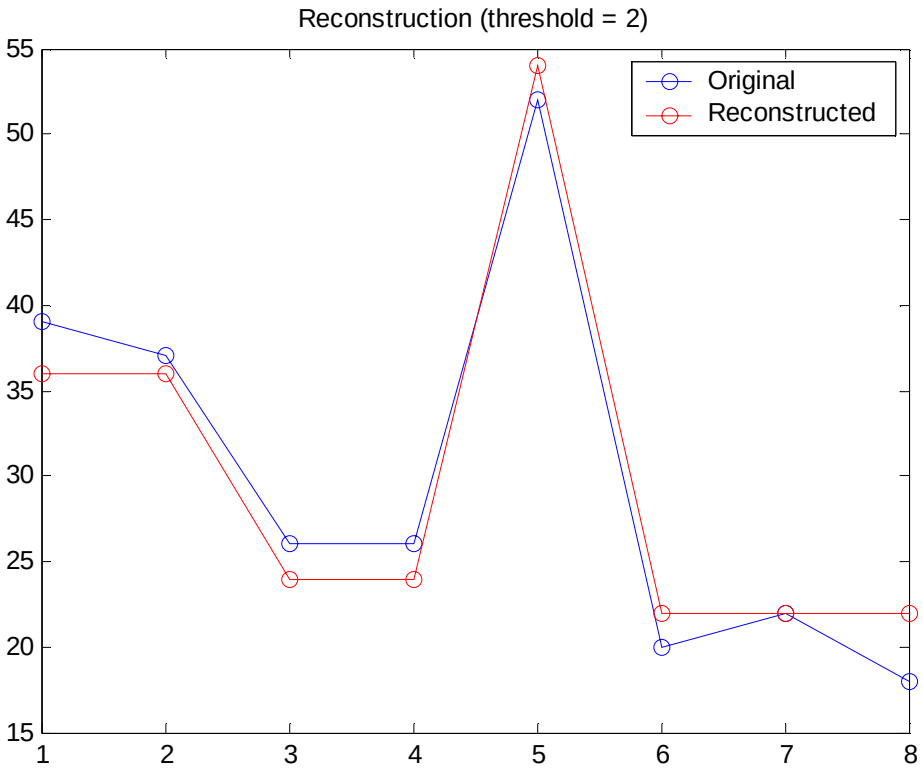

Figure 1-6. Reconstructed signal with threshold value.

1-6. Advantages of representing data with wavelets

Data representation with wavelet has several advantages in viewing and data processing such as:

- Viewing
    - Traditional signal analysis (Fourier transform) doesn't indicate when an "event" occurs.
    - It is easier to get the information about the frequency component of a signal at a particular time.
    - Fourier analysis does not work well on discontinuous or constant shaped signals.
- Processing
    - Decomposition can be done more efficiently by using the decomposition relation.
    - Fast algorithms to compute compact representation of function and datasets.

2. Data processing

LiDAR data come as scattered points so that it needs to be interpolated to get an evenly-spaced gridded data format. In this study, four interpolation methods, Kriging, inverse distance to a power, nearest neighbor (NN), and multiquadratic were tested. Once we have obtained the gridded data, we can decompose it into a maximum decomposition level. However, decomposition procedures are performed up to only level II in this study for efficient analysis. As one can infer from the Figure 1-3, Figure 1-4, Figure 1-5, decomposition at level II is sufficient to analyze the data compression of LiDAR data because detail signals occupies most of the data storage even if we choose level II as a maximum decomposition level. The threshold values from 0 to 0.1 are chosen for the computation of the ratios and the RMSs defined in previous section.

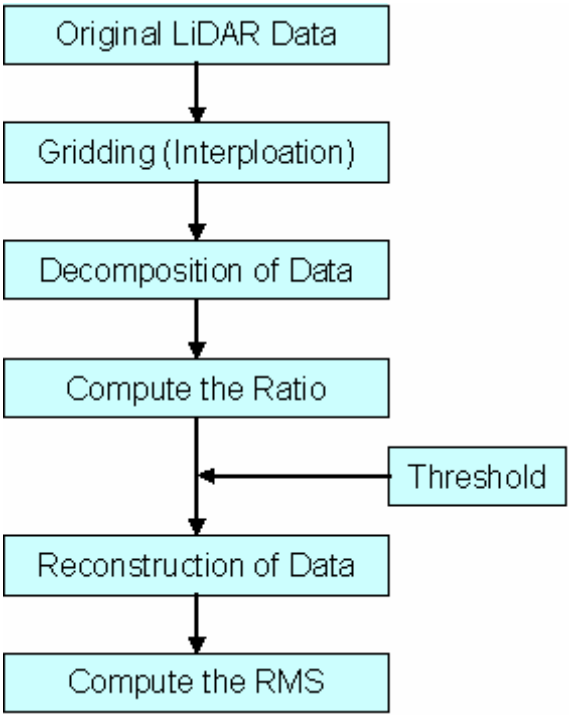

Figure 2-1. Procedures applied for this study.

2.1. Datasets

- Data type : LIDAR data
- Data size : 128×128
- Data spacing : 0.69 m (after interpolation)

2.2. Interpolation methods

Four interpolation methods are used in this study.

- ArcView (not included)
- Fourier series + Polynomial (not included)
- Kriging
- Multiquadratic
- Inverse Distance to a power
- Nearest Neighbor

* Underlined methods are applied in the analyses presented in this report.

2.2.1. Kriging

Kriging is a geostatistical gridding method that has been known to be a useful tool in many fields. This method is a very flexible gridding method which produces visually appealing maps from scattered data. Kriging also attempts to express trends suggested from the data.

2.2.2. Nearest neighbor

The nearest neighbor gridding method assigns the value of the nearest point to each grid node. This method is effective for filling in the holes in the data in cases where the data are nearly on a grid with only a few missing points.

2.2.3. Inverse distance to a power

Inverse distance to a power is a weighted average interpolator. Data are weighted during the interpolation such that the influence of one point relative to another declines with distance from the grid node. Weighting is assigned to data through the use of a weighting power that controls how the weighting factors drop off as distance from a grid node increase.

2.2.4. Multiquadratic

Multiquadratic interpolation method uses basis kernel (radial basis) function which defines the optimal set of weights to apply to data points when interpolating a grid node.

Multiquadratic : $B(h) = \sqrt{h^2 + R^2}$

Where, h is the anisotropically rescaled, relative distance from the point to the node and R^2 is the smoothing factor specified by the user

Default value for R^2: (length of diagonal of the data extent)^2 / (25*number of data points)

2.3. Wavelet functions

Six types of wavelets were chosen for the discrete wavelet transform and analysis. Figure 2-2 shows the various patterns in scaling (low-pass filter) and wavelet functions (high-pass filter). The names of those functions are as followings:

- Haar
- db2
- db3
- db4
- coif1
- sym2

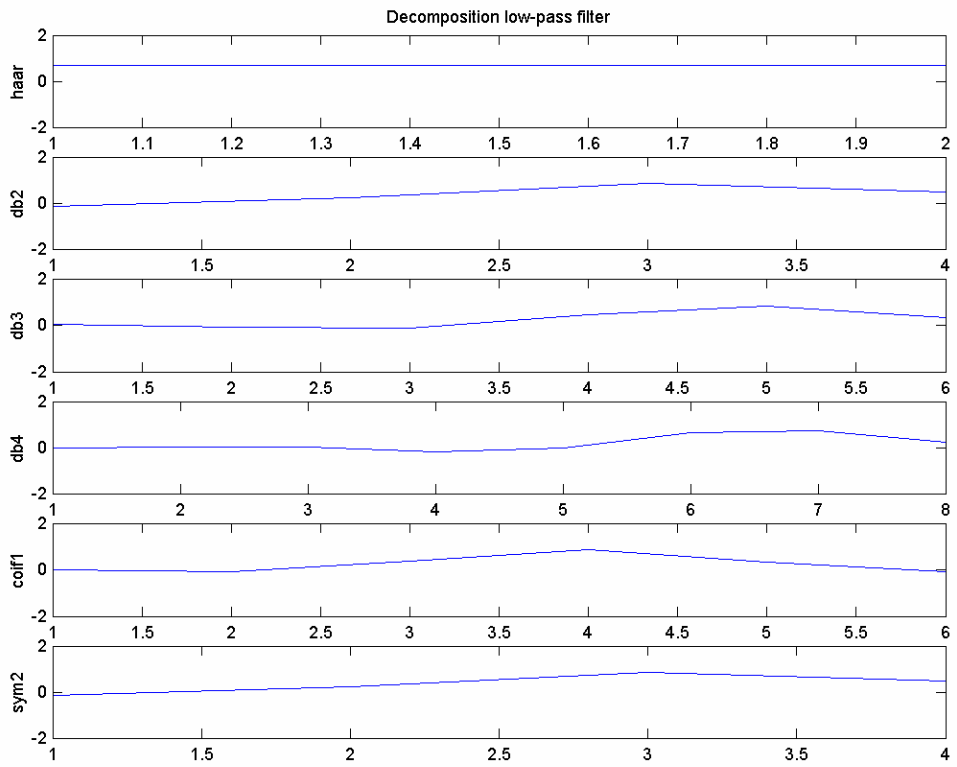

Figure 2-2. Decomposition low-pass filters used for decomposition of original data.

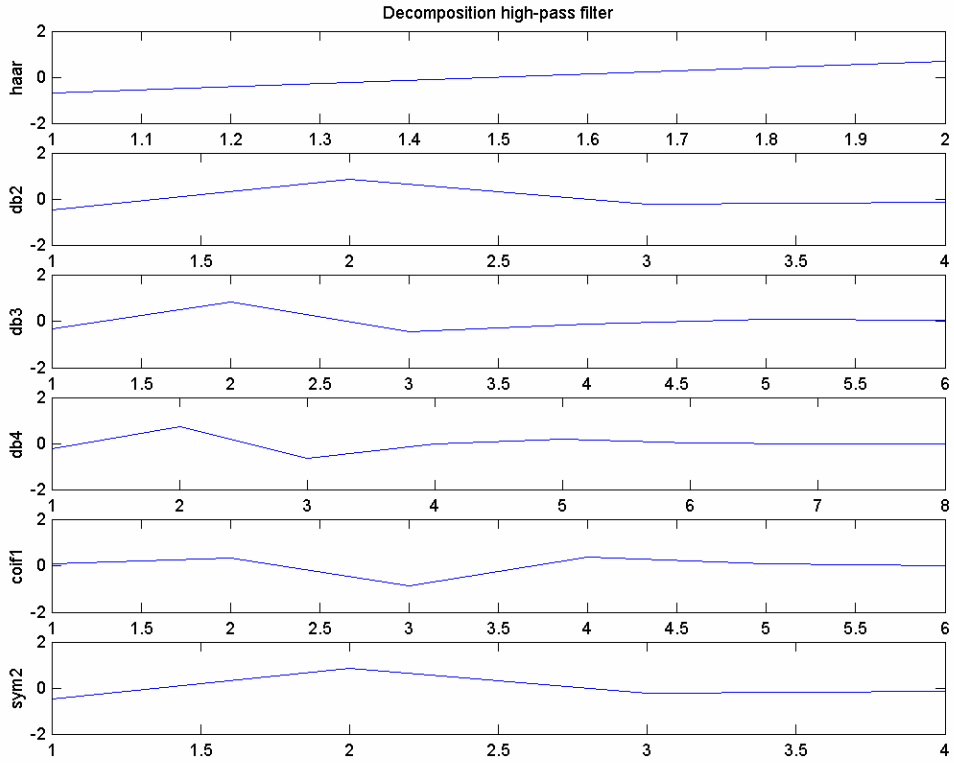

Figure 2-3. Decomposition high-pass filters used for decomposition of original data.

2.4. Decomposition of 2-D data

2-D data can also be decomposed into smoothed and detail signals by using 2-D scaling and wavelet function as described in section 1.5. Figure 2-4 shows the decomposition procedures for the 2-D data and Figure 2-5 shows one example of decomposed 2-D data. In the Figure 2-4, 'A' and 'D' denote the smoothed and detail signals, respectively. As can be seen in the Figure 2-4, $3/4$ of original data points is assigned for detail signals so that many zeros can be found in detail signals.

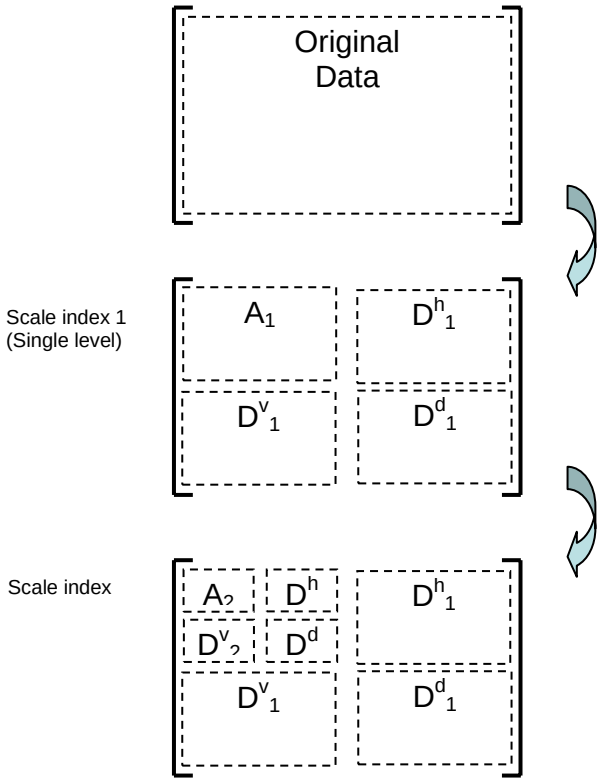

Figure 2-4. Schematic diagram of decomposition procedures for 2-D data.

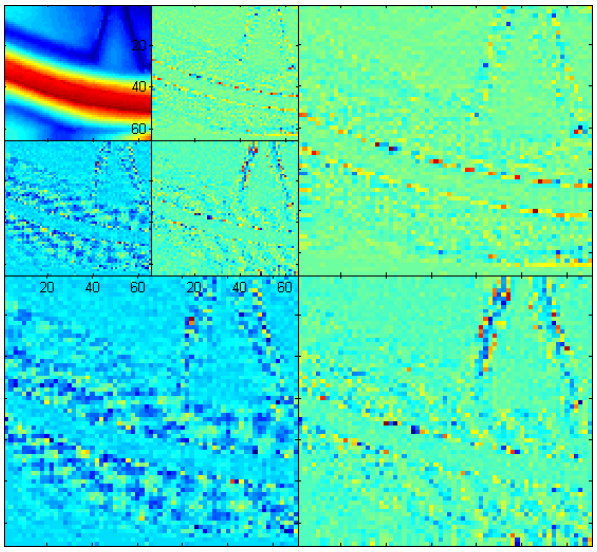

Figure 2-5. Example of data decomposition at the level II (LiDAR data).

3. Analysis on RMS errors and data compression

Four types of interpolation methods, kriging, nearest neighbor, inverse distance to a power, and multiquadratic are used for this study. The analysis was performed based on the RMS errors and ratio of total zero values in detail signals to the total number of original data with respect to the threshold values.

3.1. Interpolation by using Kriging method

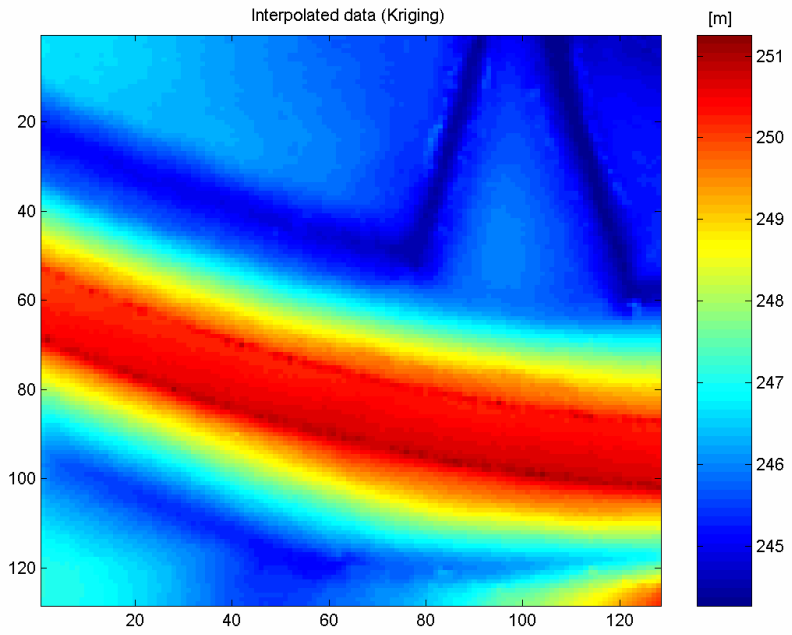

Figure 3-1. Interpolated data by using kriging method.

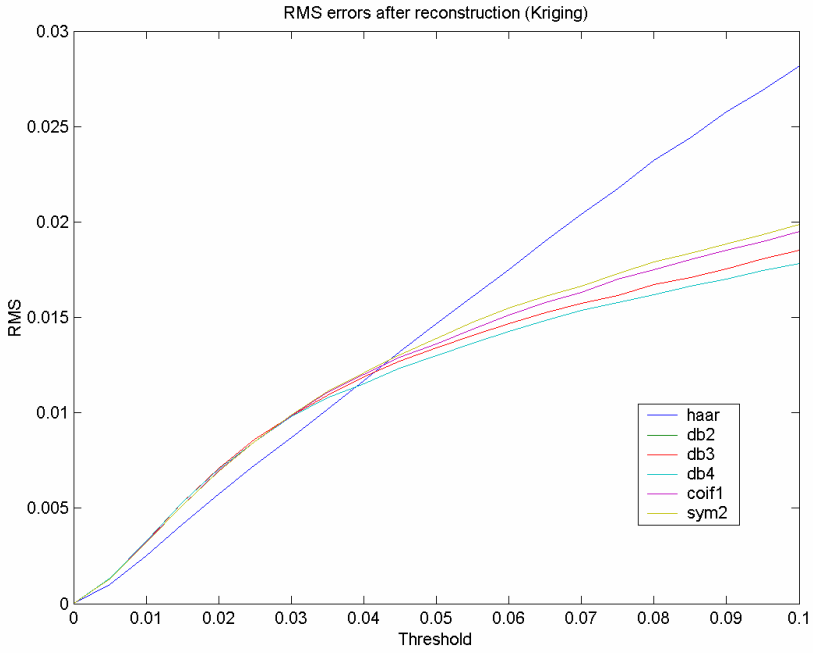

Figure 3-2. Computed RMS errors after reconstruction.

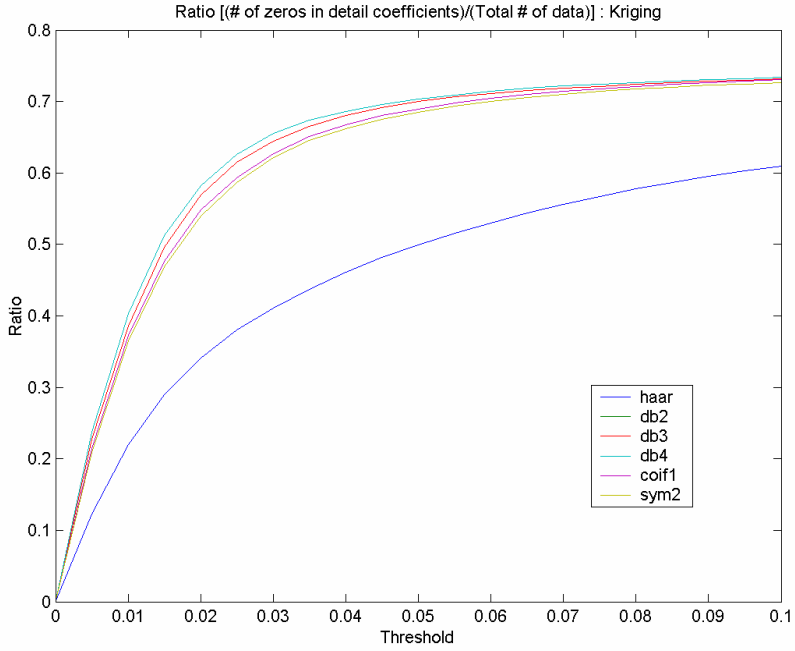

Figure 3-3. Ratio of the number of zeros in detail coefficients to the total data size.

3.2. Interpolation by using nearest neighbor method

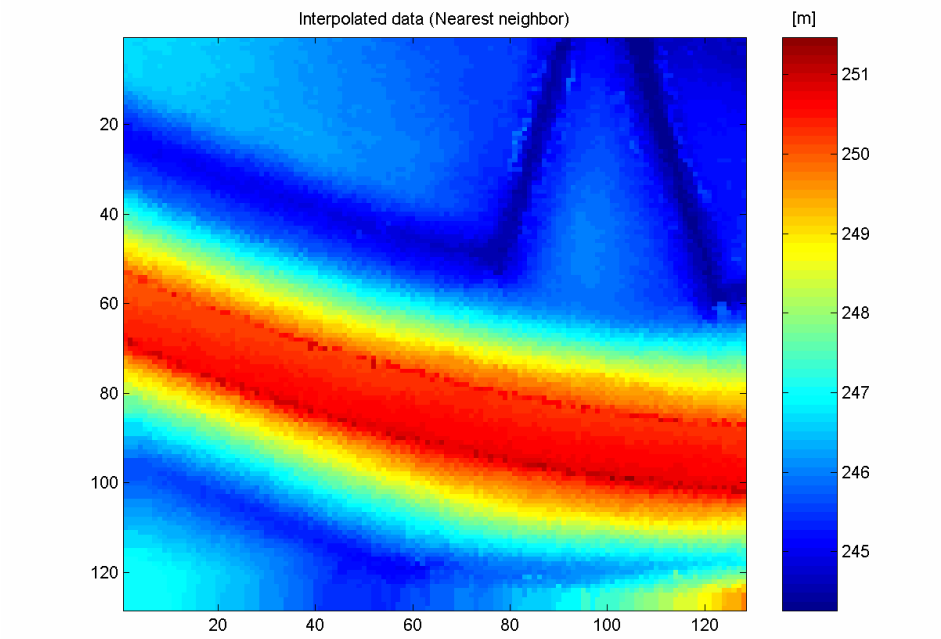

Figure 3-4. Interpolated (Nearest neighbor) data.

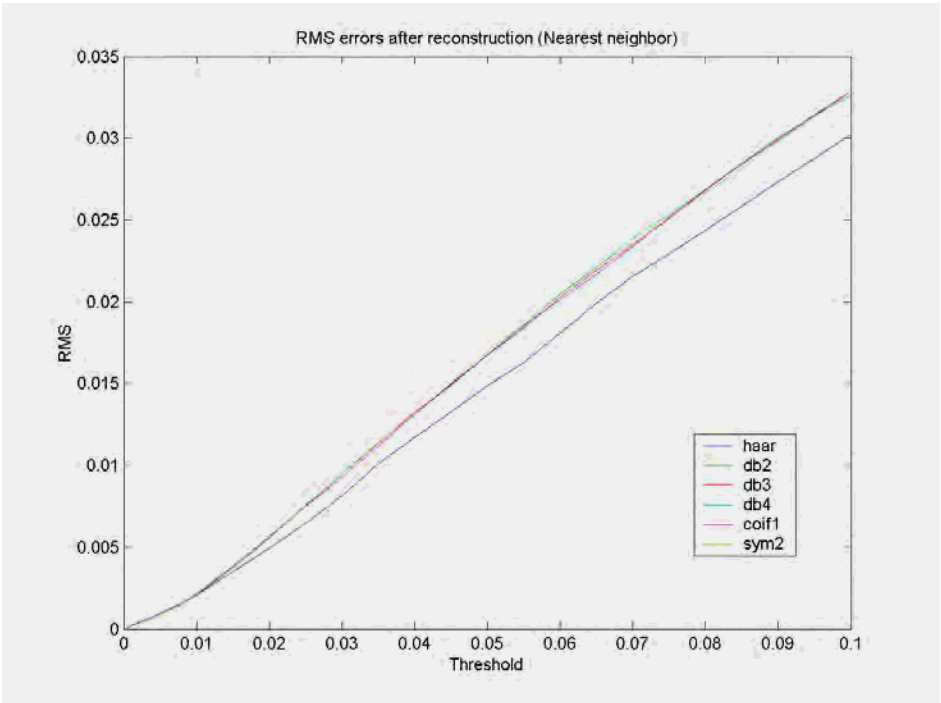

Figure 3-5. Computed RMS errors after reconstruction.

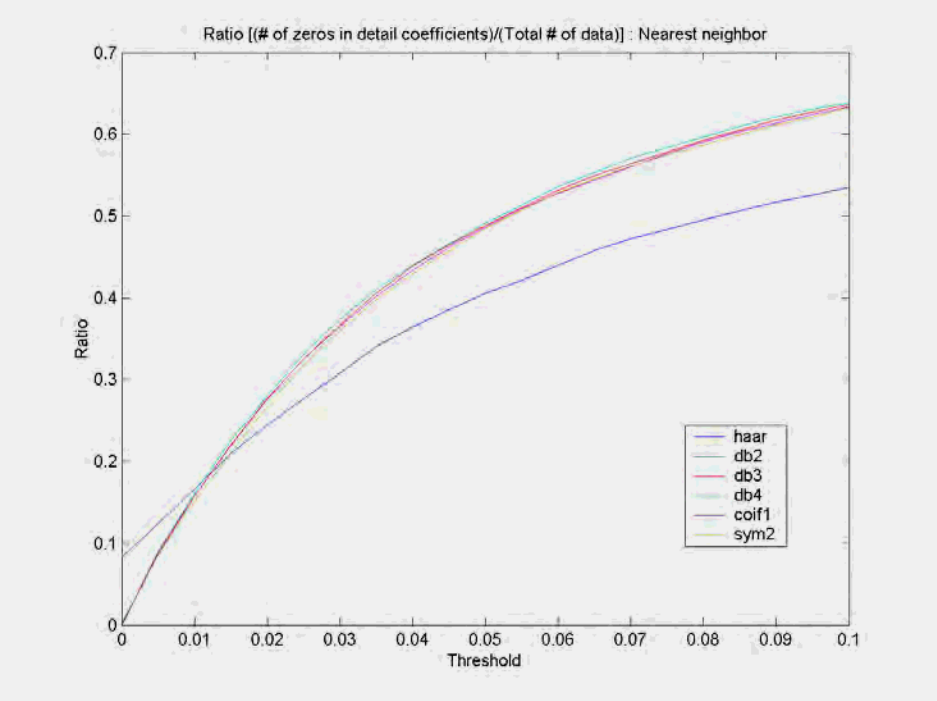

Figure 3-6. Ratio of the number of zeros in detail coefficients to the total data size.

3.3. Interpolation by using inverse distance to a power method

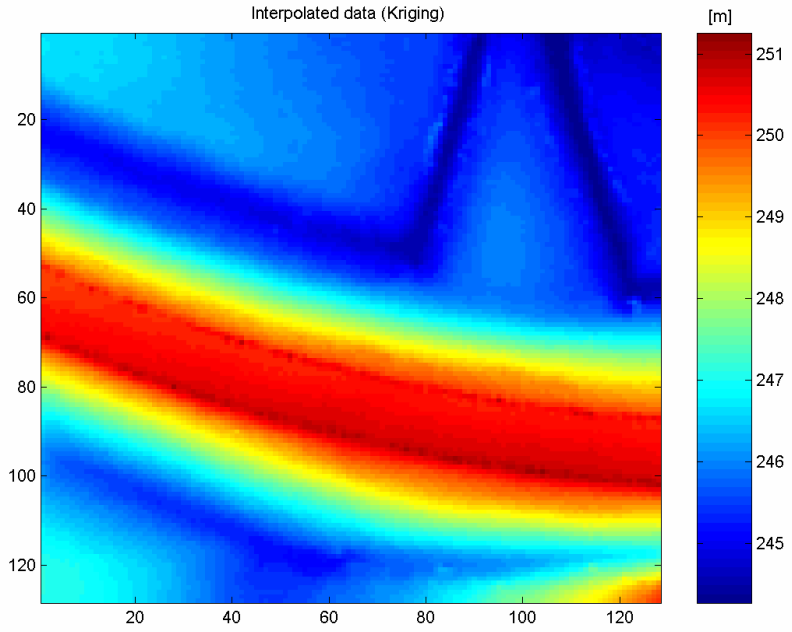

Figure 3-7. Interpolated (Inverse distance to a power) data.

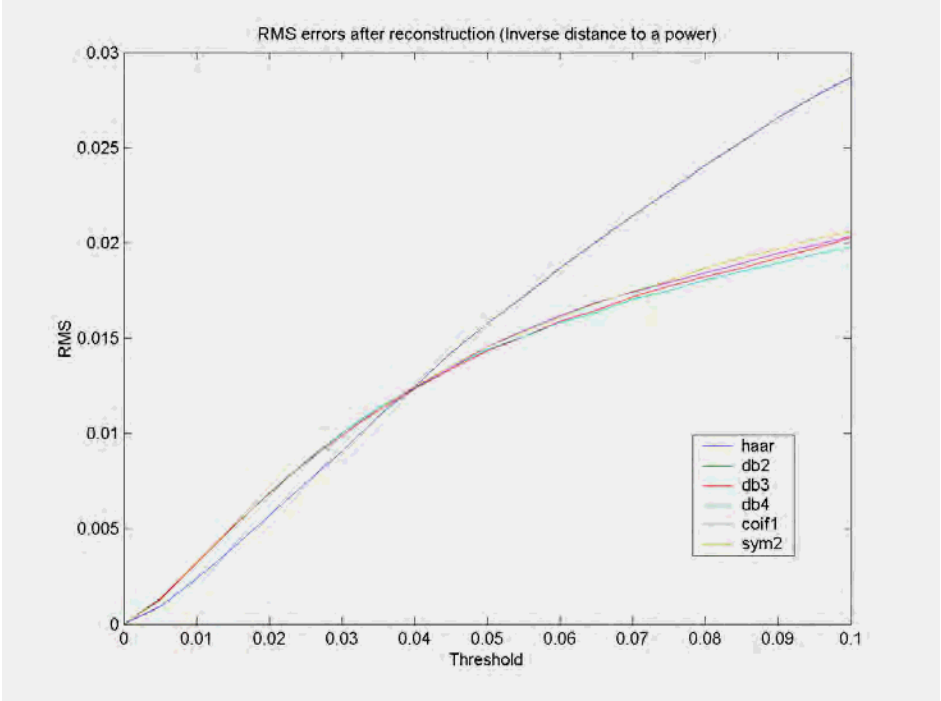

Figure 3-8. Computed RMS errors after reconstruction.

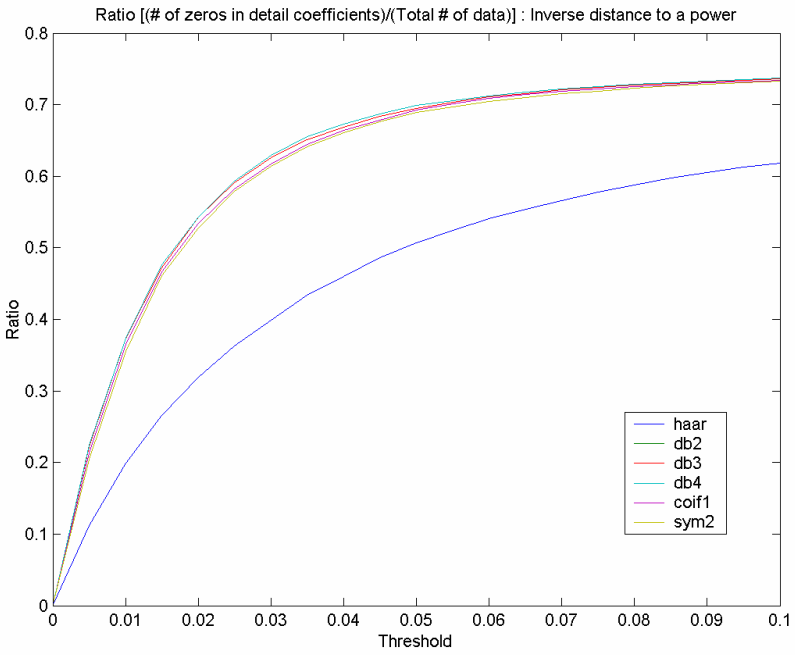

Figure 3-9. Ratio of the number of zeros in detail coefficients to the total data size.

3.4. Interpolation by using Multiquadratic interpolation method

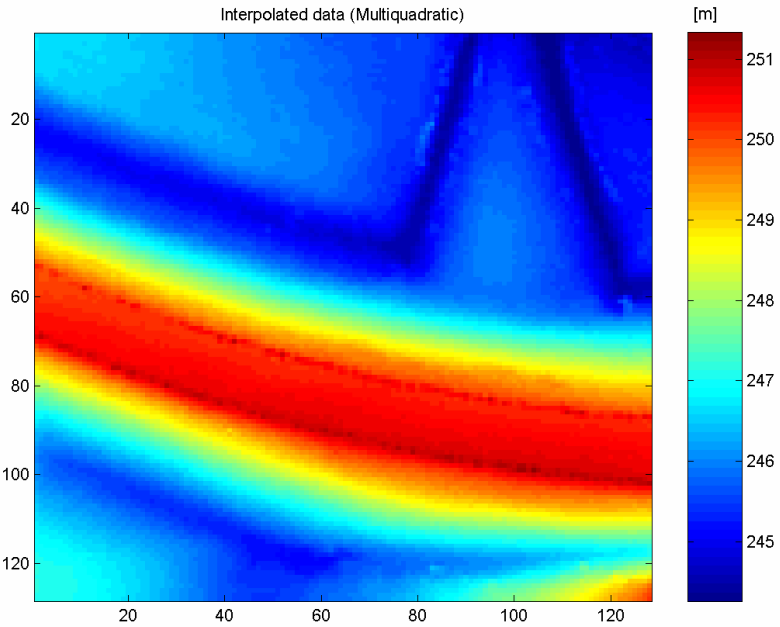

Figure 3-10. Interpolated (Multiquadratic) data.

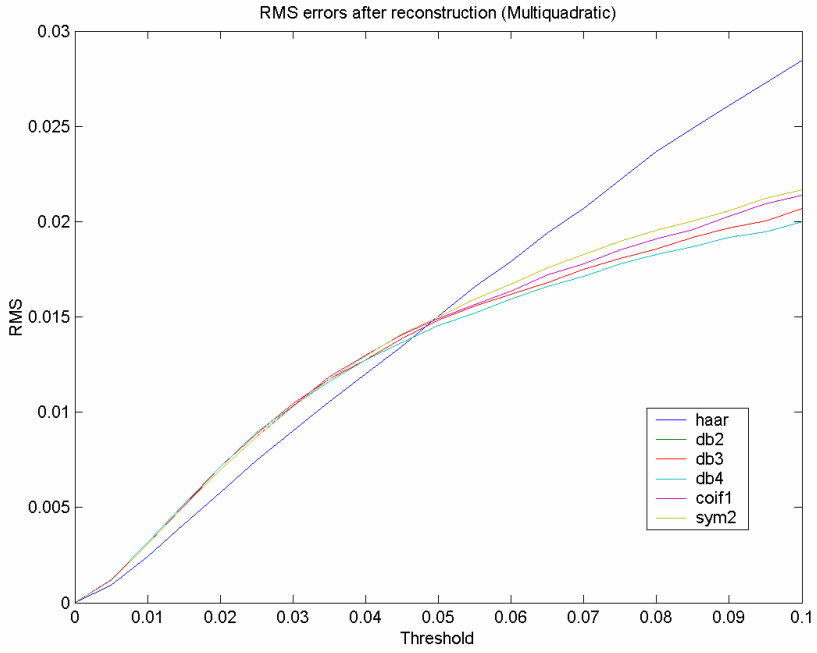

Figure 3-11. Computed RMS errors after reconstruction.

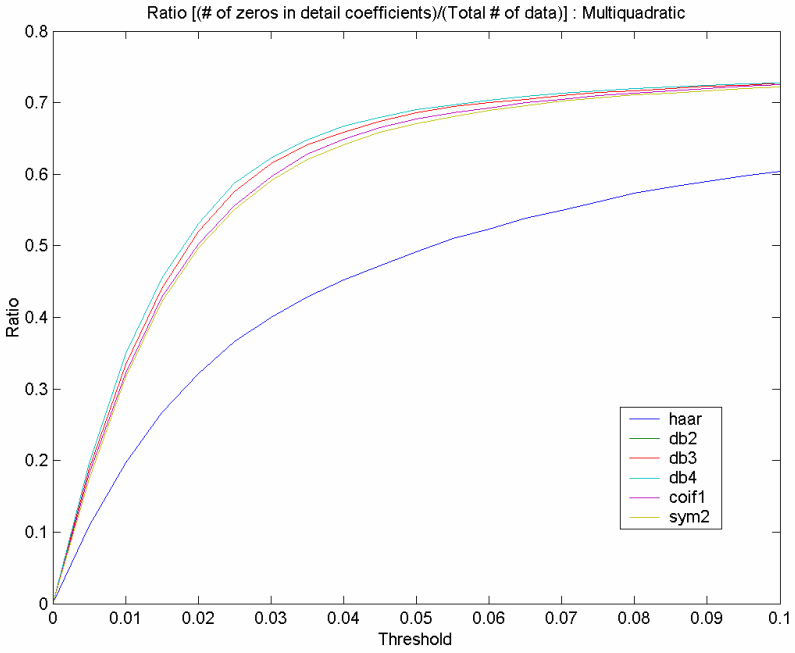

Figure 3-12. Ratio of the number of zeros in detail coefficients to the total data size.

3.5. Discussions

Four interpolation methods, kriging, nearest neighbor, inverse distance to a power, multiquadratic were applied for the analysis of the optimal representation of LiDAR data in terms of RMS errors and the ratio of number of zeros to the total number of data points, respectively. As can be seen in Figure 3-2, Figure 3-3, Figure 3-5, Figure 3-6, Figure 3-8, Figure 3-9, Figure 3-11, and Figure 3-12, one can get almost identical results with each method except for the nearest neighbor interpolation method. Also, we can see that the RMS errors after data reconstruction are increasing with the larger threshold values for all wavelets. However, Haar wavelet appears to be the most inefficient one to represent the data based on the reconstruction and storage capability. The test results show that most of the wavelets tested have almost the same capability for the efficient representation of original data (test data). However, we need to take into account that the test data only covered a small ($\sim 100\,m \times 100m$) and relatively flat area. This also means that the results could be affected by the characteristics and type of data.

Table 3-1 shows the minimum RMS values for each interpolation when threshold value is set to 1. As shown in the Table 3-1, we can reconstruct the data with highest accuracy with the kriging method among the interpolation methods used for this study.

Table 3-1. Minimum RMS errors for each interpolation method (threshold = 1).

Interpolation methods	Minimum RMS errors
Kriging	0.018
Nearest neighbor	0.030
Inverse distance to a power	0.020
Multiquadratic	0.020

4. Comparison on level-by-level representation in terms of number of coefficient (space) it takes

Figure 4-1, Figure 4-2 show the number of coefficients needed for the representation of data in the log scale at the decomposition level I and II, respectively. As can be seen in Figure 4-1, there exists a sharp decrease when the threshold value is 0.05, and we can see the low decrease rate after that point. Figure 4-2 also shows the number of coefficients at the decomposition level II. However, it does not show much difference compared with Figure 4-1. This means that the decomposition level I is sufficient for the efficient representation from the storage point of view.

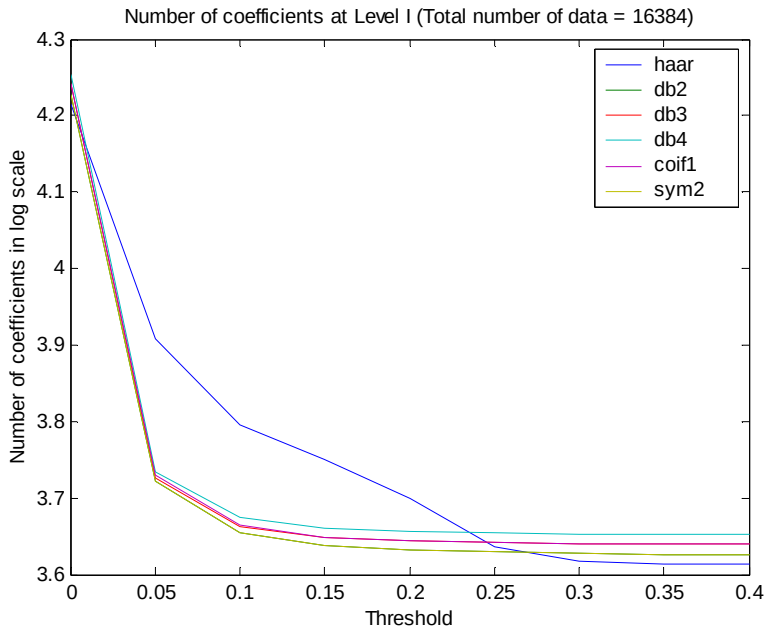

Figure 4-1. Plot of number of coefficient at decomposition level I.

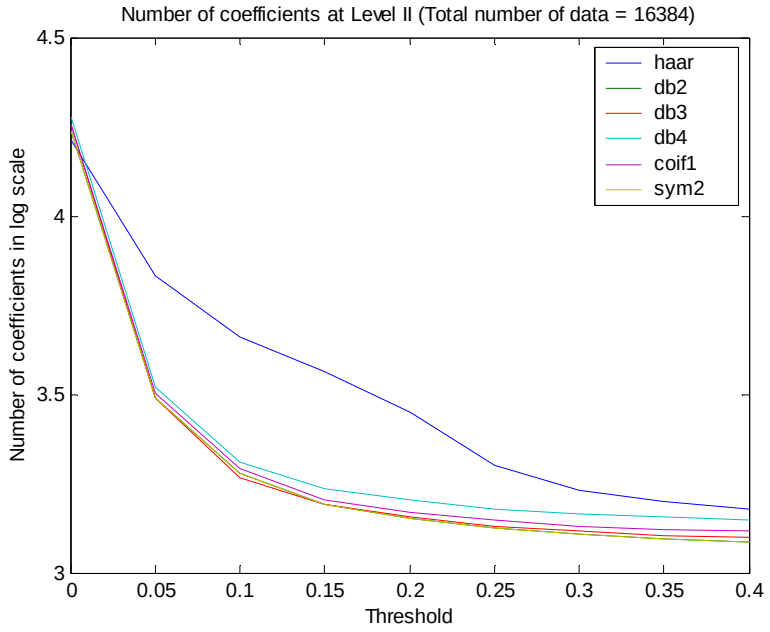

Figure 4-2. Plot of number of coefficient at decomposition level II.

5. Specific issues related to an elongated shape (highway) of a data set

Maximum decomposition level is basically determined by the number of original data points and wavelet functions. Figure 5-1 shows one example of decomposition with the Haar wavelet. As can be observed in Figure 5-1, one can only decompose the original data up to level II if 4×16 original data are given. This is a commonly used procedure for the decomposition of such data. Another procedure is to decompose the data, for example, row by row up to a maximum level for each row, and do the same for all columns. Figure 5-2 shows the schematic diagram for this decomposition procedure.

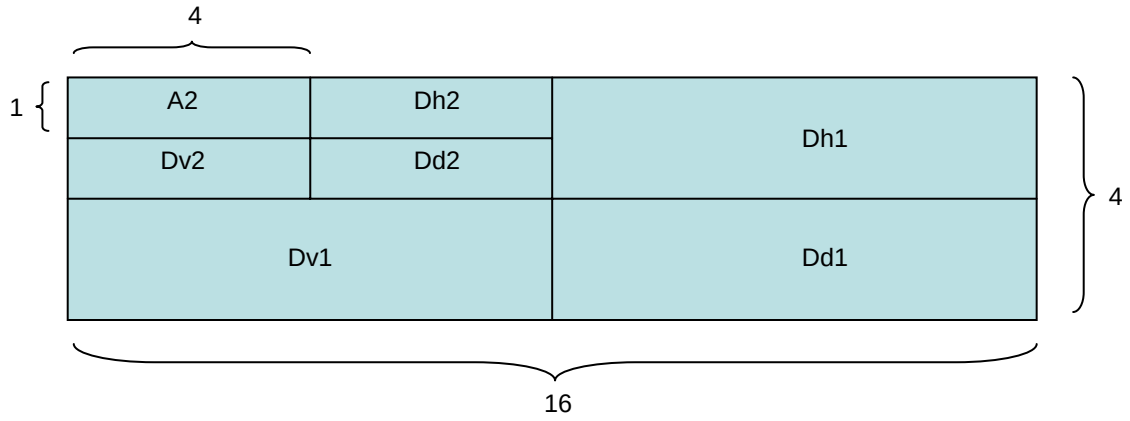

Figure 5-1. Traditional 2-D data (4×16) decomposition at level II (Method I).

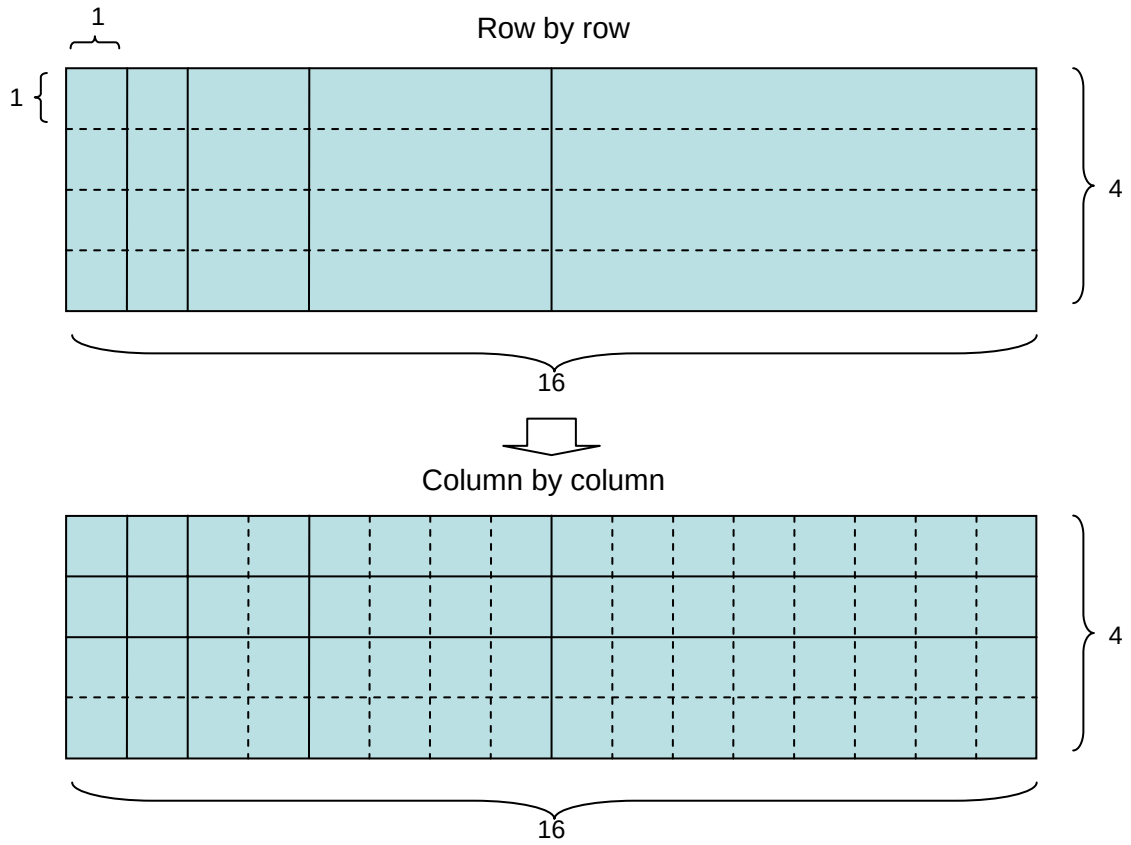

Figure 5-2. 2-D data decompositions row by row and column by column (Method II).

6. Simulation of Gaussian bell shaped data with $50m \times 50m$ size.

- Simulation of $50m \times 50m \times 10\ m$ Gaussian bell shaped data to test theperformance of the wavelet representation at the edges.

  - 2-D Gaussian bell shaped data are simulated by following function and parameters:

    $\sigma = \sigma_x = \sigma_y = 1$

    $\mu_x = \mu_y = 2.5$

    $x = y = [0.0 : 0.0393 : 5.0]$ (total number of data point = 128)

    $$f(x,y) = \frac{1}{2\pi\sigma^2} e^{-\left[(x-\mu_x)^2+(y-\mu_y)^2\right]/2\sigma^2}$$

$$F(x,y) = 100 \times f(x,y) + 10$$

- Name of wavelet used for the test: ‘db2’

Figure 6-1 shows various ways to handle the problem of border distortion. Those can be zero padding, symmetrization, first derivative interpolation, and constant extension at the edge. As can be expected, original data can be reconstructed even if we choose different edge controlling methods because we have information on the method used for wavelet transformation. However, we could have somewhat different results in wavelet transformed data. Figure 6-2 shows profiles of 2-D smoothed and detail signals after decomposition of Gaussian bell shaped data. As shown in Figure 6-2, there is not much difference in smoothed signals for all cases but we can see large distortions near the edges in detail signals when we use zero padding method. Therefore, we need to be more careful in dealing with zero padding method in decomposition procedures.

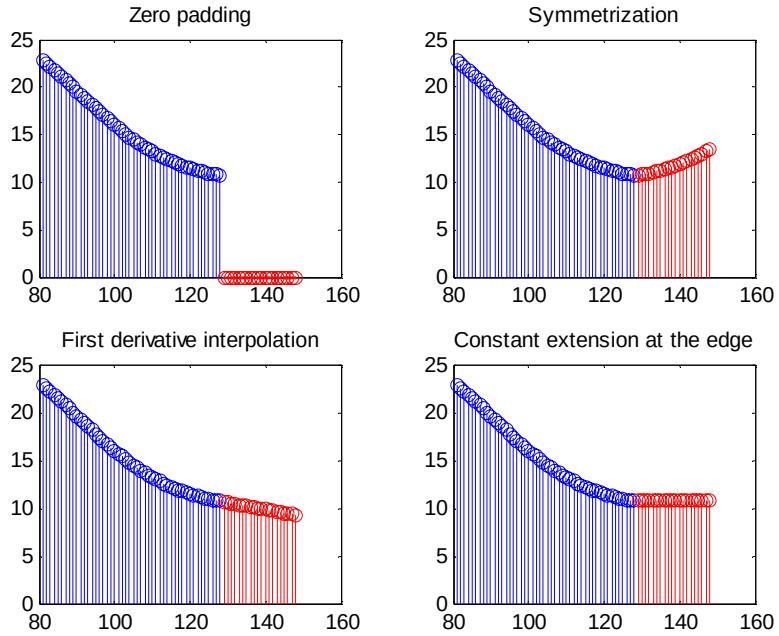

Figure 6-1. Different ways of handling the problem border distortion.

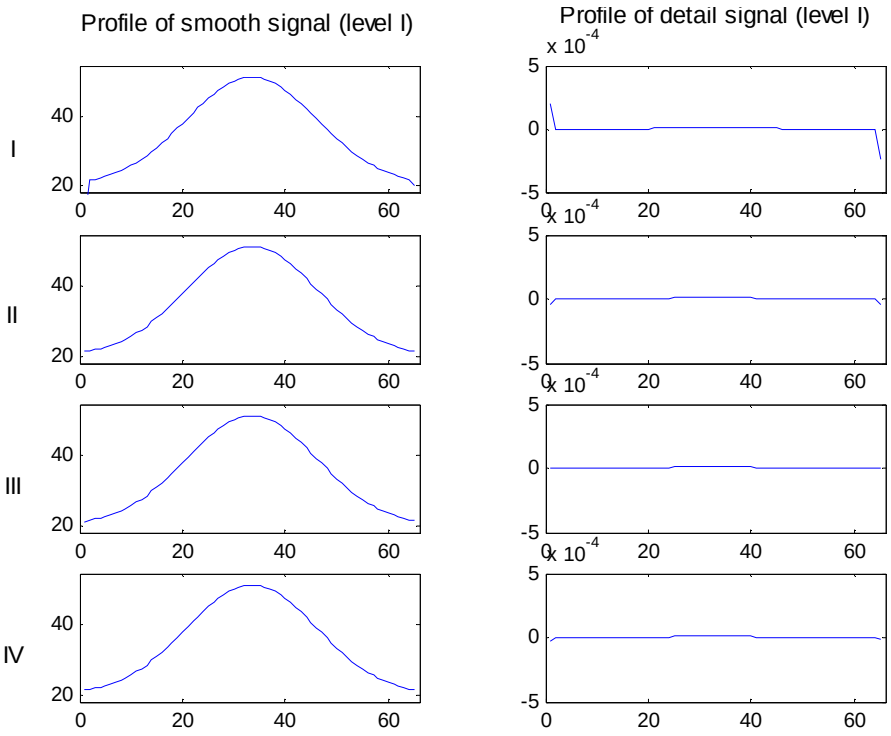

Figure 6-2. Border distortions in wavelet transforms.

7. Analysis on the selected elongated portion of LiDAR data

Figure 7-1 shows an elongated sample of LiDAR data. Two methods were tested for the efficient representation of elongated data as mentioned in section 5. As can be observed in the Figure 7-2 and Figure 7-3, method II is slightly better in efficient representations because we can get the smaller number of coefficients in wavelet transform in most cases (wavelets). Table 7-1 shows the enhancement in data storage when we choose method II for elongated data (threshold = 0.4).

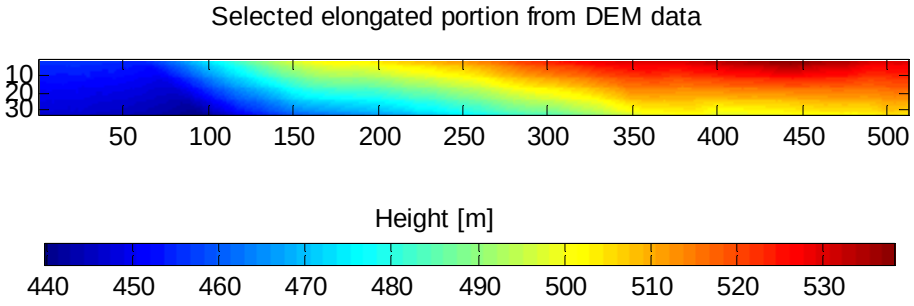

Figure 7-1. One sample of elongated LiDAR data.

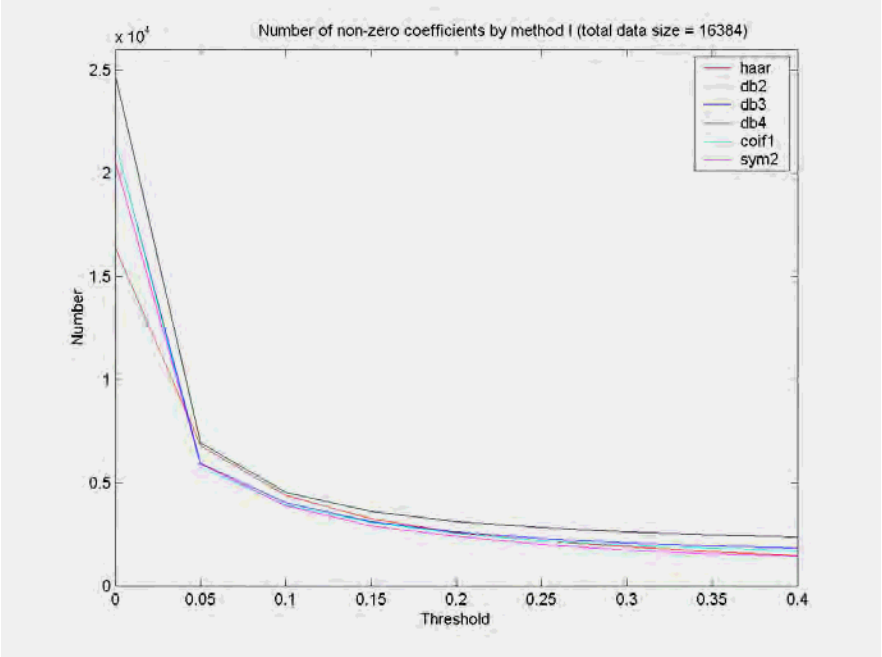

Figure 7-2. Plot of number of non-zero coefficients with respect to threshold values by method I.

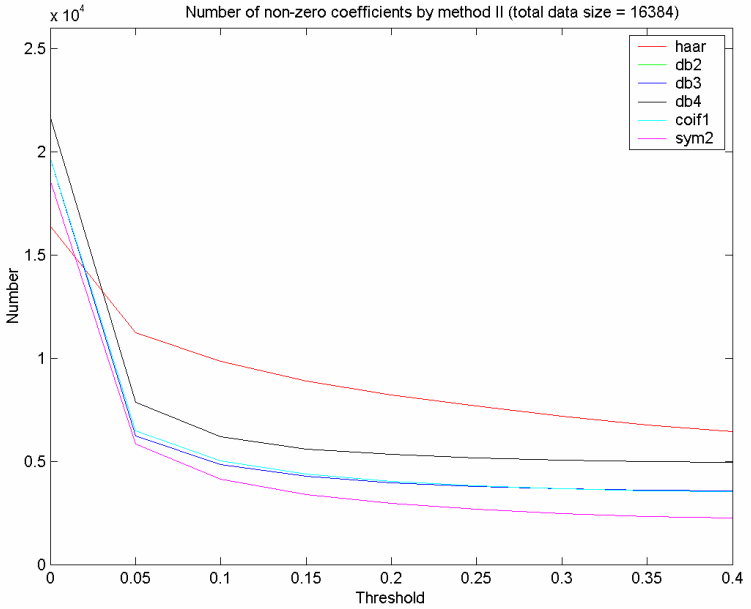

Figure 7-3. Plot of number of non-zero coefficients with respect to threshold values by method II.

Table 7-1. Enhancement of data storage from the decomposition method II.

Wavelet names	Enhancement [%]
Haar	30.2
Db2	5.1
Db3	10.4
Db4	15.9
Coif1	11.2
Sym2	5.1

8. Descriptions on the software developed for demonstration

Left hand side part of the Figures 8-1 shows the area which displays the decomposed image at each level. Right hand side part of the figure includes the various menus, ratio of zero values, and histogram of original data. For the demonstration, Haar wavelet and decomposition level I and II are chosen, respectively, and Figure 8-1 and Figure 8-2 show the decomposed data with parameters used. Also, Figure 8-3 shows the reconstructed data from the wavelet transformed data.

Followings are the names of the menu and its descriptions of the software.

- Data load: It is used for the loading the gridded data.
- Wavelet functions : Wavelet function can be chosen for the wavelet decompositions
- Level: decomposition level can be specified with this menu.
- Threshold: we can set the threshold value to check the saved data storage.
- Reconstruction: If you check the box, you can see the reconstructed image with parameters set in the menu.
- Run: Run the program with parameters set in the menu.

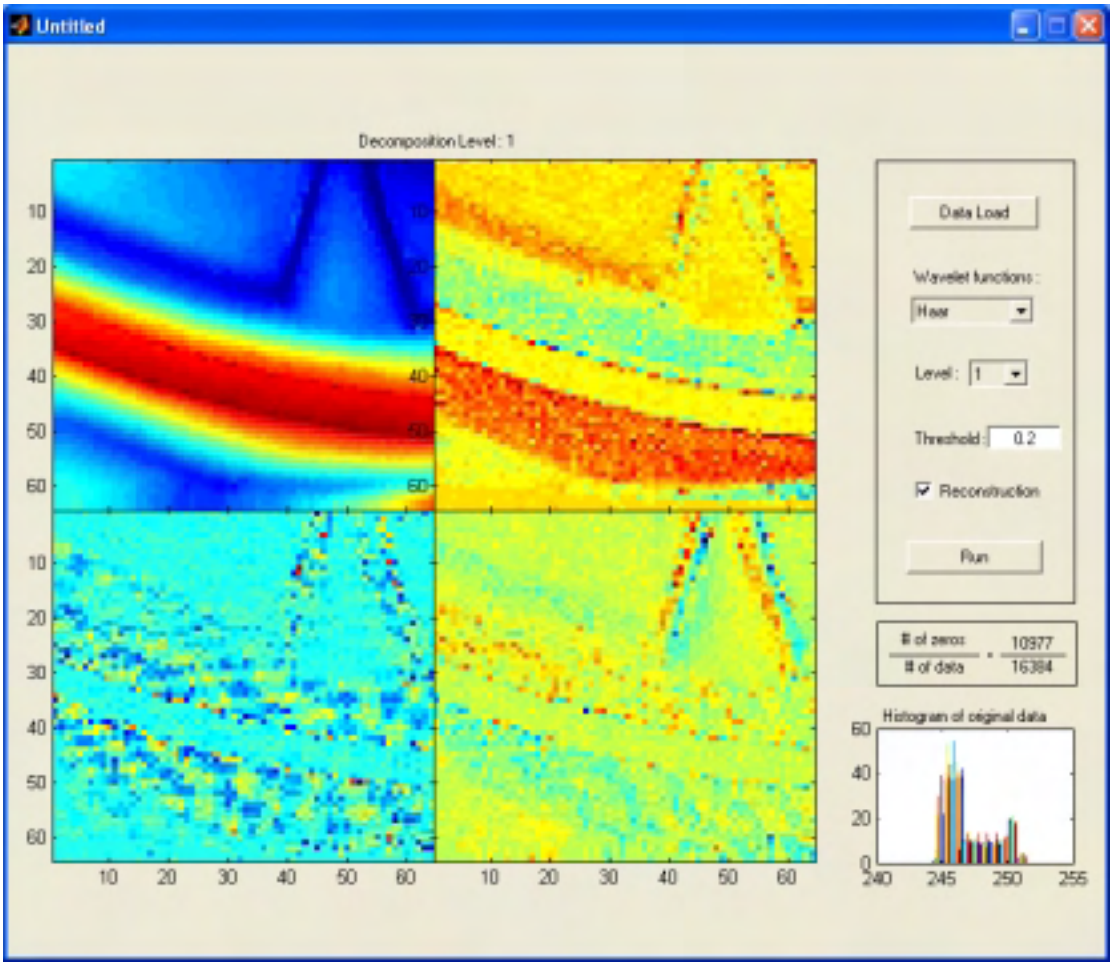

Figure 8-1. Decomposition of data at level I.

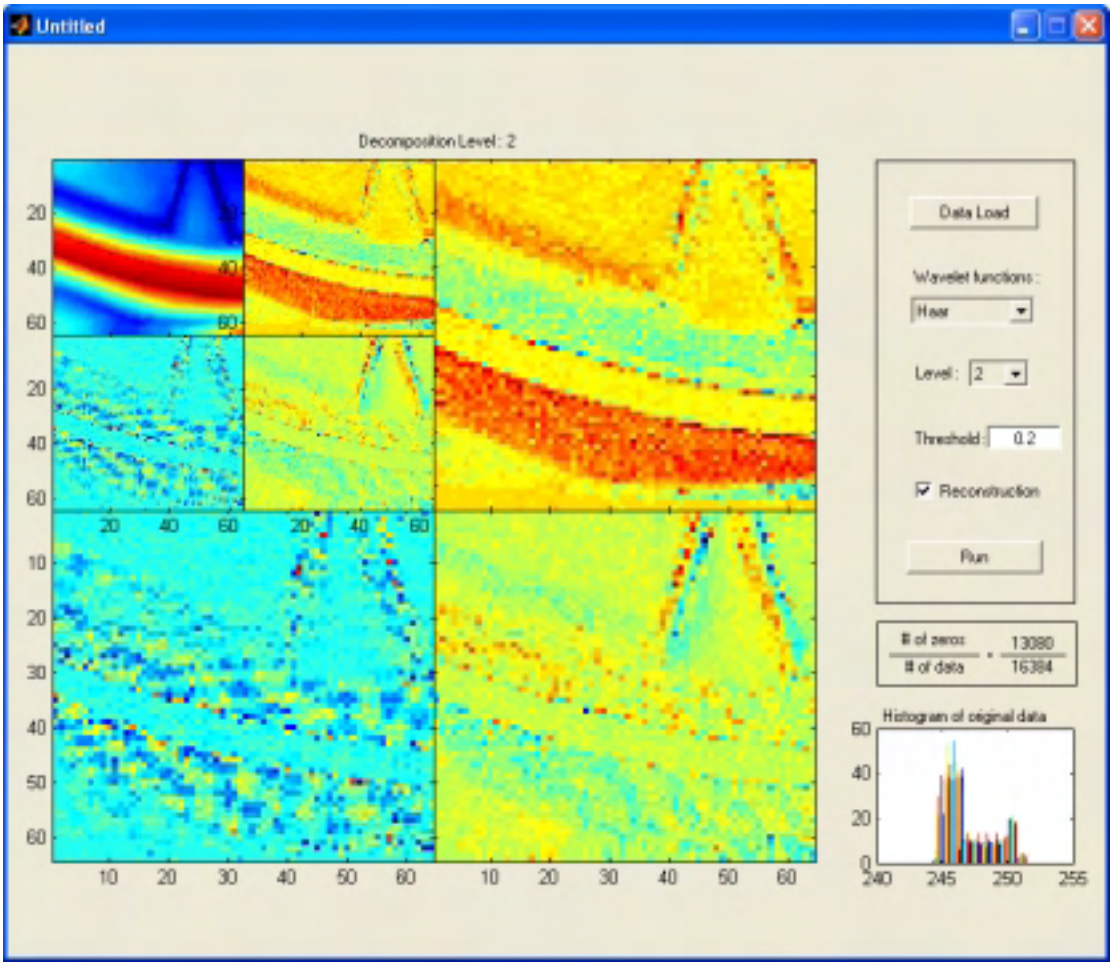

Figure 8-2. Decomposition of data at level II.

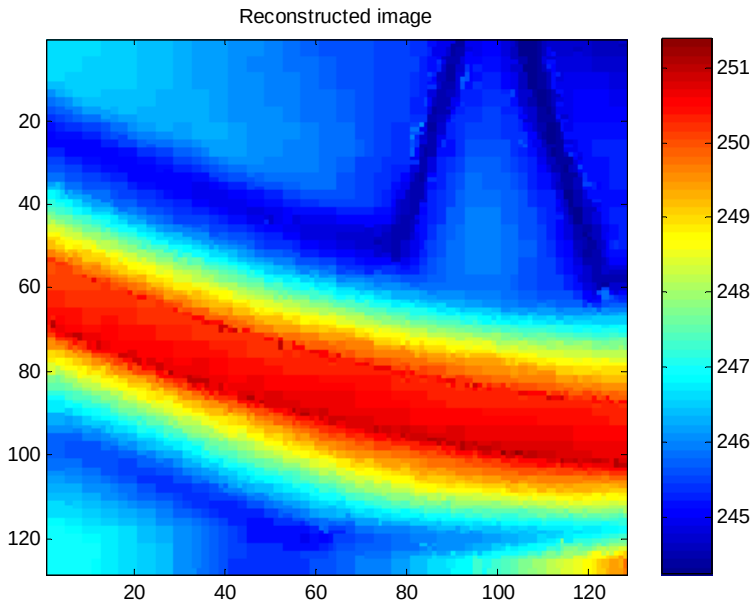

Figure 8-3. Reconstructed data by using given parameters.

References

Chui, Charles K., 1997, “Wavelets: A Mathematical Tool for Signal Analysis”, SIAM, Philadelphia.

Sweldens, Wim, P. Schroder, 1996, “Building Your Own Wavelets at Home”, In Wavelets in Computer Graphics, ACM SIGGRAPH Course notes.

Surfer 8.0 manual, 2002, Golden software, Colorado.

Comparison of Various Surface Modeling Methods

Nora Csanyi, Eva Paska and Charles K. Toth
Center for Mapping
The Ohio State University
1216 Kinnear Road, Columbus, OH 43212-1154
E-mail: toth@cfm.ohio-state.edu

ABSTRACT

Terrain modeling usually requires some type of interpolation between the measured terrain points. Using modern airborne and spaceborne sensors, terrain point observations are becoming available in a variety of formats with widely differing characteristics. More importantly, the point distribution, accuracy and density can vary greatly, depending mostly on the sensor type and the data acquisition method used. This paper analyzes and compares the most important methods for terrain modeling, in particular, in the case of low point density and irregular point distribution. A new method is proposed for surface modeling, which is based on a two-dimensional Fourier series interpolation combined with a polynomial extension. The Fourier series technique as a powerful method to describe 1D/2D signals has been widely used in several diverse applications, including surface modeling. However, because it is based on evenly spaced input data it cannot be directly applied for surface approximations from irregularly spaced points. The proposed approach, therefore, aims to determine the coefficients in the case of uneven point distributions. The key idea of the concept is that a least squares adjustment is formulated to obtain the Fourier series coefficients. Since the Fourier series cannot model surface trends well, a polynomial extension has been added to model the surface trend, thus splitting the approximation task into two parts, global trend and local variation modeling. The proposed surface modeling method has shown promising performance even in the case of low point density and scattered point distribution.

INTRODUCTION

Modeling of terrain surface plays an important role in many applications. Orthophoto production, telecommunication, engineering design, floodplain mapping, etc. all require surface data with different level of detail and accuracy. There are different sources of digital elevation data. Government agencies in North America and Europe provide base digital elevation models mostly derived from old topographic maps by contour digitization; these models usually describe larger areas and are not so detailed and accurate. A lot of applications, however, demand current, more detailed and accurate terrain models. There are currently three main technologies that provide surface data with increased level of accuracy and detail. The traditional method has been photogrammetry using stereo image pairs. DEM generation by analytical methods has been very time consuming. The introduction of digital photogrammetry automated a lot of the tasks, basically laying down the foundation for inexpensive orthophoto production in the mid 90's. Nevertheless, DEMs created on digital photogrammetric workstations still require substantial manual editing, therefore it is still labor intensive. Recently, LIDAR technology has become the primary source of surface data while InSAR has grown to be the secondary source. Surface data created by these technologies come with different point density, point distribution and error characteristics.

There are three commonly used data structures to store digital elevation data; Triangulated Irregular Networks (TINs), regular grid structure, and lines of equal elevation (contours). All representation methods have their own advantages and disadvantages, depending on the terrain characteristics and the intended applications. Grid structure is a very efficient format for analysis purposes as it makes the comparison of different datasets very simple. In addition, most of the visualization tools and processing

techniques are based on grid structure. Therefore, grid structure is the most common representation of terrain surface and is typically called DEM (DTM or DSM are also used). In practice, there is a little bit of inconsistency in the usage of the different terms. Therefore, here the definition of each term is included (Maune *at el*., 2001). A Digital Elevation Model (DEM) is elevations of the terrain with uniformly spaced z values without vegetation and man-made features. This bare earth DEM is generally synonymous with a Digital Terrain Model (DTM). A Digital Surface Model (DSM) is similar to a DEM or DTM except that it depicts the elevations of the top surfaces of buildings, trees, and other features elevated above the bare earth.

Most of the new data acquisition technologies deliver elevation data in irregular point distribution, therefore the generation of DEM in regular grid structure requires interpolation. The next section gives a brief overview of the existing methods for terrain interpolation, and then the third section introduces our proposed method, followed by test results.

EXISTING INTERPOLATION METHODS

Creating a gridded surface from irregularly spaced data requires the estimation of elevation values at the grid points, which is based on interpolation of the input data. There are several interpolation methods used for terrain approximation; each has its advantages and disadvantages. Similarly, the surfaces to be modeled can have different characteristics and there is no single interpolation technique that is the best for every situation. The interpolation methods can be grouped numerous ways. One of the possible groupings is whether the method is using the local surrounding sample points to determine an unknown elevation or all sample points together determine the unknown points. Methods of the first group usually preserve the elevation data at the sample points, while the others apply some kind of surface fitting to the sample data to determine the unknown elevations, which does not necessarily honor the sample points. This section provides a review of the existing, most commonly used interpolation methods for terrain data.

Inverse distance weighted interpolation

Inverse distance weighted interpolation (IDW) determines the unknown values as a weighted average of the surrounding known points. The weights are a function of the inverse distances between the unknown and measured points. This method works in the case of both regular and irregular point distribution, but it requires a parameter such as search radius to select sample points for the interpolation around an unknown point. However, it has drawbacks for irregular point distribution. In general, the method is not well suited for terrain data as the resulted surface has a dimpled effect at the measured locations. Figure 1 illustrates this effect in the case of LIDAR data.

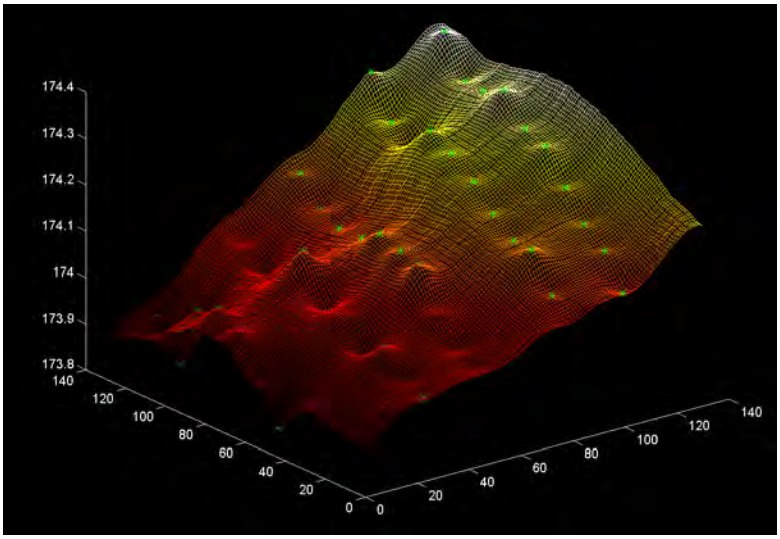

Figure 1. Dimpled effect around measured points in the case of IDW.

Natural Neighbor Interpolation

Natural neighbor uses area based weighting to determine the unknown elevations. It works for both irregular and regular point distributions. The algorithm is based on the Delaunay triangulation and Voronoi diagram. The Voronoi neighbors of the unknown point are determined in a way that the insertion of the unknown point would result in the Voronoi neighborhood of the measured points. Then these Voronoi neighbors are used to determine the elevation of the unknown point. One advantage of the method is that since the method itself founds the surrounding measured points to be included in the determination of the unknown point, there is no need for parameters such as search radius that has drawbacks when the data points have irregular distribution. After the points to be included in the calculation are found, the unknown elevation is calculated as a weighted average of these elevations. The weights are based on the common area of the Thiessen polygon of the unknown point and the Thiessen polygons of each selected point before the new point has been inserted to the triangulation. Since the weights are based on the area that would be stolen from the Thiessen polygons of the surrounding measured points if the unknown point is inserted to the network, this method is also called as 'area stealing' interpolation. The interpolated surface passes through the sample points and it is constrained by the input data range, and therefore peaks and valleys appear in the interpolated surface only if they were measured.

Spline

Spline interpolation fits a mathematical function to some neighboring measured points to determine the value at the unknown locations, like bending a sheet of rubber through the measured points. This method results in a smooth surface that passes through the sample points and in general gives a very good representation of smoothly changing terrain (no sudden elevation changes, such as buildings and other man-made objects). In addition, it allows the representation of unsampled peaks and valleys. This is a very useful method if the goal is to derive good quality contours.

Kriging

Kriging is named after a South African mining engineer, D. G. Krige who developed the technique. Kriging estimates the unknown values with minimum variances if the sample data fulfills the condition of stationarity, which means that there is no trend in the data, such as main slope. Similar to some other methods kriging calculates the unknown values as a weighted average of the sample values, however the weights are based not only on the distance between the sample points and unknown point but also on the correlation among the sample points. The first step in kriging is the determination of the variogram, which is found by plotting the variances of the z values of each sample point with respect to each other sample point versus the distance between points. Once the experimental variogram is computed, the next step is to fit a mathematical function to the variogram that models the trend in it. This fitted polynomial is called model variogram, and is then used to compute weights for the sample points for the calculation of unknown elevations. This method is called ordinary kriging.

If stationarity of the data is not fulfilled, universal kriging can be used. In this case the main trend is modeled by a polynomial function, then the difference between this polynomial and the actual values can be considered stationary. Ordinary kriging can be performed on the residuals and after kriging the polynomial function can be added to the interpolated residuals to get the interpolated values. Kriging is an exact interpolation method; the interpolated surface passes through all the sample points. It works with regular and irregular sample point distributions.

Trend Surface Analysis

Trend surface analysis approximates the surface by a fitted polynomial to the sample points. The proper order of the polynomial can be chosen considering the rule that any cross-section of an *n*-order surface can have at most *n-1* alternating maxima and minima. The coefficients of the fitted polynomial to the sample data can be determined by least squares adjustment, minimizing the square sum of the differences between the z values of measured points and fitted surface at the sample points. Obviously, increasing the order means a better fit at the sample locations, but between the points it can result in large and sudden changes due to the lack of constraint. In common practice, the order of the polynomial normally does not exceed 3-5.

This method works for both regular and irregular sample point distribution, however it has the behavior to change very rapidly between sample points at locations where the sample points are far from each other, especially near the borders of the interpolated surface. The method is appropriate to model the main trend in a surface, but it cannot model local irregularities. Therefore, it is not always applicable and usually is applied to model trend of smaller areas.

Orthogonal basis functions

There are a few methods that reconstruct a function by using a linear combination of a set of orthogonal basis functions. For example, Fourier and wavelet transformations transform the data from time or space domain to frequency domain. By inverse transformation using the coefficients, the original surface can be reconstructed and the surface values can be calculated at the unknown locations too. The numerical methods of forward and backward transformation work only for regular point distribution and therefore in their original form these series are not directly useable for the interpolation of irregularly distributed sample points.

FOURIER SERIES-BASED INTERPOLATION OF IRREGULAR POINT DISTRIBUTION

The Fourier series technique is a powerful method to approximate one and two-dimensional signals and has been widely used in a variety of applications. The discrete Fourier series is based on evenly spaced input data and thus it cannot be directly applied to irregularly distributed surface points. Therefore, a different approach has been proposed to determine the coefficients, which will be described in detail in the following.

Fourier series interpolation in two-dimensional space

A continuous function *z(x,y)* which is periodic by *Tx* in *x* direction and *Ty* in *y* direction can be expanded into Fourier series :

$$\sum_{u=-\infty}^{\infty}\sum_{v=-\infty}^{\infty} c_{uv}\, e^{i2\pi\left(\frac{ux}{T_x}+\frac{vy}{T_y}\right)} = \sum_{u=0}^{\infty}\sum_{v=0}^{\infty}\left(a_{uv}\cos 2\pi\left(\frac{ux}{T_x}+\frac{vy}{T_y}\right)+b_{uv}\sin 2\pi\left(\frac{ux}{T_x}+\frac{vy}{T_y}\right)\right)$$

If the sum is calculated until a finite number of harmonics in both directions, the Fourier series gives an approximation of *z(x,y)* function. The more harmonics are calculated, the better the approximation function fits to the original one. If the continuous *z(x,y)* function is sampled at discrete locations, the calculation of the Fourier series coefficients is identical with the calculation of the discrete Fourier transform. The discrete Fourier-transform is based on evenly spaced point distribution and therefore it cannot be directly applied to approximate surfaces from irregularly distributed points. Therefore, a different approach is proposed to determine the coefficients. The concept is that a least squares adjustment be formulated, which is not sensitive to the input data spacing.

Assuming the surface is sampled at *m* locations, we want to approximate it with a Fourier series calculated until the n^{th} harmonics in both directions. Provided that the number of the unknown coefficients is less than *m*, the coefficients of the Fourier series for the best fit are calculated by least squares adjustment with the condition that the sum of the square difference at the known points is minimum:

$$\sum\left(a_{11}\cos 2\pi\left(\frac{x_i}{T_x}+\frac{y_i}{T_y}\right)+..+b_{nn}\sin 2\pi\left(\frac{nx_i}{T_x}+\frac{ny_i}{T_y}\right)-z_i\right)^2 = \min$$

The sampling theorem states that if a continuous signal is sampled at least twice the frequency of the highest frequency in the signal then the signal can be completely reconstructed from the samples (Nyquist criterion). Therefore, the point density in *x* and *y* directions, in terms of defining the minimum sampling distance determines the maximum spatial frequency that can model the surface (whether it is enough to

properly describe the terrain is another question). Consequently, the maximum number of coefficients of the Fourier series in both *x* and *y* directions can be calculated. For that reason, it is pointless to calculate until a higher frequency, as going further, only noise will be modeled in the data. In practice, the fit of the approximated surface could be very good at the measured points, but between the known points high waves will be produced due to the lack of constraints there.

To illustrate the impact of the number of coefficients used for the surface approximation, Figure 2 shows a surface reconstructed from a small and large number of coefficients, respectively. Using data of 1001 LIDAR points, the Fourier series representation was first calculated until the 2nd harmonics (5 coefficients, Figure 2a) and then to the 10th harmonics (201 coefficients, Figure 2b) in both directions.

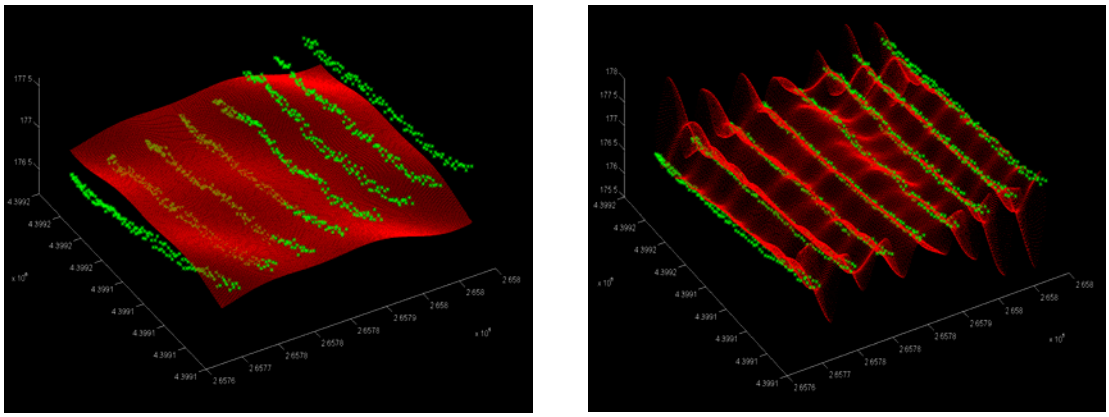

a) b)

Figure 2. Approximation by Fourier series, calculated until the 2nd and.10th harmonics.

In the case of 10 harmonics, the fit is excellent at the measured points, but between these points there are high waves due to the lack of constraints at these locations. If the Fourier series is calculated until only the 2nd harmonics in both directions, the approximation surface is smoother, there are no high waves, but the fit is not good at the measured points. These two cases clearly show the main properties of the Fourier-based interpolation. If the surface has a trend, especially due to irregular point distribution, a series of sine and cosine waves cannot always provide a good representation of the surface. The more harmonics of the Fourier series are calculated, the better the fit is at the measured points, but high frequency results in a wavy appearance of the interpolated surface. With a large number of harmonics, the fit at the measured points can be nearly perfect, but the interpolated surface may not have a good relation to the ground surface at all, due to the high wave amplitudes between the known points. Similarly, a small number of the Fourier series coefficients provides only a poor model of the surface and produces unacceptable differences at measured points. Consequently, a trade-off has to be found to obtain a smooth enough surface and an acceptable fit at the known points. This contradiction, however, cannot be solved using Fourier series interpolation itself.

Extending the Fourier series based interpolation method with a polynomial term

As a refinement to the Fourier series interpolation, a polynomial extension has been introduced to model the surface trend, thus splitting the approximation task into two parts, global trend and local variation modeling.

Figure 3a illustrates the approximation of the same 1001 LIDAR point surface, calculated as a combination of a first order polynomial (slant plane) and Fourier-series, calculated until the 7th harmonics in the LIDAR scan direction and 5th harmonics in the other direction (flight line). More harmonics were calculated in the scan direction due to the higher point density along the scan lines. The advantage of calculating different number of harmonics in the scan direction and perpendicular to this direction is that it accommodates for the more information in the scan direction due to the higher point density along the scan lines. Of course generally the scan lines are not lying in one of the main coordinate directions, but can be transformed to this position. Also, if the point density is balanced in both directions, then obviously there is no need for using different number of harmonics. Figure 3b depicts the modeled surface in the case of a 3rd order

polynomial extension with the same degree Fourier series, clearly demonstrating that this combination delivers a very good surface representation.

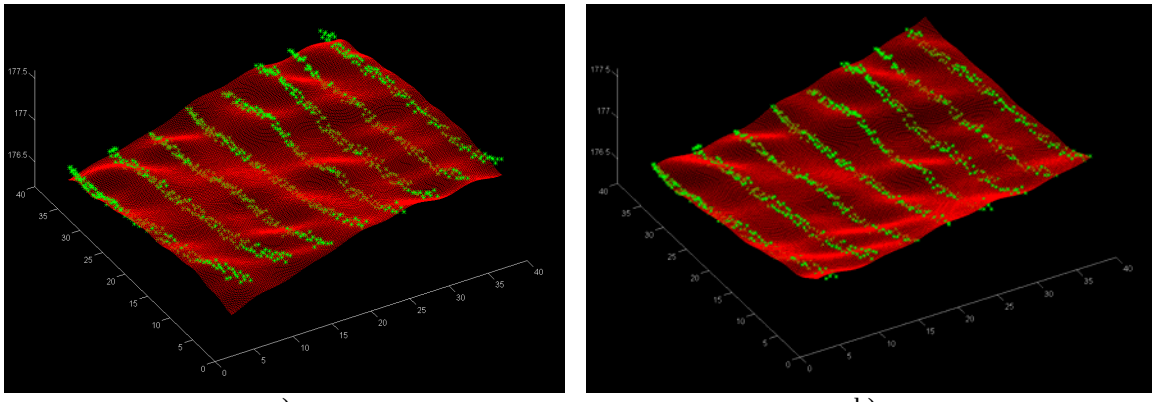

a) b)

Figure 3. Fourier series approximation with first (a) and third (b) order polynomial extension.

TEST RESULTS

The test areas were selected from two different LIDAR surveys with different point densities. The first two areas are of high point density while the third area has a very low point density. Figure 4 shows the three surfaces; the original LIDAR points are marked with red and the reconstructed surface is shown in green. In each case, an about 25 m by 25 m area was selected for the analysis. The areas were selected to assess how the proposed method works for different surface characteristics. The first (a) and third (c) areas represent typical smooth flat and sloped terrain situations with moderate elevation changes while the second (b) area has substantial elevation differences, reaching almost 8 m over the rather small area.

Based on the main characteristics of the three surfaces as well as point densities, the number of harmonics for the Fourier series as well as the order of the polynomial extension has been selected to compute the surface approximation by the proposed method. Table 1 contains the results, including important statistics along with LIDAR point density and number of points in the test area. Since the vertical accuracy of the LIDAR points is about 15 cm, the number of points where the difference between the measured and interpolated value is bigger than 15 cm is also shown.

Surface	Point density [p/m2]	No. of points	Parameters			RMS	No. of points dev>15cm	Dev >15cm [%]
			Polynomial	Fourier				
				n	m			
a	1.3	936	5	5	5	**0.028**	1	0.10
b	1.3	866	5	5	5	**0.042**	1	0.11
c	0.13	267	3	3	3	**0.030**	1	0.37

Table 1. Performance statistics.

The goodness of an interpolation method can be characterized by the discrepancies of the interpolated values from the measured values, which is expressed in the RMS terms. For all the three test areas, the RMS values are in the cm level, well within the vertical accuracy of the measured LIDAR points. As expected, the steep terrain (b) has the largest value. Of course equally important is how the interpolated surface behaves between the measured points. As shown in Figure 4, the method created nice, natural looking surfaces between the measured locations.

a)

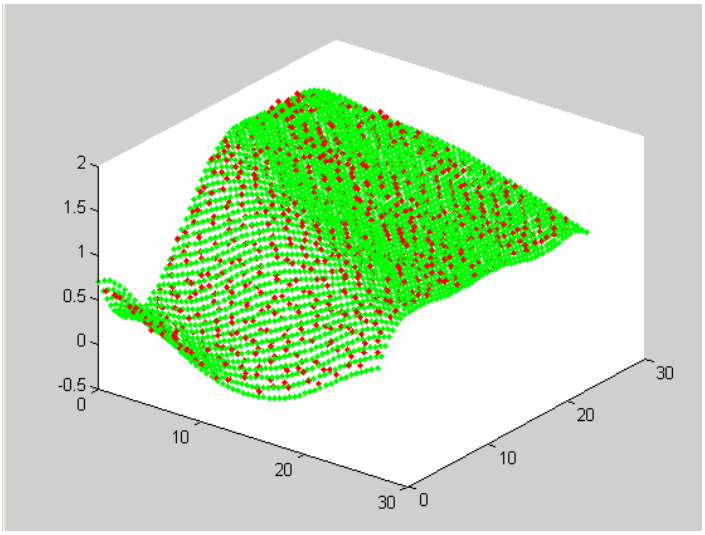

b)

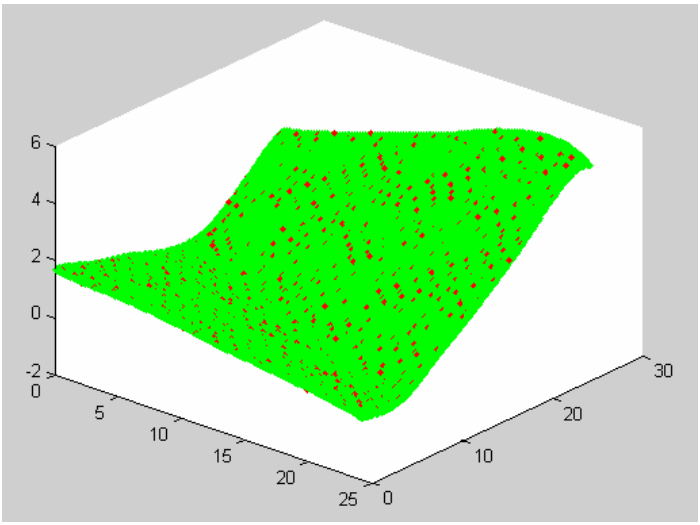

c)

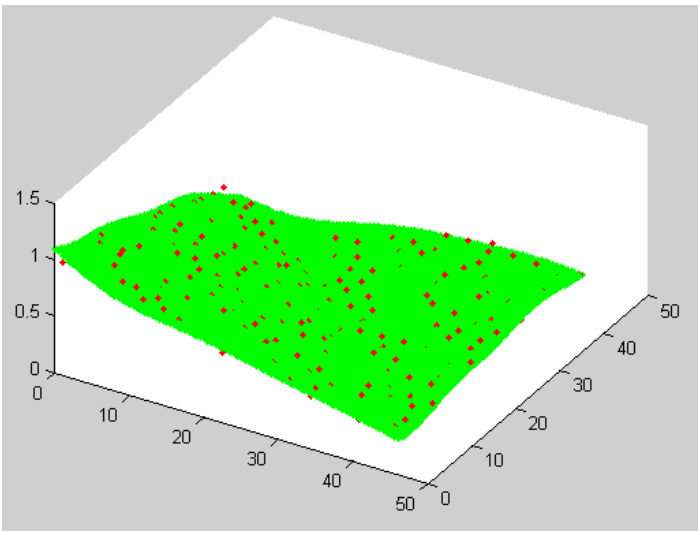

Figure 4. Various surface areas modeled by the proposed technique.

In summary, the proposed method has shown good performance with different point densities and works well with both regular and irregular point distribution. The interpolated surface is not constrained to the input data range – unsampled peaks and valleys can be represented to a certain extent. The method has the advantage that a few outliers do not disturb the interpolated surface; the surface maintains its natural shape in contrast to some other interpolation techniques. Based on the initial experiences, the method seems to be a very accurate surface modeling tool for smaller areas. The size of the areas to be modeled can be chosen by considering the terrain characteristics. In the case of smooth, rolling terrain the area can be larger, while surface with substantial undulations must be restricted to small areas. Obviously, any area size can be handled by segmentation; dividing the area into smaller surface patches and then merging them after the interpolation. Near the edges the interpolated surfaces often have unnecessary waves due to the lack of constraint from one side, therefore it is usually better to work with some overlap and cut around the edges. Due to the finite number of Fourier harmonics, this method is not suitable for modeling sharp, sudden changes and discontinuities like breaklines, buildings and other man-made objects.

CONCLUSIONS

A Fourier series based interpolation method combined with polynomial extension has been introduced. The traditional numerical procedure to calculate Fourier coefficients is based on regular input point distribution and therefore is not suitable for irregular point distribution. The proposed solution calculates the Fourier coefficients by a least squares adjustment. Tests have shown that because the Fourier series is calculated until finite harmonics, this representation has difficulty with modeling surface trends. Therefore, a polynomial extension has been introduced to circumvent this problem. In the combined solution, the polynomial part can nicely model trends in the surface while the Fourier series can adequately describe the smaller local changes in the data. This extended Fourier series based interpolation has shown promising results for modeling smoothly rolling terrain without any breaklines and other discontinuities. Besides, it has produced nice natural looking models for terrains without breaklines. The technique works well with both regular and irregular point distribution. A further improvement could be expected from using wavelet transformation as it is known for better modeling of local discontinuities and sudden changes in the data.

REFERENCES

Maune, D. F. ed. (2001). Digital Elevation Model Technologies and Applications: The DEM Users Manual, ASPRS, Bethesda.

Mesko, A. (1984). Digital Filtering Applications in Geophysical Exploration for Oil, Pitman Publishing, London.

Gold, C. (1991). Problems with handling spatial data - the Voronoi approach. *CISM Journal ACSGC*. Vol. 45, No. 1. pp. 65-80.

Isaaks, E. H., Srivastava, R. M. (1989). An Introduction to Applied Geostatistics, Oxford University Press, New York, Oxford.

Toth, Ch.K., Grejner-Brzezinska, D. A., (2000). Complementarity of LIDAR and Stereo Imagery for Enhanced Surface Extraction, *International Archives of Photogrammetry and Remote Sensing*, Vol. XXXIII, Part B3, pp. 897-904.

APPENDIX D

LiDAR Sensor Calibration and Processing

1. Csanyi N. and Toth C.: Boresight Misalignment Determination of GPS/INS Supported Camera Systems Using a Single Ground Control Point, Proc. ASPRS Annual Conference, May 5-9, CD ROM, 2003.
2. Paska E. and Toth C.: LIDAR Data Segmentation Based on Morphologic Filtering: A Performance Analysis, Proc. ASPRS Annual Conference, May 5-9, pp. 152-161, CD ROM, 2003.
3. LIDAR Data Classification and Segmentation Based on Morphologic Filtering: A Performance Analysis, Internal Report to ODOT, 2003.
4. Toth, C., N. Csanyi and D. A. Grejner-Brzezinska, 2002. A Practical Approach to LIDAR Sensor Calibration, Weikko A. Heiskanen Symposium in Geodesy, October 1-4, Columbus.
5. Toth C. K., Calibrating Airborne LIDAR Systems, ISPRS Commission II Symposium on Integrated Systems for Spatial Data Production, Custodian and Decision Support, International Archives of Photogrammetry and Remote Sensing, Vol. XXXIV, part 2, pp.475-480, 2002.

Boresight Misalignment Determination of GPS/INS Supported Camera Systems Using a Single Ground Control Point

Nora Csanyi and Charles K. Toth

Center for Mapping
The Ohio State University
1216 Kinnear Road, Columbus, OH 43212-1154
E-mail: nora@cfm.ohio-state.edu

ABSTRACT

Direct sensor orientation, measuring sensor position and attitude from physical parameters is rapidly spreading in the mapping practice. Knowing and maintaining the spatial relationship between the navigation and imaging sensors is essential in achieving mapping accuracy. The critical component of this relationship is the rotational component or boresight. In case of any boresight misalignment between the camera and the navigation system, the exterior orientation parameters of an image calculated from the navigation solution are not correct. This paper describes an adjustment method to determine the boresight misalignment using at least one ground control point that can be identified in a stereo image pair. In general, the sensor mounting bias between the camera and navigation system is defined by an offset vector and rotation between the two systems. Since the critical component is the rotation, our method focuses only on finding the boresight misalignment angles. The adjustment is based on the collinearity equation and requires an image pair and at least one known ground point with measured image coordinates.

INTRODUCTION

The determination of the exterior orientation parameters is a prerequisite for reconstructing the object space from images. Traditionally the determination of the orientation parameters is solved indirectly by using aerial triangulation (AT), which requires a number of known ground control points. Although a lot of the tasks of AT have been automated, it still requires interaction and supervision of skilled operators and needs a significant time of the mapping process.

In the last few years direct orientation has become a powerful and effective way of obtaining sensor orientation by direct physical measurements. Using integrated GPS/INS systems, the sensor orientation parameters can be determined directly without aerial triangulation. There have been several publications analyzing the performance difference between the direct and indirect orientation techniques. For example, Habib (2001) emphasizes the difference in georeferencing performance in the case of the presence of an error in the camera model. In general, indirect orientation performs better than direct orientation since the calculated EO parameters from AT compensate for the inaccuracy of the interior orientation. This mechanism is missing from direct orientation and therefore, the whole process is sensitive to sensor modeling errors.

From the applications' side, the use of GPS/INS based direct orientation is mandatory for LIDAR and RADAR systems and indispensable when using line cameras, where each scanline has its own exterior orientation parameters. In addition, direct orientation can be advantageous for frame cameras, too; see (Cramer, 2000). An important advantage is the removal of limitations of the flight path – AT needs block geometry of images. Certain applications require image acquisition over straight man-made and natural objects, such as power lines, coastlines (corridor mapping), and the like. In these cases, the block structure is simply not economical. In addition, image matching, which is required for AT, can be very problematic or impossible in areas such as forested areas, large water surface areas or areas with no texture. In these cases tie points cannot be found for AT and only direct georeferencing can solve this problem.

If direct orientation is used to determine the exterior orientation, the geometric relationship between the different sensors has to be known and maintained since the orientation sensors and the imaging sensor are spatially separated.

To relate the GPS measurements to the INS system, the lever arm (the vector between the GPS antenna and the INS) must be known. Since the navigation solution is always calculated in the INS frame and we need the orientation of the camera, the spatial relationship between the INS and the camera system also has to be determined. An offset vector and a rotation matrix between the two systems can describe this relationship. The critical component is the rotation since the object distance amplifies the effect of any angular inaccuracy, while the effect of any offset error does not depend on the flying height. The shifts can be determined using conventional terrestrial survey. The usual method of the determination of the boresight misalignment is to determine the orientation matrix of the images in the block by AT and then compute the mean rotation matrix between the GPS/INS provided orientations and the image orientations from AT (Mostafa, 2001). The calibrated boresight misalignment angles should remain constant as long as there are no relative movements between the two sensors. Once the boresight misalignment is known, the image orientation can be calculated by rotating the GPS/INS provided attitudes by the boresight matrix.

The number of medium resolution digital cameras, such as 4K by 4K systems used in airborne surveying, is steadily growing. Although AT-based orientation is possible, due to the smaller footprint, a large number of images is required to cover the same area at the equivalent ground resolution. This, in turn, results in an increased number of tie points and thus makes the AT process more time-consuming and subject to more errors. The image per ground control point ratio is also much larger. In summary, only direct orientation can offer an economically viable solution for that type of camera. Of course, for precise boresighting, AT must be used.

This paper discusses the feasibility of determining the boresight misalignment without AT, assuming the availability of at least two overlapping images and one known ground point (measured in both images). Theoretically, it is possible to determine borsesight misalignment angles if at least one ground control point measured in a stereo pair is available. However, as there are other error sources besides boresight misalignment, which influence the computation, the results must be taken with caution. The next section describes the proposed method, which is a simple least squares adjustment based on the collinerity equation. Assuming the presence of different errors in the exterior and interior orientation, the RMS of the determined boresight misalignment angles is analyzed in the following section. The last section presents simulation results with respect to the performance measured in pointing accuracy on the ground.

Motivation for this research effort is not to find a substitute for the conventional AT-based boresighting, but rather to introduce a method that can provide support for real life situations when the AT process is simply not available. For instance, if the sensor mounting has been disturbed during a flight and there was no block flown to perform a regular AT procedure, the proposed method can provide a method to salvage the data. Similarly, the technique can be used as a diagnostic tool to check the stability of the boresight or any change in the sensor model and so on.

SIGNLE GROUND CONTROL POINT BORESIGHT DETERMINATION METHOD

Initially we assume that the coarse rotation angles between the INS and camera frames are known and we are only looking for small misalignment angles. (Coarse angles mean the nominal alignment angles between the two systems; for example 90- or 180-degree κ rotation). Therefore, the differential rotation matrix of small angles is applied.

The adjustment is based on the collinerity equation extended by the three unknown boresight misalignment angles. To derive the modified collinerity equations, the following can be written:

$$\begin{bmatrix} X-X_0 \\ Y-Y_0 \\ Z-Z_0 \end{bmatrix} = \begin{bmatrix} r_{11} & r_{12} & r_{13} \\ r_{21} & r_{22} & r_{23} \\ r_{31} & r_{32} & r_{33} \end{bmatrix} \begin{bmatrix} b_{11} & b_{12} & b_{13} \\ b_{21} & b_{22} & b_{23} \\ b_{31} & b_{32} & b_{33} \end{bmatrix} \begin{bmatrix} X'-X_0' \\ Y'-Y_0' \\ Z'-Z_0' \end{bmatrix}$$

where

r_{ij}	are the elements of the rotation matrix between the mapping and INS frames
b_{ij}	denotes the elements of the boresight matrix, the rotation matrix between camera and INS frames
X, Y, Z	are coordinates of a ground point in the mapping frame
X', Y', Z'	are coordinates in the mapping frame, rotated parallel to camera system
X_0, Y_0, Z_0	are perspective center coordinates in the mapping frame
X_0', Y_0', Z_0'	are perspective center coordinates in the rotated mapping frame

After rearranging:

$$\begin{bmatrix} X'-X_0' \\ Y'-Y_0' \\ Z'-Z_0' \end{bmatrix} = \begin{bmatrix} 1 & d\kappa & -d\varphi \\ -d\kappa & 1 & d\omega \\ d\varphi & -d\omega & 1 \end{bmatrix} \begin{bmatrix} r_{11} & r_{21} & r_{31} \\ r_{12} & r_{22} & r_{32} \\ r_{13} & r_{23} & r_{33} \end{bmatrix} \begin{bmatrix} X-X_0 \\ Y-Y_0 \\ Z-Z_0 \end{bmatrix} = \begin{bmatrix} q_{11} & q_{12} & q_{13} \\ q_{21} & q_{22} & q_{23} \\ q_{31} & q_{32} & q_{33} \end{bmatrix} \begin{bmatrix} X-X_0 \\ Y-Y_0 \\ Z-Z_0 \end{bmatrix}$$

The collinerity equation modified by the boresight misalignment angles:

$$x = x_0 - c\frac{q_{11}(X-X_0)+q_{12}(Y-Y_0)+q_{13}(Z-Z_0)}{q_{31}(X-X_0)+q_{32}(Y-Y_0)+q_{33}(Z-Z_0)}$$

$$y = y_0 - c\frac{q_{21}(X-X_0)+q_{22}(Y-Y_0)+q_{23}(Z-Z_0)}{q_{31}(X-X_0)+q_{32}(Y-Y_0)+q_{33}(Z-Z_0)}$$

where

x, y	are the measured image coordinates of the ground control point
q_{ij}	are the elements of the boresight corrected rotation matrix between the mapping and INS frames, orientation of the image
$d\omega, d\varphi, d\kappa$	are the unknown boresight misalignment angles (these are contained in q_{ij})

The boresight misalignment angles can be found if the object coordinates of at least one ground point and its image coordinates are known. Applying the collinearity equation for both images, there are four equations with three unknowns. Therefore, a least squares adjustment can be formed for the misalignment angles, minimizing the square sum of the differences between the measured image coordinates and the calculated image coordinates, derived from the known ground coordinates. Since the reliability of the image coordinate measurements is the same in the two coordinate directions and no correlation between them is assumed, identity matrix is used as weight matrix in the adjustment. Obviously, in the special case of adjusting only for dκ misalignment angle, one unknown, one image is enough. As mentioned above, initially the coarse rotation angles between the INS and camera frames were assumed to be known. However, the method can be executed in an iterative way, and thus, the boresight angles can be found even if the coarse angles are not known. Although the method requires two overlapping images and at least one known ground point, it is advantageous to use more images and more ground points for better reliability.

The adjustment does not deal with the fact that the input parameters such as the attitude angles of the INS, the position of the perspective centers, and the camera model may be subject to errors. The method always works, but careful consideration should be given to the circumstances as errors from various sources may substantially affect the quality of the results. The potential errors are the following:

- orientation from the navigation solution has an error budget (shifts, attitude errors),
- camera model is not correct (focal length, principal point shift),
- measured image coordinates are affected by random errors (±5μm),
- ground control point coordinates are not error free.

In our simple adjustment method the only unknowns are the boresight misalignment angles; therefore, different errors above will affect the results as the resulted angles try to compensate for various error sources. In other words, the resulted boresight angles could be slightly different for all of the image pairs – each one is optimal for the image pair that was calculated from. In the following, the reliability of the resulted boresight misalignment angles will be studied by assessing RMS of the boresight misalignment angles in the presence of the above errors.

SIMULATION RESULTS OF THE PROPOSED METHOD

To analyze the effect of different error sources on the resulted boresight angles, simulations were carried out with two different camera types. The first one is a traditional film-based aerial camera (c=150mm); the second camera type is a 4K by 4K digital camera (c=50mm). These two camera types were selected because the large-format aerial camera symbolizes the ultimate performance limit while the 4K by 4K digital sensor represents the emerging digital cameras. In the simulations with both camera types, a stereopair with 60% overlap was used. To analyze the effect of the flying height, the simulations were carried out at three different flying heights (400m, 1200m, 3000m). To express the accuracy of the adjusted boresight misalignment angles, the RMS, derived from the differences between the resulted boresight misalignment angles and their known (preset) values were calculated.

Simulation results with a traditional film-based aerial camera

Table 1 contains the assumed standard deviations of the camera and orientation parameters in the case of a traditional film-based aerial camera. These values are intentionally larger than the results of a top of the line aerial camera calibrated by the USGS.

Table 1. Assumed random errors of traditional aerial camera

Error source	**Standard deviation**
Image coordinates	± 5μm
Focal length	± 10μm
Principal point	± 10μm
Perspective center position	± 10cm
INS attitude	± 10”

The simulations assumed a ± 5μm image coordinate measuring error. To analyze the effect of the uncertainty of the camera model, a ± 10μm standard deviation of the focal length and ± 10μm standard deviation of the principal point were assumed. (In the case of the 4K by 4K digital camera model these standard deviation values could be too optimistic since this type of camera is less stable.) Another error source, the position of the perspective centers, which mainly depends on the reliability of the GPS positioning, was characterized by ± 10cm standard deviation. For the INS attitude angles, a noise with ± 10” standard deviation was applied. The ground control point coordinates were considered to be error free since they can be determined at ±1cm accuracy and the effect of this uncertainty is negligibly small compared to the effect of other error sources.

Table 2 contains the RMS of the resulted boresight angles in the presence of different error sources in the case of different flying heights. The effect of each error source, separately and combined were studied. The magnitude of the different error sources can be found in Table 1. As we wanted to analyze the influence of the location of the used ground point on the reliability of the boresight misalignment results, the tables contain the RMS results in the case of using a ground point in nadir position, in the center of the model area, and a ground point in Gruber location 6. Simulations for ground points in all Gruber locations were performed and as expected, all the Gruber points in the corners of the model area (not in nadir position) gave approximately the same results as shown for Gruber location 6 in Table 2.

Table 2. RMS of boresight angles at traditional film-based aerial camera

Error source	**RMS [deg] Center point**			**RMS [deg] Gruber location 6**		
H=400m	**ω**	**φ**	**κ**	**ω**	**φ**	**κ**
Image coordinates	0.001	0.001	0.005	0.002	0.002	0.003
Focal length	0.001	0.001	0.004	0.002	0.002	0.003
Principal point	0.004	0.004	0.004	0.003	0.003	0.004
Focal length+princ.point	0.004	0.004	0.004	0.004	0.003	0.004
Perspective center position	0.010	0.009	0.032	0.015	0.019	0.029
INS attitude	0.002	0.002	0.008	0.004	0.005	0.008
Persp.cent.+INS attitude	0.010	0.009	0.035	0.015	0.019	0.030
All	0.010	0.010	0.033	0.015	0.019	0.030
H=1200m	**ω**	**φ**	**κ**	**ω**	**φ**	**κ**
Image coordinates	0.001	0.001	0.004	0.002	0.002	0.003
Focal length	0.001	0.001	0.004	0.002	0.002	0.003
Principal point	0.004	0.004	0.004	0.003	0.003	0.004
Focal length+princ.point	0.004	0.003	0.004	0.003	0.003	0.003
Perspective center position	0.004	0.003	0.012	0.005	0.007	0.010
INS attitude	0.002	0.002	0.008	0.004	0.005	0.007
Persp.cent.+INS attitude	0.004	0.004	0.014	0.006	0.008	0.012
All	0.006	0.005	0.013	0.007	0.008	0.013
H=3000m	**ω**	**φ**	**κ**	**ω**	**φ**	**κ**
Image coordinates	0.001	0.001	0.004	0.002	0.002	0.003
Focal length	0.001	0.001	0.004	0.002	0.002	0.003
Principal point	0.004	0.004	0.004	0.003	0.003	0.004
Focal length+princ.point	0.004	0.004	0.004	0.004	0.003	0.004
Perspective center position	0.002	0.002	0.006	0.003	0.003	0.005
INS attitude	0.002	0.002	0.008	0.004	0.005	0.007
Persp.cent.+INS attitude	0.003	0.003	0.009	0.004	0.006	0.009
All	0.004	0.004	0.009	0.005	0.006	0.009

The first row shows the RMS values caused only by the image coordinate measuring error. The next three rows illustrate the effect of the uncertainty of the camera model, the focal length, the principal point shifts and their combined effect. An uncertainty in the focal length, in addition to the image coordinate measuring error, does not have an effect on the resulted boresight angles if they were determined by using a ground point near the center of the model area. The uncertainty of the principal point shift mainly shows up in the ω and φ results. If only the interior orientation uncertainty were present, the resulted boresight misalignment angles would be more reliable if they were determined by using a ground point farther away from the nadir. Looking at the impact of the uncertainty in the INS attitude and the perspective center positions, the ω and φ results are better using a center point; κ is little bit better in the case of a point farther from the nadir. If we consider the combined effect of all the uncertainties, we get more reliable ω and φ results using a center point, but worse κ than in the case of using a ground point farther from the nadir. The κ result is less accurate, but the reliability improves as the flying height is getting higher. Considering all the uncertainties above, in the case of 1200m flying height the proposed adjustment can provide the ω and φ boresight angles with about ±0.4 arcminute reliability and κ with about ±0.8 arcminute.

Simulation results with a 4K by 4K digital camera

Table 3 contains the assumed standard deviations for a 4K by 4K digital camera. The camera model of the 4K by 4K digital camera is less stable than the camera model of the traditional film-based camera, the focal length and the principal point shifts can change significantly between calibrations (Toth, 1999); therefore, the ± 10μm standard deviation for the camera parameters would be too optimistic. Consequently, ± 20μm for the focal length and ± 100μm for the principal point shifts were used. Other than that, the same values were applied as in the case of the traditional film-based cameras.

Table 3. Assumed random errors at 4K by 4K digital camera

Error source	**Standard deviation**
Image coordinates	± 5μm
Focal length	± 20μm
Principal point	± 100μm
Perspective center position	± 10cm
INS attitude	± 10”

Table 4 contains the RMS results of the adjusted boresight misalignment angles in the presence of different error sources for the different flying heights. The table contains the results for two locations: ground point in the center of the model area and a ground point in Gruber location 6 (as in the previous simulation).

Table 4. RMS of boresight angles at 4K by 4K digital cameras

Error source	**RMS [deg] Center point**			**RMS [deg] Gruber location 6**		
H=400m	**ω**	**φ**	**κ**	**ω**	**φ**	**κ**
Image coordinates	0.004	0.004	0.015	0.004	0.006	0.010
Focal length	0.004	0.004	0.015	0.011	0.008	0.010
Principal point	0.110	0.104	0.016	0.075	0.069	0.053
Focal length+princ.point	0.110	0.104	0.016	0.075	0.065	0.050
Perspective center position	0.011	0.011	0.040	0.014	0.022	0.032
INS attitude	0.004	0.004	0.016	0.005	0.008	0.013
Persp.cent.+INS attitude	0.011	0.011	0.040	0.015	0.023	0.034
All	0.108	0.104	0.042	0.076	0.070	0.060
H=1200m	**ω**	**φ**	**κ**	**ω**	**φ**	**κ**
Image coordinates	0.004	0.004	0.015	0.004	0.006	0.010
Focal length	0.004	0.004	0.015	0.011	0.008	0.010
Principal point	0.107	0.102	0.016	0.074	0.065	0.052
Focal length+princ.point	0.112	0.102	0.016	0.075	0.063	0.051
Perspective center position	0.005	0.005	0.020	0.006	0.009	0.014
INS attitude	0.004	0.004	0.017	0.005	0.009	0.013
Persp.cent.+INS attitude	0.005	0.005	0.020	0.007	0.011	0.017
All	0.108	0.104	0.022	0.075	0.067	0.053
H=3000m	**ω**	**φ**	**κ**	**ω**	**φ**	**κ**
Image coordinates	0.004	0.004	0.014	0.004	0.007	0.010
Focal length	0.004	0.004	0.014	0.010	0.008	0.010
Principal point	0.114	0.102	0.016	0.074	0.065	0.053
Focal length+princ.point	0.112	0.103	0.016	0.074	0.065	0.052
Perspective center position	0.004	0.004	0.015	0.005	0.007	0.011
INS attitude	0.004	0.004	0.017	0.005	0.008	0.012
Persp.cent.+INS attitude	0.005	0.004	0.017	0.006	0.009	0.013
All	0.110	0.101	0.018	0.074	0.063	0.051

The principal point shift uncertainty affects mainly the ω, φ angles, but does not have significant effect on the κ angle for the ground point near the center. If the ground point is farther from the nadir point, the principal point shift uncertainty has significant effect on κ, too, but the reliability of the other two angles are better than in the case of center point. If all the uncertainties are considered, ω and φ angles are more reliable if the ground point is farther away from the center, while κ result is much more reliable if the ground point is near the center. The large uncertainty in the ω and φ results is due to the increased uncertainty in the principal point shifts. At 1200m flying height, the reliability of ω and φ is about ±4-6 arcminute, depending on the position of the ground point. The κ result is more reliable; about ±1.2 arcminute if the ground point near the center of the model area was used. Higher flying height improves all components, especially the κ result. To decide what is more advantageous, using ground points near or away from the center, the effect of the different boresight angles on georeferencing accuracy must be analyzed.

EFFECTS OF DIFFERENT ERRORS ON GEOREFERENCING

The reliability of georeferencing is analyzed only for the 4K by 4K digital camera using the boresight results of the proposed adjustment. To show how the different error sources could affect the calculated ground coordinates, first the effect of uncertainty in exterior orientation, the uncertainty in the camera model, and the uncertainty of the determined boresight misalignment angles are analyzed, separately and combined. RMSs at the 6 Gruber locations are calculated but only representative data are included in the tables (for convenience, the coordinate system was oriented with X-axis in the base direction and Y-axis perpendicular to that). The simulations were carried out at different flying heights to analyze flying height dependency; here only simulation results for 1000 m flying height are shown.

Effect of uncertainty in exterior orientation (navigation solution)

Table 5 illustrates the RMS values of the calculated X, Y, Z coordinates of the ground points at different standard deviations of the perspective center coordinates and attitude angles; Figure 1 shows a visualization of this dataset. Uncertainty of the attitude angles has significant effect on the calculated horizontal and vertical coordinates. The vertical coordinates are affected the most significantly, which can be easily understood considering that two rays with distorted directions do not intersect. The errors in the Y coordinates depend on the position of the point; Gruber points not in nadir locations are affected approximately three times more than points in nadir location. The effect of attitude errors is even bigger at higher flying heights. The errors in the calculated coordinates caused by errors in the perspective center coordinates are not amplified by the flying.

Table 5. Effect of exterior orientation errors on georeferencing

σ: Xo,Yo,Zo [cm]	σ:ωφκ ["]	RMS X [m]	RMS Y1 [m]	RMS Y3 [m]	RMS Z [m]
0	0	0.12	0.18	0.07	0.28
	5	0.13	0.19	0.07	0.30
	10	0.14	0.21	0.08	0.33
	20	0.19	0.30	0.10	0.46
	30	0.25	0.39	0.13	0.62
	45	0.33	0.55	0.18	0.87
	60	0.43	0.70	0.23	1.13
5	0	0.14	0.20	0.08	0.32
	5	0.14	0.22	0.08	0.34
	10	0.15	0.24	0.09	0.37
	20	0.20	0.32	0.11	0.49
	30	0.26	0.41	0.14	0.67
	45	0.34	0.55	0.18	0.89
	60	0.44	0.72	0.24	1.16

10	0	0.17	0.26	0.09	0.41
	5	0.18	0.28	0.10	0.43
	10	0.18	0.29	0.11	0.46
	20	0.22	0.36	0.12	0.58
	30	0.27	0.44	0.15	0.70
	45	0.36	0.59	0.20	0.95
	60	0.45	0.72	0.24	1.17
20	0	0.27	0.41	0.15	0.65
	5	0.28	0.43	0.16	0.69
	10	0.29	0.44	0.16	0.68
	20	0.32	0.50	0.18	0.79
	30	0.35	0.55	0.19	0.89
	45	0.41	0.68	0.23	1.08
	60	0.49	0.80	0.28	1.26
30	0	0.38	0.61	0.21	0.96
	5	0.38	0.60	0.22	0.98
	10	0.40	0.63	0.22	0.99
	20	0.42	0.67	0.22	1.05
	30	0.43	0.70	0.24	1.12
	45	0.50	0.81	0.28	1.29
	60	0.55	0.92	0.31	1.45

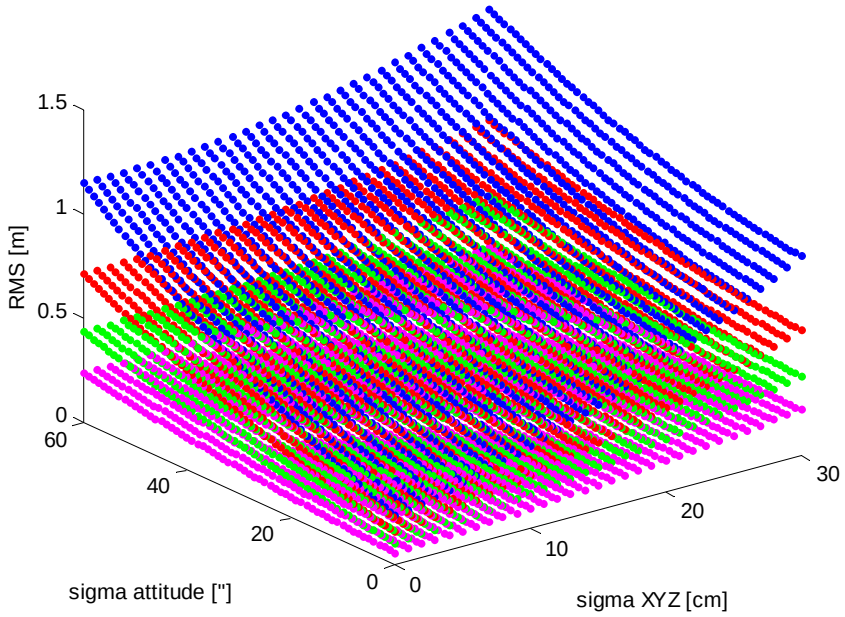

Figure 1. Effect of exterior orientation errors for RMS X, Y1, Y3 and Z; flying height is H=1000m.

Effect of uncertainty in interior orientation (camera model)

Table 6 illustrates the RMS of ground positioning at different standard deviations of the focal length and the principal point shifts; visualized results shown in Figure 2. Any uncertainty in the principal point shift affects the X and Y coordinates of the calculated ground points. In other words, the principal point shift error propagates to X, Y ground coordinate error according to the scale. Any uncertainty in the focal length affects the vertical coordinates of the calculated ground points according to the scale and it has not much effect on the horizontal coordinates.

Table 6. Effect of errors in camera model

σ: c [μm]	σ: x0,y0 [μm]	RMS X [m]	RMS Y [m]	RMS Z [m]
0	0	0.12	0.18	0.29
	10	0.23	0.28	0.28
	20	0.42	0.44	0.27
	50	0.98	1.01	0.29
	100	1.97	1.97	0.29
	200	3.87	3.92	0.28
	300	5.80	5.86	0.28
10	0	0.12	0.19	0.35
	10	0.23	0.28	0.35
	20	0.42	0.42	0.35
	50	1.00	1.00	0.35
	100	1.97	1.90	0.34
	200	3.83	4.07	0.34
	300	6.05	6.08	0.35
20	0	0.12	0.18	0.47
	10	0.26	0.27	0.48
	20	0.40	0.43	0.47
	50	0.99	0.99	0.49
	100	1.98	1.94	0.49
	200	3.90	3.94	0.48
	300	5.98	5.81	0.49
50	0	0.12	0.19	1.00
	10	0.22	0.26	0.99
	20	0.39	0.43	1.01
	50	0.97	0.99	1.01
	100	1.94	1.90	1.06
	200	4.00	4.01	1.04
	300	6.04	5.91	1.04

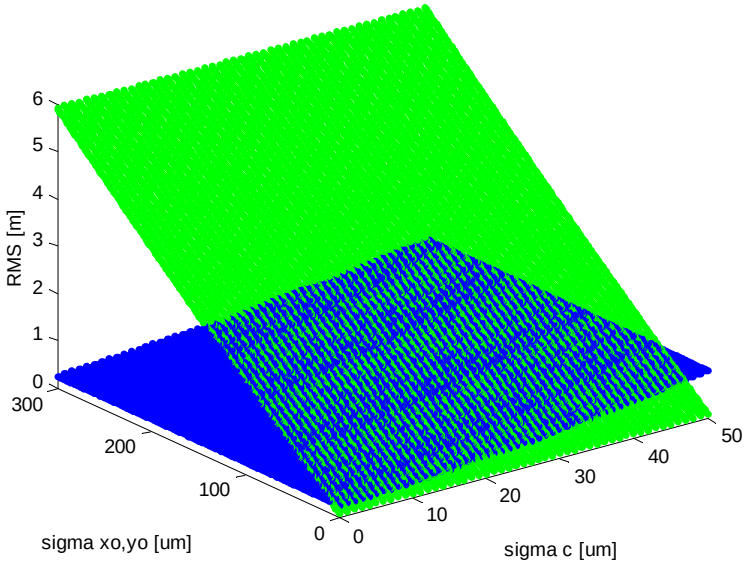

Figure 2. Effect of interior orientation errors for RMS XY (green) and Z (blue); flying height is H=1000m.

Effect of uncertainty in boresight misalignment angles

Table 7 illustrates the RMS of ground positioning at different standard deviations of the boresight misalignment. The standard deviation values were chosen according to the reliability of the boresight results of the proposed adjustment method. Errors in the ω and φ misalignment angles have significant effect on all three coordinates of the calculated ground points. If the ground point is farther from the nadir, the calculated vertical coordinates are worse. The effect of κ misalignment is much less, and practically negligible on the vertical coordinates; therefore, it is better using farther ground points to determine the boresight angles since this provides more accurate ω and φ misalignment angles.

Table 7. Effect of uncertainty in boresight misalignment

σ: ω,φ [']	σ: κ [']	RMS X [m]	RMS Y [m]	RMS Z1 [m]	RMS Z3 [m]
0	0	0.12	0.18	0.28	0.28
	1	0.21	0.20	0.28	0.28
	2	0.36	0.27	0.28	0.28
	3	0.52	0.34	0.28	0.28
1	0	0.30	0.34	0.37	0.34
	1	0.34	0.35	0.39	0.34
	2	0.45	0.40	0.39	0.34
	3	0.58	0.45	0.39	0.34
2	0	0.55	0.61	0.59	0.49
	1	0.59	0.64	0.61	0.50
	2	0.65	0.64	0.61	0.48
	3	0.78	0.69	0.60	0.49
3	0	0.82	0.90	0.84	0.68
	1	0.82	0.89	0.83	0.63
	2	0.87	0.91	0.85	0.65
	3	0.95	0.95	0.84	0.66
4	0	1.10	1.15	1.11	0.85
	1	1.09	1.15	1.09	0.84
	2	1.13	1.20	1.09	0.85
	3	1.19	1.21	1.10	0.84
5	0	1.33	1.47	1.33	1.02
	1	1.38	1.46	1.35	1.06
	2	1.41	1.51	1.37	1.06
	3	1.47	1.47	1.35	1.05
6	0	1.63	1.80	1.63	1.25
	1	1.64	1.76	1.61	1.24
	2	1.60	1.79	1.59	1.21
	3	1.72	1.81	1.62	1.24
7	0	1.92	2.07	1.90	1.45
	1	1.92	2.13	1.91	1.44
	2	1.93	2.03	1.87	1.43
	3	1.99	2.10	1.87	1.47

Reliability of ground positioning using boresight misalignment angles from proposed method

After studying the effect of different errors on georeferencing accuracy, this section analyzes the reliability of the calculated ground coordinates that can be achieved using the boresight results from the proposed method (when all kinds of error sources are present); only the 4K by 4K digital camera case is considered. Table 8 contains the RMS values of the calculated ground coordinates in the case of 400m and 1200 m flying heights. These values are calculated by simulation considering the standard deviations of the camera

and other parameters described in Table 3 and the RMS values of the boresight results described in the previous section. Table 8 contains two different RMS Z values since the calculated vertical coordinates are more accurate at nadir locations.

Table 8.

H [m]	RMS X [m]	RMS Y [m]	RMS Z1 [m]	RMS Z3 [m]
400	0.97	0.97	0.61	0.52
1200	2.82	2.82	1.57	1.29

The above results refer to the case when the camera and other parameters are independent of the boresight angles. Assuming the camera parameters did not change during a flight, the above georeferencing accuracy is too pessimistic because of the correlation between the errors in the camera model, the INS orientation, the perspective center coordinates and the resulted boresight misalignment angles. Therefore, Table 9 shows the RMS values of the calculated ground coordinates if the ground coordinates were calculated from the same image pair as the boresight angles were determined from. For this situation, the following biases were assumed:

- +100μm principal point shift bias
- +20 μm focal length bias
- +10cm perspective center position error
- +10" INS attitude error

Since the resulted boresight misalignment angles try to compensate for all errors, the accuracy of the calculated ground coordinates is better than the values in Table 8; a few decimeters in the case of 400m flying height. Since the effect of the uncertainty of the perspective center coordinates and the INS attitude on the resulted boresight angles is not significant compared to the effect of errors in the camera model, assuming that the camera parameters did not change during the flight, practically the same georeferencing accuracy can be achieved using other image pairs from the same flight.

Table 9.

H [m]	RMS X [m]	RMS Y [m]	RMS Z [m]
400	0.36	0.30	0.48
1200	1.10	0.79	1.30

CONCLUSIONS

If direct orientation is used to determine the exterior orientation, the spatial relationship between the different sensors has to be known since the orientation sensors and the imaging sensor are geometrically separated. The usual way to determine the boresight misalignment is aerial triangulation. This paper discussed the feasibility of determining the boresight misalignment without AT, assuming the availability of at least two overlapping images and one known ground point measured in both images. The motivation for this study was to introduce a method that can provide solution in situations when proper boresight calibration with an AT process is not possible; there was no block flown to perform a regular AT procedure and the sensor mounting has been changed since the last boresight calibration. Since the results of this simple adjustment are affected by other error sources, the accuracy of the determined boresight angles have been analyzed in the presence of different random errors. Simulations were carried out with traditional aerial cameras as well as 4K by 4K digital cameras. The focus was on the latter camera type due to its geometric instability. Analyzing the georeferencing performance using the resulted boresight angles, a few decimeters georeferencing accuracy has been achieved provided the computation was based on images from the same flight. The accuracy of the determined angles was a few arcminutes. These results indicate that the adjusted boresight angles compensate to a certain extent for possible errors such as sensor model anomalies.

REFERENCES

Cramer M., Haala N. (1999): Direct Exterior orientation of Airborne Sensors-an Accuracy Investigation of an Integrated GPS/Inertial System, Proc. ISPRS Workshop Comm. III/1, Portland, Maine, USA.

Cramer, M., Stallmann, D., Haala, N. (2000). Direct Georeferencing Using GPS/Inertial Exterior Orientations For Photogrammetric Applications, *International Archives of Photogrammetry and Remote Sensing*, Vol. XXXIII, Part B3, pp. 198-205.

Habib A., Schenk T. (2001): Accuracy Analysis of Reconstructed Points in Object Space from Direct and Indirect Exterior Orienation Methods, OEEPE Workshop on Integrated Sensor Orientation. Institute for Photogrammetry and Engineering Surveying, University of Hannover, (17-18 September, 2001).

Mostafa M. M. R. (2001): Digital Multi-sensor Systems - Calibration and Performance Analysis, OEEPE Workshop on Integrated Sensor Orientation. Institute for Photogrammetry and Engineering Surveying, University of Hannover, 17-18 September, 2001.

Toth, Ch. (1999): Experiences with Frame CCD arrays and direct georeferencing, Photogrammetric Week '99, *Wichmann Verlag*, pp.95-107.

LIDAR Data Segmentation Based on Morphologic Filtering: A Performance Analysis

Eva Paska and Charles K. Toth

Center for Mapping
The Ohio State University
1216 Kinnear Road, Columbus, OH 43212-1154
E-mail: eva-paska@cfm.ohio-state.edu

ABSTRACT

In the last few years, LIDAR technology has become a leading tool for obtaining surface models and to some extent for extracting various objects. One of the main tasks related to the data processing is the segmentation of the surface given by the preprocessed LIDAR points. Several methods have already been developed to classify the point cloud. The basic concept is to examine the spatial behavior of the LIDAR points; primarily, the point distribution and the number of return signals are used for classification. Depending on what the laser beam was reflected from, there might be signature information available for the LIDAR points, which can be further used for classification.

In this paper a concept for building detection based on mathematical morphology is introduced and its performance with respect to commercially available LIDAR data classification software is presented. The density of the LIDAR data used for testing was low, about 0.1 point/m^2.

INTRODUCTION

In the last few years LIDAR technology has become a leading tool for obtaining surface and terrain models and extracting various objects. Many algorithms have been developed for filtering and automatically classifying the LIDAR points. In commonly accepted terminology, filtering is referred to the determination of the terrain, while classification is used in broader terms and it includes object extraction.

The raw or unfiltered LIDAR data give the digital surface model (DSM) of the measured area, which is the upper envelope of our world that includes LIDAR points reflected from the ground as well as from natural and man-made objects. The ultimate challenge is to remove from the point cloud those points that do not belong to the ground. Different filtering methods to determine the terrain have been developed over the years. At the Institute of Photogrammetry and Remote Sensing at Vienna University of Technology a method based on iterative linear prediction was developed for the generation of terrain model in wooded and hilly areas (Kraus and Pfeifer, 1998). This method was later extended for more complex, densely built-up areas using a hierarchical, coarse-to-fine approach (Pfeifer at al., 2001); its implementation is commercially available in the software package SCOP++. Another technique by (Axelsson, 1999; Axelsson, 2000) is based on a TIN densification and was developed at the Department of Geodesy and Photogrammetry at the Royal Institute of Technology, Stockholm. The commercially available software package, TerraScan, has been built around this method. Another scheme based on mathematical morphology was presented in (Vosselman, 2000) and (Vosselman and Maas, 2001). A recent technique suited to rather dense data sets was introduced by (Elmqvist, 2002) and uses an active shape model for terrain estimation.

In addition the terrain model generation, when points are classified as either terrain or off-terrain points, automatically extracting and reconstructing objects from the point cloud have become a main research topic in the LIDAR data processing field. Several methods have been published related to building extraction and reconstruction, see (Brunn and Weidner, 1997; Hug and Wehr, 1997; Axelsson, 1999; Maas and Vosselman, 1999; Vosselman and Dijkman, 2001; Rottensteiner and Briese, 2002; Elaksher, 2002), and for forest feature extraction, see (Nilsson, 1996; Nässet, 1997; Törmä, 2000; Hyyppä at al., 2001; Pyysalo and Hyyppä, 2002; Schardt at al., 2002).

As most of the techniques are specific or customized to certain data types, it is important to understand the performance limitation of the different methods. In other words, for a given dataset what classification strategy will work well? The sensitivity of the methods is usually measured in point density and in the complexity of the area such as the terrain and the objects. Obviously, there is no perfect automatic classification method but with the algorithmic improvements the number of misclassifications can be reduced.

Recent technological advancements in LIDAR technology have resulted in better data quality and richer information content, consequently improving classification performance. The most important changes are the increased point density coupled with better point distribution, the availability of multiple return signals, and the intensity data or complete waveforms.

Our primary motivation to classify LIDAR points was to find adequate support for automated LIDAR sensor calibration. The task was to find an appropriate segmentation of the LIDAR point cloud over an overlapping area, which was usually flown in different directions. The objective of the segmentation was to find suitable regions for matching in order to determine discrepancies between the different strips. Ideal regions do not contain vegetation, buildings and cars, and they are not too flat (have some undulations). A possible approach to solve this complex task is to first mask areas with vegetation and buildings to avoid these regions and then to select areas, which exhibit the suitable surface pattern. To accomplish this objective, a method based on the principal of mathematical morphology has been developed.

SELECTED FILTERING METHODS

In this section, a short review will be given of the methods that have been considered for solving the segmentation task described above. Our objective was to start from assessing the feasibility of the various techniques and then based on performance tests select the optimal one for either directly using it or to develop an incremental method.

Robust interpolation, introduced by (Kraus and Pfeifer, 1998) initially approximates the surface calculated from all points by using the same weight. This is a coarse estimation of the surface running between terrain and off-terrain points. Next, height differences between the LIDAR points and the interpolated surface are calculated. Ground points will typically get either large negative or small residuals since the surface approximation is running above or close to the terrain. In the next step, all points will be weighted depending on their residuals using a special weight function to give new weights to each point. Points with large negative discrepancies will get large weights (assumed terrain points) while points with medium discrepancies will get smaller weights. Zero weight ignores points with discrepancies more than a user-specified value. A new surface is computed from all points using the new weights. The interpolation and weight calculation is repeated; in each step a better estimation of the terrain will be created. The final interpolated surface provides the DTM of the area that is calculated from only the selected terrain points. In this manner points are classified as either terrain or off-terrain points. This method works well on wooded areas where terrain points, points reflected from the ground, are frequently available. To handle densely built-up areas (large areas without true ground points) the original algorithm has been extended by a hierarchical, coarse-to-fine method, see (Pfeifer at al., 2001).

The technique developed by (Axelsson, 1999; Axelsson, 2000) uses a hierarchical algorithm, which is based on a TIN-representation. A grid with a user-defined size is laid over the dataset and in each pixel of this

mesh the lowest vertical point is selected. In the next step, an initial TIN is created from the selected points as the first approximation of the ground surface. Adding the LIDAR points to the triangulation leads to the final solution. Points are selected one by one; a point may be accepted or rejected as a new terrain point based on certain criteria by user-specified parameters such as iteration distance (the distance between the candidate point and the present surface) and iteration angle (the angle between the surfaces with and without the candidate point). Accepted points are inserted into the triangulation and with every new point the TIN surface is modified (altered) and consequently converging closer to the real terrain. In the initial point selection the grid size is determined with the maximum building size parameter. The size of a pixel will be equal to the maximum building size. For instance, if the maximum building size is 50 m, the application can assume that any 50m by 50m area will have at least one hit on the ground and the lowest point in the pixel will be selected as a terrain point; for additional details, see (TerraScan).

Mathematical morphology is widely used in image processing. It works as a convolution filter - applying the same processing to each element. A new value is given to the pixel on which the kernel is centered; during erosion this is the minimum value inside the window while the maximum value is used in the case of dilation. This method easily can be applied to the LIDAR data. The moving window (kernel) is centered on each point. The elevation of the examined point is replaced with the minimum or maximum elevation inside the window. The opening (dilation after erosion) is typically used for LIDAR data terrain extraction; see (Vosselman, 2000). For each window after opening, the point with the lowest elevation and all other points that are higher than that point but smaller than a predefined value are selected as terrain point. Since there is no optimal window size (Kilian at al., 1996), different sizes of the moving window are used. As the window size increases the height tolerance increases to follow the changes in terrain slope. The tolerance has to be smaller than the minimum building height to avoid classifying building roofs as terrain.

A MORPHOLOGY-BASED METHOD

To support the segmentation of the automated LIDAR sensor calibration process, a morphology-based method has been developed. The main goal is to eliminate points that do not belong to the terrain without classifying them. Thus, the presented method intends to mask areas of buildings, vegetation, and has no special interest in identifying/reconstructing features. In the computations, the original irregularly distributed LIDAR points are used; the data are not interpolated to a regular grid (e.g. as in (Oude Elberink and Maas, 2000)).

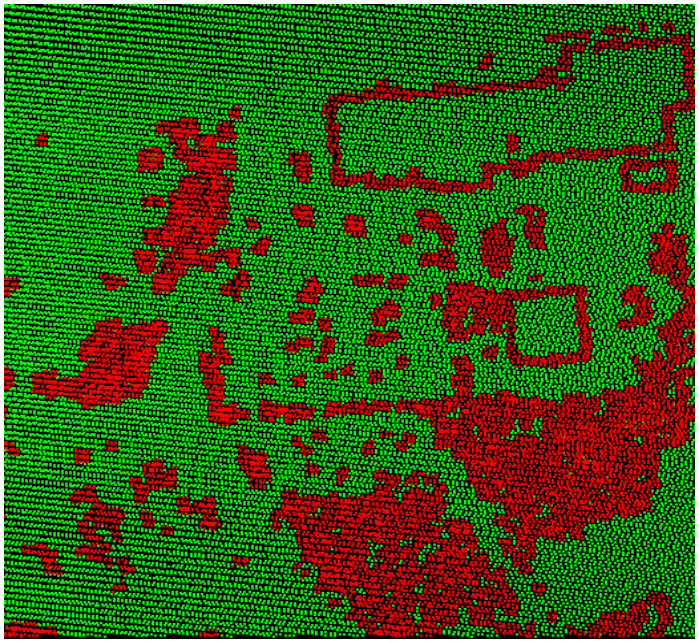

Figure 1. Breaklines extracted from Hagerstown, MD test area.

The spatial behavior of the LIDAR points is analyzed through a moving window-based algorithm. A window is moved over the entire dataset and in each window basic statistical parameters are calculated; such as standard deviation, maximum gradient among points, and the difference between the maximum and minimum elevations. In the next step, various extraction routines are executed; such as the detection of areas with given height jumps, i.e. the difference between the maximum and minimum elevations in a window is higher than a given value. In this manner breaklines (including natural breaklines) edges of buildings and local height variations can be selected from the point cloud. Figure 1 shows generic surface breaklines defined by 4 m height variation from the Hagerstown, MD dataset.

The choice of the window size depends on the data density and the purpose of the analysis. Obviously, there is no optimal window size in general. For instance, the window size must contain at least 8-9 points in order to detect generic breakline locations; for the distribution of the gradients, a larger window (including many more points) is needed. Another important parameter is overlap between the windows as they move. One extreme is when the moving window is centered on each point; the other one is if there is no overlap. A half of the window size is usually a good compromise between execution time and performance.

Removing vegetation

The distinctive spatial distribution of the LIDAR point cloud over vegetated areas is due to the capability of the laser pulse to penetrate the forest canopy through gaps. Pulses can be reflected back from many parts of the surface (from the ground as well as from different parts of the trees) and several returns can be recorded from the very same laser pulse. Differences in height variations range from zero to the canopy height over vegetated, especially forested areas. In our algorithm those areas where the variations of the surface gradients are above a predefined threshold are flagged as vegetated regions. This is similar to the procedure by (Rottensteiner and Biese, 2002), where regions with trees are also eliminated by the analysis of the second derivatives of the DSM.

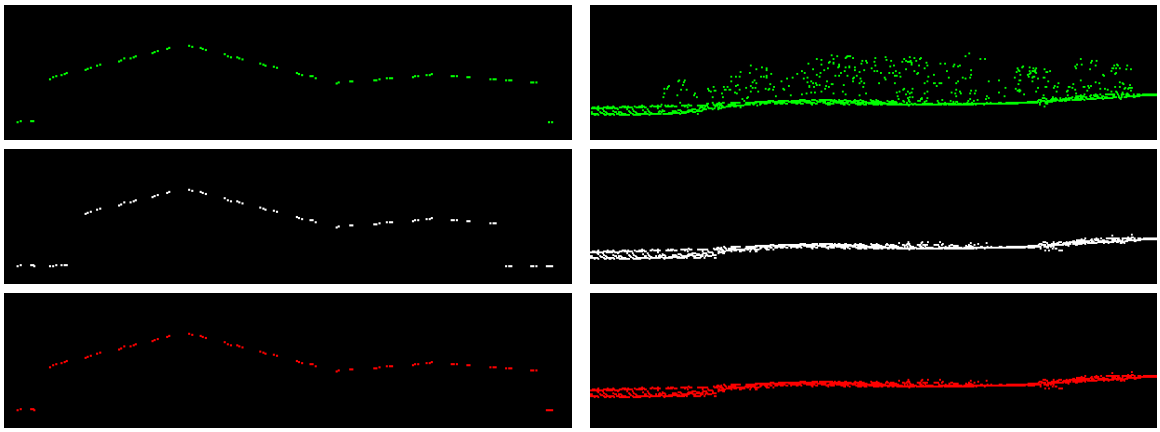

Figure 2. Morphological opening on vegetation and building profiles: original dataset (upper pair), erosion (mid pair) and dilation applied after erosion (lower pair).

A second technique selected for filtering out vegetation is based on a morphological filtering (opening); see Figure 2. This method has certain advantages such as an easy way to eliminate single trees. Choice of the window size is more crucial than in the statistical method above. To safely remove vegetation, at least one hit from the ground must exist in each window in vegetated areas. Simple opening will not filter out buildings, which are bigger than the window size, but the roofs of these buildings may be distorted. To avoid this distortion, few modifications have been introduced. During the erosion, the elevation of the examined point is replaced with the minimum elevation inside the window if the difference is more than a predefined threshold (a practical value is 2 m). Similarly, during the dilation the elevation of the examined point is replaced with the maximum elevation inside the window if the difference is more than the same predefined threshold. Furthermore, if the difference is more than a certain value (minimum building height),

the elevation of the examined point won't be replaced with the maximum value, but with the original elevation of the point. The weakness of the min/max method is that any objects that are smaller than the minimum building size will be filtered out as well. The modified dataset, optimistically without vegetation points, is adequate for detecting buildings independently whether the roofs of the buildings have changed or not.

Combining the outcome of the two independent processing techniques will result in an improved performance as the two techniques compensate for each other's weaknesses. For example, local variations are easily eliminated by the second method, but it fails if the vegetation is too dense and there is no terrain point inside the window. In contrast, the first method will detect such variations from the canopy.

Detecting buildings

Most building detection techniques start after the terrain model computation is complete and then a height threshold is applied to the difference between the DTM and DSM (Weidner, 1997; Rottensteiner and Biese, 2002). In our case, however, the availability of DTM is no prerequisite for the building extraction as it starts from the reduced data set; opening eliminates the vegetated points but preserves buildings as shown in Figure 3 for a moderately vegetated area with small buildings. In the following, this reduced data will be considered as original dataset (Figure 3b).

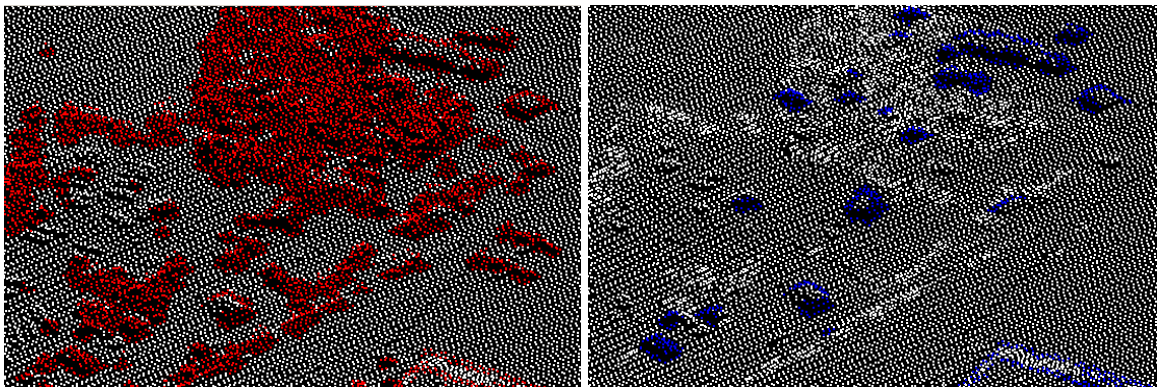

a) b)

Figure 3. Extracted generic breaklines (left) and after opening has been applied (right).

To detect building edges, the calculation begins with finding predefined height jumps, i.e., in each window the difference between the maximum and minimum elevations is computed. The processing window is moved over the data set with half of the window size in both directions. The minimum predefined height jump (H_{min}-jump) is set to the minimum building height (H); typically this is set to 4 m. Storing these computation results, an initial indicator matrix is formed and is the basis of the subsequent analysis. Each pixel in this matrix represents a window and contains the value associated with that window. Windows with the H_{min}-jumps are labeled with 1 (indicator windows); without the height jumps they are assigned a 0. Although supposedly vegetation points have been removed from the data set, besides the building edges some other breaklines (due to natural or man-made objects) may also be indicated in this matrix as shown in Figure 3b.

Once the breakline detection is complete, the contours of all buildings will be detected. The challenge at this point is to identify all the points of each building. In the next step, point-groups are created by a calculation, which is based on mathematical morphology (erosion) and is executed for each indicator window (i.e. for each pixel in the indicator matrix labeled with 1) individually. The computation starts from the indicator pixel and the original dataset is used in this process. In the indicator window, elevations of points above the minimum height point with more than H are replaced with the minimum elevation. The eight neighborhood pixels of the indicator pixel are marked in order to check the height differences inside these windows. Neighboring windows are analyzed in an iterative process. In each step the eight

neighborhood pixels of the previously studied pixels, where the H_{min}-jump was found, are marked in order to also check the height discrepancies inside these windows. The process, illustrated in Figure 4, is iterative until neighboring windows with H_{min}-jump are found. For the reason that windows are moved with overlap (half of the window size), the subsequent window will always contain points with original and previously modified elevations. This is the key for "demolishing" buildings, as shown in Figure 4. The algorithm uses the basic idea of mathematical morphology (erosion); in the kernel, the values are changed for the minimum. In our approach the principle of the erosion was modified in two aspects. First, the elevation is replaced only if the height difference from the minimum is more than H. Second, elevations in the subsequent windows are analyzed by considering the previous height modifications.

After the iterative process is finished, the elevations of the modified dataset are subtracted from the elevations of the original dataset. The subtraction results in many no difference in heights and some non-zero heights (selected points). In the case when the indicator window represents an area over building edges, points with non-zero height are building points belonging to the same building. Selected points with their original heights are stored in a layer of a multi-layer matrix. Each layer is identified by the indicator pixel (window) that began the individual iterative calculation. In summary, the execution of the iterative computation for all ***n*** indicator windows results in ***n*** point-groups stored in ***n*** layers.

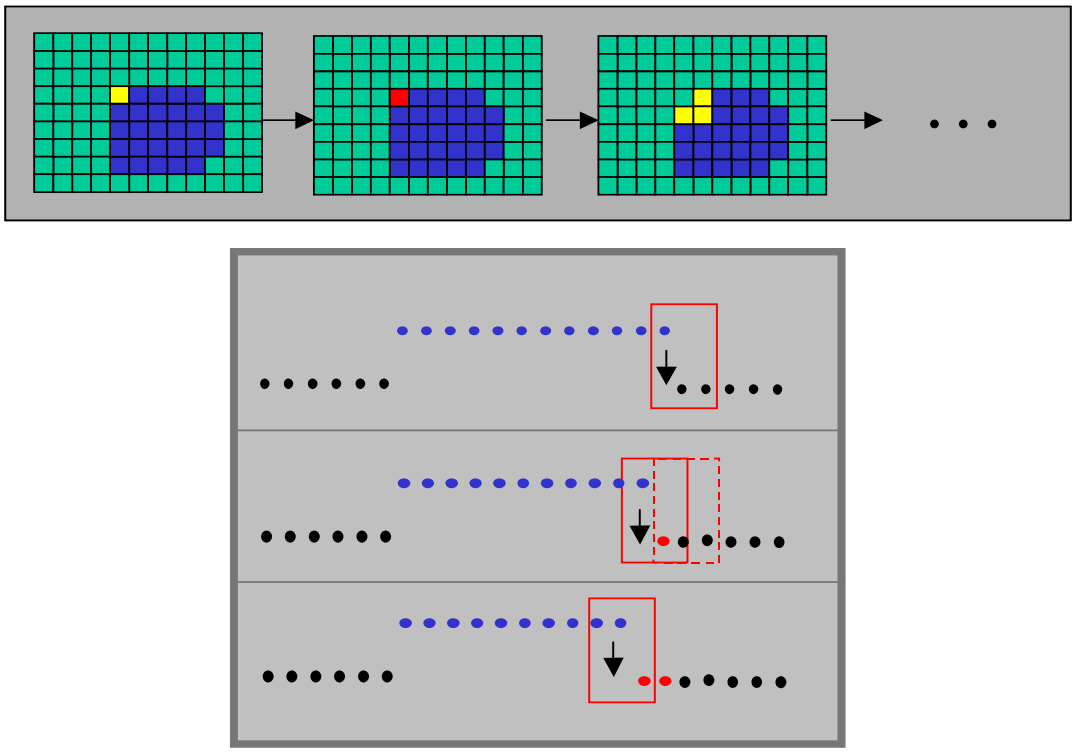

Figure 4. Concept of the iterative building demolition.

Advantages of the "demolishing" method, illustrated in Figure 5, are:

- invariant to the size and shape of the building and the type of the roof,
- the same point cloud will always be selected no matter where (which part of the building edge) the demolishing was started,
- coherent points belonging to the same building are always stored in one layer.

The iterative calculations starting from the indicator windows are independent; in each case the computation starts from the original (unchanged) data set and the results are stored on different layers. This way, buildings will not get demolished due to a natural breakline triggered events.

So far the iterative computation for all ***n*** indicator windows was executed resulting in ***n*** point-groups stored in ***n*** layers. One can assume that from the ***n*** point-groups ***m*** point-groups refer to ***q*** buildings ($0 \le m \le n$; m=n: ideal case, indicator matrix indicates only building edges; m=0: no building, and $0 \le q < m$). A building is associated to as many layers as many edge windows belong to the building that were detected and marked in the initial indicator matrix. Furthermore, each layer belonging to the same building contains the same point cloud (point-group) due to the algorithm of building "demolishing".

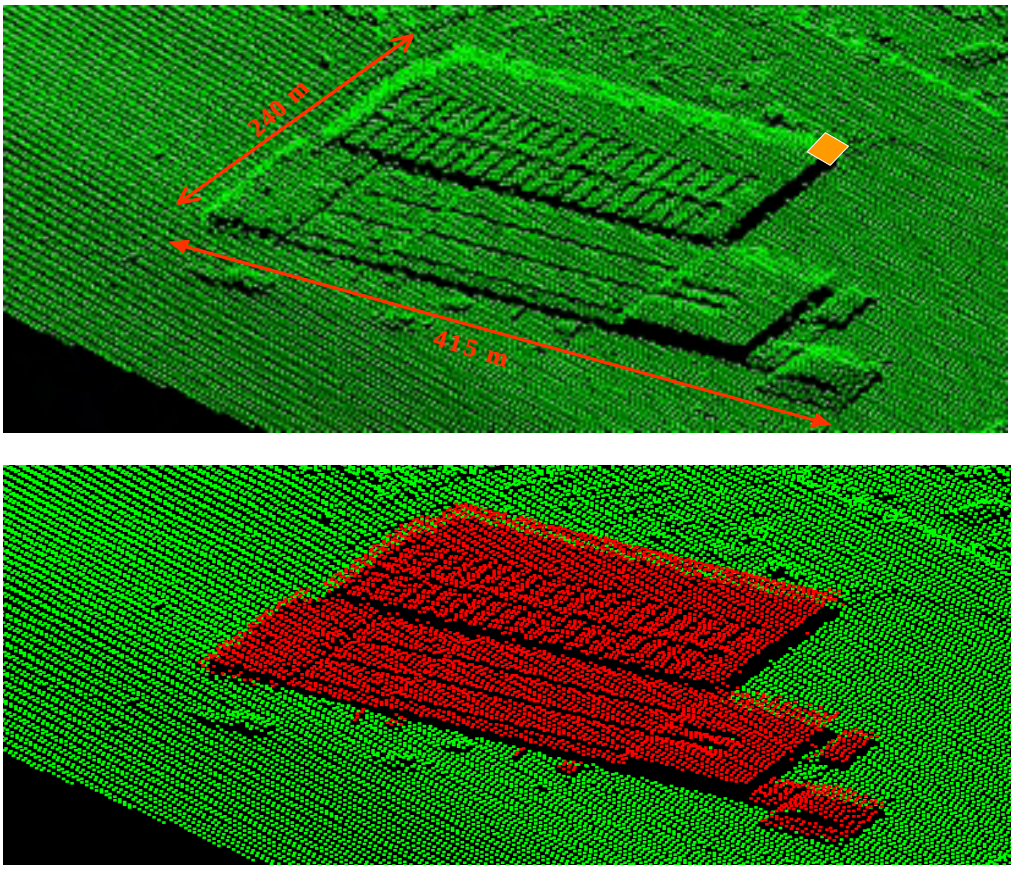

Figure 5. Selected building points (lower), the iterative calculation started from the corner (upper).

Using the above-described features, the recognition of building point-groups is accomplished in two phases:

- By comparing the different layers, layers that contain the same point cloud are combined into one layer. ***n*** point-groups become ***q+p*** point-clouds; ***q*** point-clouds refer to ***q*** buildings and ***p*** point-clouds refer to ***p*** others, i.e. $\boldsymbol{m} \rightarrow \boldsymbol{q}$ and $\boldsymbol{n-m} \rightarrow \boldsymbol{p}$. The point-group/point-cloud relationship (k:1 relationship) is registered. Each point-group (i.e. layer) is identified by an indicator pixel (which represents an indicator window, which is an edge window). In this manner, the relationship between a point-cloud and edge-windows belonging to the point-cloud ($\boldsymbol{set_1}$) has been determined.
- Since typically building edges as well as other breaklines are flagged in the initial indicator matrix, the main question is how we can distinguish between the point-clouds of building edges and the other breaklines. In order to solve the problem of selecting the ***q*** building point-clouds from the ***q+p*** point-clouds, for each ***q+p*** point-clouds the following computation is executed. Edge-windows belonging to a point cloud are extracted by dividing the original data set into cloud and off-cloud points. From all the windows, edge-windows are selected by choosing windows containing both cloud and off-cloud points ($\boldsymbol{set_2}$).

Comparing $\boldsymbol{set_1}$ and $\boldsymbol{set_2}$, the elements of the two sets will be identical for buildings, but not for other breaklines or terrain roughness.

Additional parameters (such as minimum and maximum building size) as well as aspect ratios can be defined to avoid gross errors. The introduced method, however, is suitable for the detection of complex buildings even with huge sizes.

TEST RESULTS - PERFORMANCE ANALYSIS

The test dataset, an area over Hagerstown, MD, was provided by the EarthData Group. The LIDAR point density was rather small, about 0.1 point/m^2; the data contained multiple returns. The test area, a 2 km by 2 km square is characterized by flat terrain, with various vegetation and buildings of different sizes and types. For comparison purpose, two LIDAR processing packages have been used; although there was no attempt to perform complete evaluation.

Using TerraScan, building, vegetation, ground, railway and power line points can be classified interactively or using automated processes. The program has shown a good performance in terrain point selection. There are three user-defined parameters and it is definitely worth optimizing them, especially changing the default value of the maximum building size to avoid serious misclassifications. If the maximum building size is set to 50 m, the application assumes that any 50m by 50m area will have at least one hit on the ground, hence the lowest point in each 50m by 50m mesh will be selected as terrain point. After setting the proper building size parameter, only few misclassifications may occur. The program cannot handle negative outliers; error points that are well below the ground level. Therefore, the “low points” utility must be run before the terrain determination, which flags points that fall below the average of points within a given distance.

The algorithm of RTV (Rapid Terrain Visualization) LIDAR Toolkit is proprietary. The program is implemented as an ArcView extension and is capable of extracting buildings, the bare earth, roads and trees. Feature extraction can be supported by intensity data. RTV Lidar Toolkit offers interactive classification and automated processes; although in our experiments the automated processing has shown modest performance. There seems to be less control by the user-defined parameters. Building-extraction produced better results for suburban areas than for dense, built-up urban areas, especially for areas with oversize buildings.

The combined building and vegetation performance of the RTV and the proposed morphology-based method has been tested for a few datasets. Figure 6 shows results for the Northwest segment of the test area, with better filtering results for the morphology-based method.

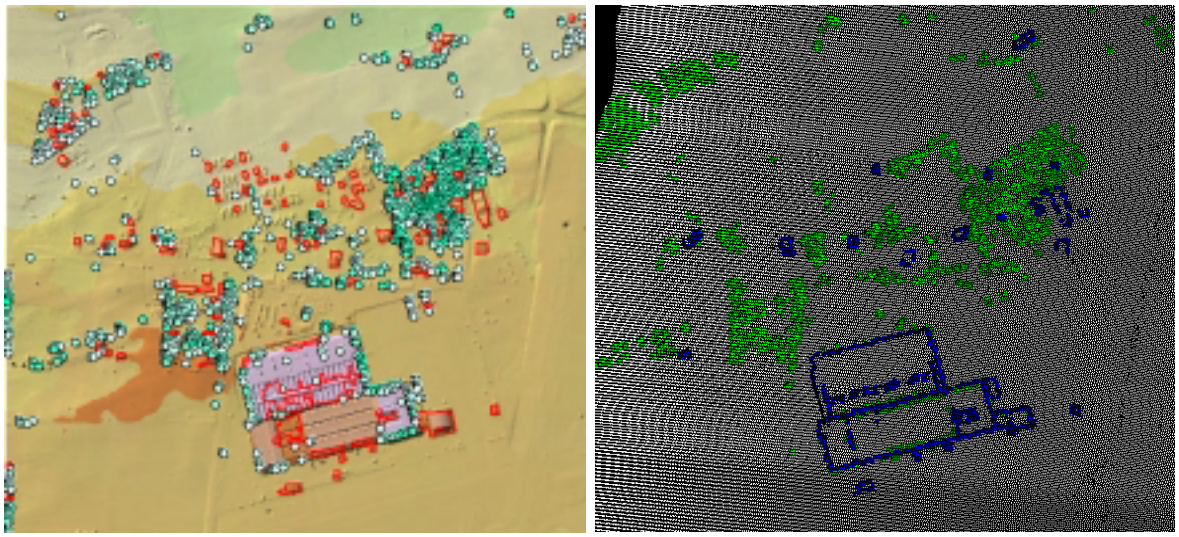

Figure 6. Buildings and vegetated areas extracted by RTV and the proposed method.

A close-up of the morphology-based method results, shown in Figure 7, covers a mixed area with vegetation and small buildings. The details clearly illustrate that all the buildings were properly extracted and there was no misclassification for that area.

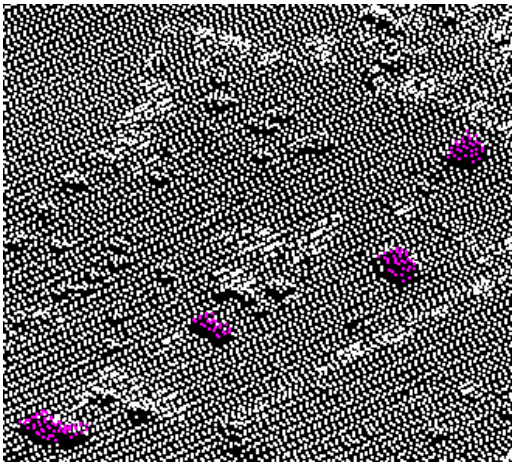

Figure 7. Small buildings in a partially vegetated area extracted by the morphology-based method.

CONCLUSION

In this paper a concept based on mathematical morphology for building and vegetation removal has been introduced. The motivation for this research was to support LIDAR sensor calibration by filtering out all the complex man-made and natural objects. The performance of the proposed method has been tested and compared to other techniques. Initial results indicate a good performance for jointly removing buildings and vegetation. Further research is expected to use LIDAR intensity data and to introduce a robust decision-making system to support the combined use of various filtering techniques.

ACKNOWLEDGEMENT

This research was partially supported by the Department of Defense Dual Use Science and Technology program. The authors would like to acknowledge the support of The EarthData Group for providing test data and valuable technical discussions.

REFERENCES

Axelsson, P. (1999). Processing Of Laser Scanner Data - Algorithms And Applications, *ISPRS Journal of Photogrammetry and Remote Sensing*, 54(2-3), pp. 138-147.

Axelsson, P. (2000). DEM Generation From Laser Scanner Data Using Adaptive TIN Models, *The International Archives of the Photogrammetry, Remote Sensing and Spatial Information Sciences*, Annapolis, MD, Vol. 33, Part B3/1, pp. 119-126.

Brunn, A., Weidner, U. (1997). Extracting Buildings From Digital Surface Models, *The International Archives of the Photogrammetry, Remote Sensing and Spatial Information Sciences*, Vol. 32, Part 3-4W2, pp.27-34.

Elaksher, A.F., Bethel, J.S. (2002). Reconstructing 3D Buildings From LIDAR Data, *The International Archives of the Photogrammetry, Remote Sensing and Spatial Information Sciences*, Graz, Austria, Vol. 34, Part A3/3, pp. 102-107.

Elmqvist, M. (2002). Ground Surface Estimation From Airborne Laser Scanner Data Using Active Shape Models, *The International Archives of the Photogrammetry, Remote Sensing and Spatial Information Sciences*, Graz, Austria, Vol. 34, Part A3/3, pp. 114-118.

Kilian, J., Haala, N., Englich, M. (1996). Capture And Evaluation Of Airborne Laser Scanner Data, *The International Archives of the Photogrammetry, Remote Sensing and Spatial Information Sciences*, Vienna, Austria, Vol. 31, Part B3, pp. 383-388.

Kraus, K., Pfeifer, N. (1998). Determination Of Terrain Models In Wooded Areas With Airborne Laser Scanner Data, *ISPRS Journal of Photogrammetry and Remote Sensing*, Vol. 53, pp. 193-203.

Hug, C., Wehr, A. (1997). Detecting And Identifying Topographic Objects In Imaging Laser Altimetry Data, *The International Archives of the Photogrammetry, Remote Sensing and Spatial Information Sciences*, Vol. 32, Part 3-4W2.

Hyyppä, J., Schardt, M., Haggre'n, H., Koch, B., Lohr, U., Scherrer, H.U., Paananen, R., Luukkonen, H., Ziegler, M., Hyyppä, J., Pyssalo, U., Friedla:nder, H., Uuttera, J., Wagner, S., Inkinen, M., Wimmer, A., Kukko, A., Ahokas, A., Karjalainen, M. (2001). HIGH-SCAN: The First European-Wide Attempt To Derive Single-Tree Information From Laserscanner Data, *The Photogrammetric Journal of Finland*, Vol. 17, No. 2, 18: 58-68.

Maas, H.G., Vosselman, G. (1999). Two Algorithm For Extracting Building Models From Raw Laser Altimetry Data, *ISPRS Journal of Photogrammetry and Remote Sensing*, 54, pp. 153-163.

Nässet, E. (1997). Estimated Timber Volume Of Forest Stands Using Airborne Laser Data, *Remote Sensing of Environment*, Vol. 61, pp. 246-253.

Nilsson, M. (1996). Estimation Of Tree Height And Stand Volume Using An Airborne LIDAR System, *Remote Sensing of Environment*, 56, pp.1-7.

Oude Elberink, S., Maas, H.G. (2000). The Use Of Anisotropic Height Texture Measures For The Segment Of Airborne Laser Scanner Data, *The International Archives of the Photogrammetry, Remote Sensing and Spatial Information Sciences*, 33 B3/2, pp. 678-684.

Pfeifer, N., Stadler, P., Briese, Ch. (2001). Derivation Of Digital Terrain Models In The SCOP++ Environment, *Proc. of OEEPE Workshop on Airborne Laserscanning and Interferometric SAR for Detaoled Digital Terrain Models*, Stockholm, Sweeden.

Pyysalo, U., Hyyppä, H. (2002). Reconstructing Tree Crowns From Laser Scanner Data For Feature Extraction, *The International Archives of the Photogrammetry, Remote Sensing and Spatial Information Sciences*, Graz, Austria, Vol. 34, Part B3/3, pp. 218-221.

Rottensteiner, F., Briese, Ch. (2002). A New Method For Building Extraction In Urban Areas From High-Resolution LIDAR Data, *The International Archives of the Photogrammetry, Remote Sensing and Spatial Information Sciences*, Graz, Austria, Vol. 34, Part A3/3, pp. 295-301.

Schardt, M., Ziegler, M., Wimmer, A., Wack, R., Hyyppä, J. (2002). Assessment Of Forest Parameters By Means Of Laser Scanning, *The International Archives of the Photogrammetry, Remote Sensing and Spatial Information Sciences*, Graz, Austria, Vol. 34, Part A3/3, pp. 302-309.

TerraScan, TerraScan for MicroStation user's guide, TerraSolid Ltd, 1999.

Törmä, M. (2000). Estimation Of Tree Speices Proportions Of Forest Stands Using Laser Scanning, *The International Archives of the Photogrammetry, Remote Sensing. ISPRS Congress Symposioum*, Amsterdam, Vol. 33., pp. 1524-1531.

Weidner, U. (1997). Gebäudeerfassung Aus Digitalen Oberflächenmodellen, PhD Thesis, Institute of Photogrammetry, Bonn University, DGK-C 474.

Vosselman, G. (2000). Slope Based Filtering Of Laser Altimetry Data, *The International Archives of the Photogrammetry, Remote Sensing and Spatial Information Sciences*, Annapolis, MD, Vol. 33, Part B3/2, pp. 935-942.

Vosselman, G., Dijkman, S. (2001). 3D Building Model Reconstruction From Point Clouds And Ground Plans, *The International Archives of the Photogrammetry, Remote Sensing and Spatial Information Sciences* 34 (3W4), pp. 37-43.

Vosselman, G., Maas, H.G. (2001). Adjustment And Filtering Of Raw Laser Altimetry Data, *Proceedings of OEEPE Workshop on Airborne Laserscanning and Interferometric SAR for Detailed Digital Terrain Models*, Stockholm, Sweden.

Geo-Referenced Digital Data Acquisition and Processing System Using LIDAR Technology

Project Study on

LIDAR Data Classification
LIDAR Data Segmentation Based on Morphologic Filtering:
A Performance Analysis

March 2003

INTRODUCTION

In the last few years LIDAR technology has become a leading tool for obtaining surface and terrain models and extracting various objects. One of the main tasks related to the data processing is the segmentation of the surface given by the preprocessed LIDAR points. Many algorithms have been developed for filtering and automatically classifying the LIDAR points. In commonly accepted terminology, filtering is referred to the determination of the terrain, while classification is used in broader terms and it includes object extraction.

The raw or unfiltered LIDAR data give the digital surface model (DSM) of the measured area, which is the upper envelope of our world that includes LIDAR points reflected from the ground as well as from natural and man-made objects. The ultimate challenge is to remove from the point cloud those points that do not belong to the ground. Different filtering methods to determine the terrain have been developed over the years. At the Institute of Photogrammetry and Remote Sensing at Vienna University of Technology a method based on iterative linear prediction was developed for the generation of terrain model in wooded and hilly areas (Kraus and Pfeifer, 1998). This method was later extended for more complex, densely built-up areas using a hierarchical, coarse-to-fine approach (Pfeifer at al., 2001); its implementation is commercially available in the software package SCOP++. Another technique by (Axelsson, 1999; Axelsson, 2000) is based on a TIN densification and was developed at the Department of Geodesy and Photogrammetry at the Royal Institute of Technology, Stockholm. The commercially available software package, TerraScan, has been built around this method. Another scheme based on mathematical morphology was presented in (Vosselman, 2000) and (Vosselman and Maas, 2001). A recent technique suited to rather dense data sets was introduced by (Elmqvist, 2002) and uses an active shape model for terrain estimation.

In addition the terrain model generation, when points are classified as either terrain or off-terrain points, automatically extracting and reconstructing objects from the point cloud have become a main research topic in the LIDAR data processing field. Several methods have been published related to building extraction and reconstruction, see (Brunn and

Weidner, 1997; Hug and Wehr, 1997; Axelsson, 1999; Maas and Vosselman, 1999; Vosselman and Dijkman, 2001; Rottensteiner and Briese, 2002; Elaksher, 2002), and for forest feature extraction, see (Nilsson, 1996; Nässet, 1997; Törmä, 2000; Hyyppä at al., 2001; Pyysalo and Hyyppä, 2002; Schardt at al., 2002).

Primarily, the point distribution and the number of return signals are used for classification; the basic concept is to examine the spatial behavior of the LIDAR points. As an example for the LIDAR point distribution, see Figure 1 that shows the profile of a laser scan line captured over a building and forested area. Figure 2 illustrates the occurrence of multiple returns.

Recent technological advancements in LIDAR technology have resulted in better data quality and richer information content, consequently improving classification performance. The most important changes are the increased point density coupled with better point distribution, the availability of multiple return signals, and the intensity data or complete waveforms.

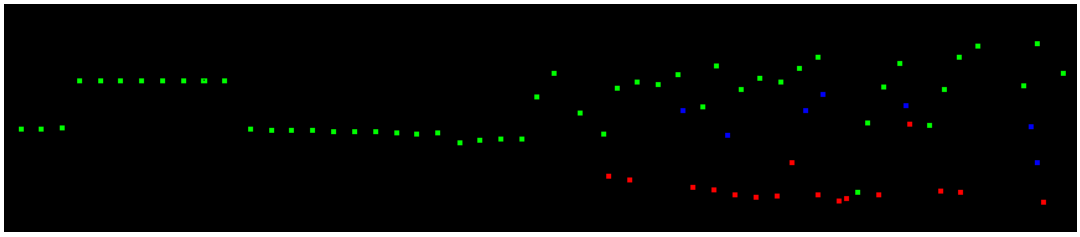

Figure 1. First (green), intermediate (blue) and last (red) reflections. Over forested area even three-four reflections can be captured from the same emitted laser pulse (since pulses can be reflected back from many parts of the surface, from the ground as well as from different parts of the trees).

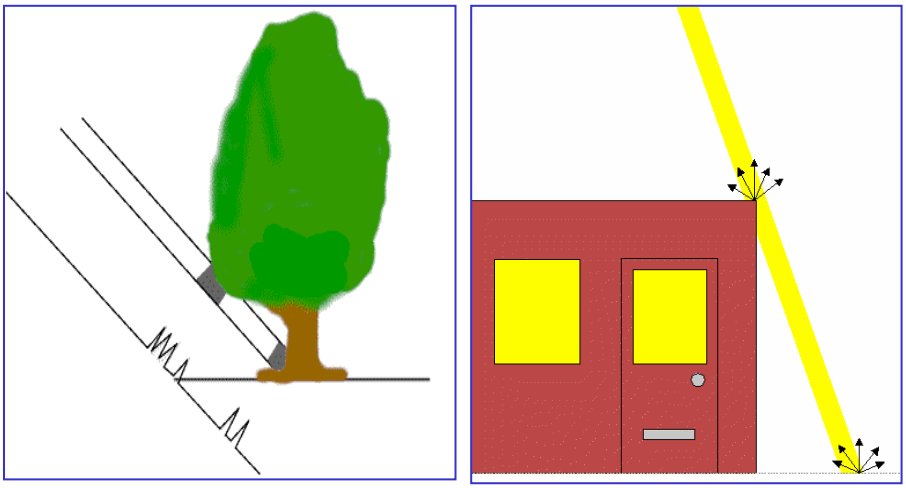

Figure 2. Double return might also occur when the laser beam hits the edge of a building and the laser pulse is reflected back from the building roof and the ground.

Obviously, there is no perfect automatic classification method but with the algorithmic improvements the number of misclassifications can be reduced. As most of the techniques are specific or customized to certain data types, it is important to understand the performance limitation of the different methods. The sensitivity of the methods is usually measured in point density and in the complexity of the area such as the terrain and the objects. Benchmarks and quantitative reports of the efficiency and accuracy of automated classification routines are generally not published, but it is commonly quoted that most automated filtering routines are 80% to 90% effective. Depending on the complexity of the area, they will accurately classify 80% to 90% of the ground points. The remaining part of the data needs to be classified manually.

A SHORT REVIEW OF THE MAIN FILTERING METHODS

At the Institute of Photogrammetry and Remote Sensing at Vienna University of Technology a method based on iterative linear prediction was developed for the generation of terrain model. This implementation is commercially available in the software package SCOP++. Robust interpolation initially approximates the surface calculated from all points by using the same weight, as shown in Figure 3a. This is a coarse estimation of the surface running between terrain and off-terrain points. Next, height differences between the LIDAR points and the interpolated surface are calculated. Ground points will typically get either large negative or small residuals since the surface approximation is running above or close to the terrain. In the next step, all points will be weighted depending on their residuals using a special weight function to give new weights to each point, see Figure 3b. Points with large negative discrepancies will get large weights (assumed terrain points) while points with medium discrepancies will get smaller weights. Zero weight ignores points with discrepancies more than a user-specified value. A new surface is computed from all points using the new weights. The interpolation and weight calculation is repeated; in each step a better estimation of the terrain will be created as shown in Figure 3c. The final interpolated surface provides the DTM of the area that is calculated from only the selected terrain points. In this manner points are classified as either terrain or off-terrain points. This method works well on wooded areas where terrain points, points reflected from the ground, are frequently available. To handle densely built-up areas (large areas without true ground points) the original algorithm has been extended by a hierarchical, coarse-to-fine method, see (Pfeifer at al., 2001).

The technique developed by (Axelsson, 1999; Axelsson, 2000) was implemented in the commercially available software, Terrascan. This method uses a hierarchical algorithm, which is based on a TIN-representation. A grid with a user-defined size is laid over the dataset and in each pixel of this mesh the lowest vertical point is selected. In the next step, an initial TIN is created from the selected points as the first approximation of the ground surface. Adding the LIDAR points to the triangulation leads to the final solution. Points are selected one by one; a point may be accepted or rejected as a new terrain point based on certain criteria by user-specified parameters such as iteration distance (the

distance between the candidate point and the present surface) and iteration angle (the angle between the surfaces with and without the candidate point). Accepted points are inserted into the triangulation and with every new point the TIN surface is modified (altered) and consequently converging closer to the real terrain. In the initial point selection the grid size is determined with the maximum building size parameter. The size of a pixel will be equal to the maximum building size. For instance, if the maximum building size is 50 m, the application can assume that any 50m by 50m area will have at least one hit on the ground and the lowest point in the pixel will be selected as a terrain point; for additional details, see (TerraScan).

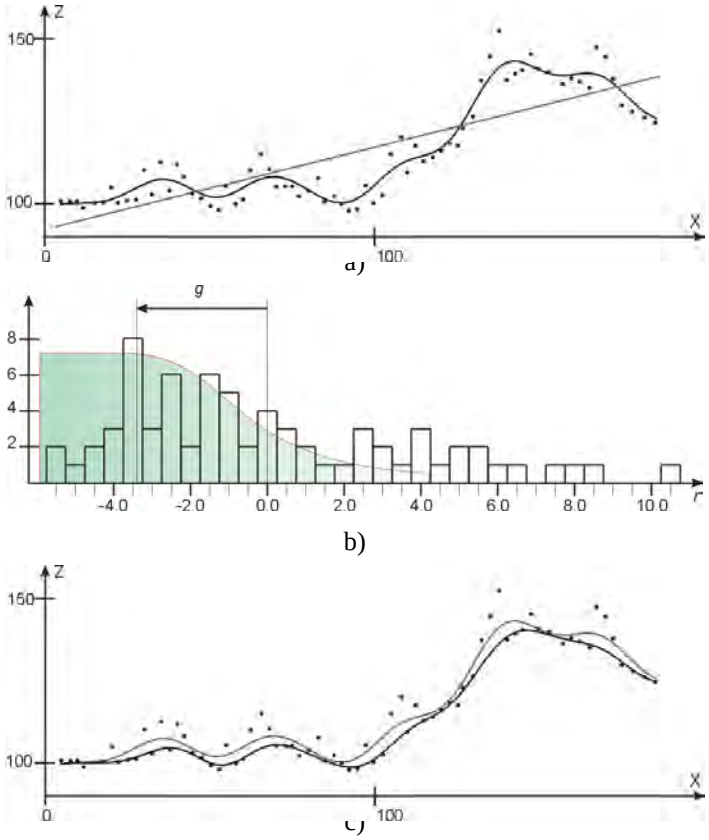

Figure 3. Step 1: Interpolation with unit weights (upper), step 2: weighting of measurements with an asymmetric weight function (middle), step 3: interpolation with new weights, iterative estimation (bottom).

Mathematical morphology is widely used in image processing. It works as a convolution filter - applying the same processing to each element. A new value is given to the pixel on which the kernel is centered; during erosion this is the minimum value inside the window while the maximum value is used in the case of dilation. This method easily can be applied to the LIDAR data. The moving window (kernel) is centered on each point, as shown in Figure 4. The elevation of the examined point is replaced with the minimum or maximum elevation inside the window. The opening (dilation after erosion) is typically

used for LIDAR data terrain extraction. For each window after opening, the point with the lowest elevation and all other points that are higher than that point but smaller than a predefined value are selected as terrain point. Since there is no optimal window size, different sizes of the moving window are used. As the window size increases the height tolerance increases to follow the changes in terrain slope. The tolerance has to be smaller than the minimum building height to avoid classifying building roofs as terrain.

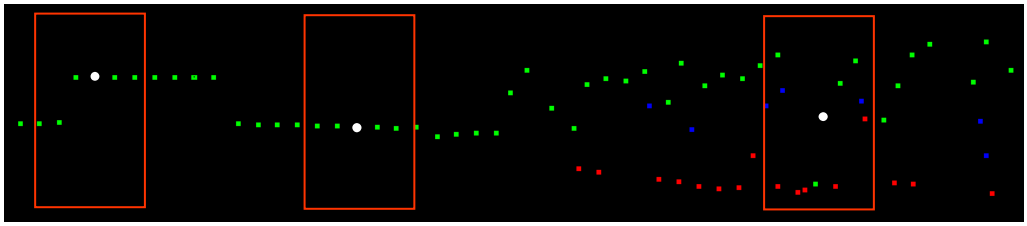

Figure 4. The moving window is centered on each point. The figure shows three cases. The elevation of the examined point (white) is replaced with the minimum (erosion) or maximum elevation (dilation) inside the window.

A MORPHOLOGY-BASED METHOD – OUR DEVELOPMENT

A morphology-based method has been developed. The presented method intends to mask areas of buildings, vegetation, and has no special interest in identifying/reconstructing features. In the computations, the original irregularly distributed LIDAR points are used; the data are not interpolated to a regular grid.

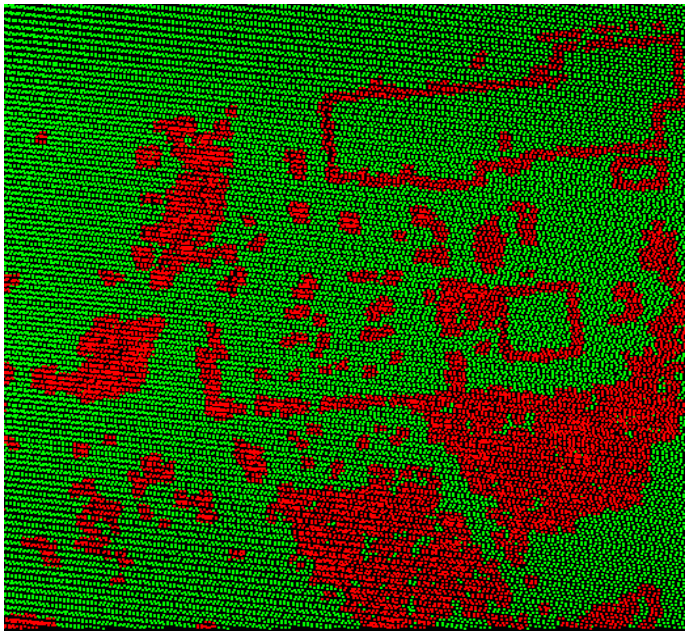

Figure 5. Breaklines extracted from Hagerstown, MD test area.

The spatial behavior of the LIDAR points is analyzed through a moving window-based algorithm. A window is moved over the entire dataset and in each window basic statistical parameters are calculated; such as standard deviation, maximum gradient among points, and the difference between the maximum and minimum elevations. In the next step, various extraction routines are executed; such as the detection of areas with given height jumps, i.e. the difference between the maximum and minimum elevations in a window is higher than a given value. In this manner breaklines (including natural breaklines) edges of buildings and local height variations can be selected from the point cloud. Figure 5 shows generic surface breaklines defined by 4 m height variation from the Hagerstown, MD dataset.

The choice of the window size depends on the data density and the purpose of the analysis. Obviously, there is no optimal window size in general. For instance, the window size must contain at least 8-9 points in order to detect generic breakline locations; for the distribution of the gradients, a larger window (including many more points) is needed. Another important parameter is overlap between the windows as they move. One extreme is when the moving window is centered on each point; the other one is if there is no overlap. A half of the window size is usually a good compromise between execution time and performance.

Removing vegetation

The distinctive spatial distribution of the LIDAR point cloud over vegetated areas is due to the capability of the laser pulse to penetrate the forest canopy through gaps. Pulses can be reflected back from many parts of the surface (from the ground as well as from different parts of the trees) and several returns can be recorded from the very same laser pulse. Differences in height variations range from zero to the canopy height over vegetated, especially forested areas. In our algorithm those areas where the variations of the surface gradients are above a predefined threshold are flagged as vegetated regions. This is similar to the procedure by (Rottensteiner and Biese, 2002), where regions with trees are also eliminated by the analysis of the second derivatives of the DSM.

A second technique selected for filtering out vegetation is based on a morphological filtering (opening); see Figure 6. This method has certain advantages such as an easy way to eliminate single trees. Choice of the window size is more crucial than in the statistical method above. To safely remove vegetation, at least one hit from the ground must exist in each window in vegetated areas. Simple opening will not filter out buildings, which are bigger than the window size, but the roofs of these buildings may be distorted. To avoid this distortion, few modifications have been introduced. During the erosion, the elevation of the examined point is replaced with the minimum elevation inside the window if the difference is more than a predefined threshold (a practical value is 2 m). Similarly, during the dilation the elevation of the examined point is replaced with the maximum elevation inside the window if the difference is more than the same predefined threshold. Furthermore, if the difference is more than a certain value (minimum building height), the elevation of the examined point won’t be replaced with the maximum value, but with the

original elevation of the point. The weakness of the min/max method is that any objects that are smaller than the minimum building size will be filtered out as well. The modified dataset, optimistically without vegetation points, is adequate for detecting buildings independently whether the roofs of the buildings have changed or not.

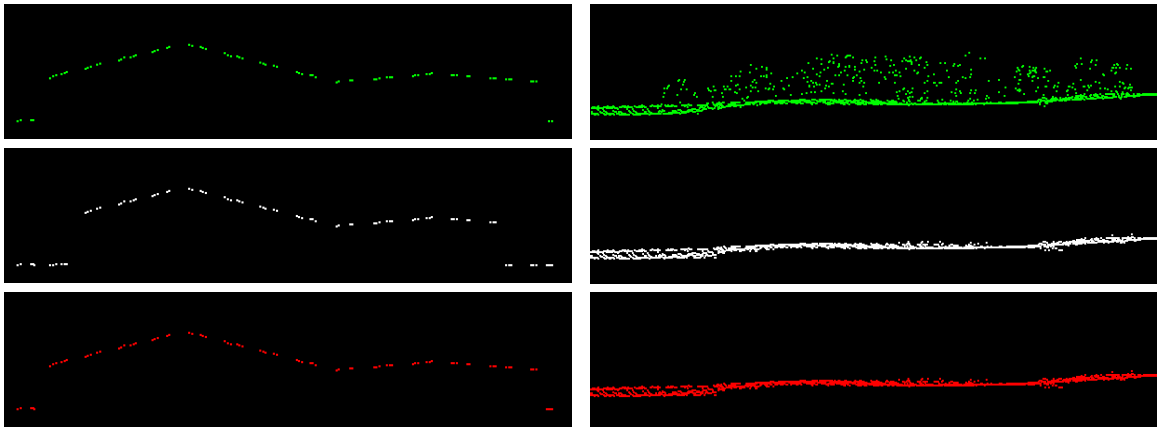

Figure 6. Morphological opening on vegetation and building profiles: original dataset (upper pair), erosion (mid pair) and dilation applied after erosion (lower pair).

Combining the outcome of the two independent processing techniques will result in an improved performance as the two techniques compensate for each other's weaknesses. For example, local variations are easily eliminated by the second method, but it fails if the vegetation is too dense and there is no terrain point inside the window. In contrast, the first method will detect such variations from the canopy.

Detecting buildings

Most building detection techniques start after the terrain model computation is complete and then a height threshold is applied to the difference between the DTM and DSM (Weidner, 1997; Rottensteiner and Biese, 2002). In our case, however, the availability of DTM is no prerequisite for the building extraction as it starts from the reduced data set; opening eliminates the vegetated points but preserves buildings as shown in Figure 7 for a moderately vegetated area with small buildings. In the following, this reduced data will be considered as original dataset (Figure 3b).

To detect building edges, the calculation begins with finding predefined height jumps, i.e., in each window the difference between the maximum and minimum elevations is computed. The processing window is moved over the data set with half of the window size in both directions. The minimum predefined height jump (H_{min}-jump) is set to the minimum building height (H); typically this is set to 4 m. Storing these computation results, an initial indicator matrix is formed and is the basis of the subsequent analysis. Each pixel in this matrix represents a window and contains the value associated with that window. Windows with the H_{min}-jumps are labeled with 1 (indicator windows); without

the height jumps they are assigned a 0. Although supposedly vegetation points have been removed from the data set, besides the building edges some other breaklines (due to natural or man-made objects) may also be indicated in this matrix as shown in Figure 7b.

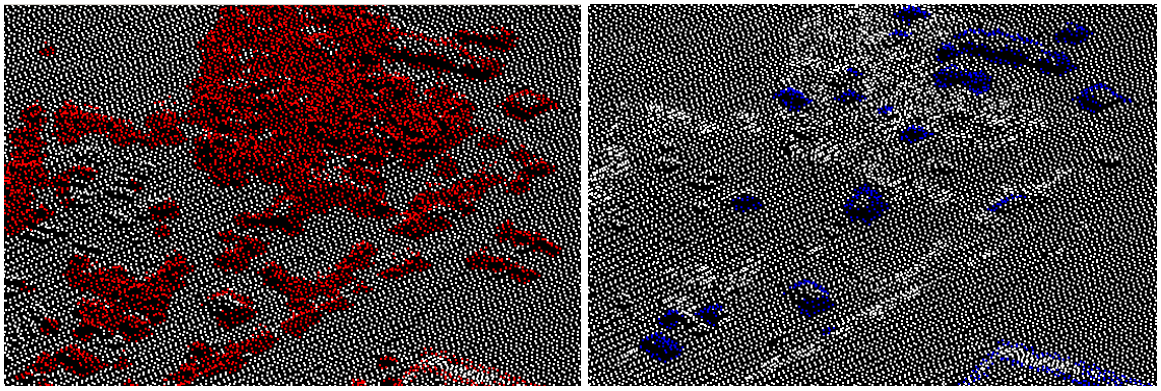

a) b)

Figure 7. Extracted generic breaklines (left) and after opening has been applied (right).

Once the breakline detection is complete, the contours of all buildings will be detected. The challenge at this point is to identify all the points of each building. In the next step, point-groups are created by a calculation, which is based on mathematical morphology (erosion) and is executed for each indicator window (i.e. for each pixel in the indicator matrix labeled with 1) individually. The computation starts from the indicator pixel and the original dataset is used in this process. In the indicator window, elevations of points above the minimum height point with more than H are replaced with the minimum elevation. The eight neighborhood pixels of the indicator pixel are marked in order to check the height differences inside these windows. Neighboring windows are analyzed in an iterative process. In each step the eight neighborhood pixels of the previously studied pixels, where the H_{min}-jump was found, are marked in order to also check the height discrepancies inside these windows. The process, illustrated in Figure 8, is iterative until neighboring windows with H_{min}-jump are found. For the reason that windows are moved with overlap (half of the window size), the subsequent window will always contain points with original and previously modified elevations. This is the key for “demolishing” buildings, as shown in Figure 8. The algorithm uses the basic idea of mathematical morphology (erosion); in the kernel, the values are changed for the minimum. In our approach the principle of the erosion was modified in two aspects. First, the elevation is replaced only if the height difference from the minimum is more than H. Second, elevations in the subsequent windows are analyzed by considering the previous height modifications.

After the iterative process is finished, the elevations of the modified dataset are subtracted from the elevations of the original dataset. The subtraction results in many no difference in heights and some non-zero heights (selected points). In the case when the indicator window represents an area over building edges, points with non-zero height are building points belonging to the same building. Selected points with their original heights are stored in a layer of a multi-layer matrix. Each layer is identified by the indicator pixel

(window) that began the individual iterative calculation. In summary, the execution of the iterative computation for all ***n*** indicator windows results in ***n*** point-groups stored in ***n*** layers.

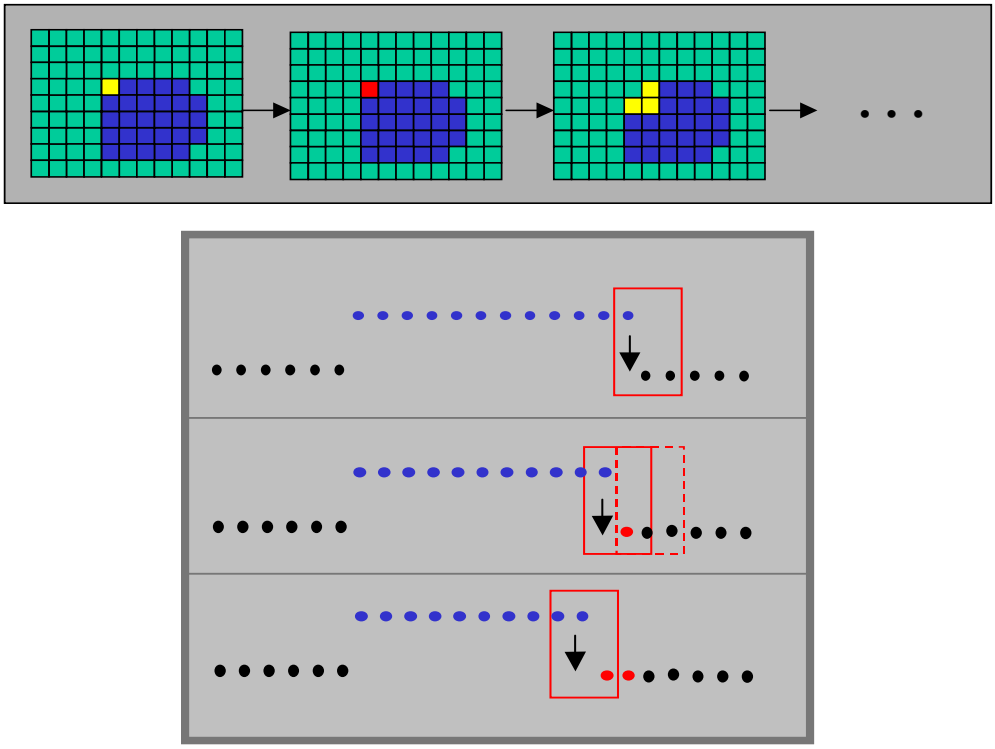

Figure 8. Concept of the iterative building demolition.

Advantages of the "demolishing" method, illustrated in Figure 9, are:

- invariant to the size and shape of the building and the type of the roof,
- the same point cloud will always be selected no matter where (which part of the building edge) the demolishing was started,
- coherent points belonging to the same building are always stored in one layer.

The iterative calculations starting from the indicator windows are independent; in each case the computation starts from the original (unchanged) data set and the results are stored on different layers. This way, buildings will not get demolished due to a natural breakline triggered events.

So far the iterative computation for all ***n*** indicator windows was executed resulting in ***n*** point-groups stored in ***n*** layers. One can assume that from the ***n*** point-groups ***m*** point-groups refer to ***q*** buildings ($0 \leq m \leq n$; m=n: ideal case, indicator matrix indicates only building edges; m=0: no building, and $0 \leq q < m$). A building is associated to as many layers as many edge windows belong to the building that were detected and marked in the initial indicator matrix. Furthermore, each layer belonging to the same building contains the same point cloud (point-group) due to the algorithm of building "demolishing".

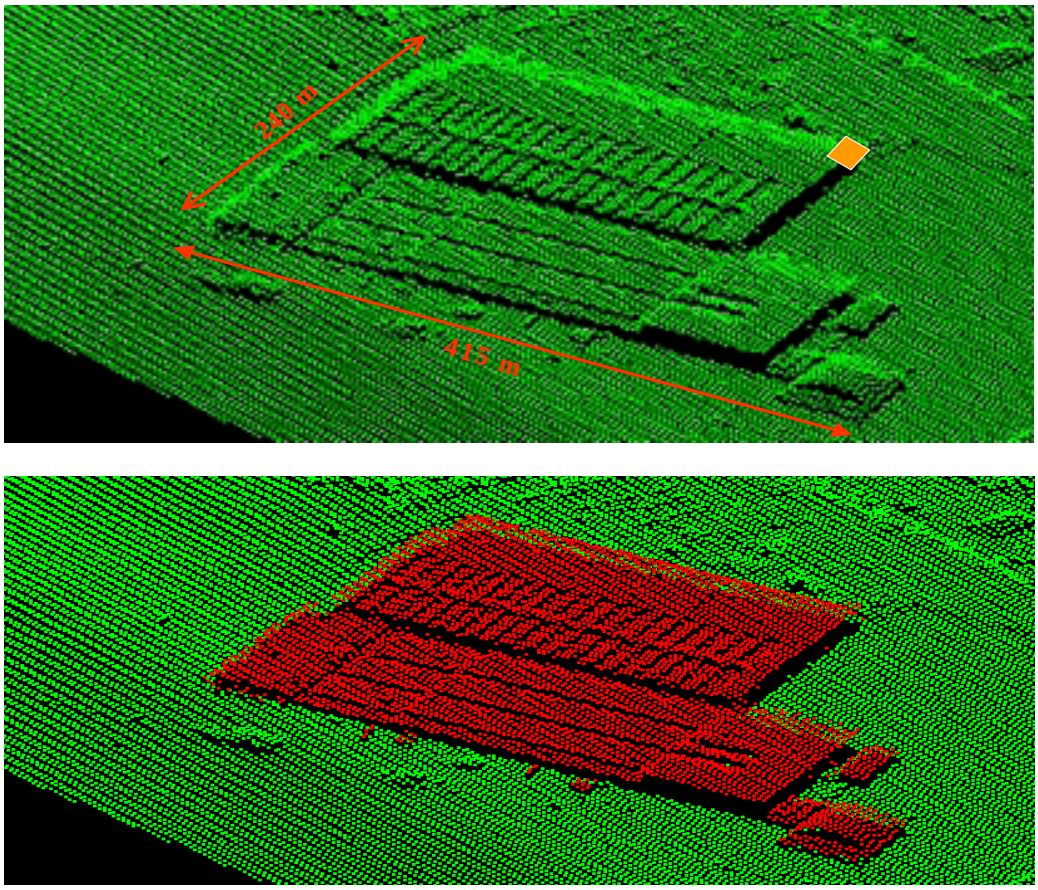

Figure 9. Selected building points (lower), the iterative calculation started from the corner (upper).

Using the above-described features, the recognition of building point-groups is accomplished in two phases:

- By comparing the different layers, layers that contain the same point cloud are combined into one layer. ***n*** point-groups become ***q+p*** point-clouds; ***q*** point-clouds refer to ***q*** buildings and ***p*** point-clouds refer to ***p*** others, i.e. $\boldsymbol{m} \rightarrow \boldsymbol{q}$ and $\boldsymbol{n}\text{-}\boldsymbol{m} \rightarrow \boldsymbol{p}$. The point-group/point-cloud relationship (k:1 relationship) is registered. Each point-group (i.e. layer) is identified by an indicator pixel (which represents an indicator window, which is an edge window). In this manner, the relationship between a point-cloud and edge-windows belonging to the point-cloud ($\boldsymbol{set_1}$) has been determined.
- Since typically building edges as well as other breaklines are flagged in the initial indicator matrix, the main question is how we can distinguish between the point-clouds of building edges and the other breaklines. In order to solve the problem of selecting the ***q*** building point-clouds from the ***q+p*** point-clouds, for each ***q+p*** point-clouds the following computation is executed. Edge-windows belonging to a point cloud are extracted by dividing the original data set into cloud and off-cloud points. From all the windows, edge-windows are selected by choosing windows containing both cloud and off-cloud points ($\boldsymbol{set_2}$).

Comparing set_1 and set_2, the elements of the two sets will be identical for buildings, but not for other breaklines or terrain roughness.

Additional parameters (such as minimum and maximum building size) as well as aspect ratios can be defined to avoid gross errors. The introduced method, however, is suitable for the detection of complex buildings even with huge sizes.

The performance of the proposed method has been tested and compared to other techniques. Initial results indicate a good performance for jointly removing buildings and vegetation. Further research is expected to use LIDAR intensity data and to introduce a robust decision-making system to support the combined use of various filtering techniques.

TEST RESULTS - PERFORMANCE ANALYSIS

The test dataset, an area over Hagerstown, MD, was provided by the EarthData Group. The LIDAR point density was rather small, about 0.1 point/m^2; the data contained multiple returns. The test area, a 2 km by 2 km square is characterized by flat terrain, with various vegetation and buildings of different sizes and types. For comparison purpose, two LIDAR processing packages have been used; although there was no attempt to perform complete evaluation.

Using TerraScan, building, vegetation, ground, railway and power line points can be classified interactively or using automated processes. The program has shown a good performance in terrain point selection. Figure 10 shows the evaluated point cloud on the test area; the white and blue points indicate the terrain and non-terrain points, respectively. There are three user-defined parameters and it is definitely worth optimizing them, especially changing the default value of the maximum building size to avoid serious misclassifications. If the maximum building size is set to 50 m, the application assumes that any 50m by 50m area will have at least one hit on the ground; hence the lowest point in each 50m by 50m mesh will be selected as terrain point. Figure 11 illustrates the effect of the parameter choice on the filtering results. After setting the proper building size parameter, only few misclassifications may occur. As Figure 10 shows, the program cannot handle negative outliers; error points that are well below the ground level. Therefore, the “low points” utility must be run before the terrain determination, which flags points that fall below the average of points within a given distance.

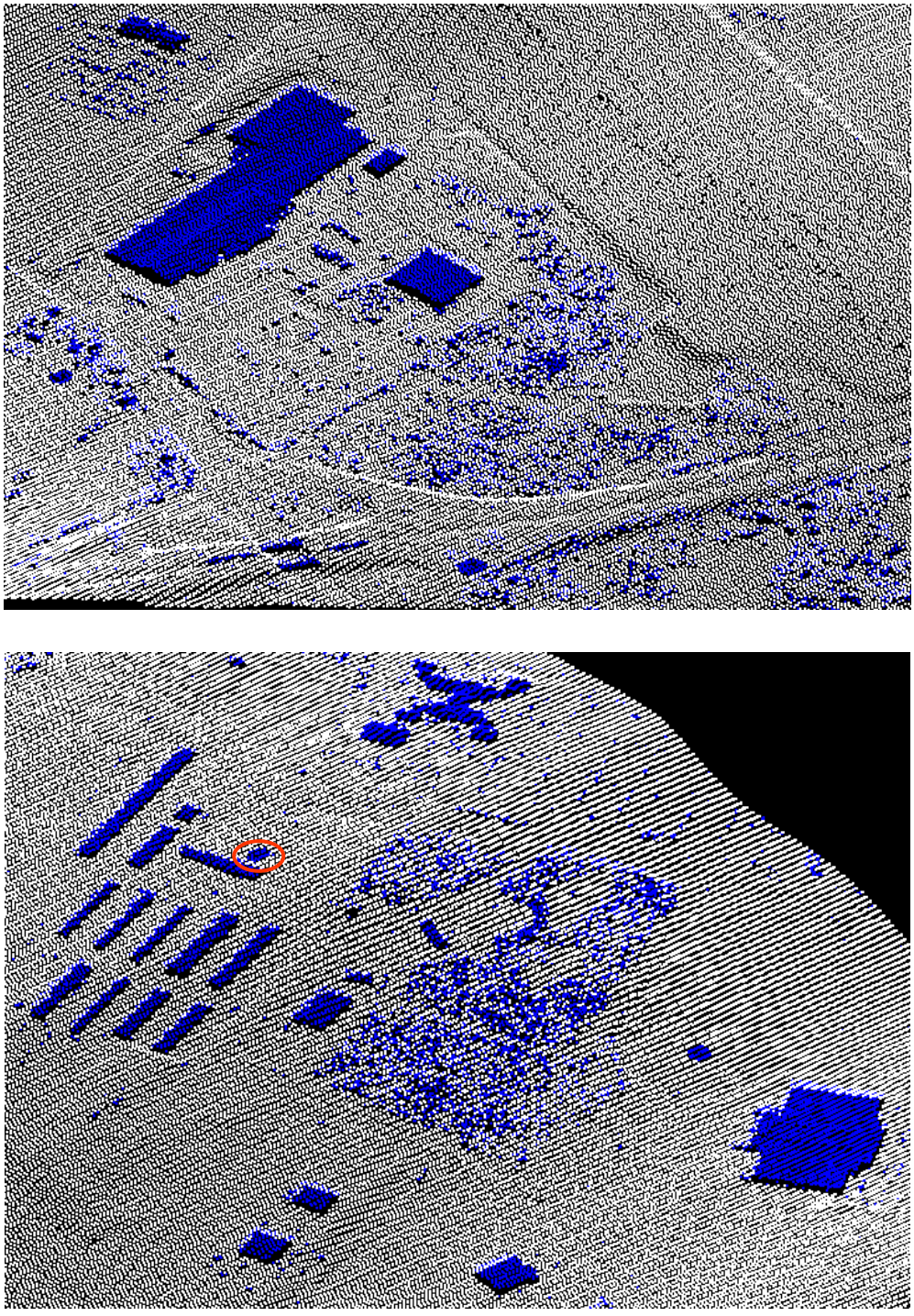

Figure 10. Terrain (white) and non-terrain (blue) points extracted by TerraScan. The red circle shows a misclassified area due to negative outlier (lower figure).

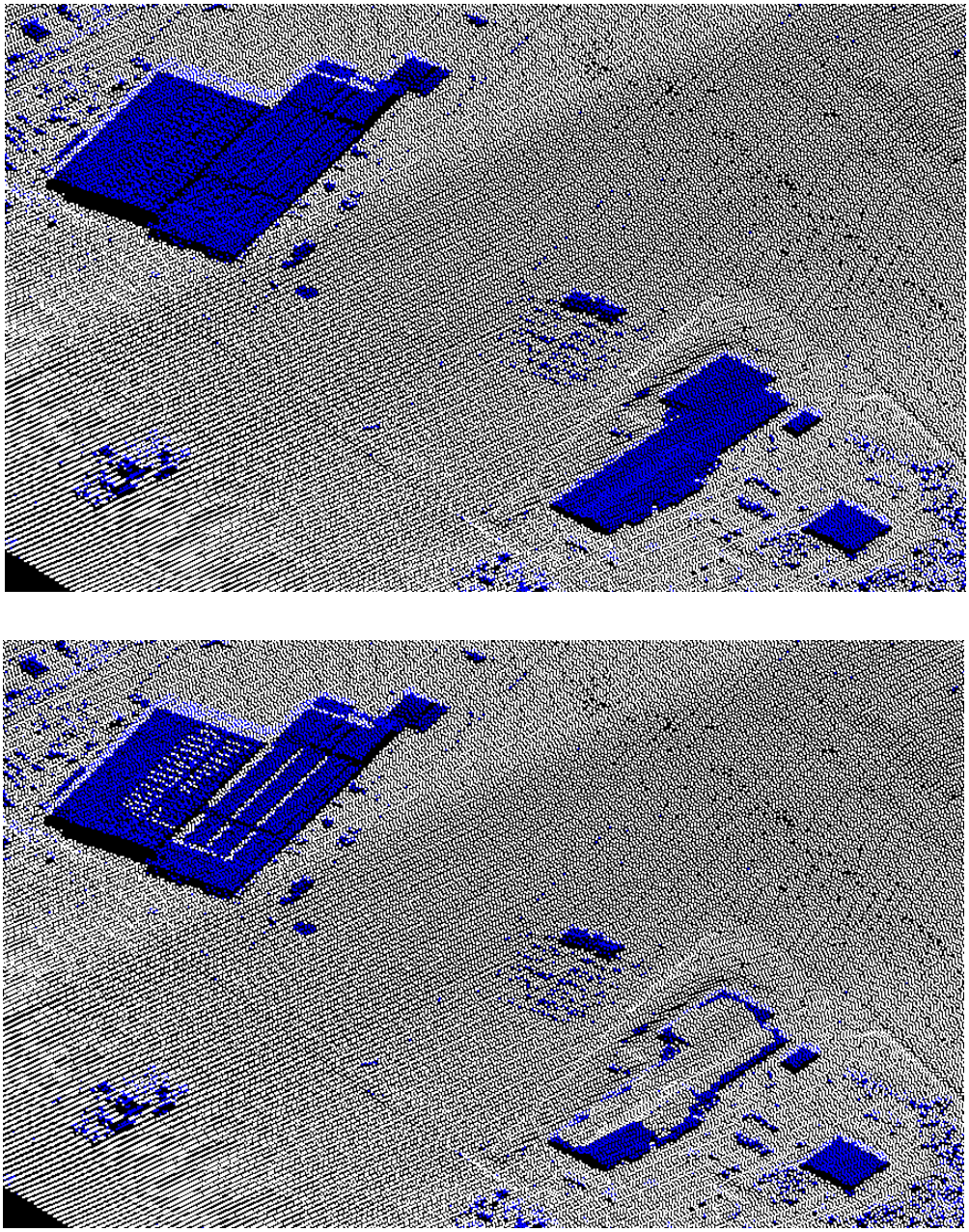

Figure 11. Effect of parameter choice on the filtering results. The maximum building size was set to 300m (upper) and 60m (lower).

The algorithm of RTV (Rapid Terrain Visualization) LIDAR Toolkit is proprietary. The program is implemented as an ArcView extension and is capable of extracting buildings, the bare earth, roads and trees. Feature extraction can be supported by intensity data. RTV Lidar Toolkit offers interactive classification and automated processes; although in our experiments the automated processing has shown modest performance. There seems to be less control by the user-defined parameters. Building-extraction produced better results

for suburban areas than for dense, built-up urban areas, especially for areas with oversize buildings.

The combined building and vegetation performance of the RTV and the proposed morphology-based method has been tested for a few datasets. Figure 12 shows results for the Northwest segment of the test area, with better filtering results for the morphology-based method.

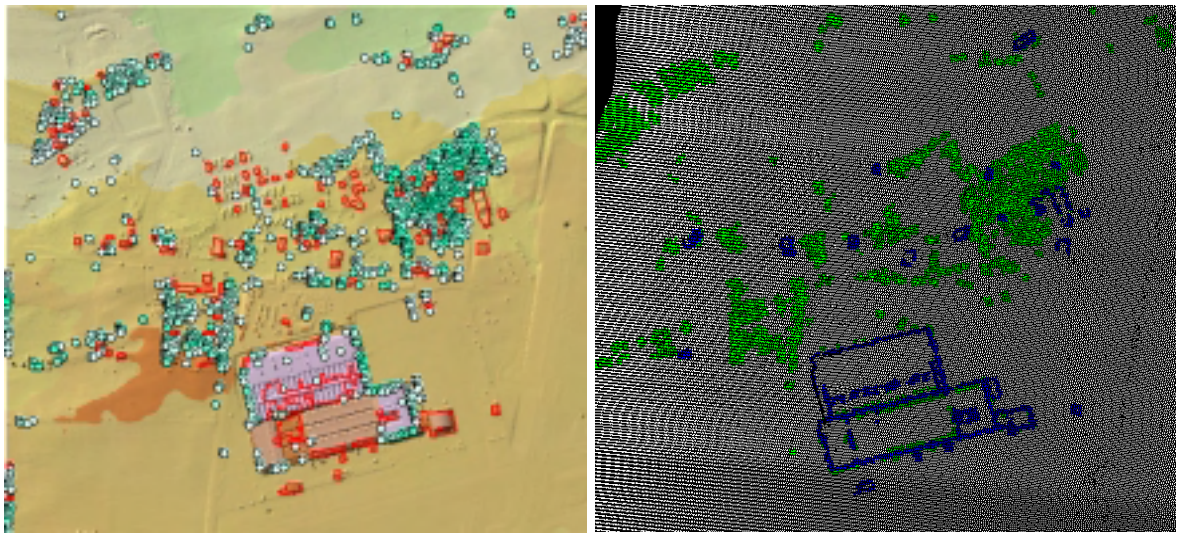

Figure 12. Buildings and vegetated areas extracted by RTV and the proposed method.

A close-up of the morphology-based method results, shown in Figure 13, covers a mixed area with vegetation and small buildings. The details clearly illustrate that all the buildings were properly extracted and there was no misclassification for that area.

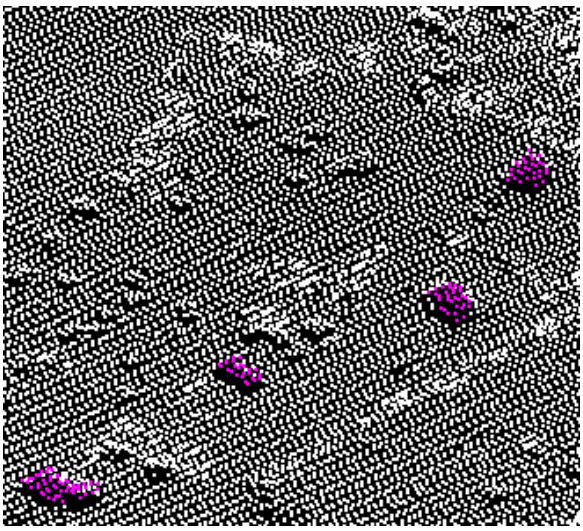

Figure 13. Small buildings in a partially vegetated area extracted by the morphology-based method.

RTV Lidar Toolkit requires the interpolation of the original data to a regular grid before process. Figure 14 and Figure 15 show how the results of the classification depend on the parameter choice.

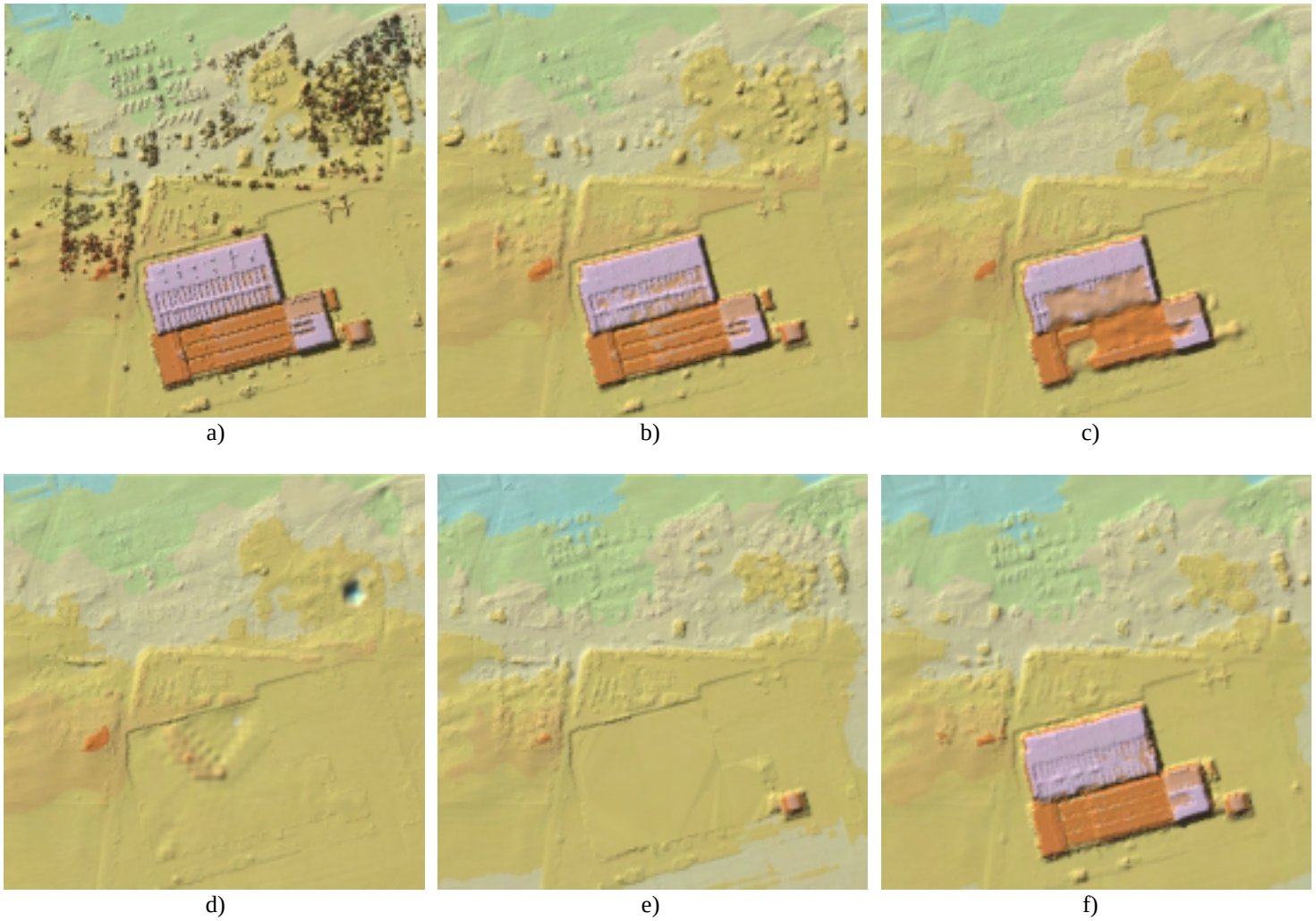

a) b) c)

d) e) f)

Figure 14. Digital Surface Model of the test area (a). Digital Terrain Models generated by RTV from the interpolated grid; grid size was set to 0.1m (b) , 0.5m (c), 1m (d), 1.5m (d) and 3m (e).

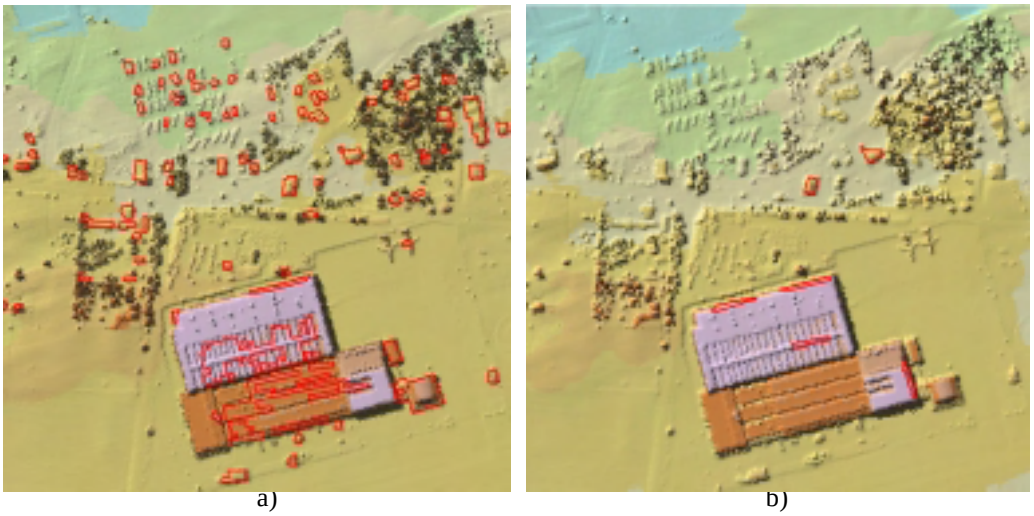

a) b)

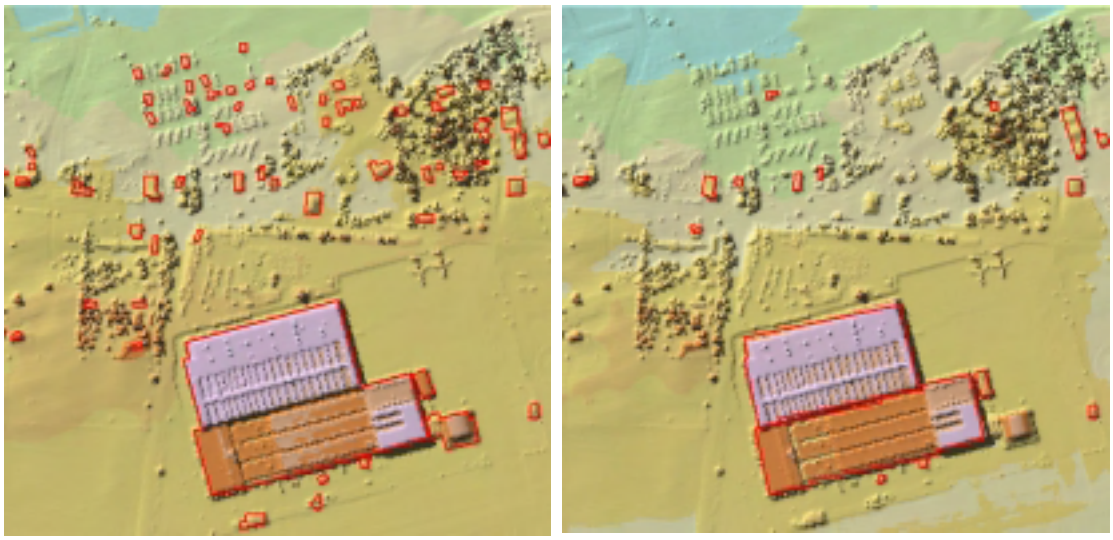

c) d)

Figure 15. Building outlines extracted by RTV in the cases the grid size was set to 0.5m (a), 3m (b), 1m (c) and 1.5m (d).

CLASSIFICATION USING INTENSITY DATA

In this report the major aspects of LIDAR data classification, based exclusively on LIDAR point cloud location information were delineated throughout the review of the current methods and a concept based on mathematical morphology for building and vegetation removal has been introduced. The performance of the proposed method has been tested and compared to other techniques.

Most laser sensors nowadays, however, provide intensity data that reflect the material characteristics of objects. Therefore intensity data can be useful for LIDAR data classification. However, their possible use is still under investigation. Since the intensity values of the laser are affected by different factors (elevation, density, reflection angle, composition of the materials), intensity data could be very noisy. Intensity may be distorted by these effects; it might even give false results of what the beam actually hit.

Different materials have specific reflectance values. In general, the value of reflectivity can be grouped as it follows. High reflectivity: light surfaces, grass, trees, water (wavy conditions); low reflectivity: dark surfaces, asphalt, coal, iron oxide, wet surfaces, mud, water.

Consequently, the major problems need to be solved are the removal of noise while preserving the original information and the proper separability between the different classes. Figure 16 shows the height and intensity images of the same area. Asphalt road can be identified very well in the intensity image, but not in the height image. Since

asphalt is often used as roofing materials, building roof has similar intensity to asphalt road. Vegetated areas and buildings are well separable in the intensity image. The contours of buildings are sharper in the height image. Figure 16 shows height and intensity data acquired by Optech Fall, 2002.

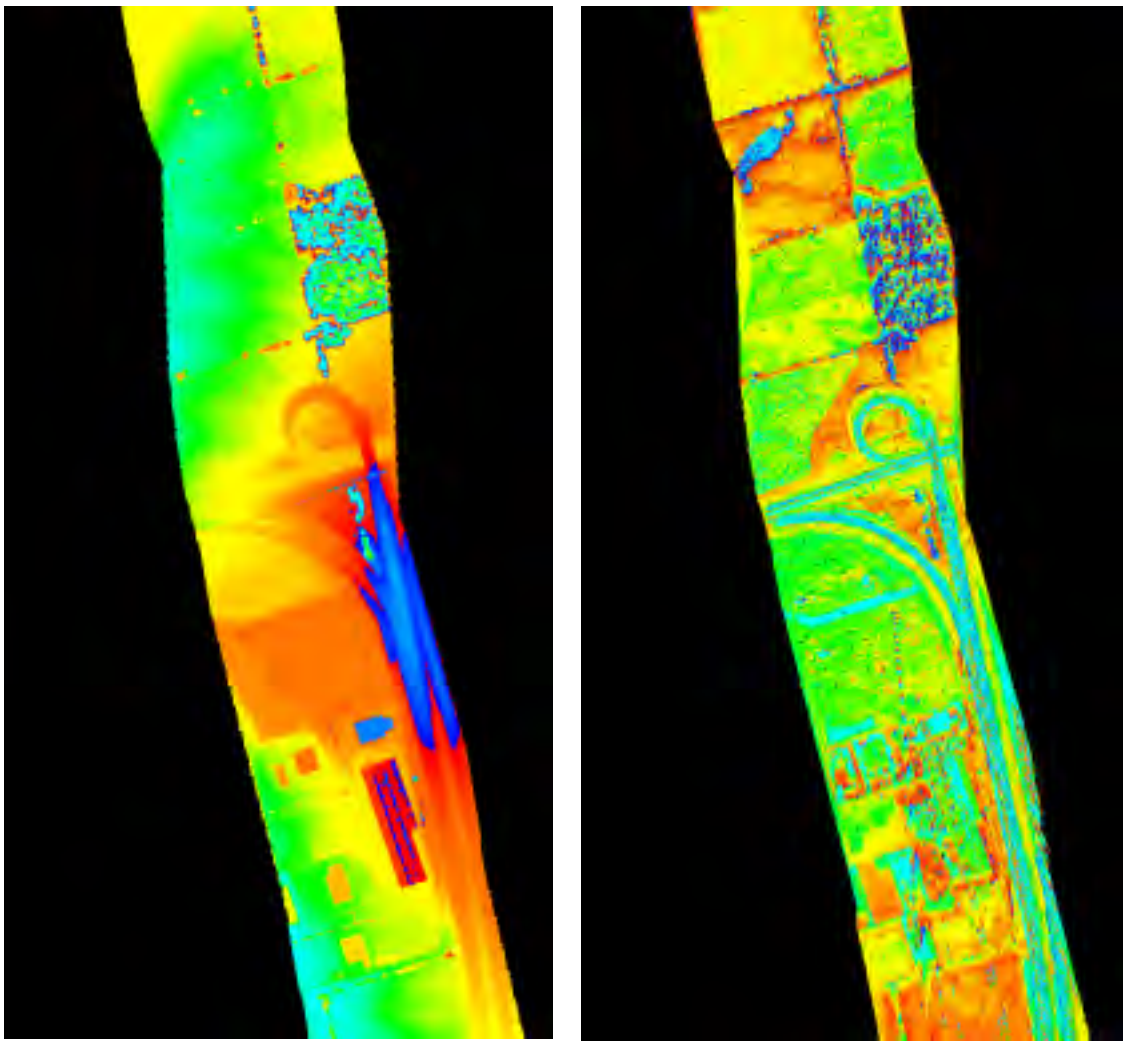

Figure 16. Height vs. intensity data

Outlier removal

Upper and lower elevation limits for valid measurements are determined from the plot of the data by latitude and elevation, see Figure 17. All the points outside the defined elevation range are eliminated from the point cloud. For more precise filtering, the mean and standard deviation of elevations of points within a fixed radius is computed. If the elevation of a point differs from the mean with more than 3 standard deviations and greater than a defined distance, the point is discarded.

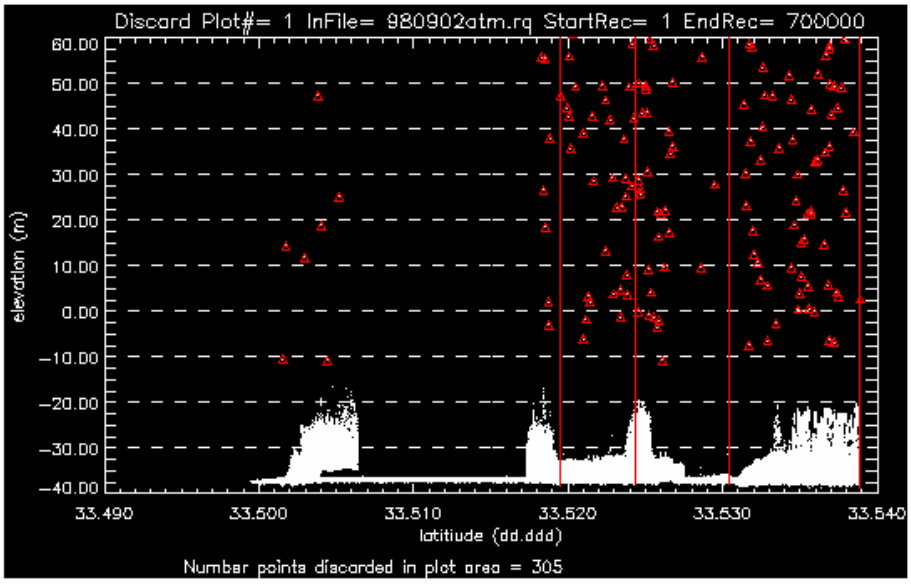

Figure 17. Removal of outliers

ROAD DETECTION

Road surface measurements are of main interest to ODOT OAE operation and therefore tests have been carried out on the Optech and LHS dataset to gain an initial understanding of the process and the performance of the existing tools.

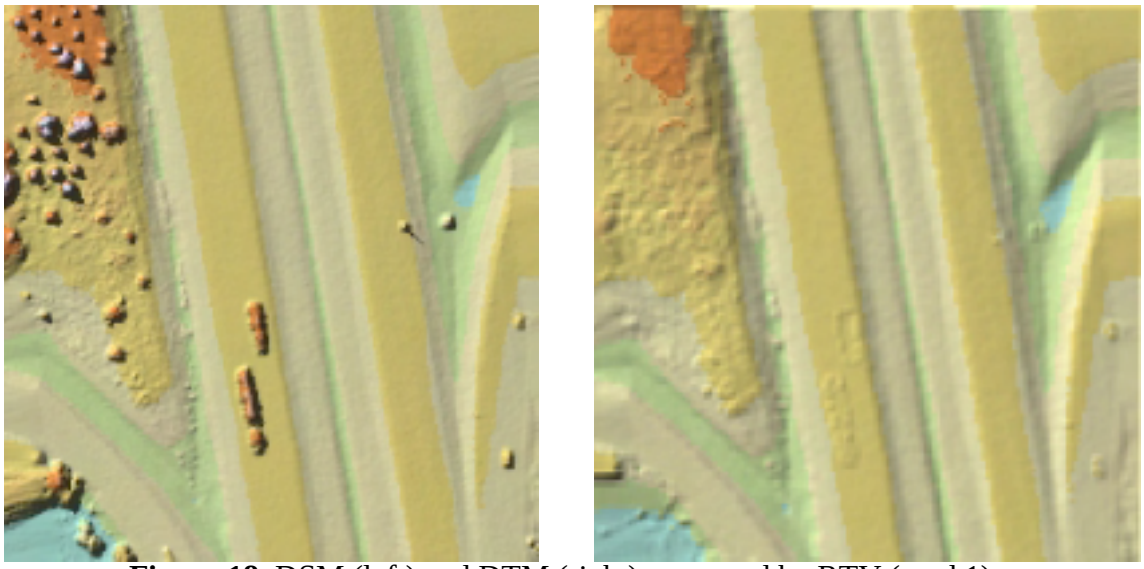

Figure 18. DSM (left) and DTM (right) generated by RTV (road 1)

Figure 18 shows how objects, including vehicles on the road are extracted. Note the remaining footprint of the vehicles. The same area processed by TerraScan is shown in Figure 19, indicating a reasonably good rate of properly detecting the vehicles. The number points not considered ground, however, is not ignorable and suggests that further processing is required to clean the road areas.

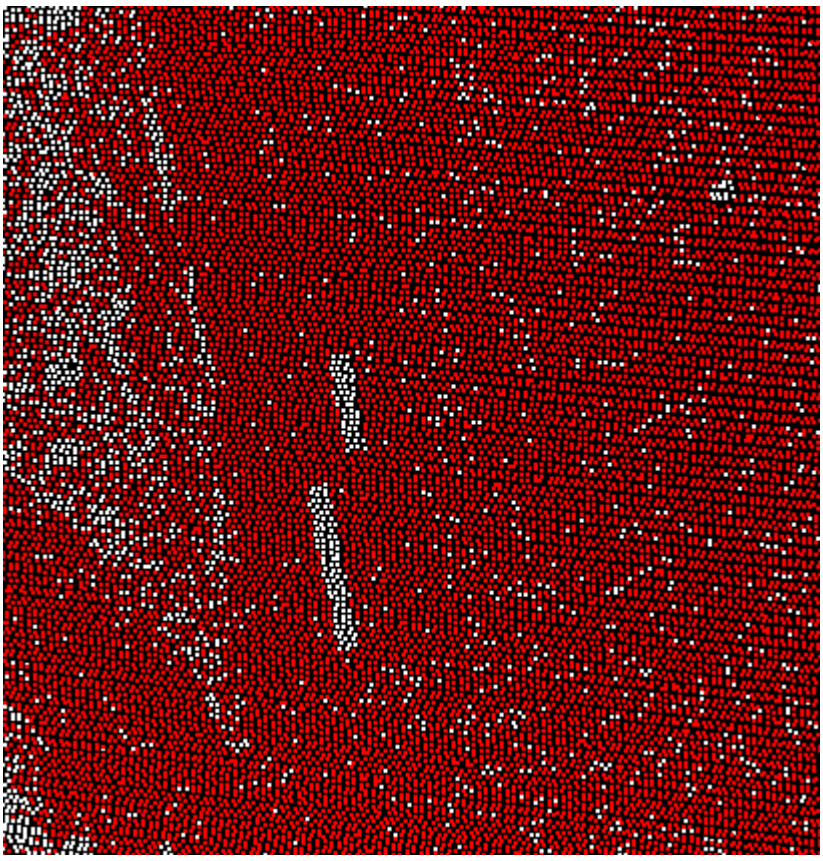

Figure 19. Selected ground points (red) by TeraaScan (road 1)

A similar dataset obtained by using the LHS test data are shown in Figures 20-21. The general observation are comparable to the Optech dataset

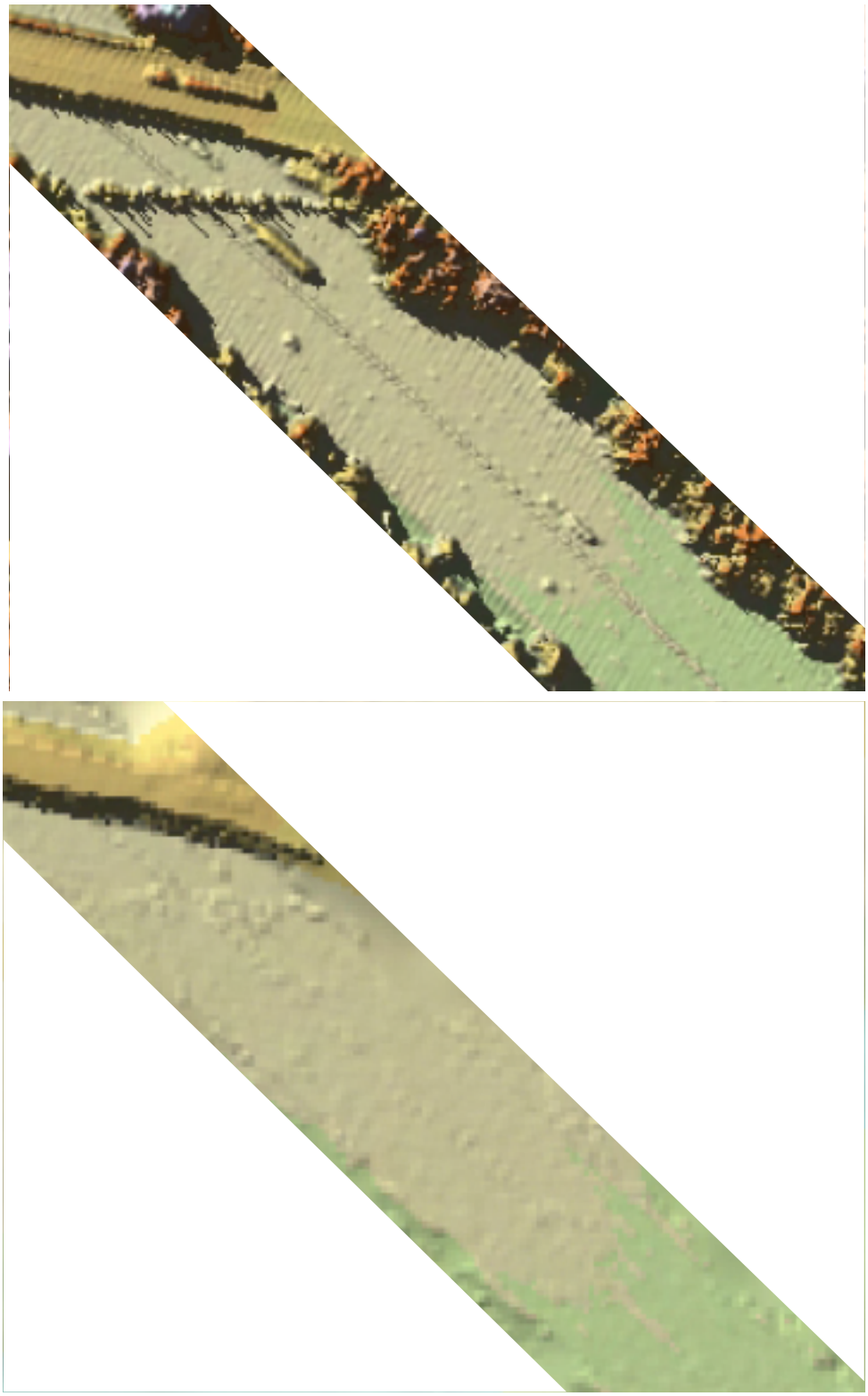

Figure 20. DSM (upper) and DTM (lower) generated by RTV (road 2)

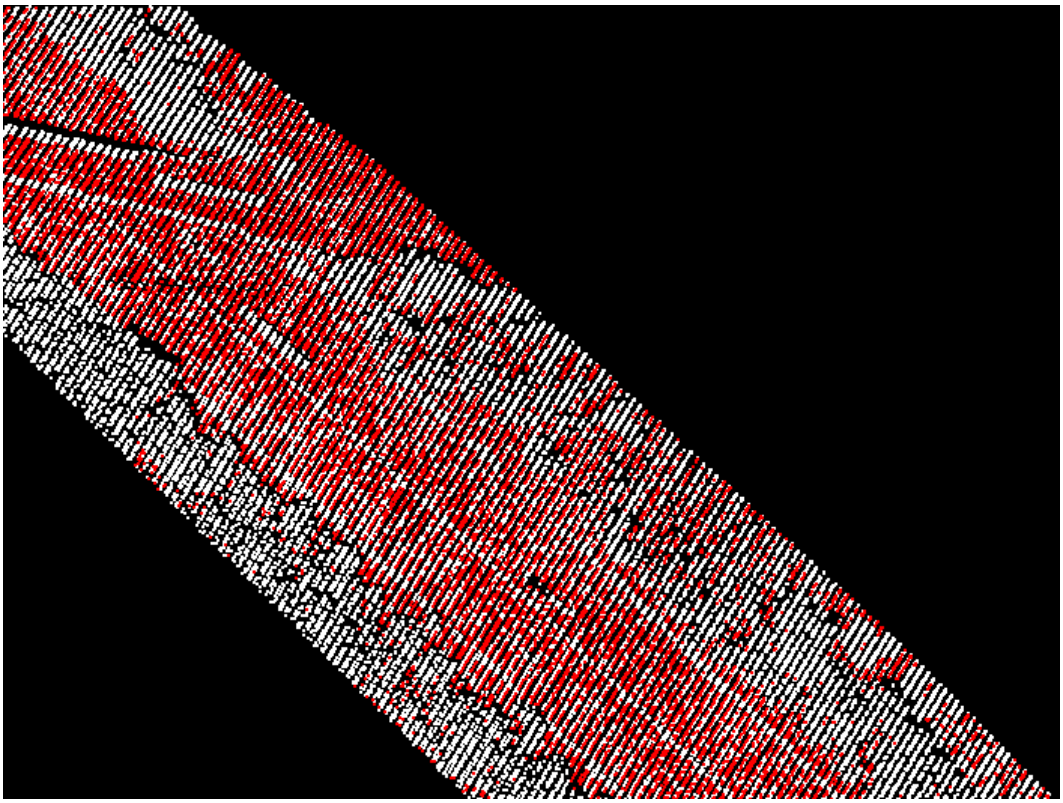

Figure 21. Selected ground points (red) by TeraaScan (road 2)

REFERENCES

Axelsson, P. (1999). Processing Of Laser Scanner Data - Algorithms And Applications, *ISPRS Journal of Photogrammetry and Remote Sensing*, 54(2-3), pp. 138-147.

Axelsson, P. (2000). DEM Generation From Laser Scanner Data Using Adaptive TIN Models, *The International Archives of the Photogrammetry, Remote Sensing and Spatial Information Sciences*, Annapolis, MD, Vol. 33, Part B3/1, pp. 119-126.

Brunn, A., Weidner, U. (1997). Extracting Buildings From Digital Surface Models, *The International Archives of the Photogrammetry, Remote Sensing and Spatial Information Sciences*, Vol. 32, Part 3-4W2, pp.27-34.

Elaksher, A.F., Bethel, J.S. (2002). Reconstructing 3D Buildings From LIDAR Data, *The International Archives of the Photogrammetry, Remote Sensing and Spatial Information Sciences*, Graz, Austria, Vol. 34, Part A3/3, pp. 102-107.

Elmqvist, M. (2002). Ground Surface Estimation From Airborne Laser Scanner Data Using Active Shape Models, *The International Archives of the Photogrammetry, Remote Sensing and Spatial Information Sciences*, Graz, Austria, Vol. 34, Part A3/3, pp. 114-118.

Kilian, J., Haala, N., Englich, M. (1996). Capture And Evaluation Of Airborne Laser Scanner Data, *The International Archives of the Photogrammetry, Remote Sensing and Spatial Information Sciences*, Vienna, Austria, Vol. 31, Part B3, pp. 383-388.

Kraus, K., Pfeifer, N. (1998). Determination Of Terrain Models In Wooded Areas With Airborne Laser Scanner Data, *ISPRS Journal of Photogrammetry and Remote Sensing*, Vol. 53, pp. 193-203.

Hug, C., Wehr, A. (1997). Detecting And Identifying Topographic Objects In Imaging Laser Altimetry Data, *The International Archives of the Photogrammetry, Remote Sensing and Spatial Information Sciences*, Vol. 32, Part 3-4W2.

Hyyppä, J., Schardt, M., Haggre'n, H., Koch, B., Lohr, U., Scherrer, H.U., Paananen, R., Luukkonen, H., Ziegler, M., Hyyppä, J., Pyssalo, U., Friedla:nder, H., Uuttera, J., Wagner, S., Inkinen, M., Wimmer, A., Kukko, A., Ahokas, A., Karjalainen, M. (2001). HIGH-SCAN: The First European-Wide Attempt To Derive Single-Tree Information From Laserscanner Data, *The Photogrammetric Journal of Finland*, Vol. 17, No. 2, 18: 58-68.

Maas, H.G., Vosselman, G. (1999). Two Algorithm For Extracting Building Models From Raw Laser Altimetry Data, *ISPRS Journal of Photogrammetry and Remote Sensing*, 54, pp. 153-163.

Nässet, E. (1997). Estimated Timber Volume Of Forest Stands Using Airborne Laser Data, *Remote Sensing of Environment*, Vol. 61, pp. 246-253.

Nilsson, M. (1996). Estimation Of Tree Height And Stand Volume Using An Airborne LIDAR System, *Remote Sensing of Environment*, 56, pp.1-7.

Oude Elberink, S., Maas, H.G. (2000). The Use Of Anisotropic Height Texture Measures For The Segment Of Airborne Laser Scanner Data, *The International Archives of the Photogrammetry, Remote Sensing and Spatial Information Sciences*, 33 B3/2, pp. 678-684.

Pfeifer, N., Stadler, P., Briese, Ch. (2001). Derivation Of Digital Terrain Models In The SCOP++ Environment, *Proc. of OEEPE Workshop on Airborne Laserscanning and Interferometric SAR for Detaoled Digital Terrain Models*, Stockholm, Sweeden.

Pyysalo, U., Hyyppä, H. (2002). Reconstructing Tree Crowns From Laser Scanner Data For Feature Extraction, *The International Archives of the Photogrammetry, Remote Sensing and Spatial Information Sciences*, Graz, Austria, Vol. 34, Part B3/3, pp. 218-221.

Rottensteiner, F., Briese, Ch. (2002). A New Method For Building Extraction In Urban Areas From High-Resolution LIDAR Data, *The International Archives of the Photogrammetry, Remote Sensing and Spatial Information Sciences*, Graz, Austria, Vol. 34, Part A3/3, pp. 295-301.

Schardt, M., Ziegler, M., Wimmer, A., Wack, R., Hyyppä, J. (2002). Assessment Of Forest Parameters By Means Of Laser Scanning, *The International Archives of the Photogrammetry, Remote Sensing and Spatial Information Sciences*, Graz, Austria, Vol. 34, Part A3/3, pp. 302-309.

TerraScan, TerraScan for MicroStation user's guide, TerraSolid Ltd, 1999.

Törmä, M. (2000). Estimation Of Tree Speices Proportions Of Forest Stands Using Laser Scanning, *The International Archives of the Photogrammetry, Remote Sensing. ISPRS Congress Symposioum*, Amsterdam, Vol. 33., pp. 1524-1531.

Weidner, U. (1997). Gebäudeerfassung Aus Digitalen Oberflächenmodellen, PhD Thesis, Institute of Photogrammetry, Bonn University, DGK-C 474.

Vosselman, G. (2000). Slope Based Filtering Of Laser Altimetry Data, *The International Archives of the Photogrammetry, Remote Sensing and Spatial Information Sciences*, Annapolis, MD, Vol. 33, Part B3/2, pp. 935-942.

Vosselman, G., Dijkman, S. (2001). 3D Building Model Reconstruction From Point Clouds And Ground Plans, *The International Archives of the Photogrammetry, Remote Sensing and Spatial Information Sciences* 34 (3W4), pp. 37-43.

Vosselman, G., Maas, H.G. (2001). Adjustment And Filtering Of Raw Laser Altimetry Data, *Proceedings of OEEPE Workshop on Airborne Laserscanning and Interferometric SAR for Detailed Digital Terrain Models*, Stockholm, Sweden.

A Practical Approach to LIDAR Sensor Calibration

Charles K. Toth, Nora Csanyi
Center for Mapping, The Ohio State University, 1216 Kinnear Road, Columbus, OH 43212-1154 USA

Dorota A. Grejner-Brzezinska
Department of Civil and Environmental Engineering and Geodetic Science
The Ohio State University, 470 Hitchcock Hall, Columbus, OH 43210-1275 USA

Abstract. The deployment of LIDAR systems has recently experienced enormous growth. Improved performance and affordability have made LIDAR a primary tool for collecting a variety of high quality surface data in much shorter periods of time than previously possible. In addition, some features unique to LIDAR, such as the capability to separate vegetation from the ground, have opened up new application areas. To achieve the highest accuracy, however, LIDAR systems have to be rigorously calibrated and the calibration parameters must be frequently checked.

LIDAR systems are complex multi-sensory systems composed of high-precision navigation and various imaging sensors. Therefore, the calibration process includes the calibration of the individual sensors and then the calibration of the integrated multi-sensory systems. High-performance integrated GPS/INS navigation systems provide the platform orientation for LIDAR systems and consequently, the geo-referencing accuracy achieved by the navigation component determines the ultimate performance limit of the whole data acquisition system. Despite the widespread use of GPS and the growing use of INS, maintaining a precise solution under various conditions is still a formidable task. The connection between the navigation system and the LIDAR scanner is described by the mounting bias or boresight. To determine and maintain the model parameters of this sensor relationship, well-planned experiments should be performed. Because of the nature of the LIDAR data, there is no direct solution for determining the boresight parameters. In this paper, we propose a method, using raw LIDAR data from overlapping flight lines, including both navigation and range components, to determine the boresight parameters.

Keywords. LIDAR systems, sensor calibration, airborne surveying, strip adjustment.

1 Introduction

To fully exploit the potential of LIDAR technology and to consequently achieve maximum accuracy of the laser points on the ground, the entire multi-sensory measurement system should be carefully calibrated. The overall system calibration is a very complex task and includes individual sensor calibration as well as the determination of the sensors' spatial relationships. High-performance integrated GPS/INS systems provide the navigation data for the LIDAR data acquisition platform, and thus, the quality of the navigation solution is primarily the determinant of the possible accuracy of the laser spots. To achieve or approach this performance level of the navigation, however, the spatial relationship between the navigation sensor and the laser scanner (called the mounting bias or boresight) must be known with high accuracy.

LIDAR systems include at least three main sensors, GPS positioning sensor, INS navigation sensor, and the laser-scanning device. The laser system measures the distances from the sensor to the ground surface. The coordinates of the ground point from where the laser pulse returned can be calculated if the travel distance of the laser pulse, the laser beam orientation, and the position of the laser scanner are known. Various things such as positioning errors, e.g., temporary GPS anomalies and/or misalignment between the laser and navigation systems can cause a misfit between the LIDAR points and the true surface or a difference between surfaces obtained from two LIDAR strips covering the same area. In general, the lack of feedback in the data flow in LIDAR systems makes the whole system more vulnerable to systematic errors and that seriously affects the quality of the LIDAR data. Baltsavias (1999) presents an overview of basic relations and error formulas concerning airborne laser scanning and a large number of publications report the existence of systematic errors. The solution for dealing with and eliminating the effect of systematic errors can be categorized into two groups. One approach is based on the introduction of a correction transformation of the laser points to minimize the difference between the corresponding LIDAR patches and ground truth. Kilian (1996) presents a method of transforming overlapping LIDAR strips to make them coincide with each other using control and tie points in a

similar way to photogrammetric block adjustment. The other technique attempts to rigorously model the system to recover the systematic errors. Burman (2000) treats the discrepancies between overlapping strips as orientation errors, with special attention given to the alignment error between the INS and laser scanner. Filin (2001) presents a similar method for recovering the systematic errors with respect to the boresight misalignment problem. The method described in this paper belongs to that second group as it addresses only a specific subtask of the overall system calibration process – finding the boresight misalignment of LIDAR systems based on measured discrepancies between overlapping strips.

There are a few methods for obtaining the boresight misalignment, which normally refers to only the determination of the rotation angles between the INS and laser scanner systems. The most common method is a simple trial and error approach, where the operator interactively changes the angles to reach some fit of the LIDAR spots with respect to some known surface. A more advanced, but still human-based technique uses block adjustment with control. Since the ground surfaces are not always known or not at the required accuracy level, preference should be given to techniques which do not require a priori knowledge of the surface.

The proposed automatic boresight determination method does not require any ground control and is based on two/three or more overlapping LIDAR strips flown in different directions. The surface differences from the different strips over the same area are considered as observations and an adjustment is formed to determine the boresight misalignment angles. The developed technique is based on the availability of multiple overlapping LIDAR strips over an unknown surface, although ground truth is also used if available. The surface where the LIDAR strips overlap must have certain characteristics in order to make the process work. There should be observable horizontal and vertical discrepancies between the different LIDAR datasets, however, extreme variations in height as well as densely-vegetated or wooded areas should be avoided. The LIDAR strips should be flown in a certain pattern as discussed later.

2 LIDAR Boresight Misalignment

The coordinates of a laser point are a function of the exterior orientation of the laser sensor and the laser range vector. The observation equation is:

$$r_{M,k} = r_{M,INS} + R_{INS}^{M}\left(R_{L}^{INS} \cdot r_{L} + b_{INS}\right) \quad (1)$$

where

$r_{M,k}$	—	3D coordinates of point k in the mapping frame
$r_{M,INS}$	—	3D INS coordinates in the mapping frame
R_{INS}^{M}	—	rotation matrix between the INS frame and mapping frame, measured by GPS/INS
R_{L}^{INS}	—	boresight matrix between the laser frame and INS frame
r_{L}	—	3D object coordinates in laser frame
b_{INS}	—	boresight offset component

The INS frame is usually considered as the local reference system, thus the navigation solution is computed for this frame. The spatial connection between the INS and laser systems, including an offset vector and rotation matrix between the two systems, has to be known with high accuracy. The critical component is the rotation since the object distance amplifies the effect of any angular inaccuracy, while the effect of any offset error does not depend on the flying height. The rotation can be described by three rotation angles, ω rotation around the x-axis, φ rotation around the y-axis and κ around the z-axis of the laser frame. The approximate values of the three rotation angles between the INS and the laser frames are known from the mechanical alignment. The actual angles differ slightly from these nominal values. The boresight misalignment problem is to determine these three misalignment angles. Any difference from the real values results in a misfit between LIDAR points and the ground surface; the calculated coordinates of the LIDAR points are not correct. In this section, the influence of the different boresight misalignment angles on the accuracy of 3D object coordinates is described briefly. The coordinate system definition (Baltsavias, 1999) shown in Figure 1 will be used in the following discussions to illustrate the effect of the boresight misalignment angles.

In order to analyze the effect of the different misalignment angles, the following simplifying assumptions are used: the terrain is flat, scanning is performed in a vertical plane perpendicular to the flight direction, and the flight line is horizontal (ω=0, φ=0, the κ rotation angle can have any value). X, Y, Z defines a right-handed object coordinate

system with the origin at the nadir of the origin of the local coordinate system, denoted by x,y,z and centered at the laser beam origin. The positive x-axis is in the flight direction, y is position starboard. The misalignment errors dω, dφ and dκ refer to the respective axes of the local coordinate system. κ is the rotation from the X-axis to the x-axis. β is the scan angle, it has positive values for scans to the left of the flying direction, else negative, h denotes the flying height.

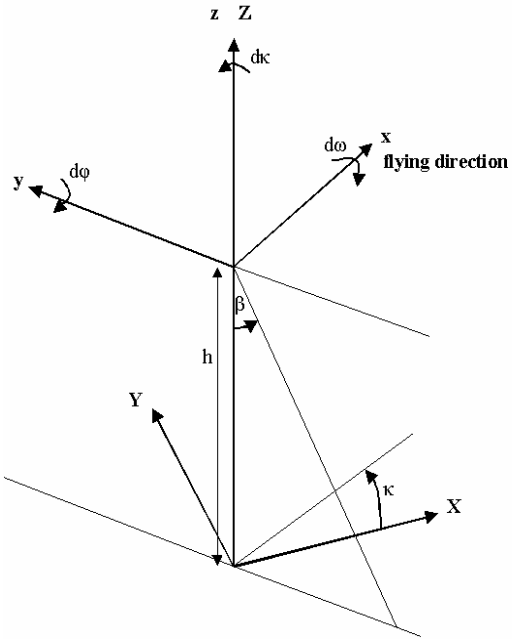

Figure 1. Coordinate system definition.

Roll misalignment, shown in Figure 2a, causes a shift across the flying direction in both horizontal and vertical coordinates. As a result, the surface becomes tilted, one side of the flying direction has a vertical shift upward and the other side has vertical shift downward. Under the flight line, at nadir there is no vertical shift; farther from the flight line the shift is becoming bigger. Roll misalignment has no effect in the flight direction. The formulas below show the errors in both the local and object coordinates caused by $d\omega$.

$$\Delta x = 0$$
$$\Delta y = h[\sin(\beta + d\omega) - \sin(\beta)] / \cos(\beta) \sim h \sin(d\omega)$$
$$\Delta z = h[1 - \cos(\beta + d\omega) / \cos(\beta)] \sim h \Delta\omega \tan(\beta)$$

$$\Delta X = -\Delta y \sin\kappa$$
$$\Delta Y = \Delta y \cos\kappa$$

Table 1 contains the coordinate errors in the local coordinate system at different scan angles in the case of a 3 arc-minute roll misalignment at 1000 m flying height.

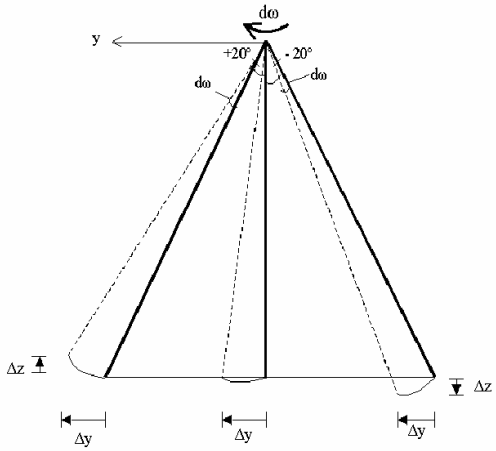

(a)

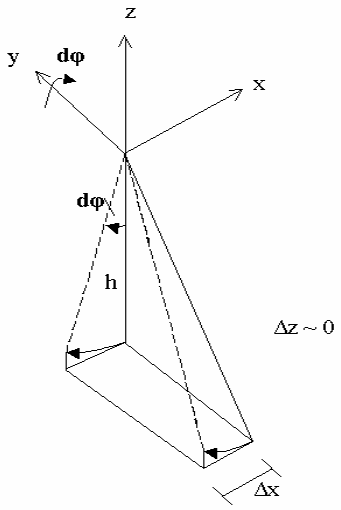

(b)

Figure 2. Effect of roll (a) and pitch (b) misalignment.

Table 1. Coordinate errors caused by roll misalignment.

	Δx [cm]	**Δy [cm]**	**Δz [cm]**
+30°	0	87	50
+20°	0	87	32
+10°	0	87	15
0°	0	87	0
-10°	0	87	-15
-20°	0	87	-32
-30°	0	87	-50

Misalignment in pitch, shown in Figure 2b, causes a constant shift along the flying direction; the vertical shift is negligibly small. dφ has no effect across the flying direction. The formulas below

show the local and object coordinate errors caused by pitch misalignment.

$$\Delta x = -h\sin(d\varphi)$$
$$\Delta y = 0$$
$$\Delta z = h[1-\cos(d\varphi)] \sim 0$$

$$\Delta X = \Delta x\cos(\kappa)$$
$$\Delta Y = \Delta x\sin(\kappa)$$

Table 2 contains the coordinate errors in the local coordinate system at different scan angles in the case of a 3 arc-minute pitch misalignment at1000 m flying height.

Table 2. Coordinate errors caused by pitch misalignment.

	Δx [cm]	**Δy [cm]**	**Δz [cm]**
+30°	-87	0	0
+20°	-87	0	0
+10°	-87	0	0
0°	-87	0	0
-10°	-87	0	0
-20°	-87	0	0
-30°	-87	0	0

Misalignment in heading, shown in Figure 3 causes a variable shift along the flying direction. Under the flight line there is no shift, the farther the LIDAR point from the flight line, the bigger the coordinate error. The sign of the shift is different on opposing sides. The shift across the flying direction is negligibly small and this misalignment has no effect on the vertical coordinates. The impact of any heading misalignment on the calculated coordinates is much less severe than the effect of same magnitude misalignment of roll or pitch; therefore, heading misalignment is the most difficult one to determine. In fact, during data processing some users just assume that the heading misalignment is zero. The formulas below show the coordinate errors caused by dκ in the local and object coordinate system.

$$\Delta x = -h\tan(\beta)\sin(d\kappa)$$
$$\Delta y = h\tan(\beta)[\cos(d\kappa)-1] \sim 0$$
$$\Delta z = 0$$

$$\Delta X = -h\tan(\beta)[\sin(\kappa+d\kappa)-\sin(\kappa)]$$
$$\Delta Y = h\tan(\beta)[\cos(\kappa+d\kappa)-\cos(\kappa)]$$

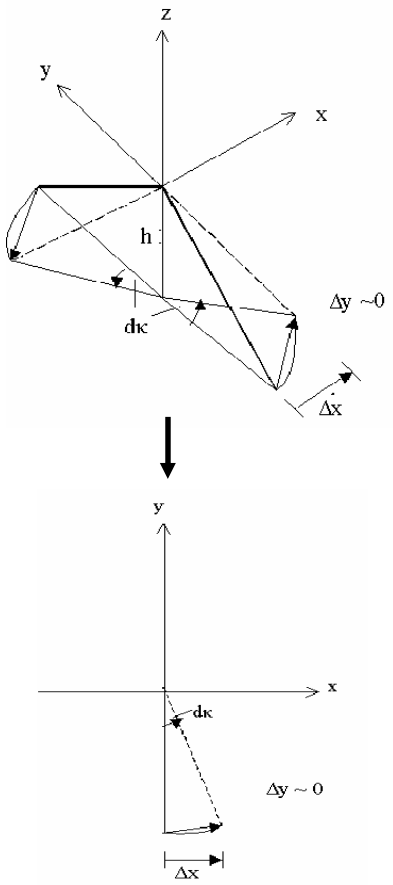

Figure 3. Effect of heading misalignment.

Table 3 contains the coordinate errors in the local coordinate system at different scan angles in the case of a 3 arc-minute heading misalignment at 1000 m flying height.

Table 3. Coordinate errors caused by heading misalignment.

	Δx [cm]	**Δy [cm]**	**Δz [cm]**
+30°	-50	0	0
+20°	-32	0	0
+10°	-15	0	0
0°	0	0	0
-10°	15	0	0
-20°	32	0	0
-30°	50	0	0

The above description of the different boresight misalignment situations clearly shows that the effect of the three misalignment angles is different and varies by location. Therefore, overlapping LIDAR strips flown in different directions will not fit to each other, resulting in observable horizontal and vertical discrepancies, which could be significant at high flying altitudes.

3 Concept of Boresight Misalignment Determination

The proposed method, shown in Figure 4 requires overlapping LIDAR strips. The more strips are used, the more reliable the results are. Without ground control, the horizontal and vertical discrepancies between the strips are used to determine the unknown misalignment angles. The discrepancies between LIDAR strips can be determined either by manual or automatic processing. Automatic processing starts with segmentation of LIDAR data. Segmentation is the process of selecting appropriate areas for obtaining reliable surface difference values. Forested areas, densely built-up areas, any moving objects are to be avoided. Since the coordinate discrepancies are bigger farther from the flight line, the ideal areas for boresight purpose are near the borders of the overlapping area, where the coordinate discrepancies are the most significant.

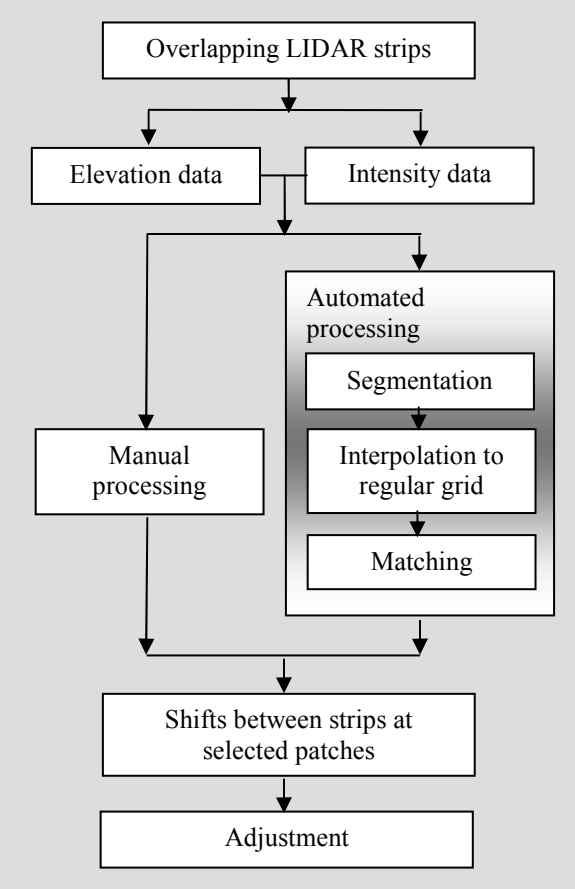

Figure 4. Concept of boresight misalignment determination.

Comparing different surfaces formed by randomly scattered points is a non-trivial task and the effectiveness of this process depends a lot on the point density of the LIDAR points and the overall terrain characteristics of the overlapping area. A frequently used technique is interpolation into regular grid. The discrepancies then can be determined by surface matching of selected segments, or profile matching of man-made objects performed between the different strips. New LIDAR systems are capable of providing intensity data besides elevation data, thus intensity data can provide excellent support for determining discrepancies between different strips. An example of how intensity data could help is matching over flat areas. In this case, elevation data cannot be matched based on the elevation differences; however, intensity contains enough information to perform matching and determine discrepancies at these areas. Figure 5 shows range and intensity data. In a sense, intensity data make it possible to use more areas in the boresight adjustment that could not be used if only elevation data were available. Finally, once the surface differences are known at regions of the overlapping area, a least squares adjustment can be formed for the unknown misalignment angles, which will be discussed in detail in the next section.

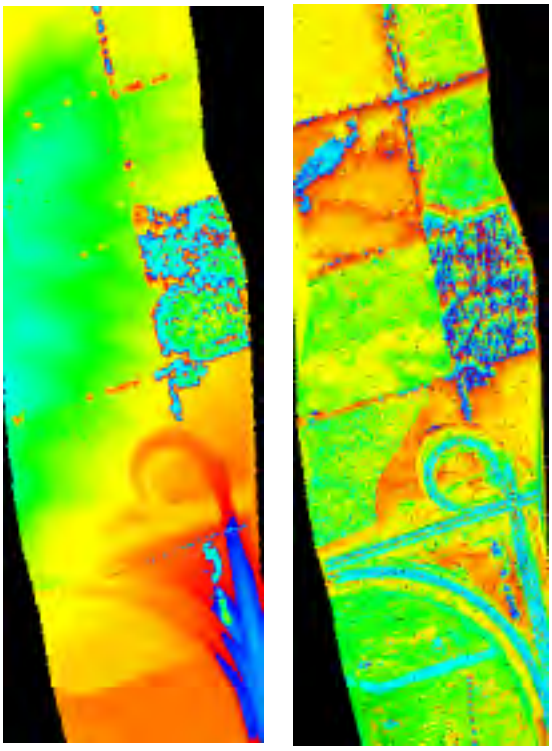

Figure 5. Elevation vs. intensity data.

4 The Proposed Adjustment Method

The proposed adjustment method is based on the observation Equation 1 and is concerned only with the rotation angles between the INS and the laser systems. The offset components are ignored since their inaccuracy is negligibly small both in absolute terms and compared to the effect of any angular inaccuracy between the two systems. The adjustment takes the observed discrepancies between the overlapping strips; expressed as matched virtual LIDAR points. The orientation of the data acquisition platform, including position and attitude, is required in addition to their coordinates. The coarse boresight angles and weights for the observed horizontal and vertical differences can be specified. The concept is to eliminate the surface differences by estimating the correct rotation angles between the INS and the laser systems.

Without proper boresight alignment, the calculated ground coordinates of a laser point or the surface they represent will be different in the overlapping area. The coordinates, however, can easily be corrected by rotating the range vector by the corrected boresight angles (R_L^{INS}) in the laser frame.

$$\begin{bmatrix} X_g \\ Y_g \\ Z_g \end{bmatrix}^{corr} = R_{INS}^{M} R_L^{INS} \begin{bmatrix} X_g \\ Y_g \\ Z_g \end{bmatrix}^{L} + \begin{bmatrix} X_a \\ Y_a \\ Z_a \end{bmatrix}^{M}$$

where

$\begin{bmatrix} X_g \\ Y_g \\ Z_g \end{bmatrix}^{corr}$ are the corrected ground coordinates in the mapping frame,

R_{INS}^{M} is the rotation matrix between the INS and mapping frame,

$\begin{bmatrix} X_g \\ Y_g \\ Z_g \end{bmatrix}^{L}$ is the range vector in the laser system,

$\begin{bmatrix} X_a \\ Y_a \\ Z_a \end{bmatrix}^{M}$ are the laser frame coordinates in the mapping frame at the time of measuring the ground point.

If the coarse boresight angles are zero, the R_L^{INS} matrix only contains the unknown boresight misalignment angles. Since the boresight misalignment angles are differential small angles, the rotation matrix can be written in the usual differential form:

$$R_L^{INS} = \begin{bmatrix} 1 & -d\kappa & d\varphi \\ d\kappa & 1 & -d\omega \\ -d\varphi & d\omega & 1 \end{bmatrix}$$

In the case of non-zero coarse boresight misalignment angles, the R_L^{INS} matrix contains (ω+dω), (φ+dφ), (κ+dκ) rotation angles.

For two overlapping LIDAR strips, the boresight angles can be found using the fact that the matched virtual points in the two strips should have the same coordinates; the difference between the corrected coordinates should be zero. In the case of two overlapping LIDAR strips, three equations containing the unknown three boresight misalignment angles can be formed at each pair of points, see Equation 2.

The unknown boresight misalignment angles can be found by least squares adjustment (A. Detrekoi, 1991) by minimizing the square sum of the discrepancies between the corrected coordinates of the matched virtual point pairs. Since the vertical matching results are more reliable than the horizontal ones, bigger weight is applied for the vertical coordinate differences than for the horizontal ones. As a consequence, the roll misalignment will be more reliable than the pitch or heading components. The more strips are used in the adjustment, the more reliable the results.

$$\begin{bmatrix} X_g \\ Y_g \\ Z_g \end{bmatrix}_1^{corr} - \begin{bmatrix} X_g \\ Y_g \\ Z_g \end{bmatrix}_2^{corr} = R_{INS\,1}^{M} R_L^{INS} \begin{bmatrix} X_g \\ Y_g \\ Z_g \end{bmatrix}_1^{L} + \begin{bmatrix} X_a \\ Y_a \\ Z_a \end{bmatrix}_1^{M} - R_{INS\,2}^{M} R_L^{INS} \begin{bmatrix} X_g \\ Y_g \\ Z_g \end{bmatrix}_2^{L} - \begin{bmatrix} X_a \\ Y_a \\ Z_a \end{bmatrix}_2^{M} \qquad (2)$$

As a standard procedure, at the end of the adjustment the residual coordinate differences between the strips at the matched virtual points are calculated. Then after removing the points with big residuals, the adjustment process starts all over again. Large residuals are mainly caused by blunders in the input data, typically due to gross matching errors.

5 Experiences

The developed method for boresight misalignment has been implemented in a Matlab environment. In addition, in house C++ software modules as well as generic programs have been used to realize some of the required processing tasks. In the first phase, extensive simulations were performed to check implementation correctness and to validate the performance potential. After some fine-tuning of both the algorithm and its implementation, tests were carried out on real datasets. For illustration purposes, a project with a higher than usual boresight alignment error was selected for our discussion. The data were acquired over the Dallas, TX, area and contains two opposite and one cross strips; the flying height was about 3,500 m with a point density of about 0.1 point/m². Three patches with an approximate size of 100m by 100m were selected from the 3-strip overlapping area, as shown in Figure 6.

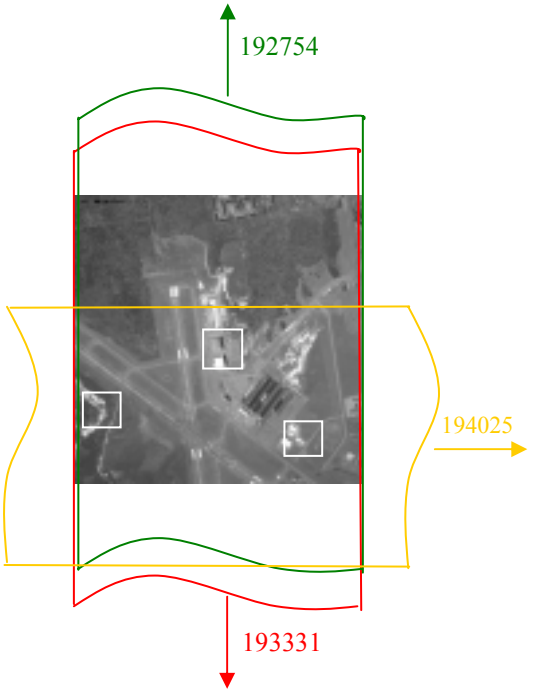

Figure 6. Overlapping strips of the test data set with the three selected patches.

During the preprocessing phase, about 50 virtual matching points were created for each patch. Then the adjustment process was performed separately for the three selected patches and also for all the three patches (174 points). Table 4 contains the results of the adjustments and the operator determined values from the trial and error method. We have to mention that in the case of the operator derived results the kappa misalignment angle was assumed to be zero. As discussed above it is the most difficult one to determine and its effect is negligible compared to the effect of the other two misalignment angles. The roll and pitch values of all the adjustments are practically the same as the operator derived values; the difference is a few arc seconds. Obviously, the adjustment including all the patches delivers the best results, but the individual adjustments of the patches have performed remarkably well, which is probably due to the large patch size and to the large number of points within the patch. As it was mentioned, the proposed method uses the observed discrepancies between overlapping LIDAR strips, and does not require ground truth. However, with this data set ground truth was available and therefore Table 4 also contains the results of the adjustment with ground truth included.

Table 4. Boresight misalignment results vs. operator derived values misalignment.

Patch included	#	Adjustment result		
		dω [rad]	dφ [rad]	dκ [rad]
1	74	-0.00406	-0.01315	0.00172
2	56	-0.00394	-0.01283	0.00217
3	44	-0.00409	-0.01270	-0.00047
1, 2, 3	174	-0.00402	-0.01292	0.00072
Ground	86	-0.00393	-0.01307	0.00064
1, 2, 3, G	260	-0.00399	-0.01294	0.00037
Operator		-0.00404	-0.01303	0

Figure 7 shows LIDAR profiles – in fact, several profiles bundled together – to visually illustrate the difference between strips before and after the boresight misalignment was applied. The three LIDAR strips are color-coded, the difference in the displayed Y ground direction was originally about 40 m. However, this difference subsequently went down to the decimeter level after applying the boresight misalignment correction (the discrepancy between the two arcs after the boresight correction is not a residual discrepancy; these are two different arcs behind each other).

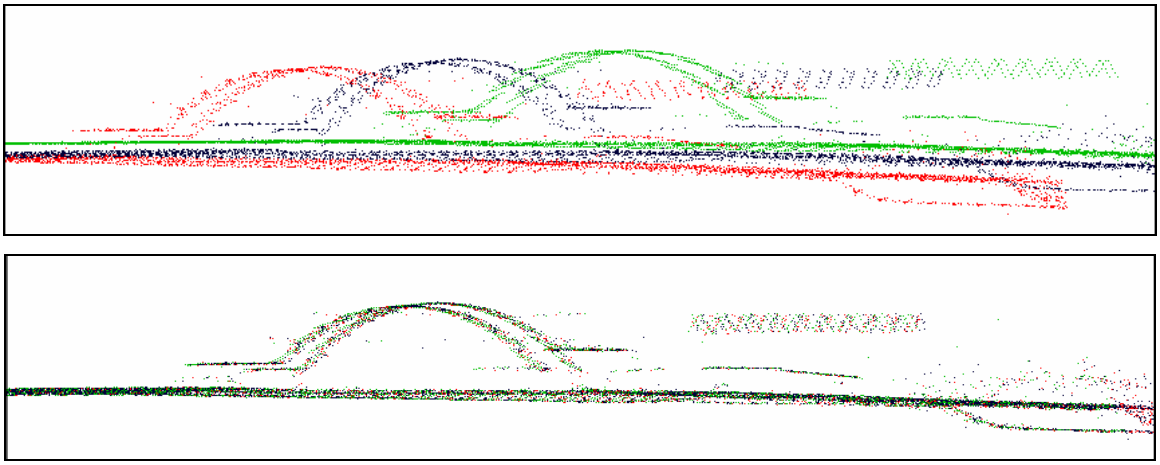

Figure 7. LIDAR profiles before and after boresight correction

6 Conclusions

LIDAR systems have to be well calibrated to deliver the most accurate three-dimensional coordinates of the measured ground surface. This paper focused on a specific subtask of the overall system calibration process – finding the boresight misalignment of LIDAR systems. A new method has been introduced to automate the determination of the boresight misalignment angles. The proposed method does not require known ground truth; it is based on the availability of overlapping LIDAR strips and navigation data. The boresight misalignment angles are found by least squares adjustment eliminating the observed discrepancies between the different strips. Results from simulations and real datasets have shown encouraging performance. The critical part of the solution is the determination of the discrepancies between the different LIDAR strips (the matching) – although the adjustment works for operator-based observations too. In the case of low LIDAR point density, the current performance of matching based on elevation data may not be sufficient. However, new LIDAR systems are capable of providing intensity data besides elevation data, which could adequately support the automatic determination of discrepancies between strips. As a future research task, the method can be extended to model other LIDAR-related errors such as variable scan angle error (smiley error).

Acknowledgement

The authors would like to acknowledge the support of The EarthData Group for providing test data and valuable technical discussions.

References

Baltsavias, E.P., (1999). Airborne laser scanning: basic relations and formulas. *ISPRS Journal of Photogrammetry & Remote Sensing* 54, pp. 199-214.

Burman, H., (2000). Adjustment of Laser Scanner Data for Correction of Orientation Errors. *International Archives of Photogrammetry and Remote Sensing*, Vol. XXXIII, Part B3, pp. 125-132.

Detrekoi, A. (1991). *Kiegyenlito Szamitasok*, Tankonyvkiado, Budapest.

Filin, S., (2001). Recovery of Systematic Biases in Laser Altimeters Using Natural Surfaces. *International Archives of Photogrammetry and Remote Sensing*, Vol. XXXIV, Part 3/W4, pp. 85-91.

Gruen, A., (1985). Adaptive Least Squares Correlation: A Powerful Image Matching Technique. *South African Journal of Photogrammetry, Remote Sensing and Cartography* 14 (3), pp. 175-187.

Kilian J., Haala, N., Englich, M., (1996). Capture and Evaluation of Airborne Laser Scanner Data. *International Archives of Photogrammetry and Remote Sensing*, Vol. XXXI, Part B3, pp. 383-388.

Sun, C., (1998). Multi-Resolution Rectangular Subregioning Stereo Matching Using Fast Correlation and Dinamic Programming Techniques, CMIS Report No. 98/246.

Toth, Ch.K., Csanyi, N., Brzezinska, D., (2000). Automating The Calibration Of Airborne Multisensor Imaging Systems, Proc. ACSM/ASPRS/FIG Congress and Annual Conference, Washington, DC, April 19-26, CD ROM.

Toth C. K., (2002). Calibrating Airborne LIDAR Systems, ISPRS Commission II Symposium on Integrated Systems for Spatial Data Production, Custodian and Decision Support, *International Archives of Photogrammetry and Remote Sensing*, Vol. XXXIV, part 2, pp.475-480.

CALIBRATING AIRBORNE LIDAR SYSTEMS

C. K. Toth

Center for Mapping, The Ohio State University, 1216 Kinnear Road, Columbus, OH 43212-1154, USA
toth@cfm.ohio-state.edu

Commission II, WG II/2

KEY WORDS: LIDAR, Boresight Misalignment, Sensor Calibration

ABSTRACT:

To fully exploit the potential of LIDAR technology and to consequently achieve maximum accuracy of the laser points on the ground, the entire multi-sensory measurement system should be carefully calibrated. The overall system calibration is a very complex task and includes individual sensor calibration as well as the determination of the sensors' spatial relationships. High-performance integrated GPS/INS systems provide the navigation data for the LIDAR data acquisition platform, and thus, the quality of the navigation solution is the primary determinant of the possible accuracy of the laser spots. To achieve or approach the performance level of the navigation, however, the spatial relationship between the navigation sensor and the laser scanner, called the mounting bias or boresight, must be known with high accuracy.

This paper deals with a specific subtask of the overall system calibration process – finding the boresight misalignment of LIDAR systems. There are a few methods for obtaining the boresight misalignment, which normally refers only to the determination of the rotation angles between the INS and laser scanner systems. The most common method is a simple trial and error approach, where the operator interactively changes the angles to reach some fit of the LIDAR spots with respect to some known surface. A more advanced, but still human-based technique uses block adjustment with control points. Since the ground surfaces are not always known or not at the required accuracy level, preference is given to techniques which do not require a priori knowledge of the surface. In this paper we propose an automatic boresight determination method that does not require any ground control and is based on using two/three or more overlapping LIDAR strips flown in different directions. The surface differences from the different strips over the same area are considered as observations and an adjustment is formulated to determine the boresight misalignment angles.

1. INTRODUCTION

LIDAR systems are complex multi-sensory systems and include at least three main sensors, GPS and INS navigation sensors, and the laser-scanning device. The laser system measures the distances from the sensor to the ground surface. The coordinates of the ground point from where the laser pulse returned can be calculated if the travel distance of the laser pulse, the laser beam orientation and the position of the laser scanner are known. Various things such as positioning errors, e.g. temporary GPS anomalies, and/or misalignment between the laser and navigation systems can cause a misfit between the LIDAR points and the true surface or a difference between surfaces obtained from two LIDAR strips covering the same area. In general, the lack of feedback in the data flow in LIDAR systems makes the whole system more vulnerable to systematic errors and that seriously affects the quality of the LIDAR data. Baltsavias (1999) presents an overview of basic relations and error formulas concerning airborne laser scanning and a large number of publications report the existence of systematic errors. The solution for dealing with and eliminating the effect of systematic errors can be categorized into two groups. One approach is based on the introduction of a correction transformation of the laser points to minimize the difference between the corresponding LIDAR patches and ground truth. Kilian (1996) introduces a method of transforming overlapping LIDAR strips to make them coincide with each other using control and tie points in a similar way to photogrammetric block adjustment. The other technique attempts to rigorously model the system to recover the systematic errors. Burman (2000) treats the discrepancies between overlapping strips as orientation errors, with special attention given to the alignment error between the INS and laser scanner. Filin (2001) presents a similar method for recovering the systematic errors with respect to the boresight misalignment problem.

This paper describes a method to automate the boresight misalignment of LIDAR systems. The developed technique is based on the availability of multiple overlapping LIDAR strips over an unknown surface, although ground truth is also used if available. The surface where the LIDAR strips overlap must have certain characteristics in order to make the process work. There should be observable horizontal and vertical discrepancies between the different LIDAR datasets, but extreme variations in height as well as densely-vegetated or wooded areas should be avoided. Finally, the LIDAR strips should be flown in certain pattern as discussed later.

2. LIDAR BORESIGHT MISALIGNMENT

Figure 1 shows the usual sensor configuration of airborne LIDAR systems. The navigation sensors are separated the most since the GPS antenna is installed on the top of the fuselage while the INS sensor is attached to the LIDAR system, which is down in the aircraft. The spatial relationship between the sensors should be known with high accuracy. In addition, maintaining a rigid connection between the sensors is also very important since modeling any changes in the sensor geometry in time would further increase the complexity of the system model

and perhaps add to the overall error. The INS frame is usually considered as the local reference system; thus the navigation solution is computed in this frame. The spatial relationship between the laser scanner and the INS is defined by the offset and rotation between the two systems. The critical component here is the rotation since the object distance amplifies the effect of an angular inaccuracy, while the effect of an inaccuracy in the offset does not depend on the flying height. The description of the effects of the different boresight misalignment angles is omitted here; for details see e.g. (Baltsavias, 1999).

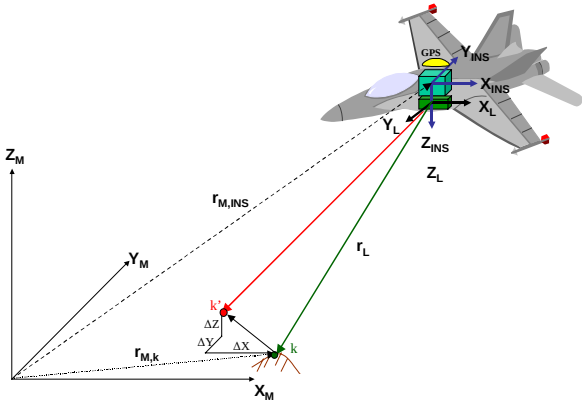

Figure 1. LIDAR system sensor configuration.

The coordinates of a laser point are a function of the exterior orientation of the laser sensor and the laser range vector. The observation equation is:

$$r_{M,k} = r_{M,INS} + R_{INS}^{M}(R_{L}^{INS} \cdot r_{L} + b_{INS}) \qquad (1)$$

where

$r_{M,k}$	—	3D coordinates of point k in the mapping frame
$r_{M,INS}$	—	3D INS coordinates in the mapping frame
R_{INS}^{M}	—	rotation matrix between the INS frame and mapping frame, measured by GPS/INS
R_{L}^{INS}	—	boresight matrix between the laser frame and INS frame
r_{L}	—	3D object coordinates in laser frame
b_{INS}	—	boresight offset component

To obtain the local object coordinates of a LIDAR point, the laser range vector has to be reduced to the INS system by applying the shift and rotation between the two systems, which results in the coordinates of the LIDAR point in the INS system. The GPS/INS-based navigation provides the orientation of the INS frame, including position and attitude; thus the mapping frame coordinates can be subsequently derived. In our discussion, the automated determination of the rotation component, the boresight matrix between the INS and the laser frame, is addressed.

The boresight rotation can be described by three rotation angles, ω rotation around the x-axis, φ rotation around the y-axis, and κ around the z-axis in the laser sensor frame. The approximate values of the three rotation angles between the INS and the laser frames are known from the mechanical alignment. The actual angles differ slightly from these nominal values. The boresight misalignment problem is to determine these three misalignment angles. Any discrepancy in their values results in a misfit between the LIDAR points and the ground surface; the calculated coordinates of the LIDAR points are not correct. In case the ground surface is unknown, the effect of the misalignment can be seen if different overlapping LIDAR strips are flown in different directions. Figures 2-3 show a situation where the overlapping strips do not fit each other; the horizontal and vertical discrepancies can be substantial at high flying altitudes.

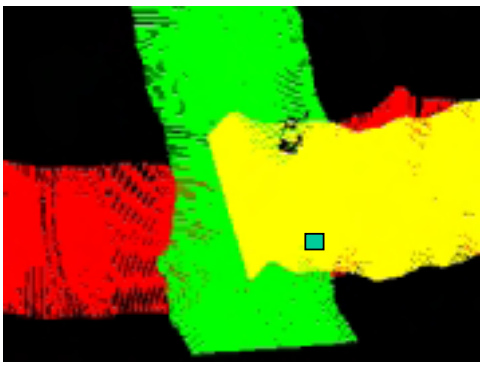

Figure 2. Overlapping LIDAR strips.

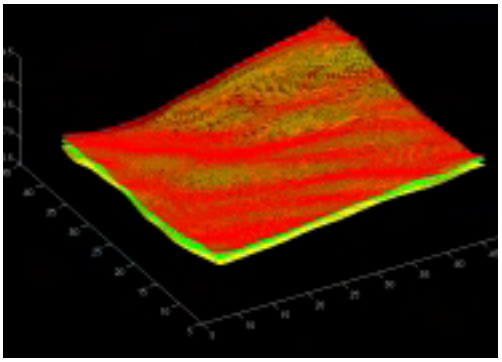

Figure 3. Surface differences at the selected area.

Boresight misalignment has to be determined to obtain correct surface from the LIDAR data. The unknown boresight misalignment angles can be found with ground control or without it by using overlapping LIDAR strips flown in different directions. Since the true ground surfaces are not always available preference should be given to techniques that do not require a priori knowledge of the surface.

3. CONCEPT OF AUTOMATED BORESIGHT MISALIGNMENT DETERMINATION

The proposed method requires overlapping LIDAR strips. The more strips that are used, the more reliable the results are. Without ground control, the horizontal and vertical discrepancies between the strips are used to determine the unknown misalignment angles. Therefore, appropriate portions of the overlapping area have to be selected for observing surface differences. The ideal portions for this purpose are near the borders of the overlapping area, where the differences are more noticeable, like the Gruber point distribution in a stereo model. Comparing different surfaces formed by randomly scattered points is a non-trivial task and the effectiveness of this process depends a lot on the point density of the LIDAR points and the

overall terrain characteristics of the overlapping area. A frequently used technique is interpolation into a regular grid. The discrepancies then can be determined relatively easily by surface matching of the selected regions or profile matching of man-made objects, etc. Once the surface differences are known at certain regions of the overlapping area, a least squares adjustment can be formed for the unknown misalignment angles. In this discussion, the main steps are introduced briefly; only the last step, the adjustment of the boresight angles, is discussed in detail.

3.1 Identifying Areas for Comparison by Segmentation

Segmentation is the process of selecting appropriate areas for obtaining reliable surface difference values. Forested areas, complex buildings, and moving objects are to be avoided. Smoothly rolling terrains, however, are ideal areas since they exhibit only limited undulations, differences can be observed yet their surface representation does not require excessive spatial sampling. These types of areas can effectively cope with various LIDAR configurations, coming from different flying heights, pulse repetition rates, scan angles and flying speeds, all resulting in different point patterns and point densities. From the potentially viable segments, a few should finally be selected based on their closeness to the overlapping area boundary and for their even distribution.

3.2 Surface Interpolation

Various surface interpolation methods exist and are used in practice to deal with irregularly spaced surface points or to convert them into a regular grid. Most techniques are based on a TIN model, although many others techniques are also reported in the literature. After testing some of the commonly used methods, we found that the local methods such as weighted average interpolation where the unknown values are calculated from the surrounding known points are not appropriate for the interpolation of the sparse LIDAR data (in our investigations, we were primarily concerned with LIDAR surveys conducted at regular or higher flying height). Similarly, global methods such as polynomial interpolation may provide a better approximation of the LIDAR surface, but these do not adequately represent smaller changes of the surface. Consequently, we decided on an interpolation method that would combine Fourier-series and polynomial models. In the first step, a least squares adjustment was formulated for determining the Fourier-series coefficients. Since the discrete Fourier-series is based on evenly-spaced data, it cannot be directly applied to approximate surfaces from irregularly scattered LIDAR points as the coefficients of the Fourier-series cannot be calculated in the usual way. Thereafter, the model was extended to include polynomial coefficients. In our experiences, the combined model has shown a promising performance, as the polynomial components seemed to preserve the overall trend of the surface while the Fourier component appeared to adequately handle the smaller local changes. Figure 3 shows surfaces modeled by the combined method (Fourier-series and third order polynomial interpolation).

3.3 Matching of Selected Areas

Matching in our context is the process of finding the differences in all three dimensions between the selected and interpolated small segments of the overlapping area. These offset values can be formed between any pairs of LIDAR data strips. Matching in general is an extremely broad topic. Although the number of image matching methods is almost countless, most of them are based on correlation or gradient discrepancies (Sun, 1998). A popular method in mapping is least squares matching, introduced by Gruen (1985), which usually delivers excellent results provided that good initial approximations are available. The reliability of the matching of LIDAR points depends primarily on the point density, which, in turn, depends on many factors such as flying height or swath width. Our investigation is concerned with relatively high flying height surveys, where the laser point density is rather low, which results in less reliable matching. During our tests, correlation matching was used primarily to determine the discrepancies of overlapping LIDAR strips. The results were mixed and this task needs further research effort to achieve consistent performance.

4. ADJUSTMENT METHOD

The proposed adjustment method is based on the observation equation (1) and is concerned only with the rotation angles between the INS and laser systems. The offset components are ignored since their inaccuracy is negligibly small both in absolute terms and compared to the effect of any inaccuracy in the rotation angles between the two systems. This results from the fact that the effect of an angular inaccuracy is amplified by the object distance, while the effect of an inaccuracy in the offset does not depend on the flying height.

The principle behind this method is very simple. Based on the observed differences, the misaligment angles are iteratively adjusted to reduce the surface discrepancies in object space. To apply the boresight misaligment and thus to correct the LIDAR point coordinates in object space, all the terms of the observation equation should be known. Therefore, the sensor platform orientation should be known for each laser point. Obviously, this is not really a strict condition since this information is always available by definition. Finding the surface differences, however, is a less than trivial task as it was briefly discussed earlier. Figure 4 shows the main steps of the adjustment method. To partially compensate for the uncertainty of the matching, a refinement has been included such that with the initial boresight misalignment results, the surface differences are recalculated and the whole adjustment process is repeated.

The adjustment process starts by taking the surface differences, which are expressed as matched virtual laser points. These points are determined a priori for all the surface patches of the overlapping area. Besides their coordinates, the orientation of the data acquisition platform, including position and attitude, is required. In addition, the coarse boresight angles and weights for vertical and horizontal control can be specified. The concept is to eliminate the surface differences by estimating the correct rotation angles between the INS and laser systems. Without proper boresight alignment, the calculated ground coordinates of a laser point or the surface they represent will be different in the overlapping area. The coordinates, however, can easily be corrected by rotating the range vector by the corrected boresight angles (R_L^{INS}) in the laser frame.

$$\begin{bmatrix} X_g \\ Y_g \\ Z_g \end{bmatrix}^{corr} = R_{INS}^{M} R_{L}^{INS} \begin{bmatrix} X_g \\ Y_g \\ Z_g \end{bmatrix}^{L} + \begin{bmatrix} X_a \\ Y_a \\ Z_a \end{bmatrix}^{M} \qquad (2)$$

where

$\begin{bmatrix} X_g \\ Y_g \\ Z_g \end{bmatrix}^{corr}$ are the corrected ground coordinates in the mapping frame,

R_{INS}^{M} is the rotation matrix between the INS and mapping frame,

$\begin{bmatrix} X_g \\ Y_g \\ Z_g \end{bmatrix}^{L}$ is the range vector in the laser system,

$\begin{bmatrix} X_a \\ Y_a \\ Z_a \end{bmatrix}^{M}$ are the laser frame coordinates in the mapping frame at the time of measuring the ground point.

If the coarse boresight angles are zero, the R_L^{INS} matrix only contains the unknown boresight misalignment angles. Since the boresight misalignment angles are differential small angles, the rotation matrix can be written in the usual differential form:

$$R_L^{INS} = \begin{bmatrix} 1 & -d\kappa & d\varphi \\ d\kappa & 1 & -d\omega \\ -d\varphi & d\omega & 1 \end{bmatrix}$$

For non-zero coarse boresight misalignment angles, the R_L^{INS} matrix contains the (ω+dω), (φ+dφ), (κ+dκ) rotation angles.

For two overlapping LIDAR strips, the boresight angles can be found using the fact that the matched virtual points in the two strips should have the same coordinates, so the difference between the corrected coordinates should be zero, Equation 3. Three equations can be formed at each pair of points, which together contain the unknown three boresight misalignment angles.

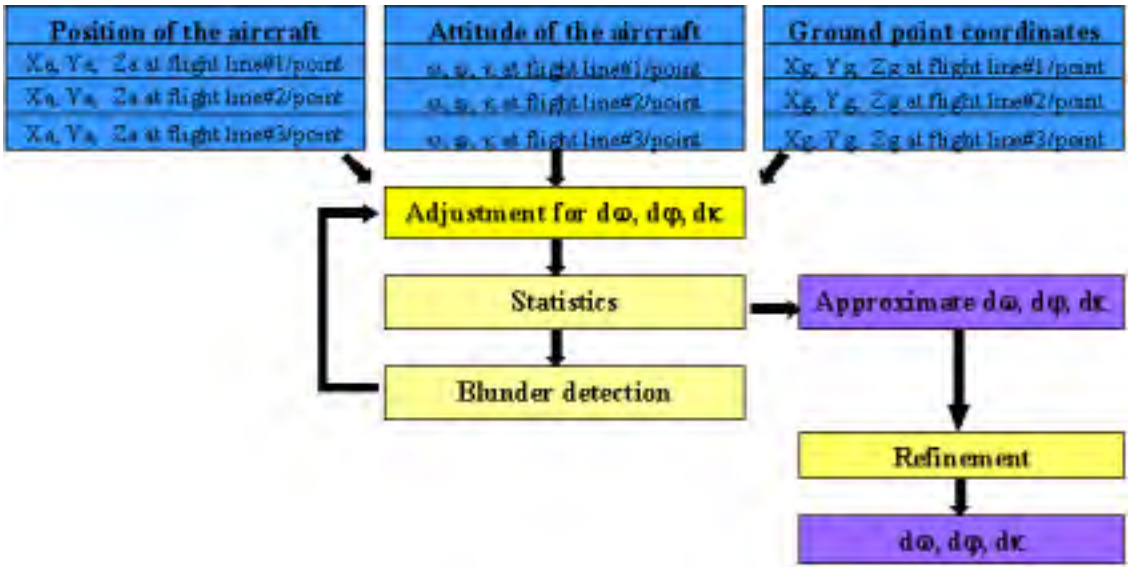

Figure 4. Main steps of the adjustment process.

$$\begin{bmatrix} X_g \\ Y_g \\ Z_g \end{bmatrix}_1^{corr} - \begin{bmatrix} X_g \\ Y_g \\ Z_g \end{bmatrix}_2^{corr} = R_{INS1}^{M} R_L^{INS} \begin{bmatrix} X_g \\ Y_g \\ Z_g \end{bmatrix}_1^{L} + \begin{bmatrix} X_a \\ Y_a \\ Z_a \end{bmatrix}_1^{M} - R_{INS2}^{M} R_L^{INS} \begin{bmatrix} X_g \\ Y_g \\ Z_g \end{bmatrix}_2^{L} - \begin{bmatrix} X_a \\ Y_a \\ Z_a \end{bmatrix}_2^{M} \tag{3}$$

$$M = \sum_1^m \left(\Delta X_{12}^2 wh + \Delta X_{13}^2 wh + \Delta X_{23}^2 wh + \Delta Y_{12}^2 wh + \Delta Y_{13}^2 wh + \Delta Y_{23}^2 wh + \Delta Z_{12}^2 wv + \Delta Z_{13}^2 wv + \Delta Z_{23}^2 wv \right) \rightarrow \min \tag{4}$$

The navigation data of the matched virtual points are either known or can be interpolated using the navigation data of the surrounding laser points. If n overlapping strips are flown, 3n equations can be formed at each matched virtual point. In this case, the unknown boresight misalignment angles can be found using least squares adjustment with the condition that the square sum of the differences between the corrected coordinates of the matched virtual points in the different strips is minimum. For the typical three overlapping strips case, Equation 4 can be formed, where m is the number of matched virtual points. Since the vertical matching results are usually more reliable than the horizontal ones, more weight is preferable for the vertical coordinate difference residuals (*wv*) than for the horizontal ones (*wh*). As a consequence, the roll misalignment will be more reliable than the pitch or heading components.

As a standard procedure, at the end of the adjustment the residual coordinate differences between the strips at the matched virtual points are calculated. Then after removing the points with big residuals, the adjustment process starts all over again. Large residuals are mainly caused by blunders in the input data, typically due to gross matching errors. As another step in dealing with the matching uncertainty, the whole matching process is repeated on the boresight misalignment corrected data as the differences should be smaller and thus better matching performance is expected.

5. EXPERIENCES

The developed method for boresight misalignment has been implemented in a Matlab environment. In addition, in house C++ software modules as well as generic programs have been used to realize some of the required processing tasks. In the first phase, extensive simulations were performed to check implementation correctness and to validate the performance potential. After some fine-tuning of both the algorithm and its implementation, tests were carried out on real datasets. For the purpose of illustration, a project with a higher than usual boresight alignment error has been selected for our discussion. The data was acquired over the Dallas, TX area and the flying height was about 3,500 m with a point density of about 0.1 point/m². Six patches with an approximate size of 100 m by 100m have been selected from the 3-strip overlapping area.

During the preprocessing phase, about 50 virtual matching points were created for each patch. Then the adjustment process was performed separately for the 6 selected patches and also for all 6 patches (291 points). Table 5 contains the results of the seven adjustments and the operator determined values. The roll and pitch values of all seven adjustments are practically the same as the operator derived values; the difference is a few arc seconds. Obviously, the adjustment including all the patches delivers the best results, but the individual adjustments of the patches have performed remarkably well, which is probably due to the large patch size and to the large number of points within the patch.

Adjustment #	Patch Included	Number Of Points	First		
			Dω [RAD]	Dφ [RAD]	Dκ [RAD]
1	1	74	-0.00406	-0.01315	0.00172
2	2	56	-0.00394	-0.01283	0.00217
3	3	44	-0.00409	-0.01270	-0.00047
4	1, 2, 3	174	-0.00402	-0.01292	0.00072
5	Ground truth	86	-0.00393	-0.01307	0.00064
6	1, 2, 3 and ground	260	-0.00399	-0.01294	0.00037
Operator			**-0.00404**	**-0.01303**	

Table 5. Boresight misalignment results vs. operator derived values.

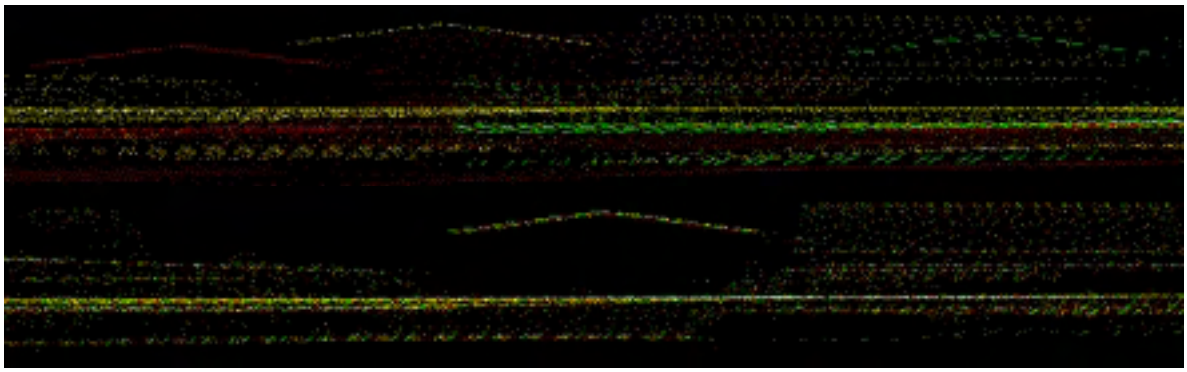

Figure 6. LIDAR profiles before and after the boresight misalignment has been applied.

Figure 6 shows LIDAR profiles – in fact, several profiles bundled together – to visually illustrate the difference between before and after the boresight misalignment has been applied. The three LIDAR strips are color-coded and the difference in the displayed Y ground direction was originally about 40 m. However, this difference subsequently went down to the meter level after applying the boresight misalignment correction (remember that this project having extreme characteristics was intentionally selected).

6. CONCLUSIONS

LIDAR systems have to be well calibrated to deliver accurate three-dimensional coordinates of the measured ground surface. Boresight misalignment as part of the overall multi-sensor system calibration problem is a source of systematic errors and thus can cause a mismatch between datasets obtained from different LIDAR strips or ground truth. The impact of these discrepancies is especially significant for higher flying height surveys.

In this paper, a new method has been introduced to automate the determination of the boresight misalignment angles. Boresight misalignment can be determined provided sufficient ground control is available. In lack of ground control, overlapping LIDAR strips can be used to achieve the same results. The developed method is based on the differences observed between the overlapping LIDAR strips and requires navigation data. Results from simulations and real datasets have shown encouraging performance. For not too complex areas, the solution is robust and there is very little dependency on the performance of matching – the process of finding the surface discrepancies. For feature-rich areas such as densely built-up urban areas or wooded areas, the current performance of matching may not be sufficient, although the adjustment will work for operator-based observations too. As a future research task, the method can be extended to model other LIDAR-related errors such as variable scan angle error (smiley error).

7. ACKNOWLEDGEMENTS

The author would like to acknowledge the support of The EarthData Group for providing test data and valuable technical discussions. The author wishes to thank Nora Csanyi and Eva Paska, interns from the Center for Mapping, OSU, for their help in the implementation and data processing.

8. REFERENCES

Baltsavias, E.P., 1999. Airborne laser scanning: basic relations and formulas. *ISPRS Journal of Photogrammetry & Remote Sensing* 54, pp. 199-214.

Burman, H., 2000. Adjustment of Laser Scanner Data for Correction of Orientation Errors. *International Archives of Photogrammetry and Remote Sensing*, Vol. XXXIII, Part B3, pp. 125-132.

Filin, S., 2001. Recovery of Systematic Biasaes in Laser Altimeters Using Natural Surfaces. *International Archives of Photogrammetry and Remote Sensing*, Vol. XXXIV, Part 3/W4, pp. 85-91.

Gruen, A., 1985. Adaptive Least Squares Correlation: A Powerful Image Matching Technique. *South African Journal of Photogrammetry, Remote Sensing and Cartography* 14 (3), pp. 175-187.

Kilian J., Haala, N., Englich, M., 1996. Capture and Evaluation of Airborne Laser Scanner Data. *International Archives of Photogrammetry and Remote Sensing*, Vol. XXXI, Part B3, pp. 383-388.

Sun, C., 1998. Multi-Resolution Rectangular Subregioning Stereo Matching Using Fast Correlation and Dinamic Programming Techniques, CMIS Report No. 98/246.

Toth, Ch.K., Csanyi, N., Brzezinska, D., 2000. Automating The Calibration Of Airborne Multisensor Imaging Systems, Proc. ACSM/ASPRS/FIG Congress and Annual Conference, Washington, DC, April 19-26, CD ROM.

APPENDIX E

Using LiDAR-Specific Targets for Ground Control

1. Csanyi N., Toth C., Brzezinska D. and Ray, J. 2005: Improvement of LiDAR Data Accuracy Using LiDAR Specific Ground Targets , Proc. ASPRS 2005 Annual Conference, Baltimore, MD, March 7-11, CD-ROM
2. Csanyi N., and Toth C., 2004: On Using LIDAR Specific Ground Targets, Proc. ASPRS 2004 Annual Conference, Denver, CO, May 23-28, CD-ROM.
3. Geo-Referenced Digital Data Acquisition and Processing System Using LIDAR Technology, Internal Report to ODOT, 2003.

IMPROVEMENT OF LIDAR DATA ACCURACY USING LIDAR SPECIFIC GROUND TARGETS

Nora Csanyi[1]
Charles K. Toth[2]
Dorota Grejner-Brzezinska[1]
John Ray[3]

Department of Civil and Environmental Engineering and Geodetic Science[1]
Center for Mapping[2]
The Ohio State University
Ohio Department of Transportation[3]
1216 Kinnear Road, Columbus OH 43212-1154
E-mail: nora@cfm.ohio-state.edu

ABSTRACT

Engineering scale mapping of highway corridors frequently requires extremely high accuracy. LiDAR technology offers an excellent tool to accomplish this task; LiDAR systems are complex multi-sensory systems, incorporating GPS and INS navigation sensors, and the laser-scanning device. The high complexity of the system, however, results potential error sources that can degrade the accuracy of the acquired LiDAR data. One way to achieve the high accuracy required by engineering scale mapping is using well-identifiable LiDAR-specific ground control targets. This paper is a continuation of a former paper titled "On the Use of LiDAR Specific Ground Targets" presented at the ASPRS Conference in Denver, 2004, where design of the optimal LiDAR targets, including shape, size, and signal response was discussed and some initial, limited experiences were presented. Since then additional tests were performed to further investigate the potential of using control targets for LiDAR data refinement. This paper provides a detailed performance analysis, investigating the achievable LiDAR data accuracy improvement using LiDAR-specific ground control targets.

INTRODUCTION

In the last few years LiDAR technology has become the preferred method for surface data acquisition. A broad range of applications exist and new applications are emerging, including forestry management, mapping of urban areas, flood and risk assessment, transportation and pipeline corridor mapping, etc., all requiring high accuracy LiDAR data. LiDAR systems are complex multi-sensory systems and incorporate at least three main sensors, GPS and INS navigation sensors, and the laser-scanning device. The complexity of the system results in possible error sources that can degrade the accuracy of the acquired LiDAR data. The errors in laser scanning data can come from individual sensor calibration or measurement errors, lack of synchronization, or misalignment between the different sensors. Baltsavias (1999) presents an overview of basic relations and error formulas concerning airborne laser scanning.

Most of the systematic errors can be corrected by strip adjustment, eliminating the discrepancies between overlapping LiDAR strips. In the last few years several strip adjustment methods have been developed (Kilian *et al.*, 1996; Crombaghs *et al.*, 2000; Burman, 2000; Filin, 2001; Toth *et al.*, 2002). All of these strip adjustment methods are based on the observed vertical or three-dimensional discrepancies between the overlapping LiDAR strips. Systematic planimetric errors are often much larger than height errors of the LiDAR data, and therefore, a three-dimensional strip adjustment is the desirable solution. Some of the strip adjustment methods work only with tie points (without any ground control information), however, the use of some type of ground control is desirable, since eliminating the relative discrepancies between overlapping strips does not provide an absolute check of the dataset. Applications demanding the highest accuracy require the elimination of absolute errors, which cannot be achieved without the use of absolute control information. Ground control information can be used in the strip adjustment process or after strip

adjustment to correct the remaining absolute errors in the corrected strips. Many times after the strip adjustment, a horizontal surface with a known elevation is used to correct remaining vertical shifts in the data. However, remaining absolute errors after strip adjustment can be more complex than just a vertical shift. Three-dimensional ground control information, buildings, known roof structures, etc., are often used. However, this type of control information is not always available. Furthermore, due to the characteristics of laser data, the identification of distinct points of buildings and roof structures in LiDAR data can result in a biased position, which could affect the accuracy of the corrected LiDAR data. Therefore, for applications with high accuracy requirements, such as corridor mapping, well-identifiable LiDAR-specific ground control targets are necessary.

Since the use of LiDAR-specific ground control targets represent a novel idea (not explored in practice yet), simulations were performed to determine the optimal LiDAR-target design; this includes the optimal target size, target shape, signal response, and a method to accurately determine the target position in the LiDAR dataset. Our previous paper titled "On the Use of LiDAR Specific Ground Targets" and presented at the ASPRS Conference in Denver, 2004 (Csanyi and Toth, 2004), provides a detailed description of the optimal target design along with some initial test results. Additional tests have been performed to investigate the potential of using the designed LiDAR-specific ground control targets for LiDAR data refinement. This paper is a continuation of our previous paper. After a brief summary of the optimal target design, test results based on two test flights are presented, providing a detailed performance analysis on the achievable improvement in LiDAR data accuracy using LiDAR-specific ground control targets.

LiDAR TARGET DESIGN AND METHODOLOGY

Preferably, an optimal LiDAR target should be automatically identifiable, easily distinguishable from surrounding objects in LiDAR data, and its horizontal and vertical position should be accurately measurable. The target design included the determination of the optimal target shape, target size, coating pattern, and related algorithms to accurately determine the planimetric and vertical position of targets in LiDAR data. To support the optimal LiDAR target design investigations extensive simulations were carried out. In this paper only a summary of the optimal target design is given, details can be found in (Csanyi and Toth, 2004).

An optimal target is rotation invariant (circular-shaped), and in order to reliably and automatically identify LiDAR points reflected from the target, it has a flat surface, elevated from the ground. Since newer LiDAR systems are capable of measuring intensity data, the target has a coating that produces a substantially different reflectance than its surroundings to facilitate the target identification. Based on simulation results with different target designs, the conclusions were the following: (1) as expected, the larger the size the better the accuracy of the determined position, although the results showed that from about 5 points per m^2 point density, a 1m circle radius can already provide sufficient accuracy, and further increasing the target size will not lead to significant improvements, and (2) the two-concentric-circle design (the inner circle has half the radius of the outer circle) with different coatings results in significant accuracy improvements in the determined position. The achievable positioning accuracies of using optimal design targets obtained by simulation for different LiDAR point densities are shown in Table 1; a 10 cm vertical accuracy was assumed for the LiDAR.

LiDAR point density [m]	Accuracy of horizontal position of target circle [cm]	Accuracy of vertical position of target circle [cm]
0.25*0.25	2-3	1.3
0.50*0.50	5-10	2.5
0.75*0.75	10-15	4.0

Table 1. Estimate of positioning accuracies based on simulation results.

Based on the above design, targets were fabricated by the Ohio Department of Transportation (ODOT) to support performance validation experiments under normal operational conditions; a target is shown in Figure 1.

Figure 1. ODOT manufactured LiDAR target.

This target design greatly facilitates the automatic target identification in LiDAR data (the target with its vicinity is extracted by the known target position and expected maximum errors). Once the points on the target circle are found, based on the elevation and/or intensity data, the horizontal and vertical position of the origin can be determined by separate algorithms. The vertical position of the target is determined by fitting a horizontal plane to the LiDAR points on the target. The accuracy of the determined target height is: $\sigma_{vertical\_pos} = \sigma_Z / \sqrt{n}$, where n is the number of points on the target, and σ_Z is the vertical coordinate accuracy of the LiDAR points. The horizontal target position is found by an algorithm similar to the Hough-transform. The search is based on the known radii of the target circles; the process finds all the possible locations of the target circle in a grid. Details can be found in (Csanyi and Toth, 2004).

Ground control targets in LiDAR data can be used in the strip adjustment procedure, or after strip adjustment, to correct for absolute error in the data. In the latter case a simple vertical shift or a more complex 3-dimensional transformation is applied to the data based on the known and measured target positions. The applied transformation depends on the characteristics of the remaining errors and the number of available targets in the dataset. If only one or two ground targets are available in the dataset, a simple vertical offset correction can be performed. If three or more targets are available, a 3-dimensional similarity or a more complex transformation can be applied on the data to correct absolute errors. Corrections can be performed by strip or in more complex case strips can be subdivided into segments and each segment can have different correction parameters.

TEST RESULTS

This section presents test results from test flights aimed at infrastructure mapping of a transportation corridor and provides an analysis of the achievable LiDAR data accuracy using the designed LiDAR-specific ground control targets.

Test area

The test area in Ashtabula, Ohio, was surveyed using an Optech ALTM 30/70 LiDAR system operated by the Ohio Department of Transportation. The data was collected from an altitude of about 620 m with a 14-degree field of view (7.0 half angle), at 70 Hz scanner frequency and 70 kHz pulse rate, resulting in a point density of about 5 points/m^2. The map of the test area is shown in Figure 2a. Several LiDAR strips were flown over a 23 km long section of I-90 in both directions. Both elevation and intensity data were collected to facilitate LiDAR target identification in the data. To support our investigation, 15 sets of LiDAR targets were placed symmetrically along the two sides of the road with an average distance of 2,000 m between two targets. The origins of the target circles were GPS-surveyed at a horizontal coordinate accuracy within 2 cm.

(a)

(b)

Figure 2. Map of the test area (a) and target locations (b).

For the discussion here, two overlapping strips flown in opposite directions were chosen; the map of the area is shown in Figure 2b. The strip flown in the SE to NW direction will be denoted as strip #1, and the strip flown in the opposite direction as strip #2. Due to the small scan angle (7-degree) and the low flying height the swath width of the strips was rather narrow. The strips flown along the road had a length of about 8.3 km, so ideally they would contain four targets on both sides of the road. Unfortunately, the overlap of the strips fluctuated and consequently a couple of targets were missed from both strips. Nevertheless, there are a couple of targets that can be found in both strips. The two strips with the targets are shown in Figure 3. Table 2 lists the targets that can be found on each strip.

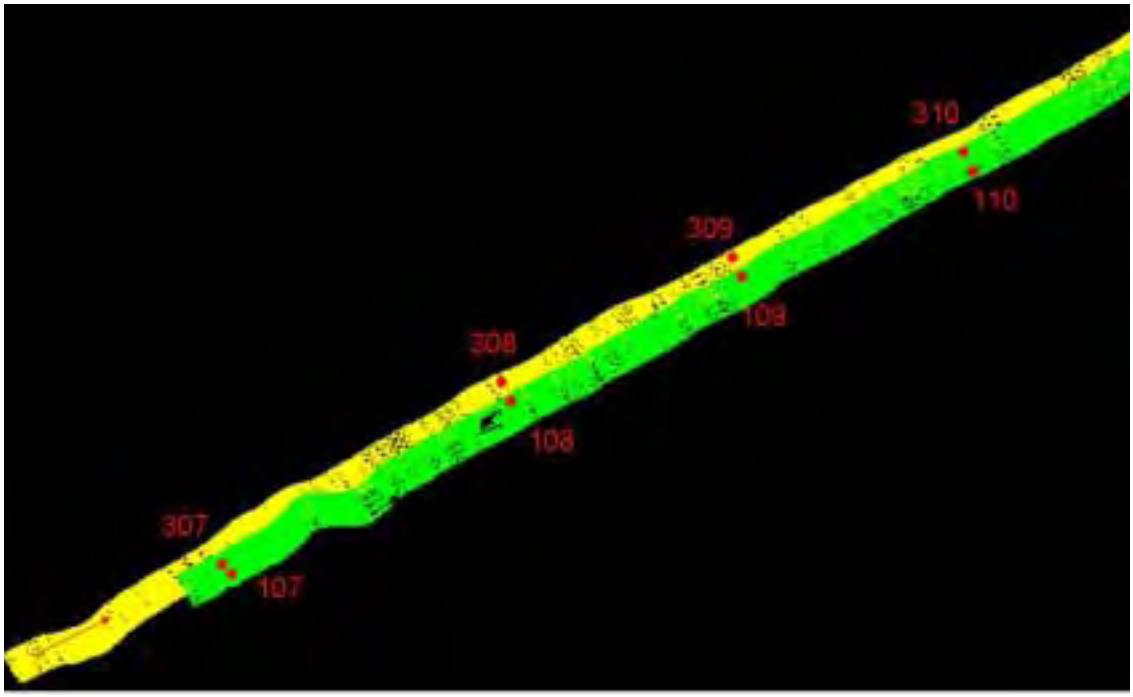

Figure 3. Strips #1 (yellow) and strip #2 (green) with targets.

Strip #1	Strip #2
307	107
108	108
308	109
109	110
309	310
110	
310	

Table 2. Targets on strip #1 and strip #2.

As Figure 3 illustrates, the distribution of targets in strip #1 is better than in strip #2. In strip #1, there are seven targets well distributed on both sides of the road. In the case of strip #2, the target distribution is not really optimal, as a couple of targets were missed – there are four targets on one side of the road and only one target on the other side. Figure 4 shows LiDAR elevation data of a smaller area containing one target on both sides of the road.

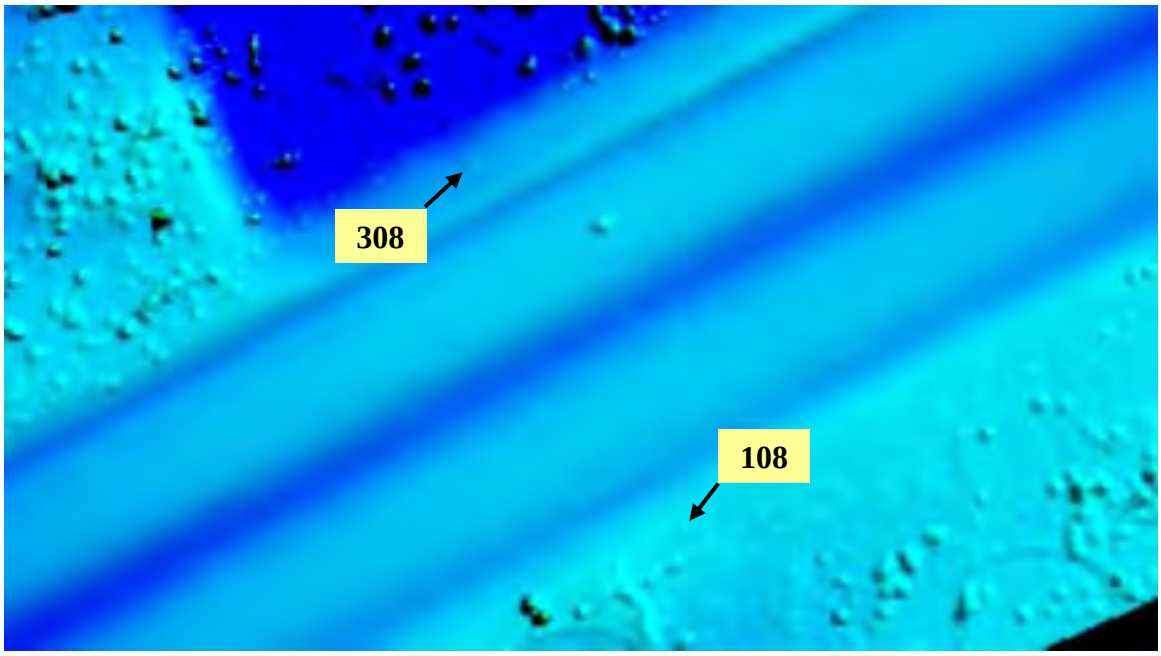

Figure 4. Targets in LiDAR data.

Target identification based on elevation and intensity data

To check the absolute accuracy of the LiDAR data, the targets are used as control points. The targets must be identified in the LiDAR strips based on their known coordinates (determined by GPS) and their expected maximum error in the data. After finding the approximate locations, a robust method, combining both the elevation and intensity information of the LiDAR points, selects the points falling on the target surface. As discussed in the target design section above, the targets have a two-concentric circle design with two different coatings resulting in significantly different intensity values of the LiDAR points on the inner circle and on the outer circle. This target design greatly facilitates the very accurate horizontal position determination of the targets in the LiDAR data by using our Hough-transform based method (Csanyi and Toth, 2004).

Figure 5 illustrates the elevation data (a) and the intensity data (b) of a 3 m by 3 m area around target #108 in strip #1 in. For better visualization, the elevation and intensity values of the LiDAR points are interpolated to grid, and they are shown in grey-scale by elevation and intensity values, respectively. The LiDAR points on the target are well distinguishable from the ground in both the elevation and intensity data and the intensity information nicely separates the target points on the inner circle (white coating) and outer circle (black coating).

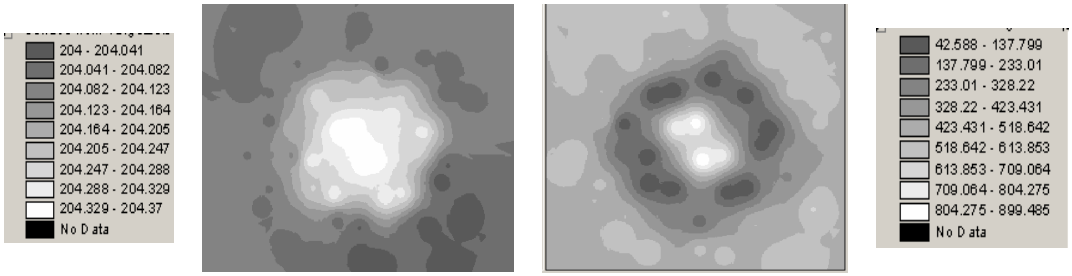

(a) (b)

Figure 5. LiDAR target in elevation (a) and intensity data (b).

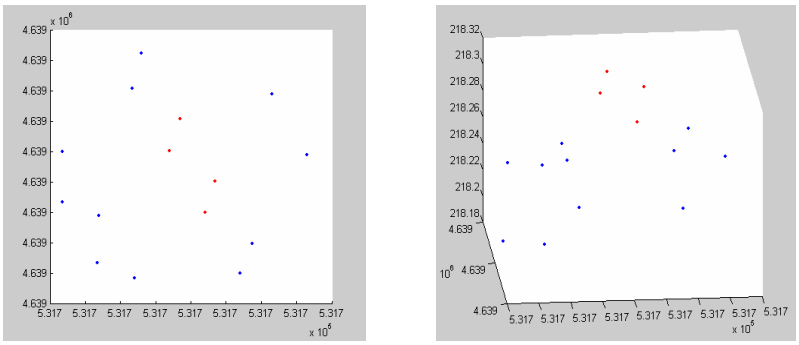

(a) (b)

Figure 6. LiDAR elevation data of target #310, top view (a) and perspective view (b).

It is interesting to mention that a few cm elevation differences between target points in the inner circle with white coating and the outer ring with black coating was noticeable in the elevation data of the target points as illustrated in Figure 6. This phenomenon does not affect the results of the investigations here but definitely requires further attention.

Table 3 contains the coordinate errors at the target locations in strip #1 and strip #2, respectively. The coordinate errors are the differences between the computed target coordinates from the LiDAR strip and their known coordinates (GPS measurements). The standard deviations of the coordinate errors are also shown in Table 3. These standard deviation values shown in the table describe the standard deviations of the computed LiDAR target center locations (provided by the target identification algorithm). The horizontal position determination accuracies for all targets are within 10 cm; that is in good correspondence with our earlier simulation results. In fact, these values can be considered as an absolute measure, as the horizontal accuracy of the GPS surveyed coordinates is almost negligible to them. The elevation accuracy of the determined target position is calculated based on the standard deviation of the vertical coordinate of the LiDAR points and the number of points falling on the target. The area of the target circle is π m (radius=1 m), and the average point density of the test data is about 5 points/m^2, thus about 15-16 points fall on each target. The vertical standard deviation provided by the ALTM 30/70 system is about 10 cm; therefore, the accuracy of the determined vertical target position is about $10/\sqrt{15}$, ~2.5 cm. This value is close to the vertical accuracy of the GPS survey of the targets.

Target #	Coordinate errors [m]			Standard deviation [m]		
	Easting	Northing	Elevation	Easting	Northing	Elevation
108	0.06	-0.07	-0.051	0.08	0.08	0.025
308	-0.04	-0.01	-0.089	0.04	0.03	0.025
109	0.13	-0.00	-0.060	0.06	0.08	0.025
309	0.03	-0.01	-0.082	0.05	0.07	0.025
110	0.03	0.08	-0.035	0.05	0.05	0.025
310	-0.01	-0.11	-0.053	0.03	0.05	0.025
307	-0.01	0.03	-0.185	0.07	0.08	0.025
Mean	0.03	-0.02	-0.079	0.05	0.06	0.025

(a)

Target #	Coordinate errors [m]			Standard deviation [m]		
	Easting	Northing	Elevation	Easting	Northing	Elevation
107	0.03	0.08	-0.112	0.03	0.05	0.025
108	0.01	-0.03	-0.144	0.04	0.05	0.025
109	-0.05	0.07	-0.153	0.02	0.01	0.025
110	-0.07	-0.01	-0.104	0.04	0.06	0.025
310	0.03	0.16	-0.139	0.08	0.07	0.025
Mean	-0.01	0.05	-0.130	0.04	0.05	0.025

(b)

Table 3. Target coordinate errors in strip #1 (a) and strip #2 (b).

Figure 7 illustrates target #109 in the two overlapping strips clearly showing a discrepancy between the two strips processed without the targets.

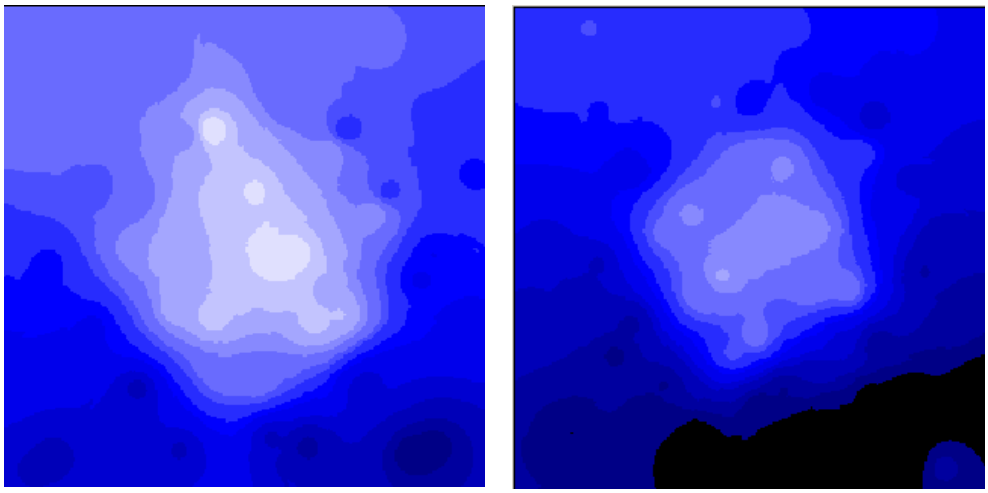

(a) (b)

Figure 7. Target #109 in strip #1 (a) and strip #2 (b).

The measured coordinate errors in Table 3 clearly show a vertical error in both strips. In general, the target coordinates fall below the GPS determined target elevations. In the case of strip #2 the vertical coordinate error is even more significant, about 15 cm. The determined horizontal coordinate errors, however, are not significant; for a couple of targets the error is within the horizontal target coordinate determination accuracy. There are only a few targets where the horizontal errors are significant. The measured coordinate errors show that the LiDAR data is of good quality, but based on the targets the accuracy can be improved, especially the vertical accuracy, where the biggest errors were detected. Therefore, a three-dimensional similarity transformation was separately applied to both strips based on the measured target positions in the LiDAR strips and their known, GPS-surveyed coordinates. Table 4 a and b lists the residual coordinate errors at the targets after the transformation was applied for strip #1 and #2, respectively.

Target #	Coordinate errors [m]		
	Easting	Northing	Elevation
307	0.06	-0.06	0.051
108	-0.04	0.00	0.004
308	0.12	0.02	0.010
109	0.03	0.01	-0.019
309	0.02	0.11	0.006
110	-0.02	-0.09	-0.021
310	0.00	0.03	-0.031

(a)

Target #	Coordinate errors [m]		
	Easting	Northing	Elevation
107	0.03	0.02	-0.002
108	0.02	-0.09	0.011
109	-0.03	0.00	-0.017
110	0.10	-0.08	0.004
310	0.06	0.07	0.003

(b)

Table 4. Residual coordinate errors at targets after transformation.

As expected, the horizontal coordinates did not improve much, since they were originally in the range of the horizontal coordinate determination accuracy (except for one or two points). However, the transformation significantly decreased the vertical coordinate errors and they are approximately in the range of the vertical accuracy of the determined target coordinates. This confirms that a similarity transformation, in general, is an adequate model to compensate for errors in this case.

To assess the spatial extent of the determined errors and the validity of the model, a conventional analysis was performed to see the impact of using only a subset of the controls in the transformation parameter determination. Therefore, two targets, #310 and #108, were selected from the available seven targets in strip#1, and one target, #109, was selected from strip #2. The transformation parameters for the strips were recomputed without including these targets in the adjustment. Then, the excluded targets were used as check points to assess the LiDAR data accuracy improvement at these locations. The targets used as check points were selected so that the remaining targets used in the adjustment had good spatial distribution. In particular, the targets used did not lie close to one line – a dangerous configuration to calculate the transformation parameters. The residual coordinate errors after the transformation for both strips are shown in Table 5 a and b, respectively.

Target #	Coordinate errors [m]		
	Easting	Northing	Elevation
307	0.04	-0.05	0.054
108	-0.06	0.00	0.005
308	0.12	0.02	0.012
109	0.03	0.01	-0.016
309	0.02	0.11	0.009
110	-0.02	-0.08	-0.019
310	-0.04	0.03	-0.028

(a)

Target #	Coordinate errors [m]		
	Easting	Northing	Elevation
107	0.01	0.03	-0.003
108	-0.03	-0.07	0.006
109	-0.09	0.03	-0.022
110	0.02	-0.04	0.001
310	-0.02	0.11	-0.003

(b)

Table 5. Residual coordinate errors at target locations.

As shown by the residual errors, the transformation decreased the errors at the check points, indicating that the transformation parameters provide a valid model for the whole strip. Nevertheless, in some cases it may be necessary to segment the LiDAR strips to smaller segments and determine transformation parameters separately for each segment in order to compensate for the different natures and amplitudes of the errors in the different parts of the strip. Obviously, it is desirable to have LiDAR targets placed not too far from each other and well distributed spatially to ensure that the transformation based on the targets indeed improves the LiDAR data accuracy.

Impact of the correction on road surface extraction

The ultimate goal of applying the specifically designed LiDAR targets is to improve the accuracy of the LiDAR data, which in our case is to obtain the most accurate road surface data possible. To analyze the impact of using LiDAR targets, a reasonable approach is to select road surface locations from two overlapping strips and then check their discrepancies before and after the target-based correction is applied. Therefore, two 5 by 5 m road surface areas were selected from the overlapping area of the two strips; one was in the vicinity of target #109 (denoted area #1) and the other one was halfway between target #110 and #310 (denoted area #2). Since ground truth surface was not available to assess the achievable accuracy improvement, the elevation differences between the road surface patches in the two overlapping strips were

checked before and after applying the three-dimensional similarity transformation for both strips separately. Figure 7 a and b illustrates area #1 in strip #1 and strip #2 before and after the similarity transformation was applied. Similarly, Figure 8 a and b illustrate the case for area #2; in both cases, strip #1 is shown in white and strip #2 is green.

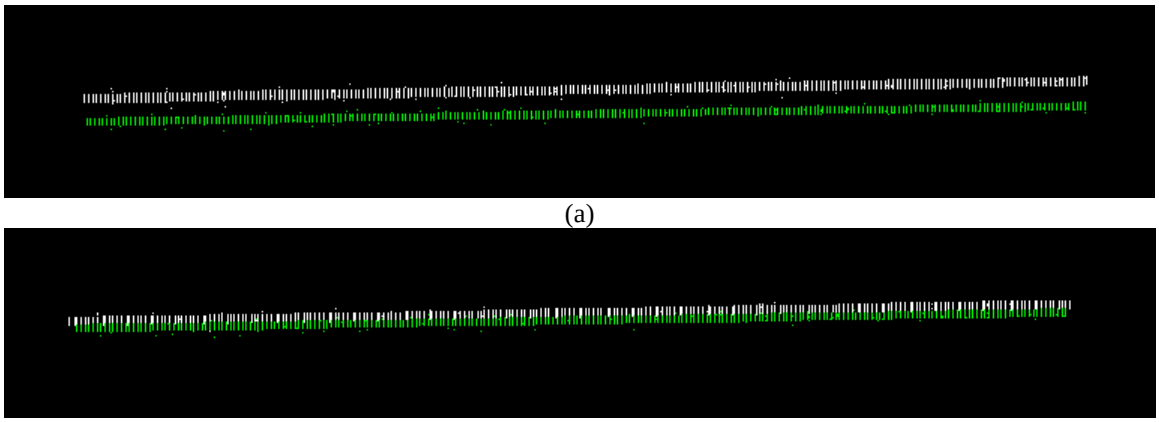

(a)

(b)

Figure 7. Elevation difference at road area #1 in the two strips before (a) and after (b) transformation.

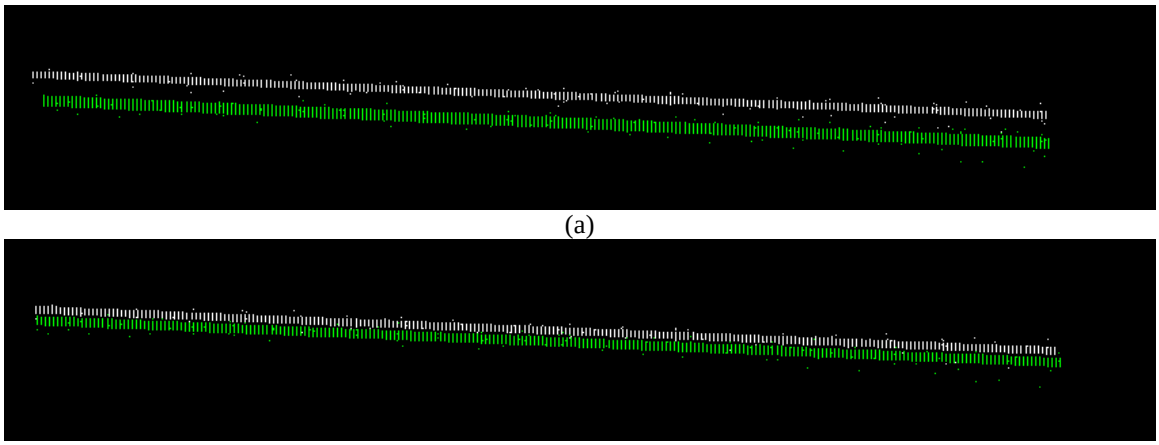

(a)

(b)

Figure 8. Elevation difference at road area #2 in the two strips before (a) and after (b) transformation.

Table 6 shows the elevation differences between the two strips at the selected two road areas before and after applying the similarity transformation to the LiDAR strips separately. The elevation difference was determined by fitting a plane to the data.

Road area	Elevation difference [m]	
	Before	After
#1	-0.127	-0.038
#2	-0.141	-0.056

Table 6. Elevation differences between the two strips at the selected road areas.

As Figures 7 and 8, and Table 6 clearly illustrate, after applying the transformation, based on the LiDAR targets, the accuracy improvement of the LiDAR data is significant. For both areas a similar magnitude of improvement was found; the original 13-14 cm elevation difference of the road surface decreased to the 3-5 cm level, which is in the range of the combined error budget of the control determination accuracy and laser ranging error.

CONCLUSIONS

Our test results showed that the specifically designed LiDAR targets are indeed useful in improving the accuracy of road surface extraction and other applications that require engineering scale mapping accuracy. Modeling the road surface with a plane, the vertical accuracy of the road was estimated at the 3-5 cm level, which is more or less the possible lower limit, as the combined error budget of the controls and laser ranging is in that range. To maintain this extremely high accuracy, a dense and well-distributed network of controls is needed. The tests also confirmed that the target design had fulfilled the expectations; the targets were automatically extracted and our combined elevation and intensity data-based algorithm facilitated improved coordinates. In summary, the use of LiDAR specific ground control is ready for normal mapping operations, although the cost of installing and surveying the targets is probably only affordable for applications requiring the highest accuracy.

ACKNOWLEDGEMENT

The authors would like to thank the Ohio Department of Transportation for the manufacturing the targets and flying LiDAR surveys to acquire essential data for this research.

REFERENCES

Baltsavias, E.P. (1999). Airborne laser scanning: basic relations and formulas. ISPRS Journal of Photogrammetry & Remote Sensing Vol. 54, pp. 199-214.

Burman, H. (2000). Adjustment of Laser Scanner Data for Correction of Orientation Errors. *International Archives of Photogrammetry and Remote Sensing*, Vol. XXXIII, Part B3, pp. 125-132.

Crombaghs, M. J.E.,R. Brügelmann, E.J. de Min, 2000. On the adjustment of overlapping strips of laseraltimeter height data. *International Archives of Photogrammetry and Remote Sensing*, Vol. XXXIII, Part B3/1, pp. 224-231.

Csanyi N, Toth C., 2004. On Using LiDAR Specific Ground Targets, ASPRS Annual Conference, Denver, CO, May 23-28, CD-ROM.

Filin, S. (2001). Recovery of Systematic Biasaes in Laser Altimeters Using Natural Surfaces. *International Archives of Photogrammetry and Remote Sensing*, Vol. XXXIV, Part 3/W4, pp. 85-91.

Kilian J., Haala, N., Englich, M. (1996). Capture and Evaluation of Airborne Laser Scanner Data. *International Archives of Photogrammetry and Remote Sensing*, Vol. XXXI, Part B3, pp. 383-388.

Toth C., Csanyi N. and Grejner-Brzezinska D. 2002. Automating the Calibration of Airborne Multisensor Imaging Systems, *Proc. ACSM-ASPRS Annual Conference, Washington, DC, April 19-26, CD ROM*.

ON USING LiDAR SPECIFIC GROUND TARGETS

Nora Csanyi[1]
Charles K. Toth[2]
Department of Civil and Environmental Engineering and Geodetic Science[1]
Center for Mapping[2]
The Ohio State University
1216 Kinnear Road, Columbus OH 43212-1154
E-mail: nora@cfm.ohio-state.edu

ABSTRACT

LiDAR technology has seen enormous developments in recent years, and became the primary tool for surface data acquisition. Since LiDAR is a complex multi-sensory system, the whole system has to be carefully calibrated to achieve the highest accuracy of the measured surface points. System calibration includes the calibration of individual sensors as well as the determination of the spatial relationship between different sensors. The calibration process has certain limitations; even after careful calibration some errors in the collected data can be experienced. Most of the systematic errors can be corrected by strip adjustment based on the observed discrepancies between overlapping strips. However, eliminating the discrepancies between the strips does not necessarily provide an absolute check of the data; even if the different strips fit together, there can be absolute error in the data. Applications, demanding high accuracy require the elimination of these remaining errors. The introduction of ground control targets specifically designed for LiDAR can further improve the accuracy of the point cloud in both relative and absolute terms. Once the control targets are identified and their positions are determined in the data either a simple vertical offset or a more complex transformation can be applied to the point cloud to reduce the errors in it. This paper investigates the potential of using control targets for LiDAR data refinement. In particular, the achievable point accuracy using LiDAR-specific ground control targets is studied. The optimal design, size and signal response of the target is also discussed.

INTRODUCTION

In the last few years LiDAR technology has became the preferred method for surface data acquisition. A broad range of applications exists and new applications are emerging, including forestry management, mapping of urban areas, flood and risk assessment, corridor mapping, etc., all requiring high accuracy LiDAR data. LiDAR systems are complex multi-sensory systems and incorporate three main sensors, GPS and INS navigation sensors, and the laser-scanning device. The high complexity of the system results in a lot of possible error sources that can degrade the accuracy of the acquired LiDAR data. Most of the systematic errors can be corrected by strip adjustment, eliminating the discrepancies between overlapping strips, however many times absolute errors remain in the data, such as height offsets or more complex errors. Applications demanding the highest accuracy require the elimination of the remaining errors, which cannot be usually achieved without well-identifiable ground control targets in the surveyed area. This paper investigates the potential of using ground control targets specifically designed for LiDAR data. The first two sections provide a brief overview of the error budget of laser scanning and the correction possibilities; special attention is given to the typically used control information, then the optimal target design is addressed. Finally, test results are presented – how the designed ground targets could improve the final LiDAR data accuracy.

ERROR BUDGET FOR LASER SCANNING

Baltsavias (1999) presents an overview of basic relations and error formulas concerning airborne laser scanning and a large number of publications report on the existence of systematic errors. The errors in laser scanning data can be a result of individual sensor calibration or measurement errors, a lack of

synchronization or a misalignment between the different sensors; the error sources can be categorized into four main groups:

- Sensor platform position and attitude errors (navigation solution)
- Sensor calibration errors
- Inter-sensor calibration errors
- Miscellaneous errors

Any of the above error sources translates to an error in the measured ground point coordinates, see Figure 1.

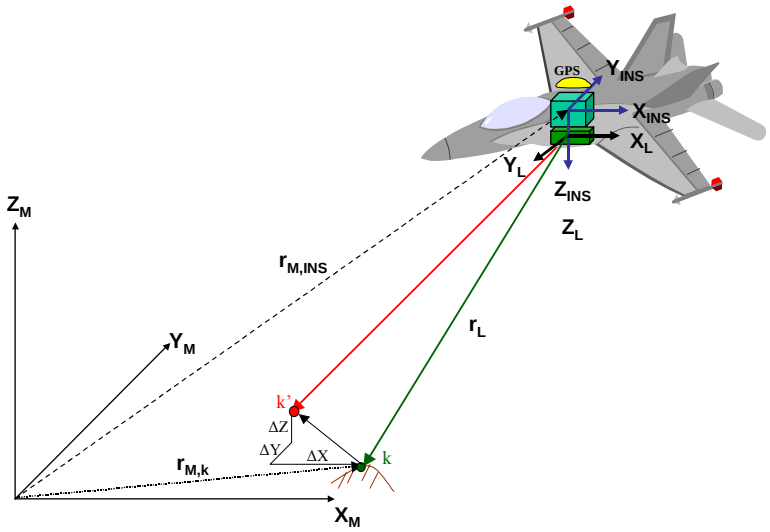

Figure 1. LiDAR system components

Sensor platform position and attitude errors are GPS/ IMU related errors. Positioning error is caused by errors related to the GPS measurements, which can be caused by atmospheric delay, cycle slip, and erroneous ambiguity resolution. Positioning errors are directly transferred to the ground coordinates of the measured points. Under normal conditions with differential GPS and post-processing, 10-15 cm positioning accuracy at 90% CEP can be expected. The attitude angles (the rotations of the aircraft) are measured by IMU, which consists of accelerometers and gyros, which are affected by time dependent drift. The accuracy of the determined aircraft attitude depends on the quality and frequency of the IMU and the combined GPS/IMU post-processing method (Kalman filtering).

Sensor calibration errors include scan angle error, range measurement error and other errors related to the movement of the rotating mirror. Scan angle error causes the sides of the measured strip to bend up or down, and therefore, it is often called smiley error. The contribution of the range measurement error to the coordinate errors is the less significant among the major error sources; however, the relative importance of this error in the total error budget is increasing with lower flying heights. Depending on the laser scanning system performance, the range measurement accuracy is a few cm. This is an important parameter to assess the maximum achievable point accuracy that can be expected from a LiDAR system if the major systematic errors are eliminated.

Inter-sensor calibration errors are errors in the measured level arms between the three sensors (GPS, IMU and laser sensors) and any angular misalignments between the IMU and laser sensors, called the boresight misalignment. The angular misalignments are the more critical error sources since any angular inaccuracy, unlike linear offsets, is amplified by the flying height of the aircraft, and therefore, a small angular error can have significant effect on LiDAR point accuracy. The effect of errors in the level arms are usually not more than a few cm, while coordinate errors caused by boresight misalignment could reach meter or even 10 meter level depending on the flying height.

CORRECTION OF LASER SCANNER DATA

The various errors can cause a misfit between measured LiDAR surface and the true surface or a difference between surfaces obtained from sevaral LiDAR strips covering the same area. Figure 2 illustrates this phenomenon.

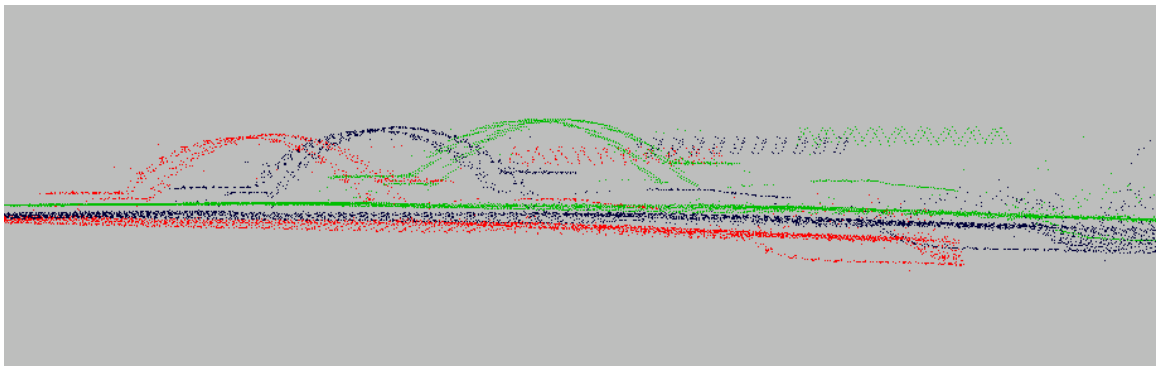

Figure 2. Discrepancies between overlapping strips.

LiDAR data need to be corrected for the systematic errors, for instance by corrections from overlapping strips, in order to get an accurate model of the terrain surface. In the last few years different solutions have been developed that are all based on the observed discrepancies between different overlapping LiDAR strips. All these solutions are some kind of strip adjustments – they try to eliminate the discrepancies between matched surface patches of the overlapping strips. The solution for dealing with and eliminating the effect of systematic errors can be categorized into two groups. One approach is based on the introduction of a correction transformation of the laser points to minimize the difference between the corresponding LiDAR patches. This type of solution does not deal with the sources of the errors; it only eliminates their effect (Kilian *et al.*, 1996; Crombaghs *et al.*, 2000)). The disadvantage of this type of solution is that some non-linear effects, such as smiley error are not properly modeled. The other technique attempts to rigorously model the system to recover the systematic errors. This method assumes the knowledge of the flight trajectory. The main difficulty of this approach is the variety of the potential error sources and that some of the error sources have similar effect and are not separable (Burman, 2000; Filin, 2001, Toth *et al.*, 2002).

All of the above strip adjustment methods are based on the observed vertical or three-dimensional discrepancies between the overlapping LiDAR strips. Systematic planimetric errors are often much larger than height errors of the LiDAR data, and therefore, a three-dimensional strip adjustment is the desirable solution. Some of the strip adjustment methods work only with tie points, without any ground control information, however the use of some type of ground control is desirable, since eliminating the relative discrepancies between overlapping strips does not provide an absolute check of the dataset. Ground control information can be used in the strip adjustment process or after strip adjustment to correct the remaining absolute errors in the corrected strips. For example, known roof structures or corners of buildings could be used as ground control; unfortunately this type of control information is not always available. Furthermore, due to the characteristics of laser data, the identification of distinct points of buildings and roof structures in LiDAR data can result in a biased position, which could affect the accuracy of the corrected LiDAR data. Many times after the strip adjustment, horizontal surface with known elevation is used to correct remaining vertical shifts in the data. However remaining absolute errors after strip adjustment can be more complex than just a vertical shift, therefore for applications with high accuracy requirements, such as corridor mapping well-identifiable ground control targets are necessary. Based on the above mentioned problems with offset determination, the desirable ground control targets to satisfy high accuracy requirements should be rotation invariant, so the scan direction does not affect the accuracy of the determined position of the targets in LiDAR data. The targets should also have a well-defined shape that facilitates the accurate determination of their three-dimensional position in the laser data (model-based determination).

In the next section the optimal target design for LiDAR data is discussed and the achievable accuracies are analyzed.

TARGET DESIGN

If an optimal target design is sought, the objective is that the target has to be easily identifiable (preferable automatically), distinguishable from surrounding objects in LiDAR data and its horizontal and vertical position should be accurately measurable. The target design includes the determination of the optimal target shape, target size, coating pattern and algorithms to accurately determine the planimetric and vertical position of targets in LiDAR data.

In photogrammetry, the usual ground controls are road intersections, signalized targets and other well-identifiable structured objects or marks. Due to the different characteristics of LiDAR data, obviously, this type of ground control design is not appropriate for LiDAR targets. Because of the different possible scan directions and different point densities in different directions, the optimal LiDAR target should be rotation invariant, i.e., circle-shaped target. In order to reliably and automatically identify LiDAR points reflected from the target, the target should have a certain height with respect to its surrounding, so that it is elevated from the ground. Since newer LiDAR systems are capable of measuring intensity data, the target should have a coating that results in substantially different reflectance than its surrounding, which could also help the target identification. This target design facilitates the automatic target identification in LiDAR data based on their known position and the expected maximum errors in the data.

Once the points on the target circle are found based on the elevation or intensity data, the horizontal and vertical position of the origin can be determined by separate algorithms. Figure 3 illustrates the circle-fitting problem once the points on the circle are found.

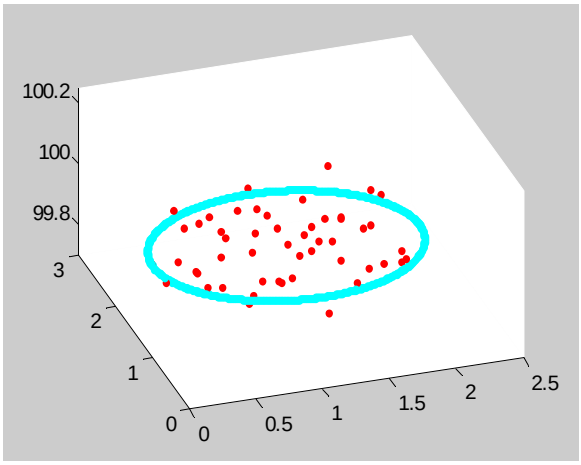

Figure 3. Circle fitting problem

To accurately determine the vertical position of the target, the optimal solution is to have a flat horizontal target surface, thus the vertical position of the target can be determined by fitting a horizontal plane to the points fallen on the target, which is basically the averaging of the elevations of the target points. The accuracy of the determined target height can be determined by error propagation based on the standard deviation of the vertical coordinates of the LiDAR points: σ vertical pos= σ z $/\sqrt{n}$, where n is the number of points on the target.

Once the points on the circle are found, the circle-fitting algorithm to accurately determine the planimetric position of the target circle is similar to the Hough-transform. The search is based on the known radius of the circle; it finds all the possible locations of the target circle in a grid. Looking at a LiDAR point lying somewhere on the circle, it is known that the origin of the circle must be somewhere within the circle drawn around the LiDAR point as origin with the known radius. Considering a second LiDAR point, the origin is somewhere in the intersection region of the two circles around the two LiDAR points, and so forth. An accumulator array is created with zero values; and then a point-by-point process will increment the grid cells under the circle with the origin of the LiDAR point. This is done for all the points lying on the target. The cells with the highest value give all the possible positions of the target origin. The center of gravity of these cells is accepted as the origin of the circle. Figure 4 illustrates the accumulator array and the fitted circle on an example at 50*50 cm LiDAR point density. The green patch shows the possible circle origin locations and the blue circles are all the possible locations of the target circle.

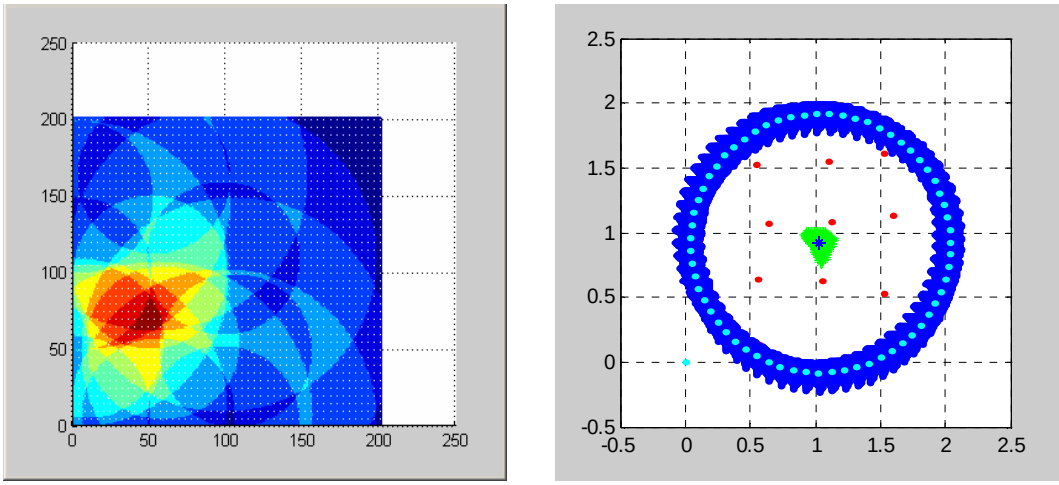

Figure 4. Accumulator array and fitted circle

Since the proposed LiDAR specific targets are mobile targets, and thus, are placed on the ground before flight, for economical reasons their size should be as small as possible. However, bigger target size means more points lying on the target, which results in better accuracy of the determined target position. Therefore to determine the optimal target size and coating pattern, extensive simulations were carried out. LiDAR points lying on the target circle were simulated in the case of different assumed circle radii and different coating patterns, such as one or two-concentric-circle design with different signal response coating. In the case of the two-concentric-circle design, the inner and outer circles have different signal responses, therefore, points on the outer ring and on the inside circle could be differentiated based on their intensity values. The achievable accuracy of the determined offsets mainly depends on the LiDAR point density with respect to the target size and, of course, on the LiDAR footprint size and the standard deviation of the elevation. Therefore, the simulations were carried out with three different point densities, 0.25*0.25, 0.50*0.50, 0.75*0.75 m and LiDAR points were simulated according to their planimetric and vertical accuracy and distribution. Noise was given to the vertical coordinates according to normal distribution with 0.05m standard deviation, while planimetric coordinates were disturbed by a noise with 0.25 m standard deviation. In the latter case, uniform distribution was assumed since the horizontal accuracy mainly depends on the footprint. Since the accuracy of the determined target position depends a lot on the actual point distribution on the target circle, whether there are points near the sides of the circle or not, to assess the achievable accuracy of the determined target position in LiDAR data, points were simulated several times and RMS (root mean square error) was calculated.

Based on the simulation results with different target designs, the major findings are the following: As expected, the larger the size the better the positioning accuracy, however the results have shown that from about 5 points per m² point density, a 1m circle radius can already provide sufficient accuracy and further increasing the target size will not lead to significant improvements. The two-concentric-circle design means

significant improvement in the determined accuracy since it provides additional geometric constraint in contrast to the one-circle design. The two concentric circles (the inner has half the radius of the outer circle) should have different coating to produce a substantial difference in reflection signal in order to differentiate them in intensity data.

The achievable positioning accuracies at the optimal target design in the case of different point densities are shown in Table 1.

LiDAR point density [m]	Accuracy of horizontal position of target circle [cm]	Accuracy of vertical position of target circle [cm]
0.25*0.25	2-3	0.7
0.50*0.50	5-10	1.4
0.75*0.75	10-15	2.2

Table 1. Achievable positioning accuracies

CORRECTION POSSIBILITIES USING GROUND CONTROL TARGETS

Ground control targets in LiDAR data can be used in the strip adjustment procedure or after strip adjustment to correct remaining height offset or to apply a more complex, three-dimensional transformation to account for remaining vertical and planimetric offsets in the dataset. The applied transformation depends on the characteristics of the remaining errors and the number of available targets in the dataset. If only one or two ground targets are available in the dataset, a simple vertical offset correction can be performed. If three or more targets are available, 3-dimensional similarity or more complex transformation can be applied on the data to correct remaining absolute errors. Correction can be performed by strip or in more complex case strips can be subdivided into segments and each segment can have different correction parameters.

TEST RESULTS

Based on the simulation results for optimal target design, targets were fabricated. The test data was acquired by the Optech ALTM 30/70 LiDAR system of the Ohio Department of Transportation in Northeast Ohio. The data was collected from an altitude of about 850 m with 16-degree field of view (8.0 half angle), at 70 Hz scanner frequency and 70 KHz pulse rate, which resulted in a point density of 5 points/m². The map of the test area with the targets is shown in Figure 5. As the objective was to accurately model road surfaces, six targets were placed along State Route 11 for initial testing of the designed LiDAR targets. The first strip was flown from north to south direction along the road and then two cross strips were done in the east-west direction; strips are shown on the map.

The data was processed in the usual way without using the LiDAR targets. Then the differences between known and measured target coordinates in the processed dataset were determined. Figure 6 illustrates target #106 in the two overlapping strips in front view (1st and 2nd strips). Note the observable difference between the two strips after processing; clearly indicating some remaining error in the data.

Figure 5. Test area with ground control targets

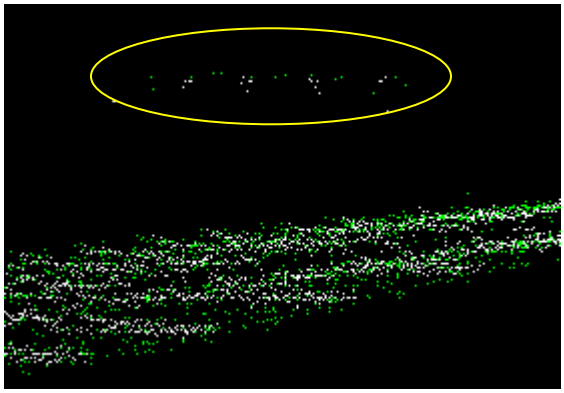

Figure 6. Target #106 in strips #1 and strip #2

The known and determined (by our algorithm) coordinates of the targets in strip #1 are shown in Table 2a. For better readability, coordinate errors at the target circles are also shown in Table 2b. The tables do not contain target #102 since accidentally the LiDAR strip did not cover this target, the LiDAR survey ended just few meters away that point. The flight was performed on January 29th, 2004 and unfortunately, the flight conditions were less than ideal; the ground was covered by deep snow. The targets were easily found in the data by elevation difference based on their known locations and the maximum expected error. Due to the snow cover, points on the inner and outer circle could not be differentiated based on the intensity data, therefore circle origins were located based on only the known outer 1m circle radius, which provides less accurate position. Figure 7 illustrates how targets #105 and #106 appeared in the elevation data in strip #1. For better visualization, the LiDAR surface was interpolated to a grid and the image was color coded by elevation.

Figure 7. LiDAR targets #105 and #106 in the elevation data

The accuracy of the determined horizontal target positions is about 10 cm, while the vertical accuracy is about 2 cm. Comparing the known and measured target positions in the LiDAR data, 20-30 cm horizontal errors and 10-15 cm vertical errors were found in the processed dataset.

Target #	Known coordinates [m]			Measured coordinates [m]		
	Easting	Northing	Elevation	Easting	Northing	Elevation
101	523843.98	4605822.60	291.065	523844.19	4605822.79	290.944
103	523829.27	4606449.44	289.362	523829.50	4606449.66	289.188
104	523910.25	4606492.86	288.534	523910.53	4606493.00	288.415
105	523842.52	4606796.61	288.804	523842.78	4606796.78	288.631
106	523913.70	4606791.64	289.094	523914.00	4606791.84	288.977

Table 2a. Known and measured target coordinates in strip #1

Target #	Coordinate errors [m]		
	Easting	Northing	Elevation
101	0.21	0.19	-0.12
103	0.23	0.22	-0.17
104	0.28	0.14	-0.12
105	0.26	0.17	-0.17
106	0.30	0.20	-0.12

Table 2b. Coordinate errors at target locations in strip #1

To improve the accuracy of the LiDAR data, a three-dimensional similarity transformation was performed on strip #1 based on the known and measured target positions. Since ground truth of the test area was not available, the transformation was performed based on targets #101, #105, and #106; then targets #103 and #104 were used as check points after the adjustment to assess the accuracy improvements of the LiDAR strip. Table 3 lists the residual coordinate errors in the dataset at the three target locations used in forming the similarity transformation as well as the remaining coordinate errors at targets #103 and #104 used as check points after applying the three-dimensional similarity transformation.

Target #	Coordinate errors [m]		
	Easting	Northing	Elevation
101	-0.01	-0.03	0.00
103	-0.02	0.03	0.01
104	0.02	-0.11	-0.03
105	-0.02	0.10	0.02
106	0.02	-0.06	-0.02

Table 3. Remaining errors after three-dimensional similarity transformation based on target # 101, #105, and #106.

Comparing the target positions with their positions in the original dataset processed without the LiDAR targets, the accuracy improvement is obvious. The residual horizontal coordinate errors at the three targets included in the three-dimensional similarity transformation are 5-10 cm, and the vertical residuals are 1-2 cm, which is within the accuracy of the determined target positions. At the two check points, the originally 20-30 cm horizontal errors of targets #103 and #104 have significantly decreased to about 10 cm, which is within the accuracy of the determined horizontal target positions. The improvement of the vertical coordinate accuracy is even more, the original 10-15 vertical errors were reduced to 1-2 cm, which is also within the accuracy of the determined vertical target positions. These results indicate that the overall coordinate accuracy of the strip increased significantly using the LiDAR specific targets.

CONCLUSIONS

This paper investigated the potential of using control targets for improving LiDAR data accuracy. Optimal target design customized for LiDAR data was developed based on simulation results. The target design includes the determination of the optimal target shape, target size and coating pattern as well as algorithms to accurately determine the target origins in LiDAR data. Based on the simulation results, targets were fabricated and an initial test flight was carried out to check the achievable improvement in the data accuracy using the designed targets. The test flight conditions, however, were less than ideal as snow cover made the identification and determination of the target positions in the dataset difficult. The test results showed that the use of the LiDAR-specific targets can significantly improve the accuracy of the final LiDAR product.

ACKNOWLEDGEMENT

The authors would like to thank the Ohio Department of Transportation and Optech International for the measurements of the target locations and providing the LiDAR data for this research.

REFERENCES

Baltsavias, E.P. (1999). Airborne laser scanning: basic relations and formulas. *ISPRS Journal of Photogrammetry & Remote Sensing* 54, pp. 199-214.

Burman, H. (2000). Adjustment of Laser Scanner Data for Correction of Orientation Errors. *International Archives of Photogrammetry and Remote Sensing*, Vol. XXXIII, Part B3, pp. 125-132.

Crombaghs, M. J.E.,R. Brügelmann, E.J. de Min, 2000. On the adjustment of overlapping strips of laseraltimeter height data. *International Archives of Photogrammetry and Remote Sensing,* Vol. XXXIII, Part B3/1, pp. 224-231.

Cramer, M., Stallmann, D., Haala, N. (2000). Direct Georeferencing Using GPS/Inertial Exterior Orientations For Photogrammetric Applications. *International Archives of Photogrammetry and Remote Sensing*, Vol. XXXI, Part B3, pp. 198-205.

Filin, S. (2001). Recovery of Systematic Biasaes in Laser Altimeters Using Natural Surfaces. *International Archives of Photogrammetry and Remote Sensing*, Vol. XXXIV, Part 3/W4, pp. 85-91.

Kilian J., Haala, N., Englich, M. (1996). Capture and Evaluation of Airborne Laser Scanner Data. *International Archives of Photogrammetry and Remote Sensing*, Vol. XXXI, Part B3, pp. 383-388.

Toth C., Csanyi N. and Grejner-Brzezinska D. 2002. Automating the Calibration of Airborne Multisensor Imaging Systems, *Proc. ACSM-ASPRS Annual Conference, Washington, DC, April 19-26, CD ROM*.

Geo-Referenced Digital Data Acquisition and Processing System Using LIDAR Technology

Project Study on

Defining Optimal Targets for LIDAR Ground Control

Investigation of Vertical Shift Using Circular Targets

March 2003

An investigation, based on simulation was carried out for circular shaped LIDAR ground control targets. Compared to the previous study to the previous simulations with square-shaped target of different sizes, this simulation was limited to only one target size, 1.5 m radius circle. An additional assumption was that the target is leveled. As the sensor calibration was not addressed in the previous report, a short description of the boresight calibration is included.

In order to use ground control targets in LIDAR data for calibration purposes or as an absolute reference to apply additional translation after the LIDAR strip adjustment, they need to be identified and modeled reliably in LIDAR data. Considering the target size and the characteristics of any error in the LIDAR data, the vertical shift of all the LIDAR points reflected from the target will be the same (of course, there are random errors too) – the horizontal target should not become tilted in the LIDAR data. The following is a short description of the effect of the different errors in LIDAR data from the perspective of sensor calibration.

Influence of LIDAR boresight misalignment on accuracy of 3D object coordinates

To show the effect of the boresight misalignment angles a coordinate system definition is needed, see Figure 1. All the latter formulas of the effects of the three misalignment angles are valid in this system.

In order to analyze the effect of the different misalignment angles the following assumptions are made: the terrain is flat, scanning is performed in a vertical plane perpendicular to the flight direction and the flight line is horizontal (ω, φ=0), the κ rotation angle can have any value. x,y,z denotes a local right-handed coordinate system centered at the laser beam origin and X, Y, Z defines a right-handed object coordinate system, the origin of this system is at the nadir of the origin of the local coordinate system. The positive x-axis is in the flight direction. The misalignment errors $d\omega$, $d\varphi$ and $d\kappa$ refer to the respective axes of the local coordinate system. κ is the rotation from the X-axis to the x-axis. β is the scan angle, it has positive values for scans to the left of the flying direction, else negative. h denotes the flying height.

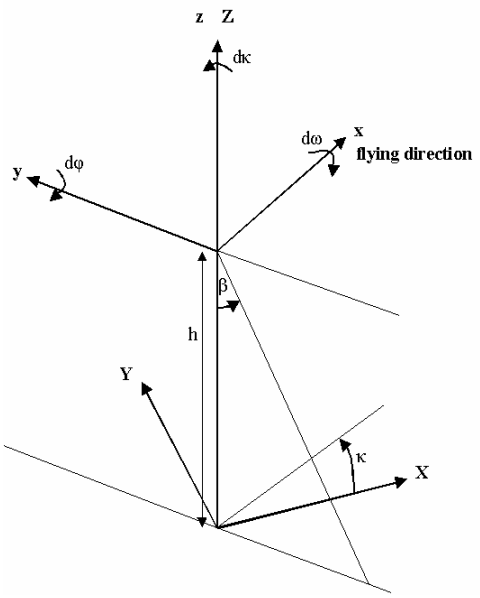

Figure 1. Coordinate system definition

Figure 2 illustrates the effect of the roll and pitch misalignment.

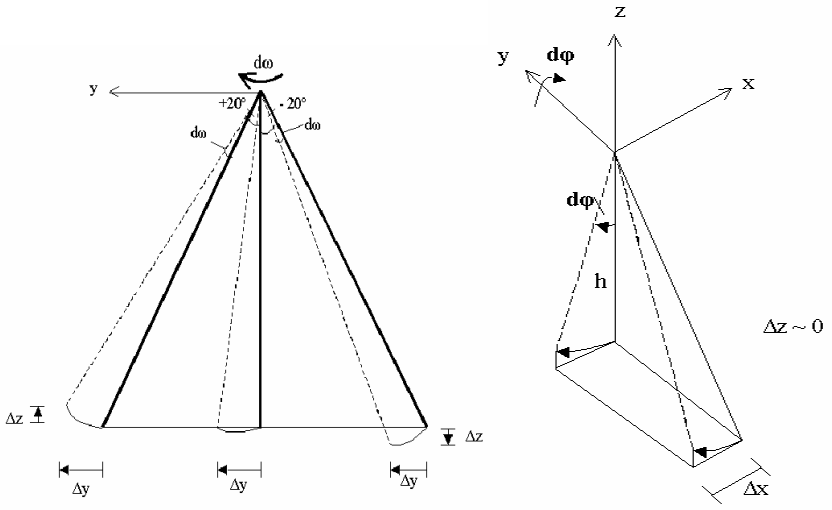

(a) (b)

Figure 2. Effect of roll (a) and pitch (b) misalignment

Roll misalignment causes a shift across the flying direction and a variable vertical shift. The surface becomes tilted, one side of the flying direction has vertical shift up, and the other side has vertical shift down. Under the flight line there is no vertical shift, farther from the flight line the shift is bigger. Roll misalignment has no effect in the flight direction. The formulas below show the coordinate errors caused by dω in the local and in the object coordinate systems.

$$\Delta x = 0$$
$$\Delta y = h[\sin(\beta + d\omega) - \sin(\beta)]/\cos(\beta) \sim h\sin(d\omega)$$
$$\Delta z = h[1 - \cos(\beta + d\omega)/\cos(\beta)] \sim h\Delta\omega\tan(\beta)$$

$$\Delta X = -\Delta y \sin\kappa$$
$$\Delta Y = \Delta y \cos\kappa$$

Table 1 contains the coordinate errors in the local coordinate system at different scan angles in the case of a 3' roll misalignment at 1000m flying height.

	+30°	+20°	+10°	0°	-10°	-20°	-30°
Δz [cm]	50	32	15	0	-15	-32	-50
Δy [cm]	87	87	87	87	87	87	87
Δx [cm]	0	0	0	0	0	0	0

Table 1. Coordinate errors caused by roll misalignment

Misalignment in pitch causes a constant shift along the flying direction; the vertical shift is negligibly small. dφ has no effect across the flying direction. The formulas below show the coordinate errors caused by pitch misalignment in the local and in the object coordinate systems.

$$\Delta x = -h\sin(d\varphi)$$
$$\Delta y = 0$$
$$\Delta z = h[1 - \cos(d\varphi)] \sim 0$$

$$\Delta X = \Delta x \cos(\kappa)$$
$$\Delta Y = \Delta x \sin(\kappa)$$

Table 2 contains the coordinate errors in the local coordinate system at different scan angles in the case of a 3' pitch misalignment at1000m flying height.

	+30°	+20°	+10°	0°	-10°	-20°	-30°
Δx [cm]	-87	-87	-87	-87	-87	-87	-87
Δy,Δz	0	0	0	0	0	0	0

Table 2. Coordinate errors caused by pitch misalignment

Figure 3 illustrates the effect of the heading misalignment.

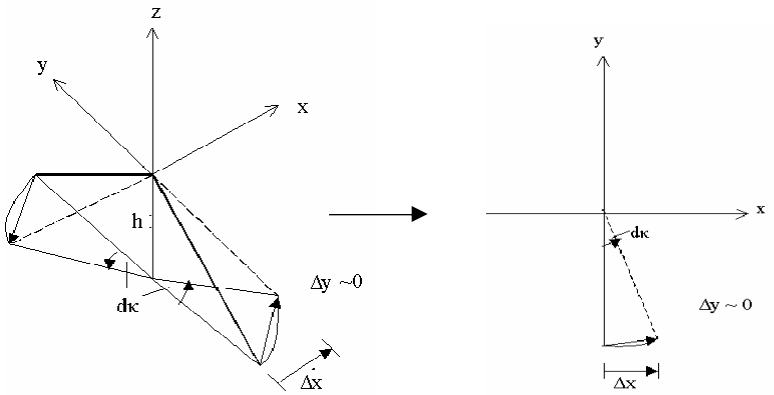

Figure 3. Effect of heading misalignment

Misalignment in heading causes a variable shift along the flying direction. Under the flight line there is no shift, the farther the LIDAR point from the flight line is, the bigger the coordinate error is. The two sides of the flight line have opposite shifts. The shift across the flying direction is negligibly small. This misalignment has no effect on the vertical coordinates. The effect of any heading misalignment on the calculated coordinates is much less than the effect of a same magnitude roll or pitch misalignment. Therefore heading misalignment is the most difficult one to determine, during data processing some companies just assume that heading misalignment is zero. The formulas below show the coordinate errors caused by dκ in the local and in the object coordinate system.

$$\Delta x = -h\tan(\beta)\sin(d\kappa)$$
$$\Delta y = h\tan(\beta)[\cos(d\kappa) - 1] \sim 0$$
$$\Delta z = 0$$

$$\Delta X = -h\tan(\beta)[\sin(\kappa + d\kappa) - \sin(\kappa)]$$
$$\Delta Y = h\tan(\beta)[\cos(\kappa + d\kappa) - \cos(\kappa)]$$

Table 3 contains the coordinate errors in the local coordinate system at different scan angles in the case of a +3' heading misalignment at 1000m flying height.

	+30°	+20°	+10°	0°	-10°	-20°	-30°
Δx [cm]	-50	-32	-15	0	15	32	50
Δy,Δz	0	0	0	0	0	0	0

Table 3. Coordinate errors caused by heading misalignment

Smiley error is the variable scan angle error. It causes the LIDAR strip tip up or down as we get farther from the nadir. It has similar effect to roll misalignment error except that this is symmetric to the flight line. Smiley error can be easily removed provided that the scanning system has been properly calibrated.

Finding vertical shifts in LIDAR data using circular targets

Considering the above described characteristics of the different errors, to model the circular targets in LIDAR data and finally to determine vertical shifts, an obvious approach is to fit a horizontal plane to the identified target points. Since the height of the target is known, the difference between this height and the height of the fitted plane provides the vertical shift of the LIDAR data at the surrounding of the target.

A simulation was carried out to analyze the achievable accuracy of the determined vertical shift in the case of different LIDAR point densities at different standard deviations of the horizontal and vertical coordinates of the measured LIDAR points. To assess the attainable accuracy, we did plane fitting to simulated LIDAR points lying on the target surface and calculated the RMS of the height of the fitted plane. Figure 4 illustrates an example of LIDAR points lying on the target circle at three different point densities (25*25, 50*50 and 75*75 cm). Table 4 shows the results at different point densities and standard deviations of the LIDAR points. This table also contains the maximum height difference between the target height and the height of the fitted plane to the LIDAR points lying on the target surface.

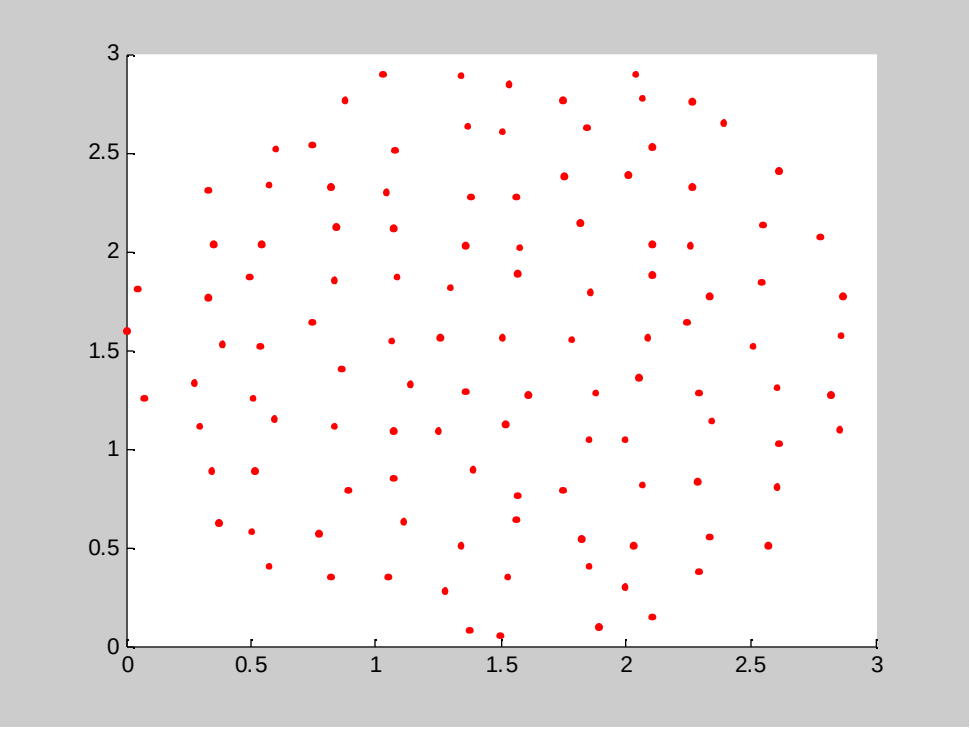

Sample LIDAR points of 0.25*0.25 m point density lying on the target circle

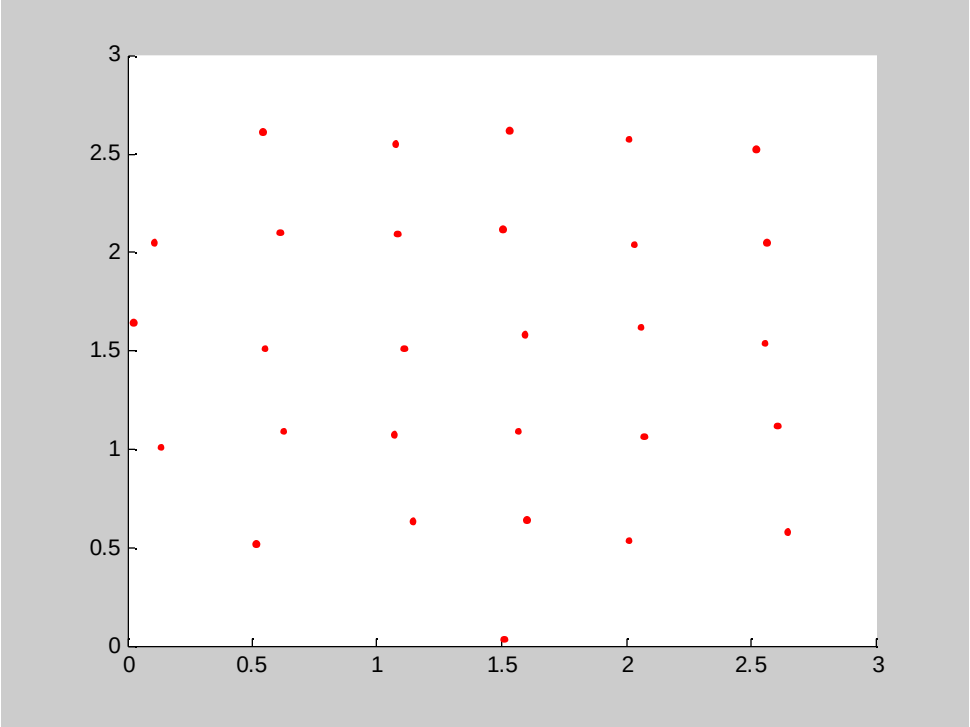

Sample LIDAR points of 0.50*0.50 m point density lying on the target circle

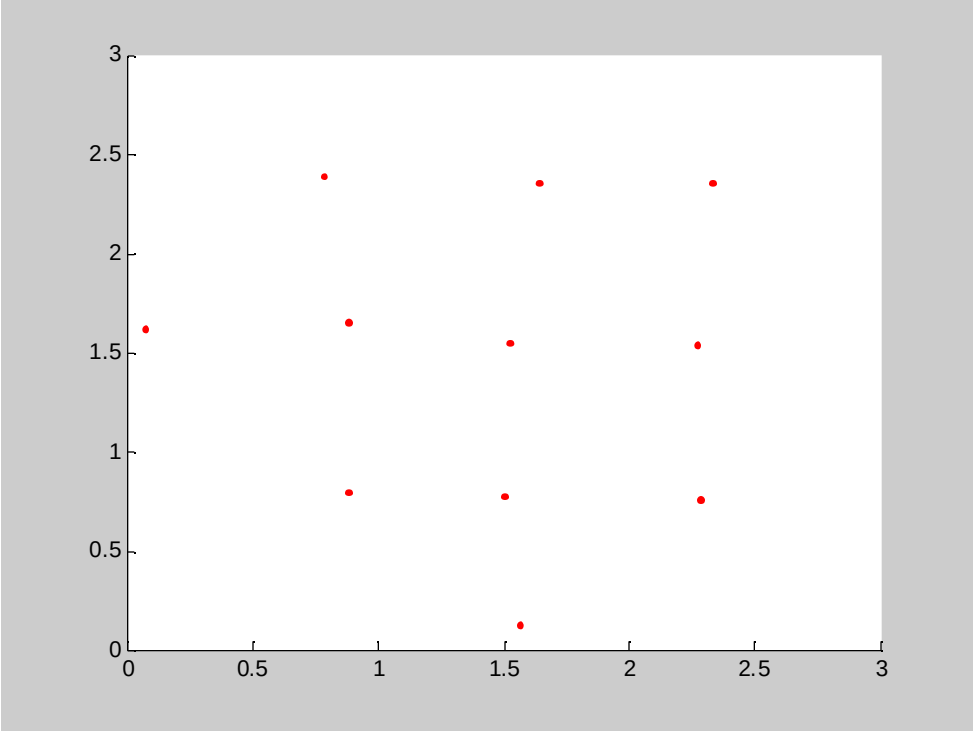

Sample LIDAR points of 0.75*0.75 m point density lying on the target circle

Figure 4 LIDAR point patterns on circular target.

	σxy=0.25m, σz=0.1m		σxy=0.15m, σz=0.1m		σxy=0.15m, σz=0.05m	
Point density [m]	RMS z [m]	Max Δz [m]	RMS z [m]	Max Δz [m]	RMS z [m]	Max Δz [m]
0.25	0.009	0.031	0.008	0.030	0.004	0.015
0.50	0.019	0.065	0.016	0.060	0.009	0.032
0.75	0.038	0.112	0.021	0.080	0.012	0.041

Table 4 Simulation results.

The simulation results clearly indicate that the LIDAR point density plays a key role in achieving good accuracy through vertical shift compensation. The actual vertical accuracy of the LIDAR points has only a secondary effect on the results. Finally, the impact of the horizontal accuracy of the LIDAR points is almost negligible.

Target design

Besides determining vertical shift of LIDAR data, 3D targets can be used to determine planimetric offsets of LIDAR data strips for calibration purposes. The recent availability of intensity data, however, makes it possible using 2D targets as the various patterns in the intensity signal can be used to determine the horizontal shift components. For an initial investigation, we considered a simple ground control design of two concentric circles with different signal response coating; see Fig. 5 (1.5 m radius for the outer circle and 0.5m for the smaller inside one). In other words, the inner and outer circles have different signal response, therefore, points on the outer ring and on the inside circle could be differentiated based on their intensity values.

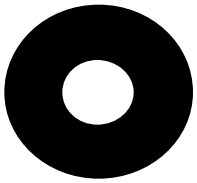

Figure 5 Circular 2D target pattern with different reflective coating.

Finding horizontal shifts in LIDAR data using the targets

The achievable accuracy of the determined planimetric offsets mainly depends on the LIDAR point density with respect to the target size and of course, from the LIDAR point footprint size. To estimate planimetric shifts of LIDAR points, first a circle has to be fitted to the LIDAR points that lie on the target circle. These points can be found by their intensity value. Once the circle was fitted, the difference between the horizontal coordinates of the origin of the fitted circle and the known coordinates of the target provides the horizontal shift values of the LIDAR points near the target.

Our circle-fitting algorithm finds all the possible locations of the target circle in a grid, the algorithm itself is quite similar to the Hough-transform. The search is based on the known radiuses of the inner and outer circle and the LIDAR points lying on the target. If we look at a LIDAR point lying somewhere in the outer circle, we know that the origin of the circle is somewhere between the circle drawn around the LIDAR point as origin with the smaller radius and the circle drawn with the bigger radius. If we consider a second LIDAR point, the origin is somewhere in the intersection region of the two rings around the two LIDAR points, and so forth. An accumulator array is created with zero values, and point-by-point the value of the grid cells under the ring with the origin of the LIDAR point is increased by one. This is done for all points lying on the target. The cells with the highest value give all the possible positions of the target origin. The center of gravity of these cells is accepted as the origin of the circle. The half of the size of the area of cells with the highest value is the accuracy of the determined circle origin; therefore it gives an estimate for the accuracy of the determined horizontal shift of the LIDAR points. Figures 6, 7 and 8 illustrate the fitted circles and the accumulator array at 25*25, 50*50 and 75*75 cm LIDAR point density.

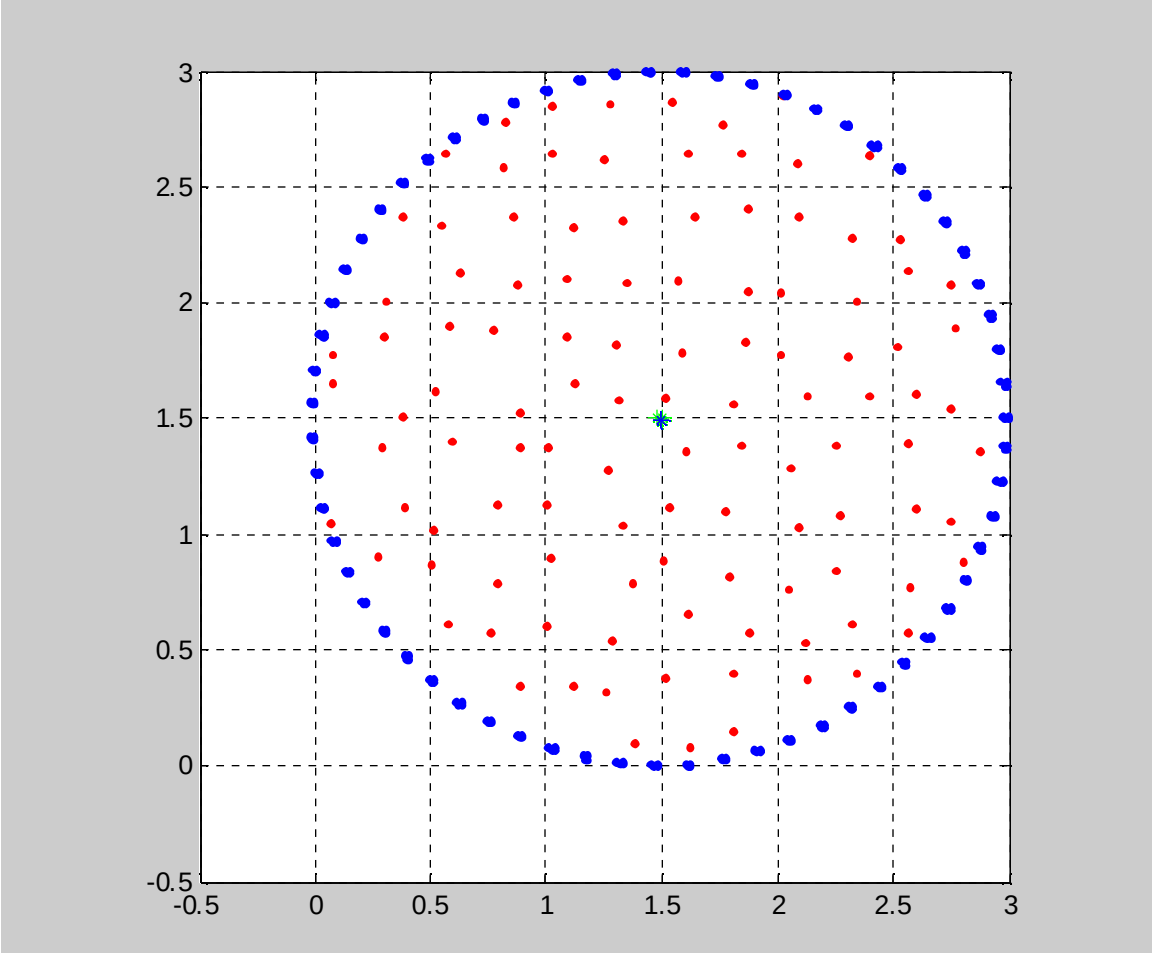

LIDAR points (red points) and possible circle origins (green points) with all possible circles drawn in the case of 25*25 cm point density

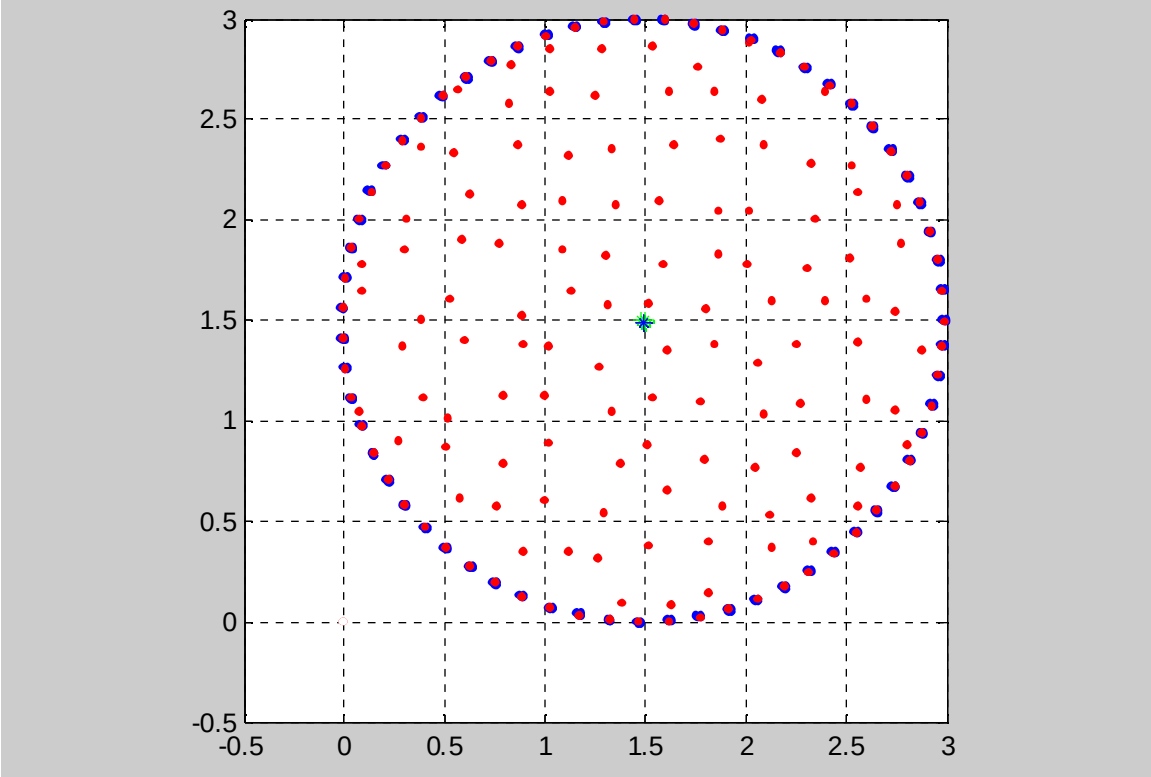

a) LIDAR points (red points) and possible circle origins (green points) with circle drawn in the case of 25*25 cm point density and main circle points (purple points)

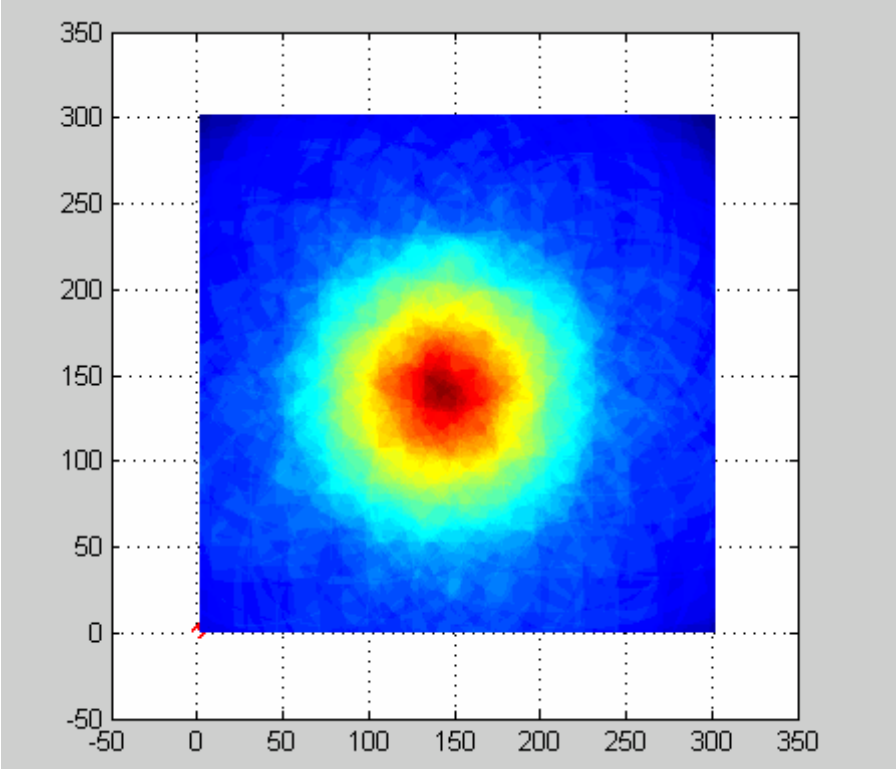

b, Accumulator array in top view

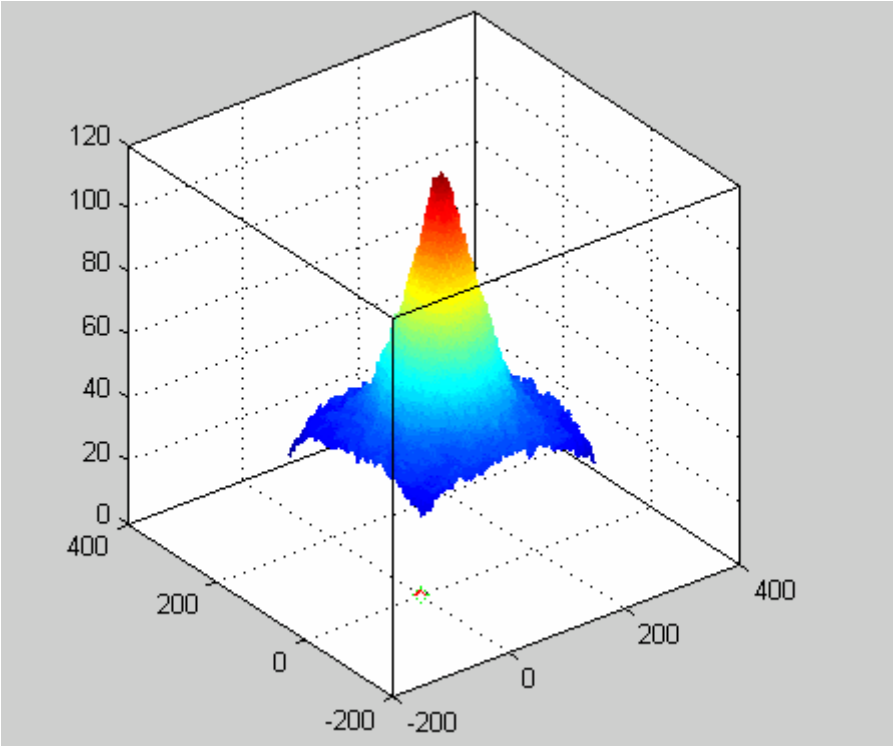

c, Accumulator array in isometric view

Figure 6.

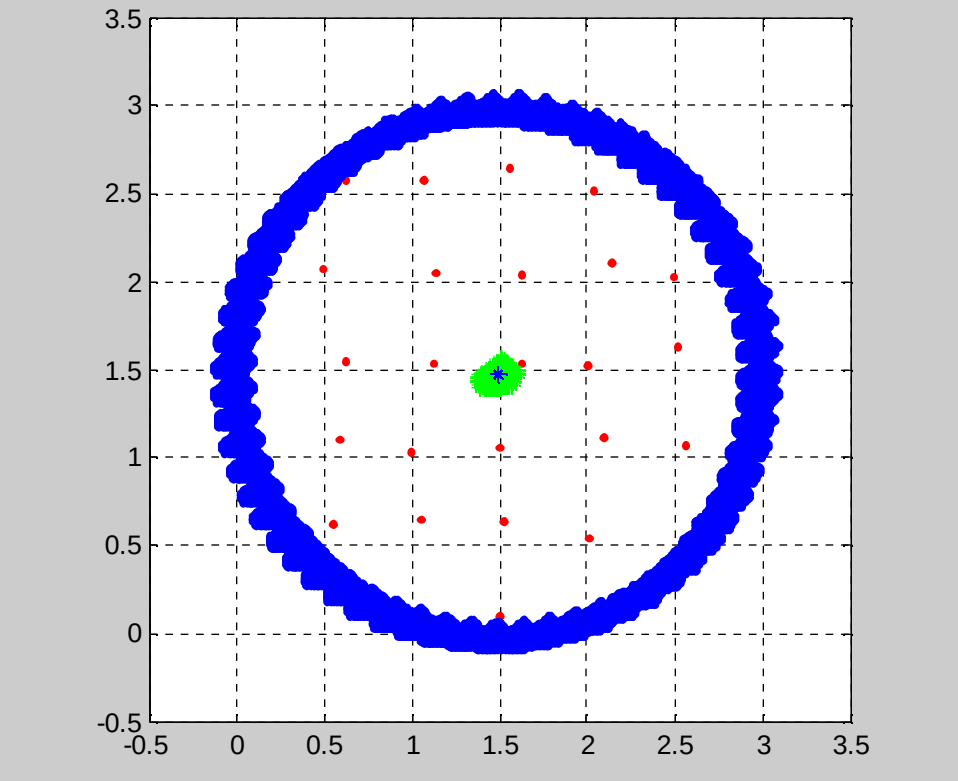

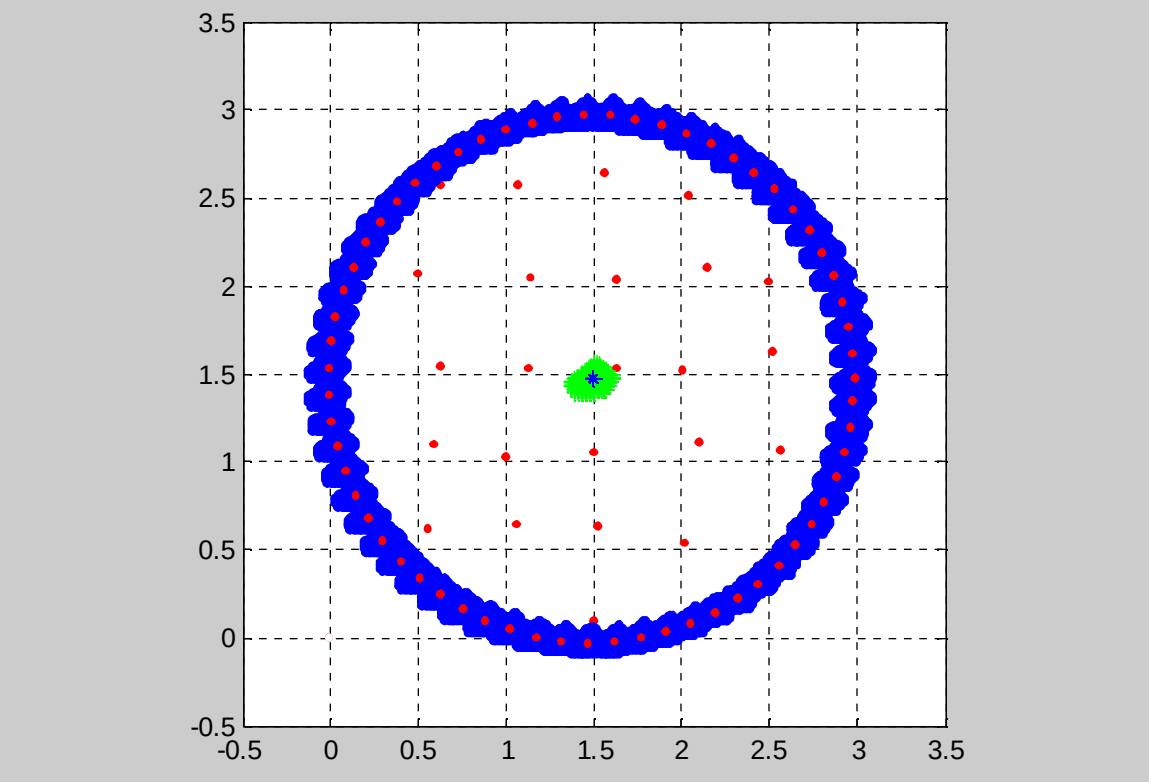

a, LIDAR points (red points) and possible circle origins (green points) with circle drawn in the case of 50*50 cm point density and main circle points (purple points)

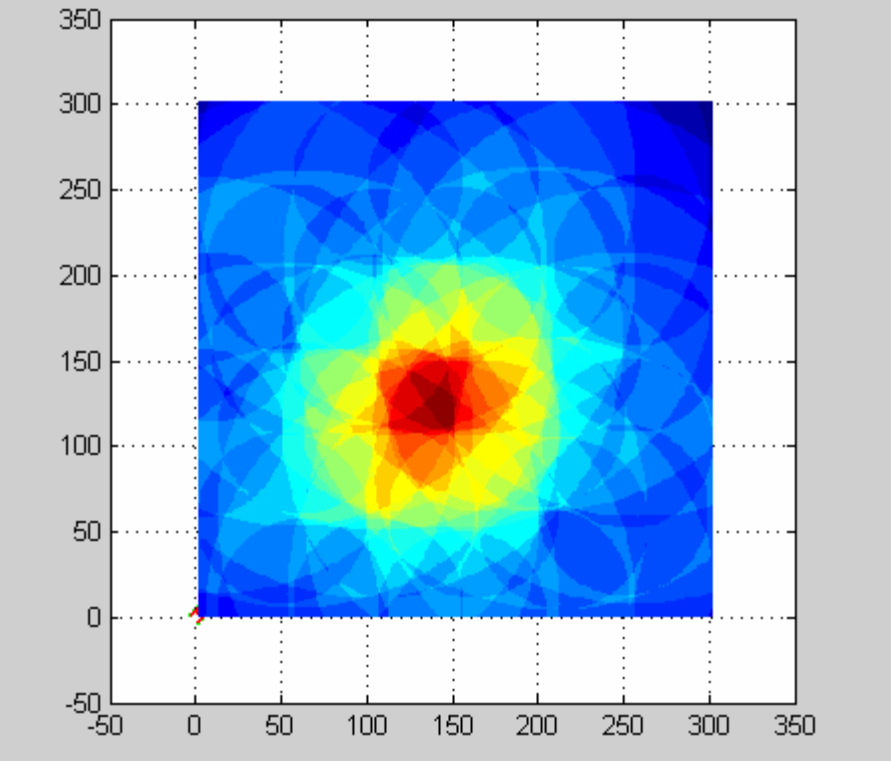

b, Accumulator array in top view

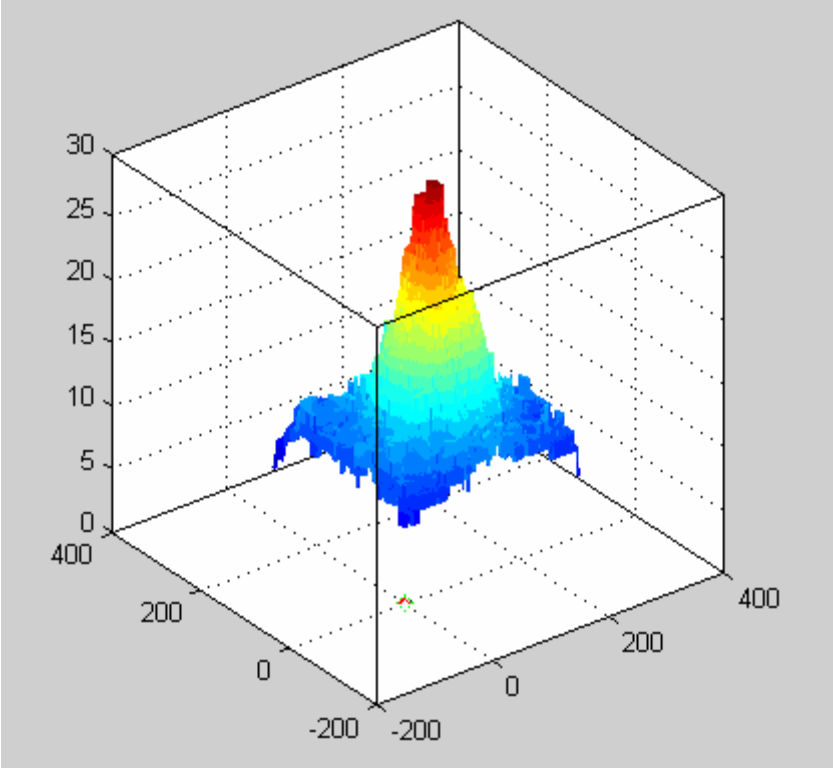

c, Accumulator array in isometric view

Figure 7.

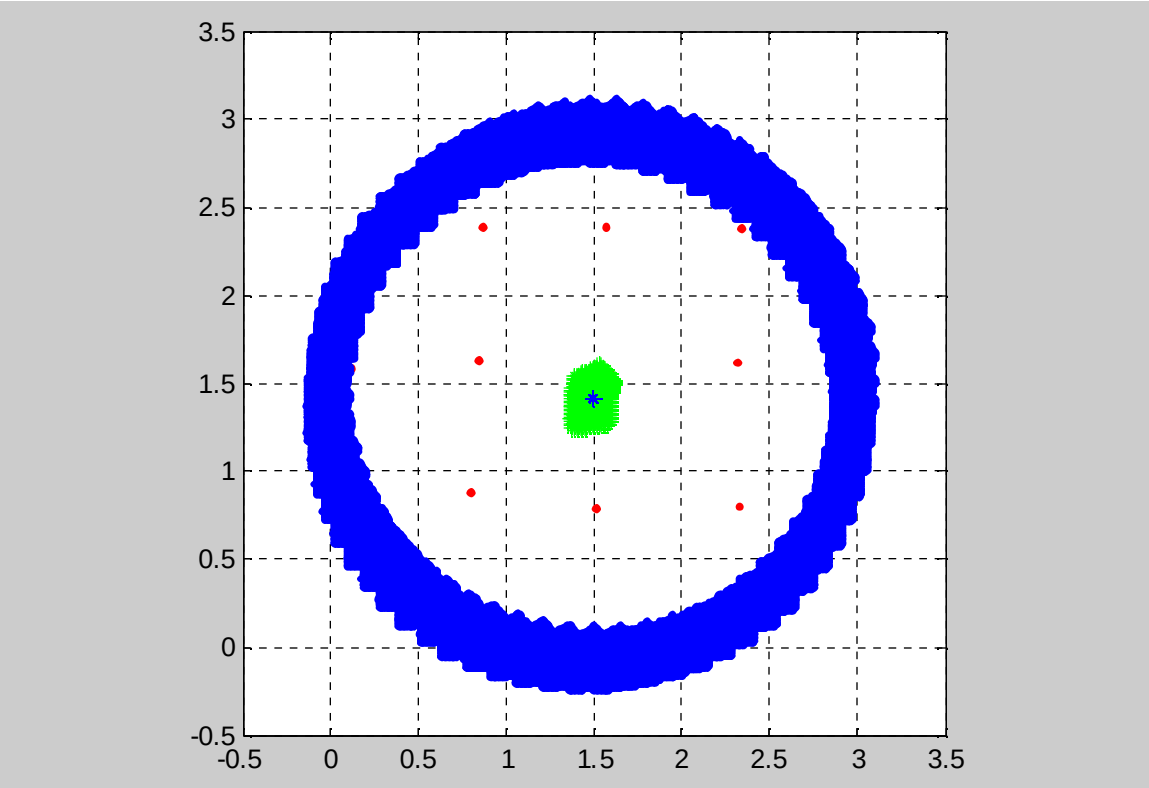

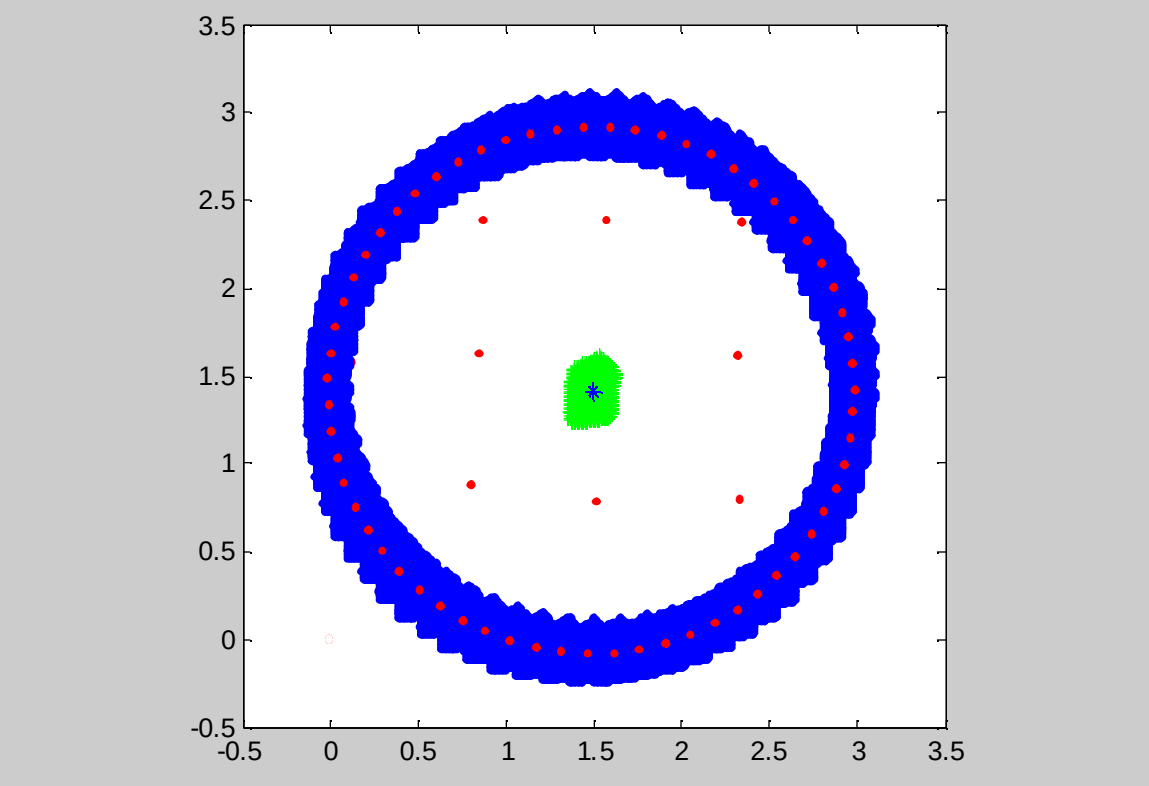

a, LIDAR points (red points) and possible circle origins (green points) with circle drawn in the case of 75*75 cm point density and main circle points (purple points)

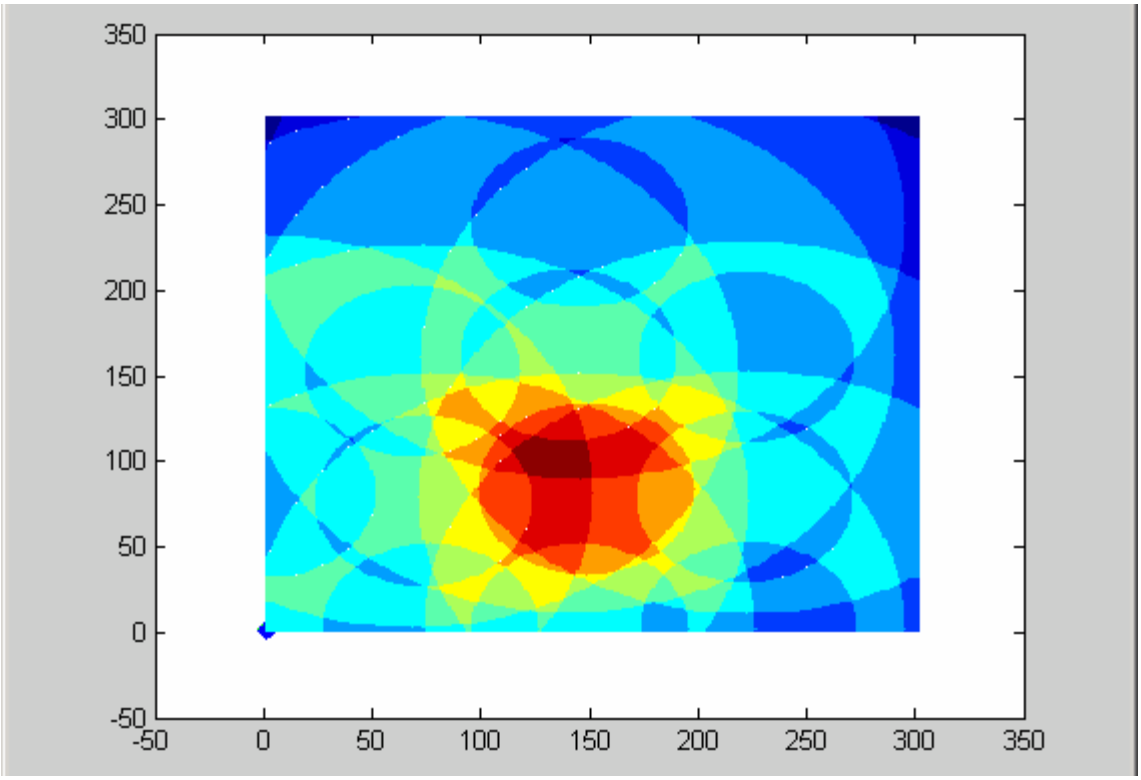

b, Accumulator array in top view

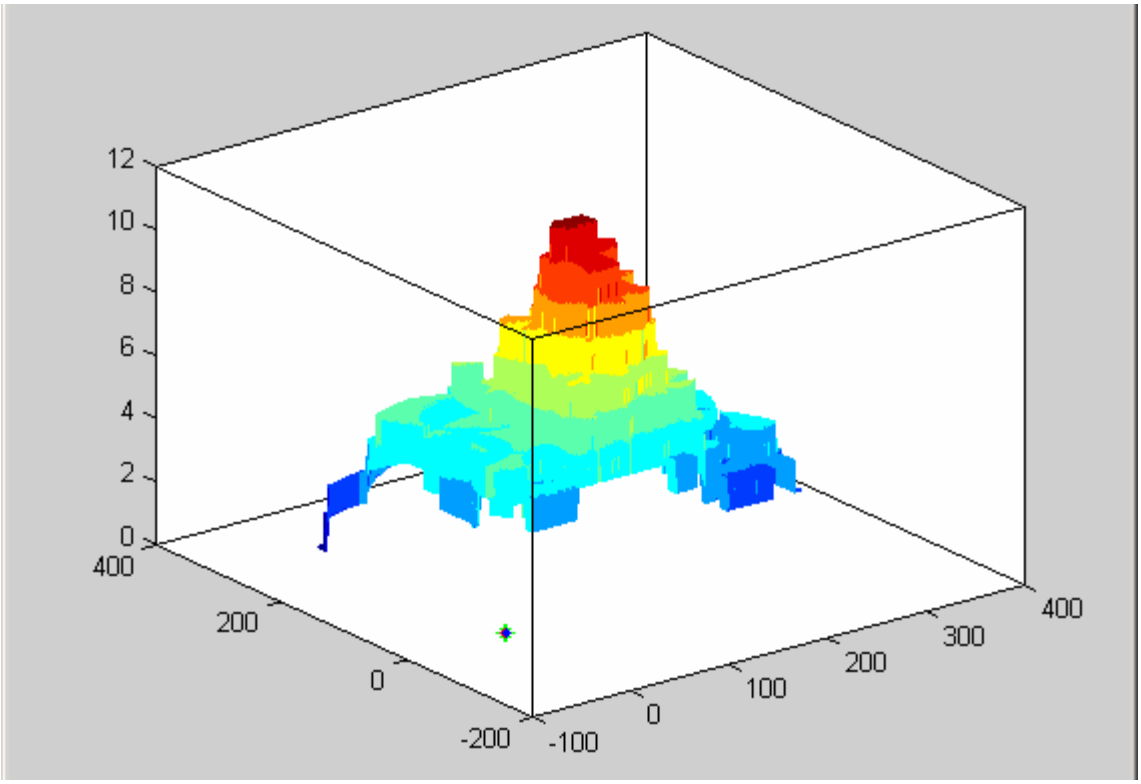

c, Accumulator array in isometric view

Figure 8.

Table 5 shows the approximated accuracy of the determined horizontal position of the target circle for different point densities. The accuracy depends a lot on the actual LIDAR point distribution on the target circle and therefore the values shown in Table 5 are only representative for the above example. If there are more points near the edge of the circle, the accuracy is much better than in the case where there are not too many points near the edge. The design of the target (two concentric circles with different signal response) makes the determination of the horizontal position of the target much more accurate compared to the case of a homogenous target circle. Basically, the information that a LIDAR point falls on the inner or the outer circle provides additional constraint to the origin search algorithm.

Point density [m]	Accuracy of horizontal position of target circle
0.25*0.25	few cm
0.50*0.50	~20-25 cm
0.75*0.75	~40-50 cm

Table 5. LIDAR points-determined accuracy of the horizontal position of the target circle at different point densities

APPENDIX F

LiDAR and Image Fusion

1. Toth C., 2003: Fusion of LiDAR and Simultaneously Acquired Digital Imagery: New Aspects of Supporting Terrain Extraction, Terrain Data: Applications and Visualization – Making the Connection, ASPRS/MAPPS, Charleston, SC, October 27-30, 2003, CD-ROM.
2. Toth C., (2002): Fusion of LIDAR with Imagery for Enhanced Surface Extraction, Proc. 29th International Symposium on Remote Sensing of Environment, April 8-12, CD ROM.

Fusion of LiDAR and Simultaneously Acquired Digital Imagery: New Aspects of Supporting Terrain Extraction

Charles K. Toth

Center for Mapping
The Ohio State University
1216 Kinnear Road, Columbus, OH 43212-1154
E-mail: toth@cfm.ohio-state.edu

ABSTRACT

Deployment of LiDAR systems has recently experienced enormous growth. Improved performance as well as affordability has made LiDAR a primary tool for collecting a variety of high quality surface data in much shorter periods of time than previously was possible. The introduction of return pulse intensity or the availability of complete waveform data has further enhanced the processing of LiDAR data in terms of better automation and better feature extraction performance. The potential of combining LiDAR data with simultaneously acquired digital imagery to further improve the terrain extraction process is investigated. A statistical model has been developed to combine surface points obtained from stereo DEM extraction with data directly acquired by LiDAR. The merging process is based on the error characteristics of the different surface data types. In addition, the method can deal with any other combination of source surface data.

INTRODUCTION

Digital elevation models (DEMs) are required by a wide variety of applications (Maune, 2001). In addition, emerging applications usually need DEMs with an increased level of detail and accuracy. Recent technological advancements have created revolutionary new techniques to acquire DEM data in large volumes, with excellent accuracy and at an affordable price. LiDAR has become the de facto leading source of high accuracy surface data at local scale; while IfSAR has a similar role at global scale to produce vast amounts of data quickly at low cost and good accuracy. The traditional DEM extraction method – photogrammetry using stereo image pairs – has been losing ground against the new techniques. Most importantly, LiDAR and IfSAR processing can be automated to a large extent, while despite solid developments in image matching, the traditional photogrammetric method is still labor intensive, especially for urban areas.

Surface data created with old and new technologies have different and often complementary error characteristics. There are a number of papers comparing DEM characteristics obtained by different technologies (Mercer, 2001; Toth and Brzezinska, 2000). Recently, discussions have intensified on combining different datasets to arrive at a better representation of the surface. The idea behind fusing DEMs is simple: if surface data are available from different sources with different sampling rates, sampling pattern, different error characteristics and each method records different properties of the terrain better, the fusion of the different surfaces obviously can provide a more detailed, more accurate, improved model of the terrain. In an early fusion method for combining photogrammetric and IfSAR DEMs, the fused DEM is a weighted average of the different DEMs, where the weights are coming from the cross correlation values (Honicel, 1999). A method to fuse DEMs, which is based on the individual error characteristics of the different surface points, is described in this paper. LiDAR data with digital imagery are used to obtain initial test results for the proposed method.

CONCEPT OF THE METHOD

Most of the papers dealing with fusion of different surface datasets consider the task of merging two different DEMs as calculating some kind of weighted average of the DEMs. In contrast, our approach is different as the concept of the proposed method is based on the fact that all points from the different sources are considered together with their individual error characteristics (in contrast to being handled as two distinct datasets). The surface points are characterized by their error ellipsoids, not only the vertical coordinate errors but also the horizontal terms are considered. For example, this is especially important in the case of LiDAR data with larger footprint sizes.

The problem of fusing different datasets can be described as finding an optimal reconstruction of the z(x,y) surface, which is sampled at the locations of the given points from the different datasets. As with all the measurements, the samples are not error free and the measured points can be characterized by their error ellipsoids, which are determined by the standard deviations of the three coordinates and the correlation between the coordinates. Hence, an optimal surface is sought that goes through all the error ellipsoids and satisfies the condition that the RMS, weighted by the coordinate accuracy terms, is minimal (Figure 1).

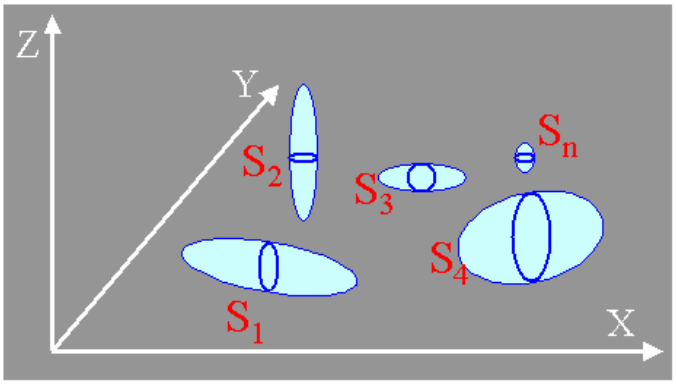

Figure 1. Problem description.

Obviously, this formulation of the above problem is ill conditioned. The suggested solution to make the surface-fitting problem well conditioned is to convert the three-dimensional uncertainties of the measured points into a single vertical term. In other words, the measured points are characterized with only one, vertical accuracy term. In this way the original ill conditioned surface fitting problem becomes a well-conditioned least squares adjustment problem, where the weight matrix is determined by the converted vertical variances. For instance, in the case of horizontal flat terrain the horizontal coordinate error does not cause additional error in the vertical coordinate. But if the terrain is sloped, a horizontal coordinate error obviously introduces an additional vertical error. This vertical error can be calculated if the surface gradient at the measured points is known. Figure 2 illustrates the error ellipse of a measured point assuming the coordinates are uncorrelated.

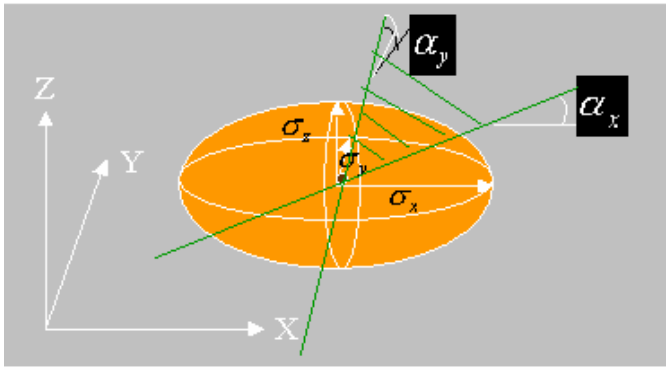

Figure 2. Converting the 3D variance into a single vertical variance.

Based on the three-dimensional variances of the coordinates and the surface gradients in x and y directions at the measured point, the converted vertical variance can be derived by error propagation:

$$\sigma_Z{}'^2 = \sigma_Z{}^2 + g_X{}^2\sigma_X{}^2 + g_Y{}^2\sigma_Y{}^2$$

where

$\sigma_X{}^2, \sigma_Y{}^2, \sigma_Z{}^2$ are the three-dimensional variances

$\sigma_Z{}'^2$ is the converted vertical variance

g_X, g_Y are the surface gradients in the X and Y directions

For simplicity, it was assumed that the X, Y, and Z coordinates are uncorrelated; however, if it is not the case, the correlation between the coordinates should be considered, and consequently the converted vertical variance can be derived similarly by error propagation.

IMPLEMENTATION OF THE METHOD

Figure 3 illustrates the implementation of the proposed method for fusing different datasets.

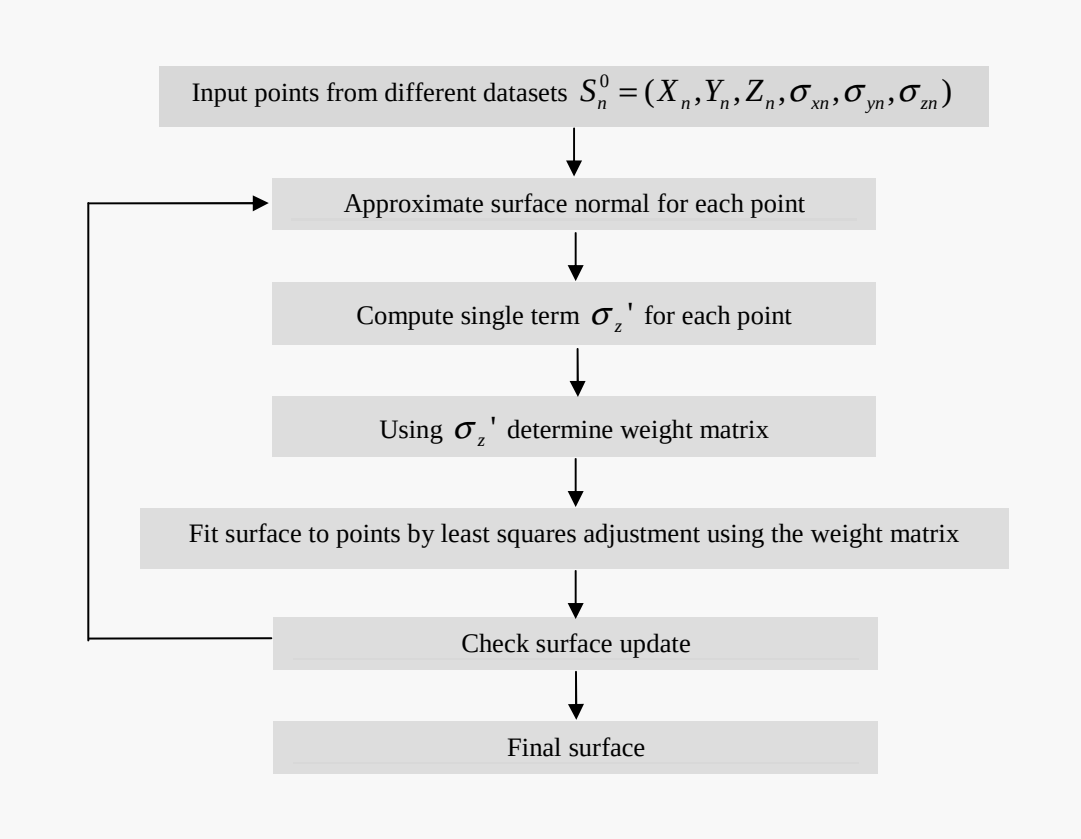

Figure 3. Implementation of the proposed fusion algorithm.

Initially there are *n* points from the two or more different datasets with their known error ellipsoids. Since surface fitting to *n* error ellipsoids is an ill conditioned problem, as described above first the three-dimensional variance has to be converted into a single one-dimensional vertical variance term based on the surface gradients. Obviously, the true surface normals cannot be determined since the true surface is not known and consequently the surface gradient must be approximated. Once the approximated surface gradients are found, the single term vertical variance is calculated for each point. Then using these values,

the weight matrix for the least squares adjustment can be constructed. Since the surface gradients are not known (they are approximated), the whole process is iterative. Once a surface is fitted by a least squares adjustment, the update with respect to the previous surface is checked. If it is above a specified threshold, the gradients are approximated again and the process starts over until the surface update goes below a predefined threshold. Usually only a few iterations are needed (depending on the threshold), as the method is likely to eliminate the outliers during the first iteration. Initially, the surface gradient at any measured point is calculated using the surrounding measured points. Thus, the calculated gradients of outlier points will be large, which causes the calculated vertical variance to be very large. For instance, points with a vertical variance above a predefined threshold can be either eliminated before surface fitting or they will have small weights and become insignificant in the adjustment.

There is no restriction on what kind of surface modeling function can be used. The optimal technique can be chosen solely based on the terrain characteristics. For the initial tests, Fourier series-based surface modeling extended with polynomial terms was used (Csanyi *et al.*, 2003). The advantage of this proposed surface modeling method is that the polynomial components describe the surface trend well while the Fourier series models the local changes in the surface. The size of the area that can be efficiently modeled by fitting a surface depends on the terrain characteristics. In the case of smooth, rolling terrain, the area can be larger, while quickly changing terrain must be restricted to small areas. To determine the fused DEM for larger areas, the area can be segmented into smaller patches that can be individually modeled by surface fitting and then the patches can be merged together after fusion.

EXPERIMENTAL RESULTS

The selected test area is a small, 10 m * 15 m area of the Madison County, Ohio test site, which has been flown regularly and therefore various datasets as well as excellent ground truth are available. Figure 4a shows the test area, which is a part of a 4K by 4K airborne panchromatic digital image and Figure 4b depicts the elevation ground truth data.

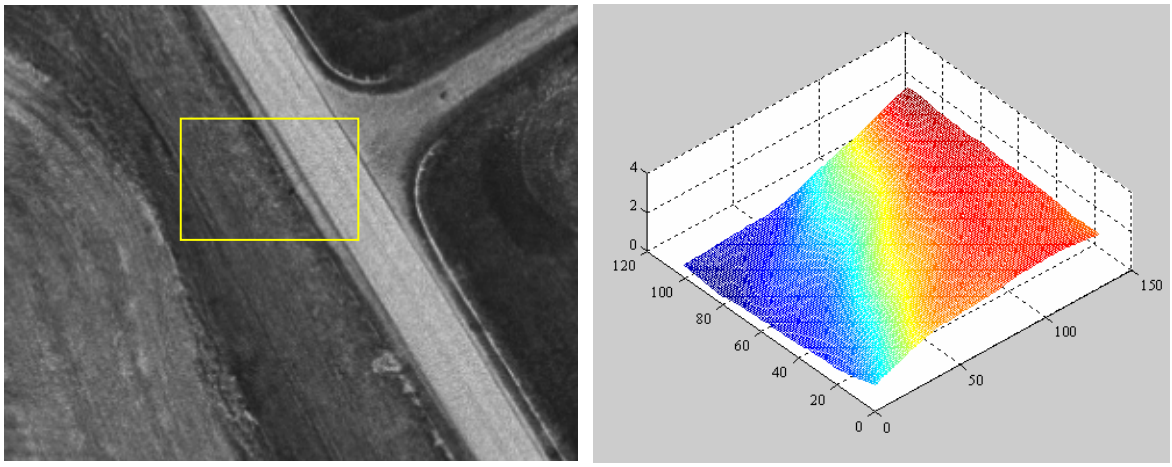

a) b)

Figure 4. Test area and ground truth.

LiDAR data acquired with digital imagery were used to test the proposed fusion algorithm. The LiDAR point density was about 0.4 point/m^2, the images were taken with a 4K by 4K digital camera from a 1250 m flying height (Toth, 1997). Figure 5 illustrates the LiDAR points and the extracted stereo points over the selected area. The stereo points were obtained in a digital photogrammetric workstation environment using StereoPlotter from Autometric; no manual editing was done on the data.

Since the proposed fusion algorithm is based on the error characteristics of the measured surface points, the error characteristics should be considered at great care. The horizontal standard deviation of the LiDAR

points was determined based on their footprint size, 0.5 m, while for the vertical standard deviation, the usual 0.15 m was considered. No scan-angle correction was applied, as the surface area was rather small with respect to the swath of the LiDAR sensor. For the stereo points, the analysis of the differences with respect to the ground truth of the area provided the error terms; 0.2 m and 0.4 m, horizontal and vertical error terms, respectively. These three-dimensional standard deviations were then converted to one-dimensional, vertical values based on the surface gradient at the measured points according to the above described process.

a)

b)

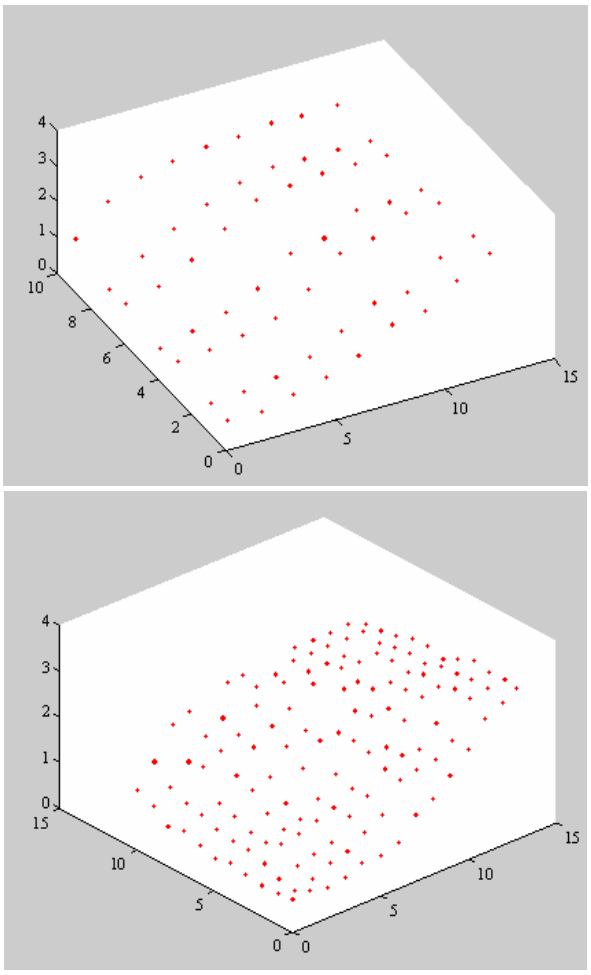

Figure 5. LiDAR and stereo points over the test area.

First, the surface was only modeled based on the measured LiDAR points. Then to assess the performance of the proposed fusion algorithm, it was performed on the LiDAR and stereo points. In both cases the surface was modeled by the above-mentioned proposed method using Fourier series with polynomial extensions, see details in (Csanyi *et al.*, 2003). The optimal order of the polynomial and the number of harmonics for the Fourier series were chosen based on the average point densities in the X and Y direction and the surface characteristics.

Table 1 shows the main statistics of the surface model based on only the LiDAR points and the surface model after fusion. As a measure of the closeness of the surface model to the ground truth, the maximum difference and the RMS values were calculated from the differences between the fitted surface and the ground truth at the grid points (the ground truth was available in grid format and these differences were calculated at grid points). The results clearly show that the fused surface data models the true surface much better. Both the RMS and the maximum difference from the ground truth decreased significantly after fusion. The limited initial test has shown a good performance of the proposed fusion method over a small area.

	LiDAR	Fusion (LiDAR+stereo)
MAX ΔZ [m]	0.31	0.14
RMS [m]	0.19	0.09

Table 1. Statistics before and after fusion.

CONCLUSIONS

An algorithm to combine surface datasets from different sources to achieve an improved accuracy DEM has been developed. The concept is that the points from different sources are individually considered together with their error characteristics and an optimal fitting surface for the points is sought. Since this problem is ill conditioned, the conversion of the three-dimensional variance into a single vertical variance has been proposed to make the problem a well conditioned least squares adjustment problem. The derivation of the combined vertical variance is based on the availability of the surface gradients. As the gradients are not known, but approximated, the solution is iterative. The test results are promising, clearly showing a good performance of the proposed algorithm. The resulting surface model improves after data fusion; both the RMS and the maximum difference from the ground truth data have decreased. The algorithm works with any combination of datasets. The main question of the method is what surface modeling function to choose. In the initial tests, the Fourier series with polynomial extension was selected.

ACKNOWLEDGMENT

This research was partially supported by the Department of Defense Dual Use Science and Technology program. The author would like to thank Nora Csanyi, graduate student at the Department of Civil and Environmental Engineering and Geodetic Science, OSU for the algorithmic implementation and data processing.

REFERENCES

Csanyi, N., Paska, E., and Toth, C. K, (2003). Comparison of Various Surface Modeling Methods, published in this proceedings.

Honikel, M. (1999). Strategies and Methods for the Fusion of Digital elevation Models from Optical and SAR Data, *International Archives of Photogrammetry and Remote Sensing*, Vol. XXXII, Part 7-4-3 W6.

Maune, D. F. Ed. (2001). Digital Elevation Model Technologies and Applications: The DEM Users Manual, ASPRS, Bethesda, MD.

Mercer, B. (2001). Combining LiDAR and IfSAR: What Can You Expect. Photogrammetric Week 2001, Stuttgart, Fritsch/Spiller (Eds.)

Toth, C. K., Berning, S., Leonard J., Grejner-Brzezinska, D. A., (2001). Integration of Lidar Data with Simultaneously Acquired Digital Imagery. Proceedings of ASPRS Annual Convention, St Louis.

Toth, C. K., Grejner-Brzezinska, D. A., (2000). Complementarity of LIDAR and Stereo Imagery for Enhanced Surface Extraction, *International Archives of Photogrammetry and Remote Sensing*, Vol. XXXIII, Part B3, pp. 897-904.

Toth, Ch.K. (1997). Direct Sensor Platform Orientation: Airborne Integrated Mapping System (AIMS)," *International Archives of Photogrammetry and Remote Sensing*, ISPRS Comm. III, Vol. XXXII, part 3-2W3, pp. 148-155.

Fusion of LIDAR with Imagery for Enhanced Surface Extraction

C.K. Toth
The Center for Mapping, The Ohio State University
1216 Kinnear Road
Columbus, Ohio 43212-1154, USA

toth@cfm.ohio-state.edu

Abstract – The deployment of LIDAR systems has recently experienced enormous growth. Improved performance as well as affordability have made LIDAR a primary tool for collecting a variety of high quality surface data in much shorter periods of time than was previously possible. In addition, some features unique to LIDAR, such as the capability to separate vegetation from the ground, have opened up new application areas. As this technology has progressed from scientific applications to everyday map production, more and more data provide feedback on how to improve the surface extraction process and how to further extend application possibilities. Massive early production experiences revealed the need for some image coverage, especially for concurrently acquired imagery. The main purpose of the images is visualization; however, the availability of such imagery may play a further role in LIDAR data preprocessing and in the overall surface reconstruction process. The fusion of the two quite different measurements (range vs. reflectance image) is based mainly on the different sampling patterns and information content. The purpose of this paper is to present an assessment of the potential for combining LIDAR data with high-resolution, simultaneously acquired, direct-digital imagery to achieve higher quality results. The application potential is enormous for LIDAR and image fusion for medium or higher flying heights where the spot density may become rather sparse.

I. INTRODUCTION

Light Detection and Ranging (LIDAR) sensors have shown remarkable developments over recent years, achieving both cost-effectiveness and reliability at the same time. They currently represent a new and independent technology for a highly automated generation of digital surface models (DSM) and digital elevation models (DEM). However, there are a few inherent shortcomings of the LIDAR technology, such as the lack of correspondence to objects, the lack of redundancy in the measurements, strong dependency on material features, and missing visual coverage. Recently, rapid digital camera developments have reached a level of performance whereby such systems can be integrated into airborne LIDAR systems. Introduction of direct digital imagery into the LIDAR system has two primary benefits: 1) it can improve the surface extraction process, and 2) it provides the necessary visual coverage of the area. Both processes can be sufficiently automated, promising a near real-time mapping performance.

II. IMAGING SENSORS

Recently, LIDAR systems have established themselves as the strongest contenders for a highly automated generation of digital elevation and surface models. Operational scanning systems easily provide a large number of elevation spots with excellent vertical accuracy (depending primarily upon the quality of the associated Global Positioning System/Inertial Navigation System (GPS/INS) data), and thus successfully compete with, thus far, mostly stereo image-based surface extraction techniques. An additional feature that makes laser systems even more attractive is the fact that they can deliver multiple echoes from one laser pulse – for example, first and last return – which allows the separation of terrain or man-made objects from vegetation, as the laser beam can penetrate the vegetation foliage, but not the terrain or solid objects. Obviously, this technological transition is made possible by the high quality of contemporary GPS/INS systems, which offer positioning accuracy in the range of 5-20 cm, a figure compatible with the range quality offered by LIDAR systems. An excellent primer for the basic principles of LIDAR systems is provided by *Baltsavias* (1999). Comparison between photogrammetry and LIDAR techniques is addressed by *Schenk* (1999) and by *Baltsavias* (1999). Advanced surface generation methods are reviewed by Kraus (2001). *Wehr and Lohr* (1999) discuss system structures and specifications. *Maas and Vosselman* (1999) and *Haala and Brenner* (1999) can be a good starting point for the subject of building extraction, while forestry mapping is discussed by *Kraus* (1998). A comprehensive review of the commercial developments is available from *Flood* (2001).

The introduction of digital camera systems into airborne surveying is a less noticeable progression than the proliferation of LIDAR systems. Nonetheless, high-resolution digital sensors, based on Charge-Coupled Devices (CCD), are rapidly approaching the resolution and performance level required in aerial mapping. A sure sign of these changes is that both major large-format analog camera manufacturers are already heavily involved in digital aerial camera developments and have recently introduced the first generation of their high-performance digital aerial mapping cameras. Commercially available

digital frame cameras in the 4K by 4K range have already been used in airborne surveying, and experimental systems are tested with 10K by 5K and 9K by 9K sensors (*Thom and Souchon* 1999, *Toth* 1999, *Bruce* 1998). The ground coverage offered by these sensors is still modest compared to that of large-format analog cameras used in airborne mapping; nevertheless, these digital cameras can efficiently provide simultaneous visual information for LIDAR data at sufficient ground resolution and coverage. Thus, combining LIDAR with these digital imaging sensors provides an excellent and novel solution to simultaneously acquiring surface data along with visual coverage and consequently to producing orthophotos. Of equal importance, the digital images can bring in much-needed redundancy to LIDAR data and consequently can offer the potential to improve the quality of the LIDAR-derived surface data.

III. IMAGE FUSION

Combining various image sensory data to improve the feature extraction process is a general trend in mapping. Because of the explicit nature of the LIDAR data, however, most LIDAR processing methods have not involved any additional source of information until recently. To change this trend, LIDAR data interpreted as image intensity, combined with multi-spectral imagery, have been studied to support the classification process in remote sensing. This research goes a step further as our objective is to achieve the fusion of the two data sets in terms of optimizing the geometrical properties of the extracted surface.

A. Comparison of DEM extraction techniques

Large-format aerial imagery was the predominant source of DEM production before the introduction of LIDAR, which has now been emerging as a market leader at an unprecedented rate. Comparing the two techniques reveals the fundamental differences in concept and performance characteristics.

Producing DSMs and DEMs, and especially surveying densely built urban areas, are in high demand and yet these are some of the most difficult mapping tasks to perform. This is primarily due to the large number of man-made objects with lots of vertical surfaces, occlusions, shadows, moving objects, etc. Probably the surface discontinuities, generally called break lines, represent the most difficult problem, and from a strictly theoretical point of view, they would require a diminishingly small sampling distance, posing a challenge for both techniques but in a somewhat different way. Although the LIDAR point density can be increased almost infinitely, the real limit is the cost. By contrast, increasing the spatial sampling rate of the imagery (by reducing the pixel size) can be accomplished without any major cost increase; however, the processing of the images becomes overly complex.

Automated surface extraction from stereo imagery has been intensely researched and numerous implementations of various concepts have been commercially available for use in production for many years. In general, the performance diminishes at larger scale. In contrast, LIDAR data processing is rather new and is usually limited to simple pre-processing of raw input data, then to vegetation removal or bald earth filtering, and in some cases to feature extraction such as road and building extraction. Because of the explicit range measurements, LIDAR data processing is substantially less complicated than the automated surface extraction from stereo images. Nevertheless, expertise in image matching is a significant asset that should be invoked in any future attempts to integrate these two sensory data types. Table I summarizes the main differences between the stereo image based photogrammetric and LIDAR techniques.

Table I

	Photogrammetry	**LIDAR**
Data Acquisition		
Flying height (H) [m]	< 6,000	< 2,000
Swath [degrees]	< 110	< 20
Sampling/Coverage	Continuous	Sparse/Irregular
Footprint (GSD) [m]	Pixel size x Scale	1 mrad x H
Surface Extraction Process		
Redundancy	2 x n – 3	0
Accuracy		
Planimetry [m]	< GSD	0.1 + -0.12 x H
Elevation [m]	~ H / 10,000	~ 0.1
Automation potential	Medium	High
Automation complexity	Medium/High	Low

To illustrate the differences in surfaces obtained by automated surface extraction and from LIDAR data, Fig. 1 shows DSMs over a test area.

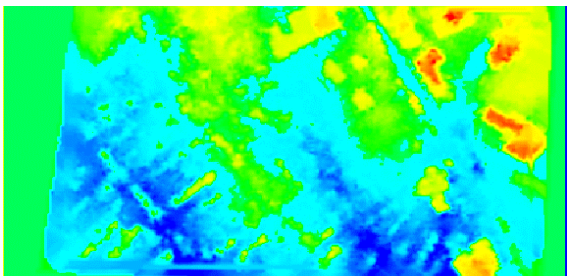

Fig. 1. Photogrammetrically derived DSM.

The stereo image-created elevation points exhibit the typical smoothed out pattern with smeared surface discontinuities. The LIDAR data show an excellent match with the ground truth for flat areas, showing at the same time buildings and other man-made objects not present in the topographic surface. The surface comparison clearly shows that the photogrammetrically derived DSM lacks high-frequency spatial components, which is primary due to the low-frequency filtering nature of the automated image

matching process. In fact, one of the principal problems in image matching is finding good approximate locations. Once they are found, however, the refinement of the matched locations is less problematic in most of the cases. In a combined approach, the LIDAR spots can serve as initial matched locations (seed points of extremely high quality) and then additional matching points can be searched around the LIDAR locations to densify the surface points. Furthermore, various processes can be built into this concept, such as inferring from certain image patterns to an object hypothesis then applying it to clean LIDAR data or vice versa.

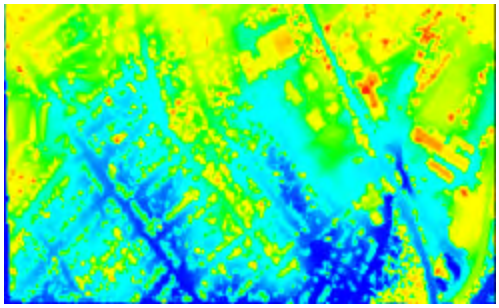

Fig. 2. LIDAR derived DSM.

B. Sensing characteristics

The raw LIDAR data represent ranges with respect to the data acquisition platform (aircraft). After the reconstruction of the aircraft motion and application of some mapping frame, the elevation spots are available as a function of the horizontal location, forming 3D point clusters or lines with the point density depending on flying height and speed, surface slope, sampling frequency, the laser's field of view, etc. The fact that laser systems provide 3D coordinates can be considered, in some sense, as their limitation, as virtually no object information is provided. In essence, laser scanning is not capable of directly pointing to any particular object, and the resulting coordinates refer to the footprints of the laser beam. From a radiometric point of view, the LIDAR system is a narrow-band active sensor, providing a spectral signature of the imaged objects (this capacity is hardly used now as LIDAR systems typically don't deal with reflectance signal intensity).

The parameters of the images acquired by airborne frame digital cameras are rather well known. Obviously, the sensor model is based on the very same central perspective projection used for large-format aerial cameras. The only notable difference with analog film comes from the radiometric behavior. CCD sensors respond to incoming light in the 0.4-1.1 micron range. Depending on the optical filter used, CCD images may cover only the visual part of the spectrum or some subpart of it. In addition, CCD sensors exhibit a linear characteristic and provide a much a finer intensity resolution compared to analog film.

C. Sampling pattern

The footprint of the laser beam and the ground pixel size of the 4K by 4K-category digital camera systems in a typical installation are very comparable as both systems work with similar FOV's. Fig. 3 depicts an image patch showing the back-projected LIDAR spots. As illustrated, the sampling patterns are independent and irregular. Of course, the irregularity depends primarily on surface undulations and to a lesser extent on the sensor orientation. The ratio between the LIDAR and image samples is about 1:70. Since the LIDAR system may receive multiple returns, the effective sampling size can be smaller. This occurs in rare situations, for instance, when the laser beam hits a break line. A completely missing LIDAR spot is another possible anomaly; for example, due to surface slant or due to specific materials such as tar (which has no response in the narrow LIDAR spectral band) it is possible that no laser return will be detected at all.

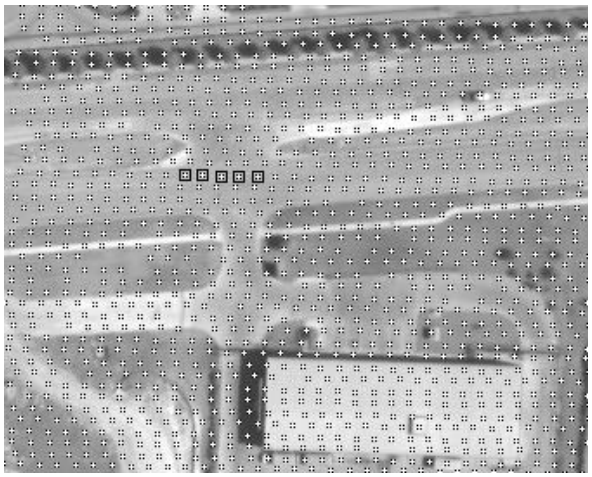

Fig. 3. LIDAR points overlaid in simultaneously acquired digital image.

To assess the impact of the different sampling rates of the LIDAR and imaging sensors with regard to the surface extraction problem, two approaches can be considered. The first is if the sampling rate of the LIDAR system (typically defined by the cross track direction) is adequate to properly describe the surface. This is usually the case for rural areas with modest surface undulations. In these situations, the use of image data to support the surface extraction process is rather limited and is mainly restricted to filling in areas with missing LIDAR spots. Except for these rare cases, the primary purpose of the simultaneously acquired image data is visual coverage, the ortho-rectified backdrop of the surface. The second and more important case is when the sampling rate of the LIDAR system is not adequate for the required surface representation with respect to the requirements of the mapping objective (*Toth and Brzezinska, 2000; and Toth et. al.* 2001).

D. Concept

To briefly illustrate the concept of fusing simultaneously acquired LIDAR data and digital imagery, a simple test has been done on a few points along a laser scanline marked by rectangles in Fig 3. As there was no ground truth available for the area, a road surface area was selected. After back-projecting the LIDAR points into a stereo model, image matching was performed to assess what surface elevation can be computed from the adjusted locations. In a totally ideal situation, matching would result in a zero shift between two image patches. As shown in Fig. 4, there is a small but noticeable difference between the original LIDAR height values and the photogrammetrically derived elevations at the LIDAR locations. Analyzing the variations along a shorter segment of the road, the results show an approximately 8.5 cm variance for the LIDAR and 6.4 cm for the stereo points. This demonstrates that the LIDAR point coordinates can be improved by stereo image-based photogrammtery, provided the image resolution and orientation are of high quality. Obviously, the impact on the horizontal component is more significant as the difference between accuracy terms is higher (LIDAR data is rather weak in planimetry).

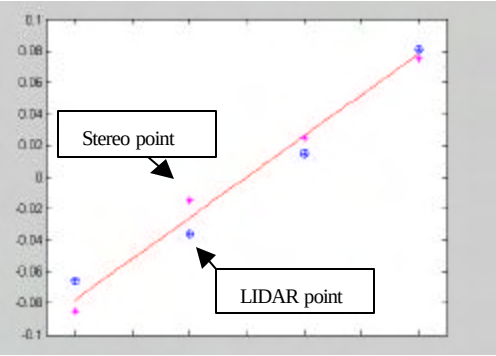

Fig. 4. Elevation profile comparison.

V. CONCLUSION

In this paper, the feasibility of combining high-performance LIDAR data with simultaneously captured digital images to improve the surface extraction process was examined. The parameters used in the example mimic those in current state-of-the-art LIDAR technology and commercially available digital camera systems. The investigation was limited to the conceptual level and addressed only one specific aspect of a rather complex topic–the question of surface sampling. Although the discussion was incomplete, the example was intended to clearly demonstrate the potential of fusing LIDAR data with simultaneously acquired imagery to improve the surface extraction process.

The already existing difference in the sampling rate between the image resolution on the ground provided simultaneously by digital cameras and the LIDAR data provides the potential to improve the surface extraction process. Currently, the rate is about 70 image pixels for every LIDAR spot. Since image matching on a pixel-to-pixel level is not feasible, by assuming small clusters of pixels, a densification factor of 5 can be achieved easily even through moderate calculations (the optimal surface point spacing vs. pixel size question itself is a topic of high interest). Since the pulse rate of current LIDAR systems cannot be increased unlimitedly due to the travel time of the pulse, while the digital camera resolution is likely to grow, it is anticipated, therefore, that the densification factor will continue to improve even further. This may change with the introduction of focal plane array LIDAR sensors.

ACKNOWLEDGEMENTS

This research was partially supported by the Department of Defense Dual Use Science and Technology program. The author would like to acknowledge the support of The EarthData Group for providing test data and valuable technical discussions.

REFERENCES

Baltsavias E. P., A Comparison between Photogrammetry and Laser Scanning, *ISPRS Journal of Photogrammetry and Remote Sensing*, 54, pp.83-94, 1999.

Bruce, M., An ultra high resolution, electro-optical framing camera for reconnaissance and other applications using a 9126 by 9126 pixel, wafer scale, focal plane array. Proc. SPIE XXII, Vol. 3431, pp. 144-154, 1998.

Flood, M., LIDAR Activities and Research Priorities in the Commercial Sector, *International Archives of Photogrammetry and Remote Sensing*, Vol. XXXIV, part 3-W4, pp. 3-7, 2001.

Haala, N., Brenner, C., Extraction of Buildings and Trees in Urban Environment, *ISPRS Journal of Photogrammetry and Remote Sensing*, 54, pp. 131-137, 1999.

Kraus, K, Pfeifer, N., Determination of terrain models in wooded areas with airborne laser scanner data, *ISPRS Journal of Photogrammetry and Remote Sensing*, 53(4), pp. 193-203, 1998.

Kraus, K, Pfeifer, N., Advanced DTM Generation from LIDAR Data, *International Archives of Photogrammetry and Remote Sensing*, Vol. XXXIV, part 3-W4, pp. 23-30, 2001.

Maas, HG, Vosselman, G., Two Algorithms for Extracting Building Models from Raw Laser Altimetry Data, *ISPRS Journal of Photogrammetry and Remote Sensing*, 54, pp. 153-163, 1999.

Schenk, T., Photogrammetry and Laser Altimetry, *International Archives of Photogrammetry and Remote Sensing*, Vol. XXXII, part 3-W14, pp. 3-12, 1999.

Thom, C., Souchon, J.P., The IGN digital camera system in progress, Photogrammetric Week '99, pp. 89-94, 1999.

Toth, Ch., (1999): Experiences with Frame CCD arrays and direct georeferencing, Photogrammetric Week '99, *Wichmann Verlag*, pp.95-107, 1999.

Toth, Ch.K., Grejner-Brzezinska, D. A., Complementarity of LIDAR and Stereo Imagery for Enhanced Surface Extraction, *International Archives of Photogrammetry and Remote Sensing*, Vol. XXXIII, Part B3, pp. 897-904, 2000.

Toth C., Berning S., Leonard J. and Grejner-Brzezinska D., Integration of LIDAR Data with Simultaneously Acquired Digital Imagery, Proc. ASPRS Annual Conference, April 23-25, CD ROM, 2001.

APPENDIX G

Software Developments

1. LIFT, Target Processing Software, User's Manual.
2. Microsoft VC++ source code (only electronic version)

Target Processing Software

Users' Manual
June 2005

1. Software Overview

The purpose of the software is to automatically find and identify the LiDAR targets in the LiDAR strips and correct the errors in the LiDAR data based on the target control coordinates.

1.1. Main menu

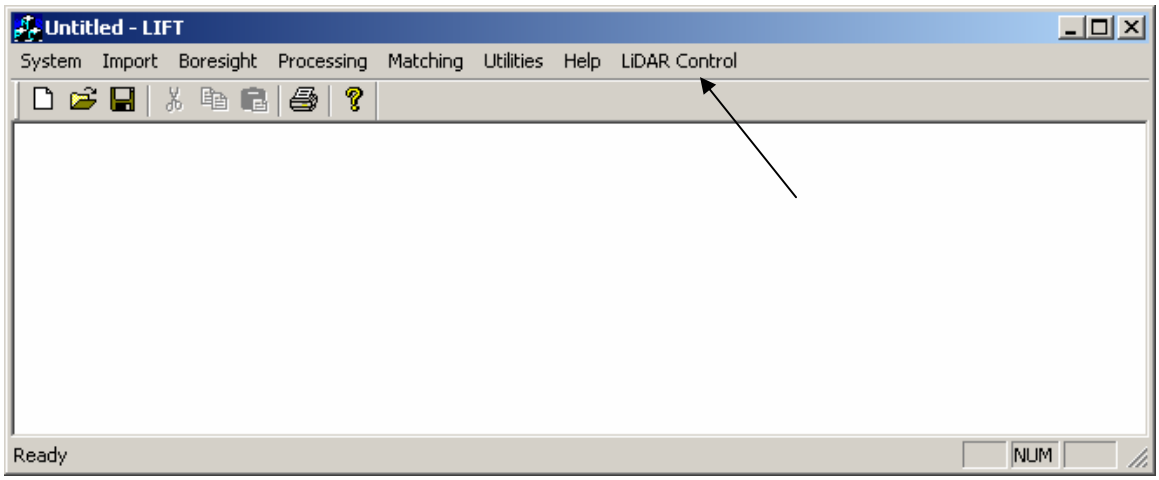

1.2. Menu points in LiDAR Control

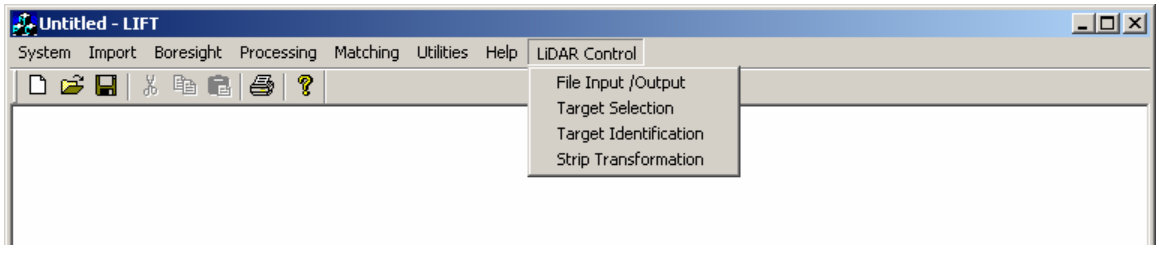

- File Input/Output
- Target Selection
- Target Identification
- Strip Transformation

1.3. Data processing steps

1. Create input LiDAR file (LiDAR Control / File Input/Output)
2. Create raw LiDAR target file (LiDAR Control / Target Selection)
3. Determine LiDAR target coordinates (LiDAR Control / Target Identification)
4. Select optimal transformation for the LiDAR strip (LiDAR Control / Strip Transformation)
5. Transform the LiDAR strip using the selected transformation (LiDAR Control / Strip Transformation)

These steps have to be performed for each LiDAR strip separately.

2. Description of target processing steps

2.1. File Input/Output

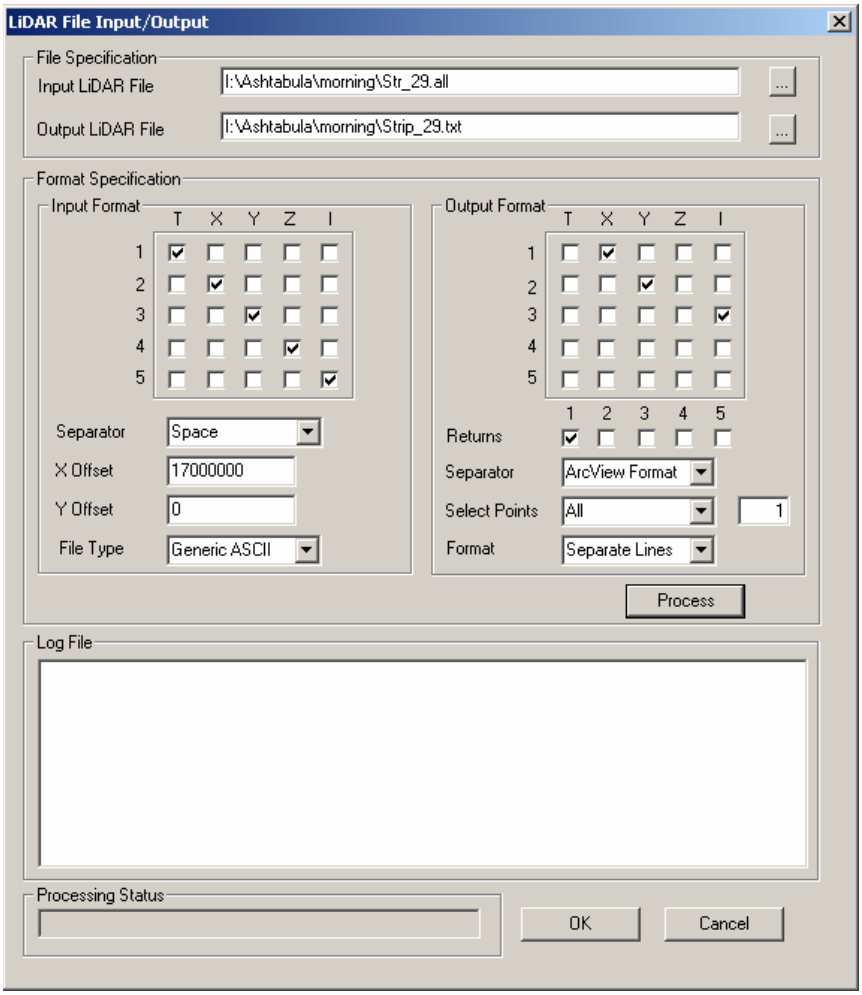

Objective:

Read LiDAR files in LAS format or any user defined ASCII file format and create output ASCII LiDAR file in user defined format.

File Specification Group Box:

Input LiDAR File	input LAS file or ASCII LiDAR file
Output LiDAR File	output LiDAR file name

Format Specification / Input Format Group Box:

Check boxes Input format has to be specified only if the input file is an ASCII LiDAR file, if the input file is an LAS file, these fields are disabled. The LiDAR file can contain GPS Time (T), X, Y, Z coordinates and Intensity values (I). The values can appear in any order, and the order has to be specified. The default order is 1: Time, 2: X, 3: Y, 4: Z, 5: I. If there are more returns in a line they will be read automatically based on the format specification.

Separator Select how the values in the input files are separated.
Options:
-Space
-Comma
-ArcView Format (1, X, Y, Z)

X Offset Define the value to be subtracted from X coordinates (the units are the same as for the X coordinates). Default value is 0, but sometimes different value could be necessary.

Y Offset Define the value to be subtracted from Y coordinates (the units are the same as for the Y coordinates). Default value is 0, but sometimes different value could be necessary.

File Type Select the input file type.
Options:
-Generic ASCII
-LAS format

Format Specification / Output Format Group Box:

Check boxes Specify output file format. Default is the same as the default input file format: 1: Time, 2: X, 3: Y, 4: Z, 5: I. The example setting above shows the output order: X Y I. If the user wants to create input file for the LiDAR target selection step, the output format has to be: X, Y, Z, I !!!

Returns Select LiDAR returns to be written to the output file. Up to 5 returns can be selected. The software automatically recognizes how many returns are in the input file, and if the selected return number for output is larger than that, the software neglects those user return selections.

Separator Specify how the values in the output files to be separated.
Options:
-Space
-Comma
-ArcView Format (1, X, Y, Z)

Select Points Define which points to be written to the output file.
Options:
-All: write out every point in the input file
-Every Nth point: write out every Nth point of the input LiDAR file
If this option is selected, N has to be specified in the text field next to the option.

Format Specify that the LiDAR returns for one GPS time tag are written to separate lines in the output file or in one line.
Options:
-Separate Lines
-One Line
Necessary to select only if more than one LiDAR return is written to the output file.

Log File Has no functionality at this point

Processing Status Show the number of lines of the input file that have been processed, and indicate the end of processing.

Process Read and write out specified ASCII LiDAR file or LAS file to specified output format

OK Save window settings

Cancel Quit

2.2. Target Selection

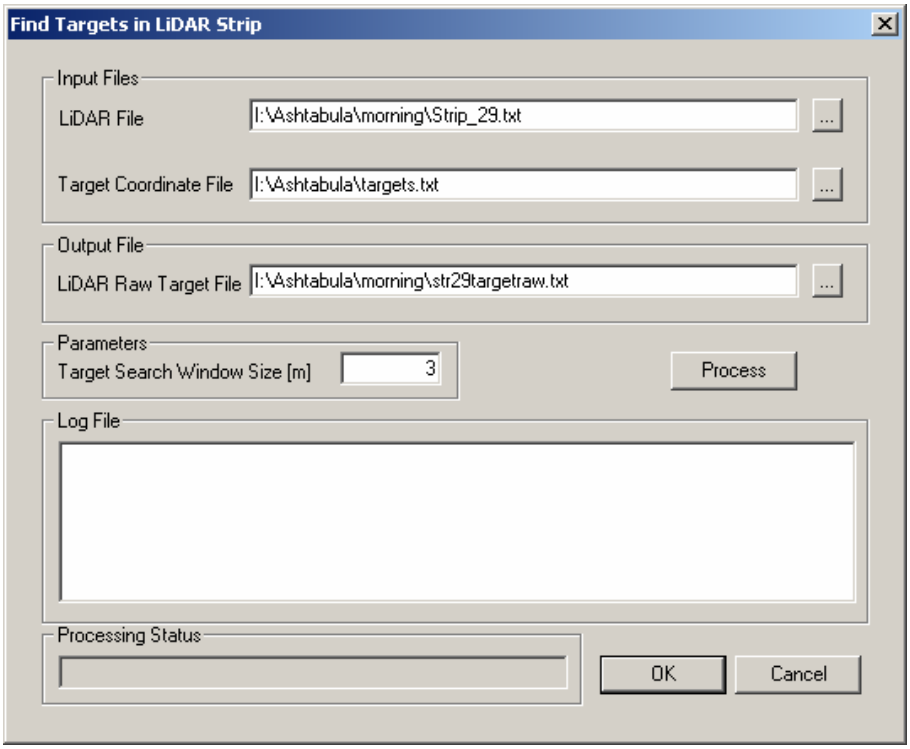

Objective:
Select target areas with defined window size from the input LiDAR strip for further processing. The output is a raw target file containing all the targets (windows with defined size around targets) from the target list found in the LiDAR strip.

Input Files Group Box:

LiDAR File LiDAR file is required to be in X Y Z I format and must contain one return.

Target Coordinate File This file is the GPS measured target coordinate list in format: ID X Y Z. The target ID has to be integer!

Output File Group Box:

LiDAR Raw Target File The output file, contains the list of LiDAR points in the target areas, the areas are identified with the target ID. The format is: ID X Y Z I

Parameters Group Box:

Target Search Window Size	Define the rectangular window size for target area selection. Default is 3m for the 2m target circle radius. Selected size depends on the maximum expected horizontal error in the LiDAR strips.
Log File	Has no functionality at this point
Processing Status	Show the number of lines of the input file that have been processed, and indicate problem with opening the input files and the end of processing.
Process	Select target areas from input LiDAR file
OK	Save window settings
Cancel	Quit

After selecting the LiDAR points at the target areas, the next step is to identify the target points and determine the target circle origin coordinates.

2.3. Target Identification

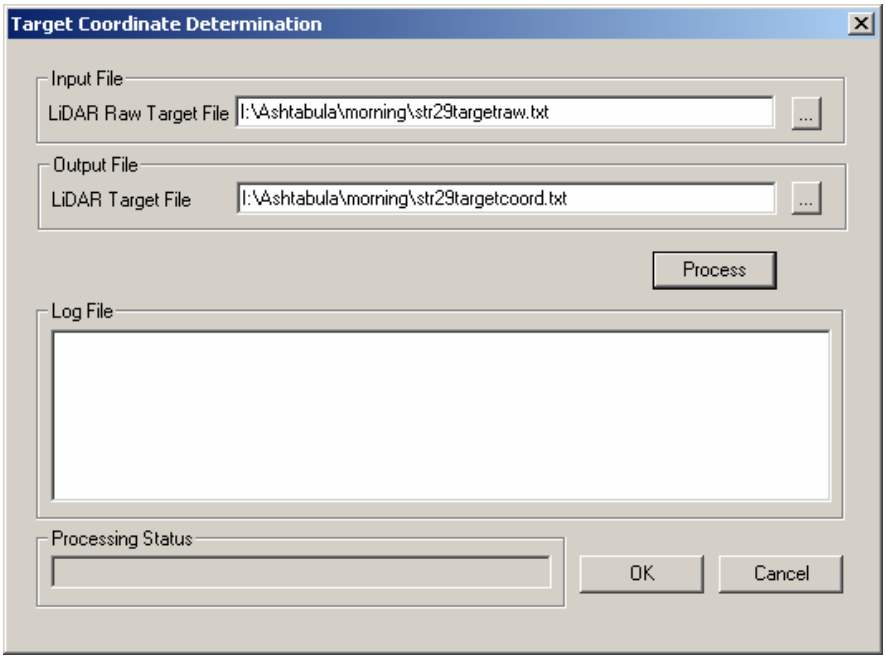

Objective:
Select target points (LiDAR points fallen on the targets) from the raw LiDAR target file based on intensity and elevation and determine target center coordinates in the LiDAR data together with their standard deviation and diagnostic parameters.

Input File Group Box:

LiDAR Raw Target File This file is the output file of the target selection step.

Output File Group Box:

LiDAR Target File The determined target coordinates with standard deviation values and diagnostic parameters will be written to this file.

Output File format:

ID	X	Y	Z	Std X	Std Y	Std Z	#inner	#outer	X size	Y size	flag

where

ID	Target ID
X	X coordinate of target circle origin
Y	Y coordinate of target circle origin
Z	Z coordinate of target circle origin

Std X	Standard deviation of determined X position
Std Y	Standard deviation of determined Y position
Std Z	Standard deviation of determined Z position
#inner	Number of LiDAR points on inner target circle
#outer	Number of LiDAR points on outer target ring
X size	Size in X direction of patch of all possible circle origin locations
Y size	Size in Y direction of patch of all possible circle origin locations
flag	Indicates if the determined target position was found to be valid or not (1/0)

The identified target points are subject to various acceptance tests and the determined target is accepted (gets flag 1) only if it passes each test.

Log File Show determined target positions together with standard deviations and diagnostic parameters.

Processing Status Indicate problems with opening the input file and the end of processing.

Process Determine target coordinates

OK Save window settings

Cancel Quit

Once the targets are identified in the LiDAR strip and their coordinates are determined, the next step is to find the optimal transformation for the strip based on the targets and transform the strip.

2.4. Strip Transformation

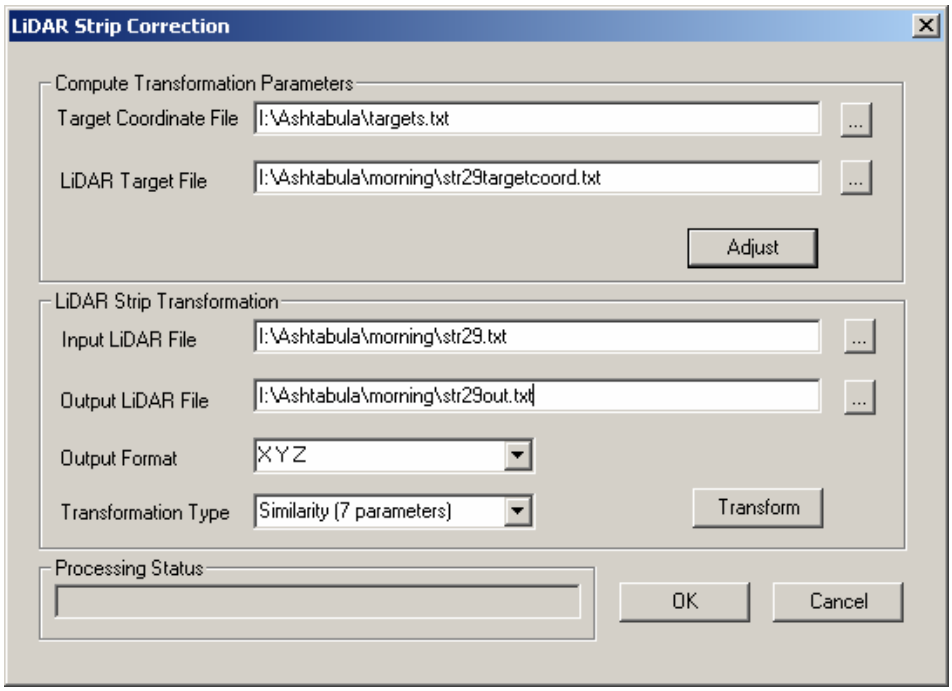

Objective:
Select optimal transformation for the LiDAR strip and transform the strip using the selected transformation.

2.4.1. Select optimal transformation for the LiDAR strip:

Compute Transformation Parameters Group Box:

Target Coordinate File — File containing the GPS measured target circle origin coordinates. The file format is: ID X Y Z
The target ID must be integer !!!

LiDAR Target File — This file is the output of the target identification step. It contains the determined target coordinates and their standard deviation for the target IDs together with some diagnostic parameters.

Adjust Button — Opens Adjustment Window

Adjustment Window:

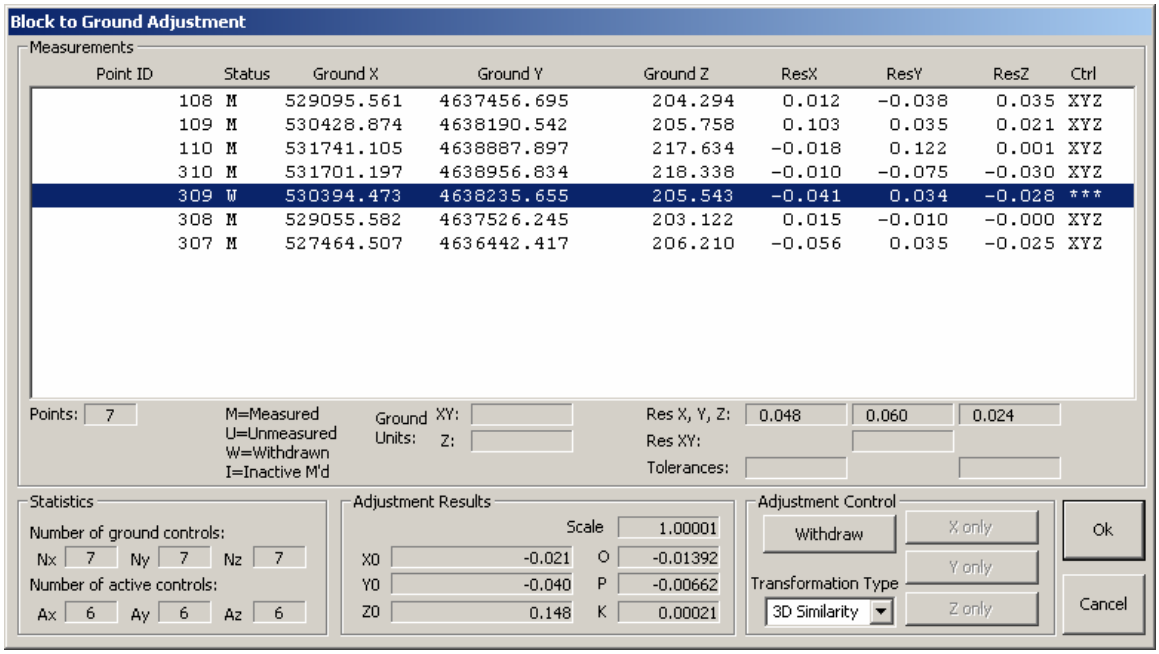

Measurements Group Box:

The Measurement Group Box lists all the targets in the strip with target ID, X, Y, Z coordinates and X, Y, Z residuals after applying a user defined transformation on the targets. Initially the coordinate errors at the target locations (difference between target coordinates in the LiDAR data and GPS measured target coordinates) are displayed. The window also shows the Status of the targets, namely, if they are part of the transformation coefficient calculation (M) or withdrawn (W) from the adjustment, or were not accepted by the target identification algorithm (has flag 0) as valid target coordinates (U). To withdraw a target from the transformation calculation, select the target by clicking on it and click on the Withdraw button. Pushing the Withdraw button twice will result in that the target will again be part of the adjustment.

Point ID is the first column in the list box that displays the point names.

Status is the second column in the list box that displays the status of the targets. The status includes `U` (unmeasured), `M` (measured), and `W` (withdrawn). A withdrawn target is not used in the computation of the transformation coefficients. However, its coordinates are transformed with the calculated coefficients and compared with the target control coordinates. The differences are then displayed in the respective residuals columns.

GroundX is the third column in the list box that displays the determined X-coordinate of the LiDAR targets in the LiDAR data.

GroundY is the fourth column in the list box that displays the determined Y-coordinate of the LiDAR targets in the LiDAR data.

GroundZ is the fifth column in the list box that displays the determined Z-coordinate of the LiDAR targets in the LiDAR data.

ResX is the sixth column in the list box that displays the X-coordinate residual for the targets after the strip transformation.

ResY is the seventh column in the list box that displays the Y-coordinate residual for the targets after the strip transformation.

ResZ is the eighth column in the list box that displays the Z-coordinate residual for the targets after the strip transformation.

Ctrl is the last column in the list box that displays *(XYZ)* for targets that take part in the computation of transformation coefficients, and *(***)* for targets that are either not accepted as reliable targets (has flag 0) or are withdrawn from the adjustment.

Points is a display-only text box that displays the number of targets.

Ground XY Inactive for this version of the software

Units Inactive for this version of the software

ResX, Y, Z are three display-only text boxes that display the RMS (root mean square) residuals respectively in X, Y, Z coordinates. These values are computed from the individual residuals of all targets that are not U (unmeasured).

ResXY Inactive for this version of the software

Tolerances Inactive for this version of the software

Statistics Group Box:

Nx Number of X controls, for this version equals to the number of

	targets
Ny	Number of Y controls, for this version equals to the number of targets
Nz	Number of X controls, for this version equals to the number of targets
Ax	Number of active X controls, for this version equals to the number of targets that were measured and not withdrawn
Ay	Number of active Y controls, for this version equals to the number of targets that were measured and not withdrawn
Az	Number of active Z controls, for this version equals to the number of targets that were measured and not withdrawn

Adjustment Results Group Box:

Shows the calculated transformation coefficients; in case of 3D similarity transformation (Scale, X0, Y0, Z0, O (omega in degrees), P (phi in degrees), K (kappa in degrees)), for vertical shift, only naturally Z0 is shown, and for 3D affine transformation no coefficients are displayed.

X0	Shift in X direction
Y0	Shift in Y direction
Z0	Shift in Z direction
Scale	Scale factor
O	Rotation angle along X-axis (omega)
P	Rotation angle along Y-axis (phi)
K	Rotation angle along Z-axis (kappa)

Adjustment Control Group Box:

Withdraw	To withdraw a target from the transformation calculation. To withdraw a target from the transformation coefficient

calculation, select the target by clicking on it and click on the Withdraw button. Pushing the Withdraw button twice will result in that the target will again be part of the adjustment.

Adjustment Type Three different transformation types can be applied:

- Vertical Shift

One parameter transformation, minimum one target is required.

- 3D Similarity

Seven parameter 3-dimensional similarity transformation, minimum 3 targets are required.

- 3D Affine

Twelve parameter 3-dimensional affine transformation, minimum 4 targets are required.

- None

No transformation is applied on the targets; the original errors at the target locations are displayed.

By changing the selected transformation or withdrawing a target from the adjustment, the transformation coefficients are automatically recalculated and the residuals at the target locations are refreshed. The actual transformation parameters are saved automatically to a parameter file. There are three separate parameter files for the three types of transformations. If the same transformation type is calculated many times with different targets included, the parameter file will contain the transformation coefficients from the last transformation.

OK Saves the actual window settings and quits
Cancel Quits the transformation window

After selecting the optimal transformation for the LiDAR strip, the next step is to transform the whole LiDAR strip based on the selected transformation.

2.4.2. Transform LiDAR strip

LiDAR Strip Transformation Group Box (of LiDAR Strip Transformation dialog box):

Input LiDAR File The input LiDAR file to be transformed. It has to be in X Y Z format.

Output LiDAR File The output file that will contain the transformed LiDAR strip.

Output Format	Define the output file format. Options: • X Y Z • X,Y,Z • 1, X, Y, Z (ArcView format)
Transformation Type	Define the transformation type. Options: • Vertical Shift (1 parameter) • Similarity (7 parameter) • Affine (12 parameter) The calculated transformation parameters from the adjustment step are saved in parameter files. One separate file is created for each transformation type, the vertical shift, the 3D similarity and the 3D affine transformations.
Transform	Transform LiDAR strip
Processing status	Show the number of lines of the input file that have been processed, and indicate problem with opening the input files and the end of processing.
OK	Save dialog box settings
Cancel	Quit the LiDAR Strip Transformation dialog box